Trinity College Dublin
Coláiste na Tríonóide, Baile Átha Cliath
The University of Dublin

PhD Thesis

Compact Beamforming Antennas for IoT-Enabled Directional Modulation and Localization

Author:
Abel Zandamela

Supervisor:
Prof. Adam Narbudowicz

Co-supervisor:
Prof. Nicola Marchetti

28th March 2024

Declaration

I declare that this thesis has not been submitted as an exercise for a degree at this or any other university and is entirely my own work.

I agree to deposit this thesis in the University's open access institutional repository or allow the Library to do so on my behalf, subject to Irish Copyright Legislation and Trinity College Library conditions of use and acknowledgement.

I consent to the examiner retaining a copy of the thesis beyond the examining period, should they so wish (EU GDPR May 2018).

Signed:

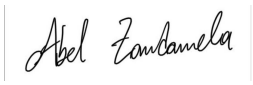

Abel Zandamela, 28th March 2024

Summary

In recent years, there has been a considerable focus in various research domains directed towards the miniaturization of wireless communication devices. This increasing demand for highly compact systems is a growing trend to facilitate cutting-edge technologies like the Internet of Things (IoT). In this regard, a fundamental component of wireless communication systems is the antenna that transmits or receives the radio waves, enabling information broadcast. With the rapidly expanding number of IoT applications, increasing constraints are placed on the available space for antenna installation while demanding more functionalities like beamforming and multi-band operation. The beamforming technology is critical to enable the control of the shape and direction of the antenna generated radiation pattern. This, in turn, enhances the overall wireless link by providing improved antenna gain, enhanced Signal-to-Noise Ratio (SNR), elimination of undesired interference, and enabling several modern applications like localization in terms of Angle of Arrival (AoA) and emerging physical layer security techniques like Directional Modulation (DM).

Traditionally, antenna arrays have been applied to realize flexible beamforming properties to enable AoA measurements and DM techniques. However, antenna arrays comprise a set of radiators requiring inter-element spacing of typically half of the free space wavelength at the antenna center operating frequency. Such a requirement makes the final structure too bulky for integration into compact IoT devices, especially those operating on the Sub-6 GHz frequency bands. Miniaturization of classical arrays can be accomplished by reducing the inter-element spacing. However, such miniaturization usually results in stronger mutual coupling between the elements, which leads to undesired effects like the radiation of distorted antenna pattern, reduced gain, polarization mismatch, among other issues. This ultimately degrades the beamforming characteristics and the performance of AoA-based localization and DM security approach.

The main goal of this thesis is to address the problem of performing beamforming while using miniaturized antennas. This thesis contributes to this issue by proposing novel beamforming solutions based on the theory of Spherical Modes. The work also highlights the benefits of using Spherical Modes Beamforming (SMB) antennas to enable AoA estimation and DM in small IoT platforms, and provides a framework linking the SMB characteristics with the performance metrics of both AoA estimation and DM techniques. Although the SMB solution provides significant miniaturization compared to classical arrays, non-planar geometries and single-band operation may still be limiting factors for its integration in emerging compact IoT devices, like on-body systems. This thesis addresses those limitations by introducing planar antennas capable of performing beamforming within the upper hemisphere and extending the SMB principle to support multi-band operation.

Acknowledgements

This thesis is a result of the research carried out during my four years as a Doctoral student in CONNECT, the Science Foundation Ireland Research Centre for Future Networks and Communications, at Trinity College Dublin, the University of Dublin, under the supervision of Prof. Adam Narbudowicz and co-supervision of Prof. Nicola Marchetti. The work was supported by Science Foundation Ireland under grant number 18/SIRG/5612 and in part by grant number 13/RC/2077_P2. For this, I am immensely grateful. During these years, a few other grants were essential for completing the work. For this, I am indebted to the Institute of Electrical and Electronics Engineers (IEEE) Antennas and Propagation Society C. J. Reddy travel grant, TICRA, the European Association on Antennas and Propagation (EurAAP), and the IEEE Antennas and Propagation Society Doctoral Research Grant.

I would like to express my deepest gratitude to my supervisor for his invaluable guidance, constructive criticism, incredible learning opportunities, unwavering kindness, patience, and encouragement, as without him, this dissertation would not have been possible. I am eternally grateful for his help, trust he placed in me since my years as a Master student, for all the discussions, ideas, and continuous support that often extended far beyond academic research. I am forever indebted to my co-supervisor for all the support, mentorship, productive discussions, unfailing kindness, and motivation, which were critical throughout this work and helped me improve many aspects of my research path. Without his dedication, this thesis would not have been possible. I would like to express my sincere gratitude to Prof. Max Ammann from the Antenna and High Frequency Research Centre at the Technological University Dublin for all the support, guidance, motivation, and brilliant suggestions throughout these years. I would also like to thank Prof. Stefano Sanvito for his support as a member of my Doctoral Committee. I would also like to thank Prof. Anja Skrivervik and Prof. Arman Farhang for reviewing this thesis, for the brilliant comments and suggestions.

I would like to extend my appreciation to Prof. Alessandro Chiumento from the University of Twente for his invaluable insights throughout this work. I am also forever indebted to Prof. Suramate from King Mongkut's University of Technology North Bangkok for his guidance and collaboration, which have been an immeasurable part of my career progression.

I would like to thank all my colleagues in CONNECT, the School of Engineering, and the School of Computer Science and Statistics. Your professionalism, kindness, and support have been key to my research. To Felix, Jeremias, Tomas, Bekti, Valentina, Lara, Priyanka, Tahar, Fadhil, Andre, Arijeet, Agastya, Pieter, Mouli, Jean-Baptiste, Jawad, Prakorn, Linta, Danh, Stefan, Merim, Harun, Sandeep, Sumaiya, Bruno, Yan, and Everson, the friendship, laughter, food, support, and kindness has been an essential element since I arrived in Dublin. My genuine appreciation also extends to Jakub, Khatereh, Neeraj, Irina, Wong, Hossein, and Wasi from the Antenna and High Frequency Research Centre at Technological University Dublin for the productive interactions, learning opportunities, constant support, friendship, smiles, and unshakable kindness.

I am deeply grateful for my family's support. Thank you for the love and inspiration, which have given me strength throughout all the difficult times during these years. I am beyond thankful to my beloved partner, Ping. I could never give enough credit for her sacrifices, immeasurable support, encouragement, patience, perseverance, trust, hopes, dreams, and endless love, which have made the road to this dissertation especially sunny. This achievement is as much yours as it is mine. Finally, I would like to express my deepest gratitude to my dear parents, Abdul and Alice. I am forever grateful for their love, encouragement, guidance as a person, and all other things that I cannot possibly express in these pages or words. I hope that completing this thesis fills you with joy and pride and that one day, I can give back all the kindness, support, love, happiness, and life you gave me.

Acronyms

AHFR Antenna and High Frequency Research

AoA Angle of Arrival

APs Access Points

AUT Antenna Under Test

AWGN Additive White Gaussian Noise

BER Bit Error Rate

CAD Computer-Aided Design

DM Directional Modulation

ESA Electrically Small Antenna

ESAs Electrically Small Antennas

EurAAP European Association on Antennas and Propagation

FEM Finite Element Method

FCC Federal Communications Comission

FDTD Finite Difference Time Domain

FNBW First Null BeamWidth

FoV Field of View

FS Free Space

FSH Folded Spherical Helix

HPBW Half-Power BeamWidth

IBW Impedance BandWidth

ICNIRP International Commission on Non-Ionizing Radiation Protection

IEEE Institute of Electrical and Electronics Engineers

IoT Internet of Things

IQ In-phase and Quadrature

LoS Line of Sight

MAE Mean Absolute Error

MIMO Multiple Input Multiple Output

MUSIC Multiple Signal Classification

OB On-Body

OFDM Orthogonal Frequency-Division Multiplexing

PCB Printed Circuit Board

QPSK Quadrature Phase-Shift Keying

RL Return Loss

Rx Receiver

SAR Specific Absorption Rate

SLL Side Lobe Level

SMB Spherical Modes Beamforming

SNR Signal-to-Noise Ratio

TE Transverse Electric

TM Transverse Magnetic

Tx Transmitter

UCA Uniform Circular Array

UCAs Uniform Circular Arrays

ULA Uniform Linear Array

ULAs Uniform Linear Arrays

VNA Vector Network Analyzer

1D One-Dimensional

2D Two-Dimensional

3D Three-Dimensional

Nomenclature

$(.)^*$	conjugate
$[.]^{\mathrm{T}}$	vector or matrix transpose operation
$[.]^{\mathrm{H}}$	hermitian operation
$\boldsymbol{A}$	matrix $\boldsymbol{A}$
$\boldsymbol{I}$	identity matrix
$\Delta\psi_n$	phase shift for port n
ϵ	permittivity of the medium
ϵ_r	relative permittivity
η	specific impedance of the medium
λ	free space wavelength
$\mathbb{C}$	set of complex numbers
$\mathbb{C}^{M\times N}$	an $M \times N$-dimension linear space in complex domain
$\mathbb{E}\{.\}$	statistical expectation
μ	permeability of the medium
$\nabla \times \vec{C}$	curl of $\vec{C}$
$\neg$	negation
$\neq$	not equal

ω	angular frequency
ϕ	azimuth angle
ψ_n	phase value of port n
ρ	electric charge density
σ	electrical conductivity
$\sum$	sum
θ	elevation angle
$\vec{a}$	vector $\vec{a}$
$\vec{C}$	electric or magnetic field
$\vec{E}$	electric field
$\vec{F}$	spherical mode functions
$\vec{H}$	magnetic field
$\vec{J}$	electric current density
$\vec{K}$	far-field spherical mode patterns
$\vec{M}$	magnetic current density
$\vec{Q}$	spherical modes coefficients
$\wedge$	and
a	scalar a
D	directivity
e_{rad}	radiation efficiency
e_{tot}	total efficiency
f	generating function

f_0 center frequency

G antenna gain

G_{real} realized gain

P_{accep} power accepted by the antenna

P_{rad} radiated power

P_{source} power generated by the source

R_{in} input resistance

R_{loss} loss resistance

R_{rad} radiation resistance

U_{int} radiation intensity

U_{iso} radaition intensity of isotropic antenna

X_{in} input reactance

Z_{in} input impedance

Z_{source} source impedance

Contents

List of Figures

List of Tables

1 Introduction

Introduction

1.1 Overview

Over recent years, the Internet of Things (IoT) technology has become indispensable, expanding to fields like healthcare, localization and tracking, environmental monitoring, smart homes, and manufacturing processes. Despite this rapid growth, security issues still pose complex challenges to IoT technology, especially for small-scale IoT systems like on-body devices [1–3]. A few reasons contribute to these security issues, and they mainly arise because small-scale IoT platforms are resource-constrained systems [3–5]. Therefore, among other constraints, they present low computational power, are battery-operated, and have limited space to install the antenna component responsible for wireless transmissions. Such constraints may limit the use of sophisticated encryption techniques that modern wireless communications rely on to enable secure transmissions [6–8]. Combining these limitations with the broadcast nature of wireless communications translates into sensitive personal data being transmitted in an open wireless medium, where undesired users may retrieve the transmitted information for malicious purposes.

Physical layer security approaches are becoming popular techniques to enhance the security aspects of modern wireless communications [9–11]. In this approach, the physical characteristics of the wireless propagation channel, like noise, fading, and interference, are exploited to improve the secrecy of the transmitted data at the physical layer. Because of this fundamental property, i.e., enhancing the security of wireless transmissions based on the exploitation of the physical layer characteristics, such security solutions may be suitable to tackle the security of resource constrained IoT systems.

Directional Modulation (DM) is among some of the most popular physical layer se-

curity techniques [11–13]. It is a direction-dependent approach where the symbols of the transmitted data are spatially scrambled in undesired directions by using artificially generated noise, while this noise cancels out in the desired secure direction to enable correct transmission of the symbols [12, 14, 15]. Although the solution attracted much research, its standard implementation relies on the beamforming characteristics of classical antenna arrays. However, traditional arrays still present a challenge for installation in small IoT devices due to their inter-element spacing requirements [16].

Another essential aspect to highlight is that DM is based on the assumption of a predefined direction for secure data transmission. It is, therefore, ideal that the transmitting device can perform localization to determine the desired user's direction. A popular approach to perform localization is via the Angle of Arrival (AoA) estimation [17], where the phase difference as the signals impinge at different elements of the antenna array is used.

Similarly to DM, a critical issue that limits the implementation of AoA estimation in small IoT devices is the requirement for antenna arrays. This problem is mainly seen for applications operating at sub-6 GHz frequency bands, where the antenna arrays become over-sized for small IoT platforms due to the inter-element spacing, which typically needs to be $\lambda/2$ (where λ is the wavelength at the center operating frequency). Such size requirements are challenging to realize with the increasing miniaturization trends of small IoT devices, like those used in smart home applications, on-body systems, and others.

To address the above challenges, the aim of this thesis is to:

- Investigate the current limitations of antenna arrays comprising closely spaced elements for DM and AoA estimation.
- Identify drawbacks of available compact beamforming concepts to enable DM and AoA estimation.
- Propose a number of novel antenna designs, that support advanced beamforming from compact devices.
- Demonstrate the benefits of the proposed antennas for advanced IoT applications from small platforms, i.e., AoA-based localization and DM.
- Investigate the suitability of Electrically Small Antennas (ESAs) for DM applications.

- Investigate the feasibility of planar beamforming antennas for integration within on-body IoT devices.
- Propose novel planar multi-band compact antenna designs to realize advanced beamforming characteristics in on-body IoT applications.

1.2 Contributions

The novel contributions of this thesis are summarized here below:

- A beamforming principle based on the theory of *spherical modes*. The method exploits different phase characteristics of excited omnidirectional *spherical modes* to realize beamforming within a miniaturized antenna size. The beamforming solution allows to effectively direct the antenna generated main beam across the entire azimuthal plane, with advanced design flexibility, e.g. using co-located antennas or annular rings, while also providing good efficiency and gain characteristics.
- Design of compact antennas based on the above principle to realize beamforming characteristics to enable DM and AoA estimation in small IoT platforms.
- Design of a compact antenna for Three-Dimensional (3D) beamforming. Its performance is extended to enable dual-plane DM, i.e., realize secure transmissions across the horizontal and elevation planes.
- Design of a stacked-patch antenna for DM and AoA estimation from on-body IoT devices.
- Design of an electrically small 3D beamforming antenna.
- Design of planar 3D beamforming antennas to realize DM and AoA from on-body IoT devices.
- Design of planar dual-band beamforming antenna for on-body IoT devices.

1.3 Methodology

To evaluate the performance of the proposed antennas for DM and AoA estimation, this thesis uses a multi-disciplinary approach that combines the antenna design with the desired

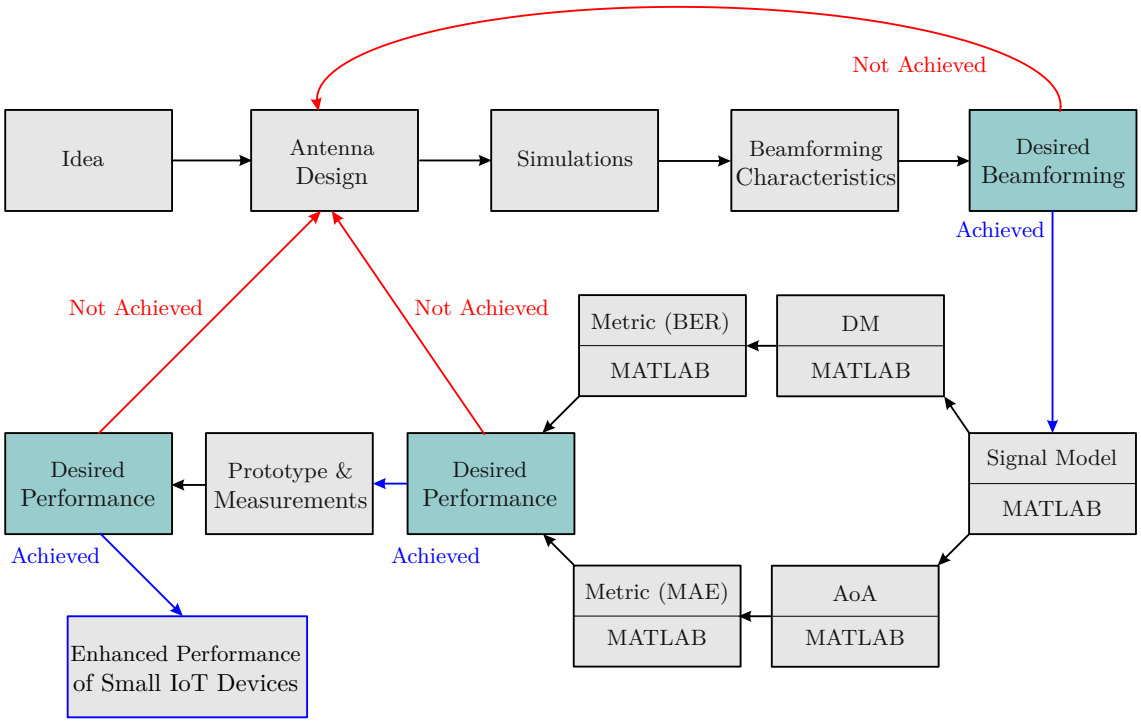

Figure 1.1: Schematic outlining the research methodology used in this thesis.

transmission directions. Since the beamforming characteristics dictate the transmission directions, the methodology approach allows for calculating performance metrics for DM and AoA estimation. The DM metric for this work is based on Bit Error Rate (BER) computations obtained by the ratio of bit errors and the total number of transmitted bits. For the AoA estimation, the Mean Absolute Error (MAE) is used as the performance metric. It is computed considering the actual AoA and the angle computed using an estimation algorithm. Since the performance metrics for DM and AoA estimation are not fundamental antenna parameters, the methodology used in this thesis provides a design flow to calculate the required system parameters (i.e. BER and MAE) from antenna measurements or simulation.

Fig. 1.1 outlines the methodology, which begins with the idea for the antenna design. Once the idea is theoretically validated, full-wave simulations are conducted using a 3D electromagnetic Computer-Aided Design (CAD) tool, specifically CST Studio Suite [18]. The following steps comprise analyses of the beamforming characteristics of the proposed models. If the expected performance is realized, the response of the antenna is modeled using the

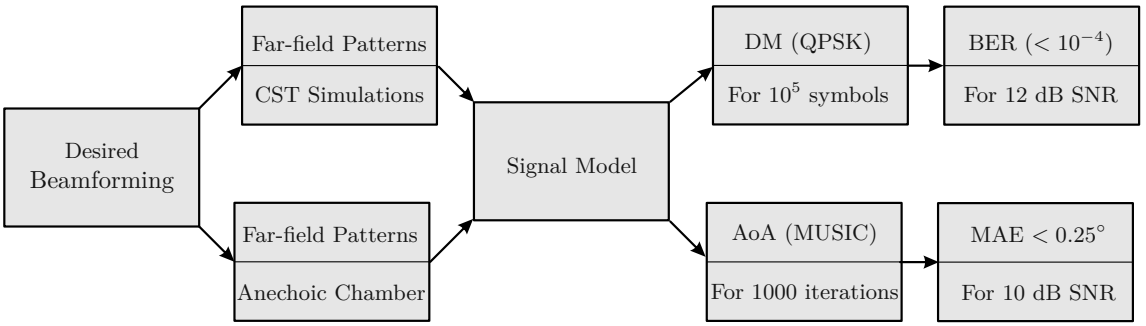

Figure 1.2: Schematic outlining the methodology used for testing the performance of the proposed antennas for DM and AoA estimation applications.

MATLAB tool [19]. Next, the performance metrics for DM and AoA are computed to evaluate the efficacy of the proposed antennas. The antenna is prototyped if the required BER and MAE performance are obtained. This is done using the LPKF Proto Mat C60 milling machine [20] available at the Antenna and High Frequency Research (AHFR) Centre of Technological University Dublin. The LPKF machine allows to shape the metallic layer on the Printed Circuit Board (PCB) and drill holes for the shorting pins used in some designs. The fabricated antenna is tested using a four-port Vector Network Analyzer (VNA), the ZVA-40 from Rohde & Schwarz [21]. The VNA is used to measure the reflection and transmission coefficients of the proposed antennas. Next, the anechoic chamber from AHFR Centre in Technological University Dublin is used to perform antenna radiation patterns and realized gain measurements. The chamber gives the far-field measurements using the ZVA-40 VNA and a Schwarzbeck BBHA 9120 D horn antenna [22].

Since the work aims to obtain an optimal antenna design, the methodology becomes an optimization cycle where the antenna characteristics are modified to achieve the required BER and MAE values for DM and AoA estimation, respectively. Fig. 1.2 shows the actual procedure used to optimize the performance of DM and AoA estimationapplications. It can be seen that once the desired beamforming characteristics are realized in both the simulated and measured cases, the corresponding far-field patterns are extracted and the signal modelling is done in MATLAB. The DM performance is tested using Quadrature Phase-Shift Keying (QPSK) and a total of 10^5 symbols are used to compute the BER. Finally, the optimization loop is considered satisfactory once the BER is smaller than 10^{-4} is realized for a Signal-to-Noise Ratio (SNR) level of 12 dB. Next, for the AoA estimation

performance, the Multiple Signal Classification (MUSIC) algorithm is used and a total of 1000 Monte Carlo runs are conducted to compute the MAE, where the optimization process is completed once the MAE is smaller than 0.25° for a SNR level of 10 dB. It is essential to highlight that this optimization cycle includes analyses of different factors that may create discrepancies between the simulated and measured performances. These may include manufacturing and dielectric substrate tolerances, among other factors. Lastly, because some chapters involve discussion of on-body antennas, the optimization will first include the free space scenario cycle, followed by the on-body cases tested with multi-layer phantoms. For experimental validations, pork trunks are used during the S-parameters and anechoic chamber measurements.

1.4 Thesis Outline

The outline of this thesis is shown in Fig. 1.3. Chapter 2 reviews the fundamental antenna parameters related to the performance of the proposed compact beamforming antennas. This chapter provides a literature review of DM, AoA estimation, and limitations of state-of-the-art compact beamforming antennas in enabling the above mentioned technologies.

Chapter 3 introduces the concept of *Spherical Modes Beamforming (SMB)*. The chapter provides a comprehensive treatment of the *spherical modes* topic and describes how it is applied to realize the proposed beamforming. The chapter finishes with a discussion of full-wave simulation results of a compact antenna design, which is used to demonstrate how the proposed beamforming can be implemented in practical scenarios and how a given omnidirectional *spherical mode* can be excited.

Chapter 4 first highlights the challenges related to mutual coupling mitigation when estimating AoA for closely spaced ESAs. Next the chapter presents the implementation of *SMB* antennas for AoA estimation and the respective performance. The chapter provides a detailed discussion on the signal modelling of the *SMB* antennas response, the MUSIC algorithm, and the MAE computation.

Chapter 5 discusses the use of *SMB* antennas for DM applications and its respective performance. The chapter also provides a comprehensive formulation of the DM technique

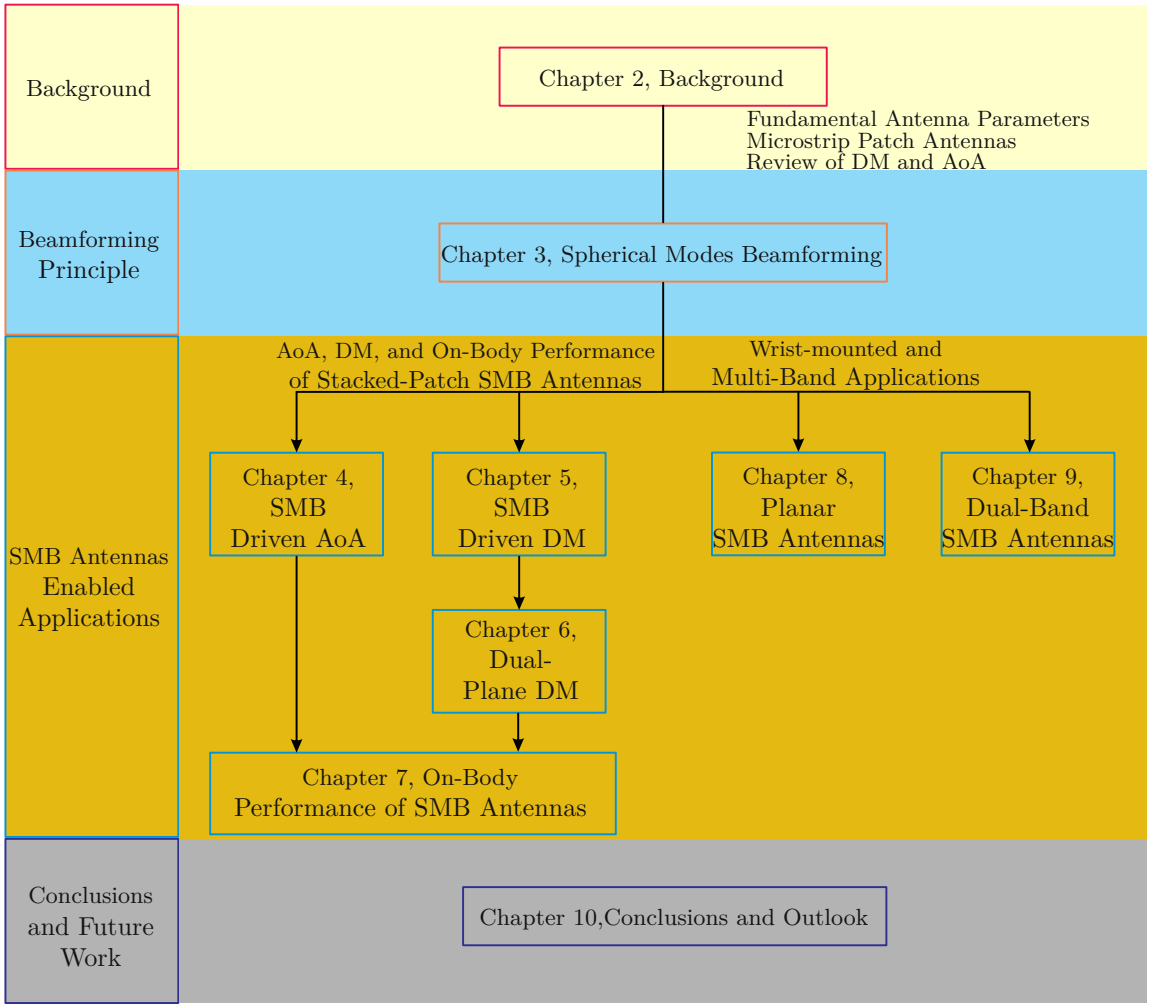

Figure 1.3: Outline of this thesis.

and how the BER performance metric is computed.

Chapter 6 proposes compact 3D beamforming antennas to expand the DM principle discussed in the previous chapter to a dual-plane DM scheme. The new schem DM enables secure transmission in both the azimuthal and the elevation planes. This chapter also proposes ESAs that offer 3D beamforming characteristics to realize dual-plane DM.

Chapter 7 investigates the performance of the proposed *SMB* antennas for on-body IoT applications. This chapter studies both the DM and AoA techniques in an on-body scenario via the use of a multi-layer forearm phantom. The chapter is limited to full-wave simulation analyses, with on-body measurements validations of the *SMB* principle conducted for more advanced antennas in the following chapters.

Chapter 8 introduces planar *SMB* antennas for on-body IoT applications, specifically

for wrist-mounted smart watch devices. The chapter first provides a framework on how a *SMB* planar antenna with azimuthal beamforming properties can be modelled. Next, this principle is extended to support 3D beamforming properties and is validated for on-body IoT applications using full-wave simulations and anechoic chamber measurements.

Chapter 9 proposes a concept to realize planar multi-band *SMB* antennas. The principle is demonstrated using a compact dual-band antenna which is also tested for on-body IoT applications. This chapter also provides full-wave simulations and anechoic chamber measurements to experimentally validate the proposed concept.

Lastly, Chapter 10 outlines the conclusions of this thesis. This chapter provides a summary of the main findings of the thesis, highlights the relevance of these results, and outlines future challenges that need to be addressed to further enhance the beamforming, security and localization capabilities from small IoT devices.

1.5 Dissemination

This section lists the dissemination efforts during the project.

Patent applications

1. A. Zandamela, A. Narbudowicz, "*Ultrathin Fully Planar Compact MIMO and Beam-steering Antenna for Smart Watches and other Wrist-Wearable Devices*," UK Patent Office, Application No. 2212785.6, filed on 29$^{\text{th}}$ Aug. 2022.

Journal Publications

1. A. Zandamela, N. Marchetti, Max J. Ammann, and A. Narbudowicz, "Dual-Band Compact MIMO Antenna for Directional Modulation Applications," *IEEE Transactions on Antennas and Propagation*, under review.
2. A. Zandamela, N. Marchetti, Max J. Ammann, and A. Narbudowicz, "A Dual-Band Planar Antenna for Angle of Arrival Estimation in On-Body IoT Devices," *IEEE Internet of Things Journal*, major revisions.
3. A. Zandamela, N. Marchetti, Max J. Ammann, and A. Narbudowicz, "3D Beam-Steering MIMO Antenna for On-Body IoT Devices," *IEEE Transactions on Antennas and Propagation*, 2024.

4. A. Zandamela, N. Marchetti, Max J. Ammann, and A. Narbudowicz, "Pattern and Polarization Diversity Multisector Annular Antenna for IoT Applications," *IEEE Transactions on Antennas and Propagation*, vol. 71, no. 9, pp. 7241-7249, Sept. 2023.
5. A. Zandamela, N. Marchetti and A. Narbudowicz, "Directional Modulation for Enhanced Privacy in Smart Watch Devices," *IEEE Antennas and Propagation Magazine*, vol. 66, no. 2, 2024.
6. A. Zandamela, Nicola Marchetti, Max J. Ammann, and A. Narbudowicz, "Spherical Modes Driven Directional Modulation with a Compact MIMO Antenna," *IEEE Antennas and Wireless Propagation Letters*, vol. 22, no. 3, pp. 477-481, March 2023.
7. A. Zandamela, A. Chiumento, N. Marchetti, Max J. Ammann, and A. Narbudowicz, "Exploiting Multimode Antennas for MIMO and AoA Estimation in Size-Constrained IoT Devices," *IEEE Sensors Letters*, vol. 7, no. 3, pp. 1-4, March 2023.
8. A. Zandamela, A. Chiumento, N. Marchetti, and A. Narbudowicz, "Angle of Arrival Estimation Via Small IoT Devices: Miniaturized Arrays vs MIMO Antennas," *IEEE Internet of Things Magazine*, vol. 5, no. 2, pp. 146-152, June 2022.
9. A. Narbudowicz, A. Zandamela, N. Marchetti, and Max J. Ammann, "Energy Efficient Dynamic Directional Modulation with Electrically Small Antennas," *IEEE Antennas and Wireless Propagation Letters*, vol. 21, no. 4, pp. 681-684, April 2022.
10. A. Zandamela, K. Schraml, S. Chalermwisutkul, D. Heberling and A. Narbudowicz, "Digital pattern synthesis with a compact MIMO antenna of half-wavelength diameter," Available Online: *AEÜ – International Journal of Electronics and Communications*, vol. 135, June 2021.

Conference Publications

1. A. Zandamela, N. Marchetti and A. Narbudowicz, "Low-Profile Electrically Small Antenna with Pattern and Polarization Diversity," *2024 European Conference on Antennas and Propagation (EuCAP)*, Galsgow, Scotland, 2024.
2. A. Zandamela, N. Marchetti and A. Narbudowicz, "Bandwidth-Enhanced Compact Beamsteering Antenna for IoT Platforms," *2024 European Conference on Antennas*

and Propagation (EuCAP), Galsgow, Scotland, 2024.

3. L. Antony, A. Zandamela, N. Marchetti and A. Narbudowicz, "Angle of Arrival Estimation Methods Using Spherical-Modes-Driven Multiport Antennas," *2024 European Conference on Antennas and Propagation (EuCAP)*, Galsgow, Scotland, 2024.
4. P. Pratoomma, A. Zandamela, S. Chalermwisutkul and A. Narbudowicz "Non-Contact Radio Frequency Level Sensor Based on Wheeler Cap," *2023 International Symposium on Antennas and Propagation (ISAP)*, Kuala Lumpur, Malaysia, 2023.
5. A. Narbudowicz and A. Zandamela, "Compact Beamforming Antennas for Directional Modulation in IoT," *2023 International Symposium on Antennas and Propagation (ISAP)*, Kuala Lumpur, Malaysia, 2023.
6. A. Zandamela, N. Marchetti and A. Narbudowicz, "Small Dual-Band 3D Beamforming MIMO Antenna," *European Microwave Conference*, Berlin, Germany, 2023, pp. 778-781.
7. A. Zandamela, N. Marchetti and A. Narbudowicz, "Flexible Multimode-Based Beamforming MIMO Antenna," *2023 European Conference on Antennas and Propagation (EuCAP)*, Florence, Italy, 2023.
8. A. Zandamela, N. Marchetti and A. Narbudowicz, "Energy-Efficient Physical Layer Security Method for Wearable IoT Devices," *2023 European Conference on Antennas and Propagation (EuCAP)*, Florence, Italy, 2023.
9. A. Zandamela, N. Marchetti and A. Narbudowicz, "Electrically Small Multimodal 3D Beamforming Antenna for PHY-Layer Security," *2023 European Conference on Antennas and Propagation (EuCAP)*, Florence, Italy, 2023.
10. A. Zandamela, N. Marchetti and A. Narbudowicz, "Compact Stacked-Patch Antenna for Directional Modulation in Azimuth and Elevation Planes," *IEEE International Symposium on Antennas and Propagation and USNC-URSI Radio Science Meeting (AP-S/URSI)*, Denver, CO, USA, 2022, pp. 1206-1207.
11. A. Zandamela, N. Marchetti and A. Narbudowicz, "Compact MIMO Antenna for MUSIC-Based Angle of Arrival Estimation in Wrist-Worn Devices," *2022 International Workshop on Antenna Technology (iWAT)*, Dublin, Ireland, 2022, pp. 227-230.
12. A. Zandamela, N. Marchetti and A. Narbudowicz, "Directional Modulation from a Wrist-Wearable Compact Antenna," *2022 European Conference on Antennas and*

Propagation (EuCAP), Madrid, Spain, 2022.

13. A. Zandamela, N. Marchetti and A. Narbudowicz, "Stacked-Patch MIMO Antenna for Dual-Plane Beamsteering," *2021 IEEE International Symposium on Antennas and Propagation and USNC-URSI Radio Science Meeting (AP-S/URSI)*, Singapore, Singapore, 2021, pp. 311-312.
14. P. Pratoomma, A. Zandamela, S. Chalermwisutkul and A. Narbudowicz, "Feasibility Study of an Industrial Moisture Content Sensor Based on Wheeler Cap," *2021 European Conference on Antennas and Propagation (EuCAP)*, Dusseldorf, Germany, 2021.

Presentations

1. A. Zandamela, N. Marchetti and A. Narbudowicz, "Small Dual-Band 3D Beamforming MIMO Antenna," *European Microwave Conference*, Berlin, Germany, 2023, pp. 778-781.
2. A. Zandamela, N. Marchetti and A. Narbudowicz, "Flexible Multimode-Based Beamforming MIMO Antenna," *2023 European Conference on Antennas and Propagation*, Florence, Italy, 2023.
3. A. Zandamela, N. Marchetti and A. Narbudowicz, "Energy-Efficient Physical Layer Security Method for Wearable IoT Devices," *2023 European Conference on Antennas and Propagation*, Florence, Italy, 2023.
4. A. Zandamela, N. Marchetti and A. Narbudowicz, "Electrically Small Multimodal 3D Beamforming Antenna for PHY-Layer Security," *2023 European Conference on Antennas and Propagation*, Florence, Italy, 2023.
5. A. Zandamela, N. Marchetti and A. Narbudowicz, "Directional Modulation for Enhanced Privacy in On-Body IoT Devices," *Inaugural School of Engineering Research Symposium (SERS)*, Dublin, Ireland, 2023.
6. A. Zandamela, N. Marchetti and A. Narbudowicz, "Compact Stacked-Patch Antenna for Directional Modulation in Azimuth and Elevation Planes," *IEEE International Symposium on Antennas and Propagation and USNC-URSI Radio Science Meeting (AP-S/URSI)*, Denver, CO, USA, 2022, pp. 1206-1207.
7. A. Zandamela, N. Marchetti and A. Narbudowicz, "Compact MIMO Antenna for

MUSIC-Based Angle of Arrival Estimation in Wrist-Worn Devices," *2022 International Workshop on Antenna Technology (iWAT)*, Dublin, Ireland, 2022, pp. 227-230.

8. A. Zandamela, N. Marchetti and A. Narbudowicz, "Directional Modulation from a Wrist-Wearable Compact Antenna," *2022 European Conference on Antennas and Propagation (EuCAP)*, Madrid, Spain, 2022.
9. A. Zandamela, N. Marchetti, Max Ammann and A. Narbudowicz, "Compact MIMO Antennas for Localization and PHY-layer Security in Wrist-Worn IoT Devices," *2022 CONNECT Plenary*, Waterford, Ireland, 2022.
10. A. Zandamela, N. Marchetti and A. Narbudowicz, "Stacked-Patch MIMO Antenna for Dual-Plane Beamsteering," *2021 IEEE International Symposium on Antennas and Propagation and USNC-URSI Radio Science Meeting (AP-S/URSI)*, Singapore, Singapore, 2021, pp. 311-312.

Non-Peer Reviewed Presentations

1. A. Zandamela, N. Marchetti and A. Narbudowicz, "Directional Modulation for Enhanced Privacy in On-Body IoT Devices," *Inaugural School of Engineering Research Symposium (SERS) Trinity College Dublin*, Dublin, Ireland, 2023.
2. A. Zandamela, N. Marchetti, Max Ammann and A. Narbudowicz, "Compact MIMO Antennas for Localization and PHY-layer Security in Wrist-Worn IoT Devices," *2022 Science Foundation Ireland CONNECT Research Centre Plenary*, Waterford, Ireland, 2022.

2 Background

Background

This chapter provides a comprehensive review of antenna theory concepts necessary to understand the performance of the compact antennas proposed in this thesis. The chapter is divided into two major parts. The first one presents a discussion of the fundamental antenna parameters and the configuration of the microstrip patch antenna. The second part provides a literature review of the Directional Modulation (DM) and Angle of Arrival (AoA) estimation techniques, while highlighting the current limitations of these solutions for implementation within compact integrated Internet of Things (IoT) devices.

2.1 Antenna Parameters

This section briefly reviews key antenna parameters that are used to evaluate the performance of the antennas investigated in this thesis.

2.1.1 Input Impedance

The input impedance of an antenna is defined in [23] as "the impedance presented by an antenna at its terminals or the ratio of the voltage to current at a pair of terminals". As shown in Fig. 2.1, the input impedance Z_{in} (Ω) is the circuit equivalent model of the antenna, which helps to easily characterize its behaviour when connected to an electrical circuit. The antenna input impedance as the ratio of the voltage to current at the terminals $a - b$ (see Fig. 2.1), is given as

$$Z_{\text{in}} = R_{\text{in}} + jX_{\text{in}}, \tag{2.1}$$

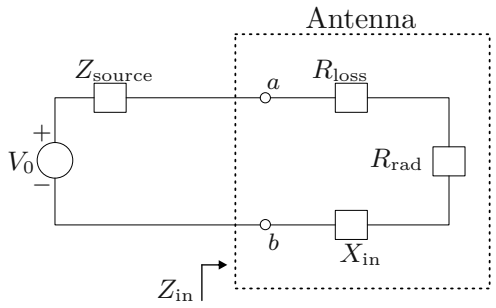

Figure 2.1: Circuit equivalent model of an antenna connected to a source.

where $R_{\text{in}}(\Omega)$ and $X_{\text{in}}(\Omega)$ are the input resistance and reactance at terminals $a - b$. The real part of the input impedance includes the antenna losses and is represented as

$$R_{in} = R_{\text{loss}} + R_{\text{rad}}, \tag{2.2}$$

where R_{loss} is the loss resistance, and R_{rad} is the radiation resistance associated with the radiated wave that escapes from the antenna to the surrounding space [16].

2.1.2 Reflection and Transmission Coefficients

The reflection coefficient $|\Gamma|$ is defined as the ratio between the amplitude of the reflected voltage wave V_0^- and the amplitude of the incident voltage wave V_0^+ and is expressed as [24]

$$|\Gamma| = \frac{|V_0^-|}{|V_0^+|} = \left| \frac{Z_{\text{in}} - Z_{\text{source}}}{Z_{\text{in}} + Z_{\text{source}}} \right|. \tag{2.3}$$

When the antenna input impedance (Z_{in}) is not properly matched to the internal impedance of the source (Z_{source}), only part of the power generated by the source (P_{source}) will be accepted by the antenna (P_{accep}), and this power is computed using

$$P_{\text{accep}} = (1 - |\Gamma|^2) P_{\text{source}}. \tag{2.4}$$

A few conclusions can be drawn from the expressions (2.3) and (2.4). First, it can be seen that when the input impedance is the conjugate of the source impedance, i.e.,

$Z_{\text{in}} = Z_{\text{source}}$, the reflection coefficient is $|\Gamma| = 0$ and all the power from the source is delivered to the antenna, i.e., $P_{\text{accep}} = P_{\text{source}}$. Next, for all the cases where $Z_{\text{in}} \neq Z_{\text{source}}$, some reflection is present at the antenna terminals since $|\Gamma| \neq 0$. This means that less power is accepted by the antenna, and consequently less power is also radiated. Lastly, it can be seen that the worst mismatch case is observed when $|\Gamma| = 1$, where no power is delivered to the antenna.

For practical antennas almost always $Z_{\text{in}} \neq Z_{\text{source}}$, meaning that not all power from the source will be delivered to the antenna. This loss is denoted Return Loss (RL) and is computed in (dB) as follows

$$RL = -20\log\left(|\Gamma|\right) \text{ dB} = -20\log\left(|S_{ii}|\right) \text{ dB}, \tag{2.5}$$

where $|\Gamma| = |S_{ii}|$. The representation $|S_{ii}|$ is obtained from the scattering matrix (see Fig. 2.2), which provides a comprehensive description of the network from the perspective of its i-ports as shown in Fig. 2.2b. $|S_{ii}|$ corresponds to the scattering parameter (S-parameter) at port i, i.e., is the reflection coefficient of port i when all other ports in the system are terminated with matched loads [24].

The bandwidth of an antenna is defined in [23] as "the range of frequencies within

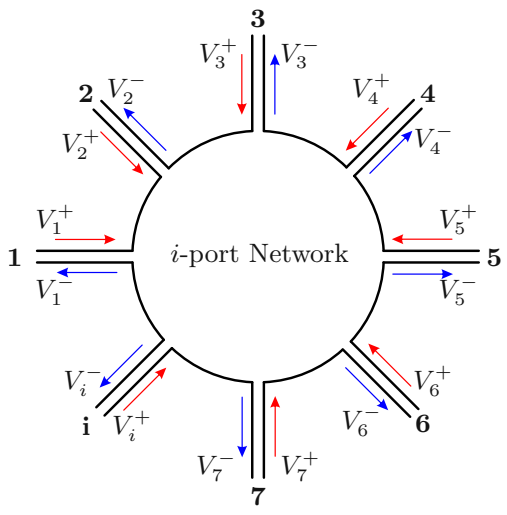

(a)

$$\begin{bmatrix} S_{11} & S_{12} & S_{13} & S_{14} & \cdots & S_{1i} \\ S_{21} & S_{22} & S_{23} & S_{24} & \cdots & S_{2i} \\ S_{31} & S_{32} & S_{33} & S_{34} & \cdots & S_{3i} \\ \vdots & \vdots & \vdots & \vdots & \ddots & \vdots \\ S_{i1} & S_{i2} & S_{i3} & S_{i4} & \cdots & S_{ii} \end{bmatrix}$$

(b)

Figure 2.2: Scattering matrix. (a) A network comprising a total of i ports. (b) Corresponding S-parameters of the network.

which the performance of the antenna conforms to a specified standard with respect to some characteristic". For this thesis, the antenna bandwidth is defined in terms of S-parameters $|S_{ii}|$. However, because the antennas investigated in this thesis comprise more than one port, $|S_{ii}|$ alone cannot accurately characterize the antenna performance, since the power can be transmitted from one port to another. To this end, the *transmission coefficient* ($|S_{ij}|$) parameter is introduced. $|S_{ij}|$ represents the amount of power that is transferred from port j to port i, when all the other ports are terminated in matched loads, and its positive value, i.e., $-|S_{ij}|$ is denoted *antenna isolation*. Therefore, for this thesis, the antenna bandwidth, called Impedance BandWidth (IBW) is defined as the range of frequencies overlapping between all ports where

$$|S_{ii}| \leq -10\,\text{dB} \wedge \forall_j |S_{ij}| \leq -10\,\text{dB}. \tag{2.6}$$

Note that by ensuring that $|S_{ii}| \leq -10\,\text{dB}$ for each antenna port, $|\Gamma| \leq 0.316$ within the *impedance bandwidth* region, and equation (2.4) becomes

$$P_{\text{accep}} = 0.9 P_{\text{source}}, \tag{2.7}$$

which ensures that at least 90% of the power is accepted by the antenna.

2.1.3 Radiation Efficiency and Total Efficiency

As shown in Fig. 2.1 the losses in the antenna apart from radiation are usually modeled as a series loss resistor R_{loss}, and the *radiation efficiency* e_{rad} can then be represented as

$$e_{\text{rad}} = \frac{R_{\text{rad}}}{R_{\text{rad}} + R_{\text{loss}}} = \frac{R_{\text{rad}}}{R_{\text{in}}}. \tag{2.8}$$

Because this thesis discusses compact antennas for integration into small IoT devices, it is important to note that as the antenna size decreases, the radiation resistancce R_{rad} will also decrease and the R_{loss} term dominates the expression (2.8). This is mainly due to the frequency-dependent conductivity and dielectric losses within the antenna [25].

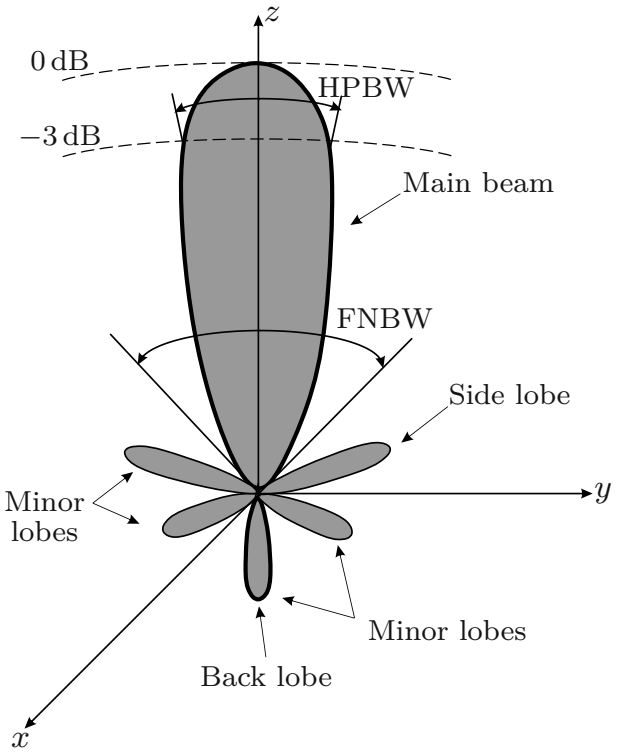

Figure 2.3: Visualization of *antenna radiation pattern.*

To take into account the losses at the input terminals, the *total antenna efficiency* e_{tot} parameter is defined as

$$e_{\text{tot}} = e_{\text{rad}}(1 - |\Gamma|^2), \tag{2.9}$$

where $(1 - |\Gamma|^2)$ is referred to as reflection (mismatch) efficiency which accounts for the losses at the input terminals.

The expression (2.9) further highlights the importance of having a good matching at the antenna terminals, in other words, for the case without any mismatches ($|\Gamma| = 0$) the *total efficiency* will be the same as the *radiation efficiency.*

2.1.4 Radiation Pattern, Directivity, Gain, and Realized Gain

Radiation pattern or antenna pattern describes the spatial dependence of the radiation properties of an antenna. In other words, it is a mathematical function or graphical representation describing how the antenna radiates energy out into space. Note that because

of the *Lorentz Reciprocity Theorem* [16], the *antenna pattern* also shows the graphical representation of how the antenna receives energy. The *radiation pattern* can be plotted in a spherical coordinate system as the radiated power versus the elevation angle (θ) or the azimuth angle (ϕ), typically shown in decibel (dB) and normalized with respect to the maximum value. As shown in Fig. 2.3, a typical *radiation pattern* has *main lobe, minor lobes, side lobes, back lobe and nulls.* The *main lobe* or *main beam* is "the radiation lobe containing the direction of maximum radiation" [23]. The remaining lobes (i.e., excluding the main beam) can be denoted as *minor lobes.* The *side lobe* is a *minor lobe* adjacent to the *main beam*, i.e., occupying the same hemisphere as the *main beam*, but pointing to the direction other than the desired beam. *Back lobe* is a *minor lobe* occupying the hemisphere in a direction opposite to the *main beam*, and is defined in [23] as "a radiation lobe whose axis makes an angle of approximately 180° with respect to the antenna *main beam*." In Fig. 2.3 two types of beamwidths are also indicated in the *main beam*, one related to the *antenna pattern nulls* referred to as First Null BeamWidth (FNBW) and the Half-Power BeamWidth (HPBW), which corresponds to the angle where the radiation intensity is half of its maximum value.

The *antenna radiation patterns*, can be essentially classified as *isotropic, omnidirectional*, and *directional.* An *isotropic antenna* is an ideal lossless antenna with equal radiation in all directions. This means that the *radiation pattern* of such an antenna resembles a perfect sphere with value one, and at each angle it radiates and receives the same amount of electromagnetic radiation. Note, however, that such an antenna is a theoretical construction that cannot be physically realized [26], but it is used as a reference for real antennas. A *directional antenna* radiates or receives electromagnetic waves more effectively in specific directions. An example of a directional pattern is the one shown in Fig. 2.3, where the *main beam* is pointing towards $\theta = 0°$, for a given ϕ cut. *Omnidirectional* pattern is a special case of a *directional pattern* and is defined in [23] as "having an essentially non-directional pattern in a given plane and a directional pattern in any orthogonal plane."

An important parameter to charecterize *directional antennas* is the *directivity* $D(\theta, \phi)$, which is a measure of how the antenna concentrate its radiated power in a particular direction. In simpler terms, the *directivity* of an antenna equals to the ratio of the antenna's

radiation intensity at a given (θ, ϕ) direction over that of an *isotropic antenna*. Since the radiation intensitiy of an *isotropic antenna* can be written as [16]

$$U_{\text{iso}}(\theta, \phi) = \frac{P_{\text{rad}}}{4\pi}, \tag{2.10}$$

where P_{rad} is the total radiated power, the *antenna directivity* can then be mathematically written as

$$D(\theta, \phi) = \frac{U_{\text{int}}(\theta, \phi)}{U_{\text{iso}}(\theta, \phi)} = \frac{4\pi U_{\text{int}}}{P_{\text{rad}}}, \tag{2.11}$$

where $U_{\text{int}}(\theta, \phi)$ is the radiation intensity of the antenna in a given direction.

The *antenna directivity* $D(\theta, \phi)$ given in (2.11) uses the antenna radiated power (P_{rad}) as the reference power. Therefore, it does not consider the losses generated in the antenna due to the frequency-dependent conductivity and the dielectric material, i.e., *radiation efficiency*. To account for the antenna losses, the parameter *gain* is introduced, and is defined in [23] as "the ratio of the radiation intensity in a given direction to the radiation intensity that would be produced if the power accepted by the antenna were isotropically radiated". This means that the *antenna gain* can be related to the *directivity* via

$$G(\theta, \phi) = e_{\text{rad}} D(\theta, \phi). \tag{2.12}$$

From the above expression, it can be observed that for the case of a lossless antenna, where the *radiation efficiency* is $e_{\text{rad}} = 1$, the *directivity* and *gain* will be identical.

While the *antenna gain* does take into account the losses generated in the antenna, it does not consider the losses due to mismatches generated at the antenna terminals. To this end, the *realized gain* $G_{\text{real}}(\theta, \phi)$ is introduced which takes into account the reflection losses and is defined as

$$G_{\text{real}}(\theta, \phi) = (1 - |\Gamma|^2) G(\theta, \phi) = e_{\text{tot}} D(\theta, \phi), \tag{2.13}$$

where e_{tot} is the *total efficiency* as defined in (2.9).

The *realized gain* parameter offers a much better insight into the antenna performance as compared to *directivity* and *gain*, and for this reason all the results presented in this thesis, either measured or simulated are outlined in terms of the *realized gain* parameter.

2.1.5 Polarization

Polarization can be defined as the curve traced by the electric field ($\vec{E}$) wave as a function of time [16]. Therefore, it describes the direction of $\vec{E}$ at every point in time.

Let the electric field orthogonal components in the x and y directions (for a wave travelling in a negative z-direction) be expressed as follows

$$\vec{E}_x(z,t) = \vec{E}_{x0}\cos(\omega t + kz + \psi_x), \tag{2.14a}$$

$$\vec{E}_y(z,t) = \vec{E}_{y0}\cos(\omega t + kz + \psi_y), \tag{2.14b}$$

where $\vec{E}_{x0}$ and $\vec{E}_{y0}$ respectively represent the maximum electric field magnitudes in the x and y-directions, and k is the propagation constant. *Polarization* is then given by the phase difference between the two orthogonal components, i.e., $\vec{E}_x(z,t)$ and $\vec{E}_y(z,t)$, also taking into account the amplitude ratio between the two components.

Waves radiated from a *linearly polarized* antenna exhibit electric field possessing either one component, or two orthogonal components that have a phase difference (ψ_x and ψ_y) at every instant of time is given as

$$\Delta\psi = \psi_y - \psi_x = n\pi, \qquad n = 0, 1, 2, 3, \cdots . \tag{2.15}$$

The electric field of *linearly polarized* waves is always directed along the same line at any point in space and time, i.e., it is always parallel to the same axis. Additionally, when a reference plane is defined, e.g. ground, the *linear polarization* can be separated into horizontal and vertical. When the electric field propagates in parallel to the ground plane, the antenna is referred to as *horizontally polarized*, while for the case where the waves propagate perpendicularly with respect to the ground plane, the antenna is called *vertically polarized*.

Circularly polarized antennas radiate waves that exhibit electric field with two orthogonal components of the same magnitude and odd multiples of $\pi/2$ of phase difference. For *elliptical polarization*, the field must have two orhtogonal components, and they can be of the same or different magnitudes. For the case where the two components have different magnitude, the phase difference between the two components must not be 0 or multiples of π (since it will be *linearly polarized*). For the case where the two components are of the same magnitude, then the phase difference between the two components must not be odd multiples of $\pi/2$ (since in this case it will be *circularly polarized*). Lastly, for simplicity the beamforming principle presented in this thesis is demonstrated using *linear vertically polarized* antennas.

2.2 Microstrip Patch Antennas

Microstrip patch antennas belong to the category of printed antennas, i.e., the radiating elements are developed using printed circuit technology. The term *patch* refers to the shape of the printed conducting element of the antenna, which can take many forms, but the most popular ones are rectangular or circular. Patch antennas offer many attractive qualities such as thin profile, lightweight, ease of integration with circuits, and low-cost production [16, 27, 28]. Since those characteristics are some of the key requirements in compact IoT systems, microstrip patches are the main antenna elements investigated in this thesis. While circular and rectangular patch both allow for easy tuning of impedance, radiation pattern, and frequency, the circular patch is selected as the primary antenna type in the thesis because of its smaller size as compared to the rectangular patch [27, 28].

2.2.1 Configuration

Fig. 2.4 shows a general configuration of a circular patch antenna, comprising a thin metallic conductor, etched on a grounded dielectric substrate with relative permittivity ϵ_r. There are different methods to analyse the microstrip patch antenna, and they can be grouped as approximate techniques or full-wave analyses. The approximate techniques, like transmission line and cavity models, can provide accurate performance with reduced complexity in

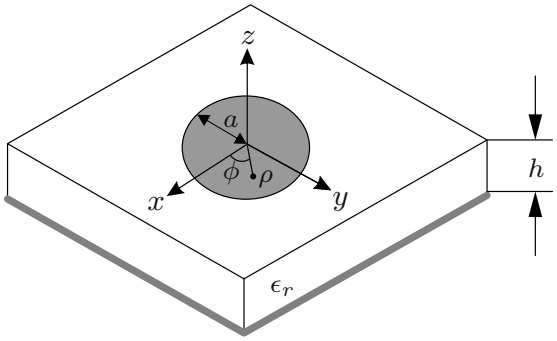

Figure 2.4: Configuration of a circular patch antenna, where the metallic layer of the patch and ground plane are shown in gray.

the analysis of patch antennas under certain conditions (e.g. requirement that the patch has a very thin substrate). On the other hand, full-wave analyses like integral equation approach, the Finite Difference Time Domain (FDTD) and Finite Element Method (FEM), offer the most accurate results by numerically solving the Maxwwell's Equations for the specific problem, while applying the associated structure boundary conditions [28]. However, they are computationally demanding, for this reason the antennas discussed in this thesis are first analyzed using the *cavity model*, and a more rigorous analysis is then conducted using full-wave simulations.

2.2.2 Cavity Model Analysis

By assuming that the patch in Fig. 2.4 is supported by a very thin substrate, i.e., $h \ll \lambda$ where λ is the wavelength, the following conclusions can be drawn [27, 28]:

- The fields do not vary along the z-direction. Therefore, $\vec{E}$ has only z component, while the magnetic field $\vec{H}$ has only the transverse components in the region bounded by the circular patch and the ground plane, i.e., has only the ρ and ϕ components.
- Because the electric current in the patch does not have a component normal to the edge of the patch, the tangential component of $\vec{H}$ along the edge is negligible.
- The region between the patch and the ground plane can then be modeled as a cavity bounded by electric walls on the top and bottom, and by magnetic wall on the edge.

Thus, the electric field of TM_{nm} modes within a microstrip cavity of radius a can be obtained by solving the wave equation and is given by [28]

$$E_z = E_0 J_n(k_{nm}\rho)\cos n\phi, \tag{2.16}$$

where E_0 corresponds to the amplitude of the field, ρ is a radial value within the patch (i.e., $\rho < a$), ϕ represents the azimuthal angle, and $J_n(k_{nm}\rho)$ is the Bessel function of the first kind of order n and $k_{nm} = \chi_{nm}/a$, where χ_{nm} is the mth zero of $J_n^{'}(k_{nm}\rho) = 0$. The resonance frequency for the specific TM_{nm} mode can then be approximated using

$$f_{\mathrm{res}} = \frac{\chi_{nm}c}{2\pi a\sqrt{\epsilon_r}}. \tag{2.17}$$

The χ_{nm} values for the first few TM_{nm} modes of interest in this work, are as follows: $\chi_{11} = 1.841$, $\chi_{21} = 3.054$, $\chi_{02} = 3.831$, and $\chi_{31} = 4.201$.

2.3 Introduction to Directional Modulation

Directional modulation DM can be classified as part of the more general field of wireless physical layer security techniques, where the secrecy and privacy of communication systems are enhanced by exploiting characteristics of the wireless propagation channel [9–11]. In more details, the DM solution is a transmitter based security technique which ensures that the transmitted information is only decipherable in a pre-specified secure direction of the legitimate receiver.

While in traditional wireless communication systems, the signal modulations are typically carried out at the digital baseband level, the DM concept was introduced in [12, 14]. These works demonstrated that because each element of an antenna array generates far-field radiation patterns that are spatially dependent (i.e., they can be summed in a manner that varies across different directions). Therefore, signal modulations can be performed at radio frequency stages to produce differently combined signal waveforms that radiate along distinct spatial directions in free space. This means that signal waveforms containing specific information could be generated along a pre-selected secure communication direction. Consequently, only receivers in the specified directions could retrieve the correct signal signature. Meanwhile, signal waveforms radiated in other directions become distorted, which

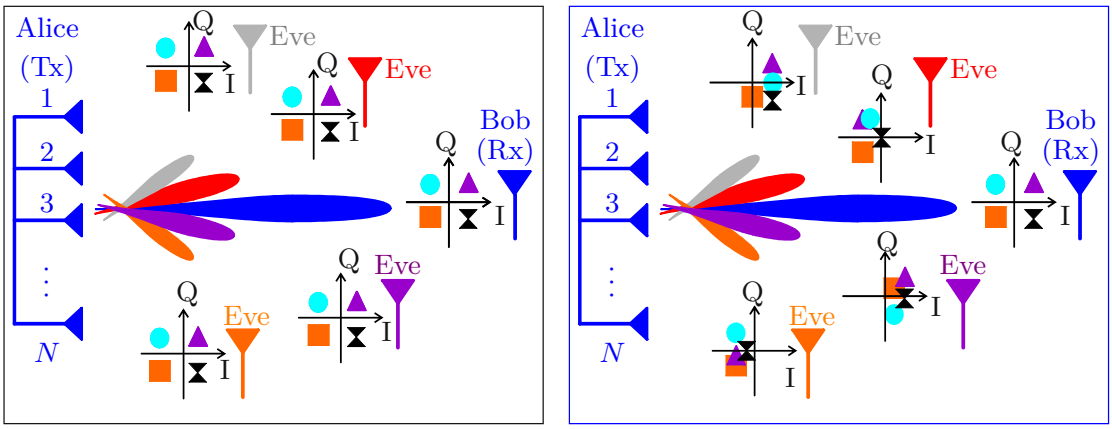

Figure 2.5: Illustration of the DM concept. (a) Shows the traditional beamforming concept. (b) Highlights the DM scheme. Alice is the Transmitter (Tx), Bob is the direction of the legitimate receiver Receiver (Rx), while Eve denotes eavesdroppers.

makes it challenging for eavesdroppers to retrieve the information.

To illustrate the DM concept, consider a system modulated for Quadrature Phase-Shift Keying (QPSK), as depicted in Fig. 2.5. In this example, the traditional beamforming is highlighted in Fig. 2.5a, where an array transmitter (Alice) comprising N elements has the maximum power in the direction of the legitimate user Bob, with the power in all other directions being as low as possible. It can be seen that for the typical beamforming case (Fig. 2.5a), the standard QPSK constellation patterns that form a centrally symmetric square in In-phase and Quadrature (IQ) space, are preserved along all the transmitting directions. However, for the DM scheme (Fig. 2.5b), the constellations are preserved exclusively along the pre-defined observation direction of the legitimate receiver Bob. Along all other spatial directions, the signal formats experience distortion, which enhances the overall security of the communication system.

2.3.1 Review of Directional Modulation Technology

The DM concept was initially presented in [14], where a technique called near-field direct antenna modulation used a single driven antenna with multiple switched parasitic elements to modulate a continuous wave signal. Specifically, the system comprised a driven dipole antenna combined with passive reflectors that are controlled using switches to change the reflectors' effective length and scattering properties. This concept highlighted that different

phases and amplitudes of the reflected signal can be produced to distort the IQ space in different spatial directions. Therefore, the method enabled direction-dependent signal transmissions for secure wireless communications.

In [12], a DM transmitter was realized by substituting the elements of the system in [14] — the central active-driven dipole antenna and the surrounding passive reflectors — with a phased antenna array. In this approach, when phase shifts are accurately introduced in each element, amplitude and phase for every symbol are generated in a digital modulation scheme within a specified direction, and the data rates are calculated by the phase shifters' switching speed. The method also showed that if the radiation patterns of the arrays are known, an optimization algorithm can be used to either find the phases for transmitting in multiple directions simultaneously, or to distort the constellations in all directions except that of the legitimate receiver.

The DM transmitters presented in [12, 14], were simplified in [29]. In the new approach, the DM technique used a simpler configuration, i.e., an array comprising pattern reconfigurable square spiral microstrip antennas, and the DM is realized by repeatedly switching the array elements to synthesize digital symbols.

In [30], a dual-beam DM method is presented. The approach resembles the near-field direct antenna modulation proposed in [14]. However, this method significantly simplifies the antenna structure (driven dipole and passive reflectors), i.e., it only requires two transmit beams, which exploit the orthogonality between the IQ baseband signals. Therefore, the constellation points of the transmitted signal remain fixed in their positions, like traditional digital modulation signals in the intended direction. However, in the eavesdroppers' directions, the phase becomes randomized due to the modulation of the transmit signal at both the baseband and antenna levels.

Fourier transform-based beamforming networks like Butler matrix and Fourier Rotman lens [31, 32] can simultaneously produce orthogonal beams. This property helps them project correct signals along the desired direction of the legitimate receiver from the excited information beam port. At the same time, the far-field side lobe modulation content can be scrambled, as demonstrated in [33]. A key advantage of the above systems is that only two radio frequency chains are needed to control the beam ports of the Fourier transform-based

network architecture. One port is dedicated to the information data insertion, and the other injects orthogonal side-lobe interference into the system.

In [34], the authors proposed a DM technique called antenna subset modulation. This new low-complexity approach is based on optimally utilizing the entire antenna array by using only some of the radio frequency chains. By implementing a fundamental inter-antenna phase shift and activating distinct subsets of antennas during each symbol interval, it was demonstrated that the method could generate a modulated signal sensitive to direction. Therefore, the concept enables the transmitter to introduce variability in the signal constellations observed at angles other than the intended direction of the legitimate receiver. A similar approach based on switched antenna arrays is proposed in [35]. This method uses radio frequency switches to introduce time modulation into conventional arrays. In this way, the array transmits the correct signals when no time modulation is present in the direction of the legitimate receiver. However, time-modulated signals are transmitted in other directions. The method demonstrated that when the time modulation frequency is less than the bandwidth of the transferred signal, the time-modulated signals are not demodulated correctly, which means that they are distorted in the eavesdroppers' directions. Another work exploring switched arrays for DM is presented in [36]. Unlike the previous design, the method is not restricted to phase modulation. It can be implemented with any modulation type, including quadrature amplitude modulation, and allows to scramble the constellation points by randomly switching off one or more transmitting antennas.

Further advances in DM technology are presented in [15], where an orthogonal vector approach is introduced. This new method uses orthogonal vectors/interference in the channel vectors' null space between the DM transmitters and the desired legitimate receivers. The method was demonstrated to be readily employable in state-of-the-art digital wireless transmitters and can be extended to DM transmitters for multiple independent beam transmissions. Moreover, the concept can be considered a process of injecting artificial interference orthogonal to the transmitted information signals along a pre-selected direction.

Multi-user Multiple Input Multiple Output (MIMO) DM systems are investigated in [37–39]. The authors in [37] employed both the channel information and symbols in-

tended for the users, to design symbol-level precoders to enhance security across various transmitters and eavesdropper antenna configurations. The work also reformulated each proposed design into a linearly constrained quadratic problem, and outlined an iterative algorithm with a non-negative least squares solution for a computationally efficient modulation scheme. In [38], the authors presented a secure multiple access scheme. The approach explores the multipath structure of the channel to create a multi-user interference environment, where the generated interference allows legitimate users to share time and frequency resources across spatially secure links.

In [13], a new type of DM transmitter based on retro-directive arrays was introduced, where the injected orthogonal interference is not dependent on the pre-selected secure direction, and real-time behavior can be obtained using low-cost, and low-complexity analog solutions.

Time-modulated arrays are investigated in [40], where DM transmitters are proposed for Orthogonal Frequency-Division Multiplexing (OFDM) wireless data transmission. The study demonstrated that by appropriately configuring the switch controlling the time sequences, the proposed time-modulated DM system needs only a single radio frequency chain, eliminating the necessity to reconstitute array excitation vectors for diverse secure communication directions, modulation schemes, and DM power efficiencies. The method also presents the ability to flexibly adjust the tradeoff between secrecy performance and power efficiency. In [41], the authors propose a hybrid MIMO phased-array time-modulated DM system. In this approach, the transmit array is split into multiple sub-arrays, each forming a secure directional beam, and all sub-arrays can be combined to work as a MIMO system for increased angular resolution or multi-user communications.

Concerning energy efficient DM schemes, a few works have been proposed in the last years, e.g., in [42–45]. A method to improve the efficiency of the radio frequency power amplifiers in DM transmitters is presented in [42]. In [43], time-modulated phased arrays are proposed to synthesize multicarrier DM symbols, where the modulated waveform synthesis is achieved by careful design of the switching time sequences, which reduces the peak-to-average power ratio of signals going through the radio frequency chain. In [45], the authors propose reconfigurable power divider enabled energy efficient DM transmitters for OFDM

modulated data transmission. It was demonstrated that the method can recycle the energy in the off-state antennas, which is otherwise wasted in the conventional DM transmitter that are constructed using a fixed power divider and switches.

2.3.2 Directional Modulation from Compact Antennas

As highlighted in the previous section, the design of DM transmitters has attracted much research interest. *However, the current state-of-the-art is based on the beamforming of classical antenna arrays.* Since those typically require inter-element spacing (usually taken as $\lambda/2$, where λ is the wavelength at the array center operating frequency), *array structures are too large for compact integrated IoT devices*, especially those operating at the sub-6 GHz frequency bands. Therefore, such compact systems cannot avail of the benefits provided by the DM security technique.

Due to the above constraints, only some works have investigated DM schemes in small IoT devices [46–50], and the following discussion reviews the advances introduced by DM schemes using compact antennas. In [46], the authors proposed a DM system using a compact dual-mode antenna of approximately $\lambda/2$ diameter, comprising a $\lambda/4$ monopole antenna and a dielectric-loaded circular patch. The solution explores different phase variations across its beam space for beamforming around the azimuthal plane and uses the complex radiation patterns as weights for the DM coding. The work in [47] proposed a DM scheme using a stacked patch design of 0.7λ diameter and 0.05λ thickness. The work demonstrated secure steerable direction-dependent antenna modulation in the full-azimuthal plane, and the analyses of simultaneous transmission of two uncorrelated signals along two pre-selected transmitting directions were further executed in [48]. Although the system achieved a low-profile design, *it was indicated that the beamforming produced high side lobes, which can compromise the security of the transmitted signals in directions other than that of the desired legitimate receiver* in both the single direction transmission case and the two simultaneous transmissions case.

Other works that attempted to realize DM schemes from compact antennas are presented in [49, 50]. The new approach integrates a $3\lambda/2$ switched dipole antenna. The system comprises parasitic elements as a dynamic antenna to constantly and rapidly change current

distribution, generating a static radiation pattern in the desired direction of the legitimate receiver. In contrast, a dynamic radiation pattern is generated in other directions.

2.3.3 Limitations of Highly Miniaturized Antennas

While in recent years significant advances have been realized in DM systems using compact antennas, numerous challenges still exist to implement DM schemes in emerging compact IoT systems. *As highlighted above, the size constraints are still a key issue in allowing steerable, secure, direction-dependent modulation, especially when considering integrating the DM technique into on-body IoT devices.* This is because such systems typically require highly miniaturized antennas, i.e., Electrically Small Antennas (ESAs), to meet the tight size limitations in on-body operation scenarios. ESAs are considered to be those with electrical size $ka \leq 1$, where $k = 2\pi/\lambda$ and a is the radius of the smallest sphere that completely encloses the antenna. *However, prior to our work [51] (see Chapter 6), no DM systems are implemented using ESAs, and all state-of-the-art compact DM models require at least $\lambda/2$ diameter [46–48].*

It is worth pointing out that recent years have seen significant advances in the topic of compact beamforming antennas, e.g., in [52–59]. In [53], a planar beam switching antenna comprising four arc dipoles and a feeding network loaded with radio frequency p-i-n diodes, are used to produce four directional patterns in the azimuthal plane with an electrical size $ka = 2.72$. The work in [54] presented a unilateral turnstile-shaped patch equivalent magnetic dipole combined with a slotted ground plane, that behaves like an electric dipole to produce unilateral radiation patterns with an electrical size of $ka = 1.32$. The radiation properties of a loop and dipole antennas controlled using two p-i-n diodes are combined to generate three unidirectional radiation patterns in [55], using a structure with $ka = 1.74$. In [56], two pairs of magnetic and electric near-field resonant parasitic elements are used to realize Huygens dipoles. The solution includes two p-i-n diodes and produces two unidirectional end-fire patterns with an electrical size of $ka = 0.98$. A planar shared aperture quasi-Yagi antenna is proposed for pattern diversity, using a coplanar waveguide type feeding with even–odd mode excitation while using an electrical size of $ka = 3$. In [58], a driven patch antenna is combined with a stacked-patch, an embedded filtering feeding line,

two vertical switchable elements, and p-i-n diodes, to produce three radiation nulls. Lastly, in [60], a modified array structure is used to electrically switch into two unidirectional radiation modes and an omnidirectional pattern, while using an electrical size of $ka = 0.98$. *While the above works present significant contributions in highly miniaturized beamforming antennas, their beamforming characteristics are still limited to a few discrete states, which is still insufficient to implement DM schemes, such limitations are addressed in Chapter 5.*

Another critical challenge limiting DM systems' implementation in emerging IoT applications is the high-profile issue. Planar antenna solutions are often required for easy integration into IoT systems, like on-body IoT devices. *However, current compact DM solutions that integrate a planar antenna still require at least* $3\lambda/2$ *size [49, 50], which is impractical for on-body and other size-constrained IoT applications.* It should also be pointed out that none of the current compact DM solutions (with approximately $\lambda/2$ diameter [46–48]) *provides a complete beamforming framework that allows to generate different beams while providing a comprehensive relation to their corresponding DM performance. More importantly, none of the above solutions can realize DM transmissions outside the horizontal plane.* This is a challenging problem because, in practice, the desired receiver can be located in different directions across the Three-Dimensional (3D) space.

Significant advances have been achieved in terms of scanning range, low-complexity steering methods, bandwidth enhancement, gain improvements, antenna size, and profile miniaturization [61–70]. More specifically, a reconfigurable Yagi-Uda array with a central driven element and movable liquid metal parasitic sections is used for azimuth plane beamforming in [61]. A multi-modal concentric circular patch antenna is proposed for elevation plane beamforming in [62]. In [63], an azimuth beamforming quasi-Yagi dipole design is investigated for wireless local area network applications. A high impedance surface ground is explored to design an elevation plane beamforming antenna in [64]. The work in [65] generates beamforming functionalities by employing crossed dipoles, to design a planar low-profile electronically steerable parasitic array radiator antenna. In [66], a broadside and conical beam switchable antenna is investigated for ceiling-mounted indoor wireless systems. The work in [67] presents an electrically small beamforming near-field resonant parasitic Huygens source antenna. In [69], an elevation plane beamforming antenna is designed using a

fluidically programmable metasurface. Lastly, in [70], miniaturized multi-mode antennas with adaptive beamforming capabilities are proposed for IoT applications. *However, the problem of integrating these solutions in many on-body IoT systems to realize DM (e.g., in wrist and foot wearables IoT devices) still needs to be solved.* This is because some beamforming techniques still use relatively large antenna sizes [61–64, 68, 69, 71]. Moreover, they still have a relatively bulky structure and are not planar solutions [61, 64, 66, 67, 70, 71]. In addition, *all the above beamforming methods are incompatible with digital beamforming, which is required to implement a DM solution that flexibly covers different directions across the 3D space. Moreover, their steering characteristics are limited to one plane, either azimuth or elevation plane [61–71].* As will be demonstrated in Chapter 6 and Chapter 8, this thesis overcomes the above issues by proposing compact antennas capable of 3D beamforming.

On-body beamforming antennas have been proposed in [52, 72–82]. Where elevation plane beamforming is discussed in [72]. Dual-mode pattern synthesis, i.e., omnidirectional and broadside patterns at different bands, are achieved in [73–75]. In [76], the theory of characteristic modes is used to design a dual-port smart-watch antenna with a bi-directional and omnidirectional pattern in the xz and yz-planes. Dual-mode pattern synthesis is also obtained using tunable ring slots in [81] and rectangular patches in [82]. *Note that the beamforming performance of the above works is still constrained to only yz-plane [72], dual-mode patterns in [73–75, 81, 82], or bi-directional and omnidirectional patterns in xz and yz-planes [76]. Such beamforming characteristics still need to be improved for a DM system covering the azimuth and elevation planes.* To enhance the security in on-body IoT devices, Chapter 8 introduces novel planar antennas suitable for on-body DM applications.

Lastly, *all the works involving compact DM systems [46–50], are single-band systems, which makes their integration with modern multi-band IoT devices a challenging issue.* Additionally, to provide multi-band beamforming operation, multiple antennas operating at different frequency bands are integrated into the IoT system. Such an approach can further complicate the limited antenna space installation within compact IoT devices. This issue is overcomed in Chapter 9, which introduces planar dual-band antennas suitable for DM applications in compact integrated IoT systems.

2.4 Introduction to Angle of Arrival Estimation

Angle of Arrival AoA estimation is a popular localization technique based on relative angle measurements. *In the state-of-the-art, the method is implemented using antenna arrays*, where the AoA algorithms exploit the differential phase information from the array's output [17], from which the arriving signal's source direction can be computed.

An example of a classical array used for AoA measurements is shown in Fig. 2.6, where K uncorrelated sources illuminate a linear array configuration comprising N elements. When the time variation of the sources is taken as $e^{j\omega t}$, the antenna array response due to the impinging wavefronts from $\phi_1, \phi_2, \cdots, \phi_K$ directions can be described from a complex matrix $\boldsymbol{A}$ comprising the array steering vectors

$$\boldsymbol{A} = [\vec{a}(\phi_1), \vec{a}(\phi_2), \cdots, \vec{a}(\phi_K)], \tag{2.18}$$

$$\vec{a}(\phi_i) = [e^{-jkd_1 \cos\phi_i}, e^{-jkd_2 \cos\phi_i}, \cdots, e^{-jkd_N \cos\phi_i}]^{\mathrm{T}}, \tag{2.19}$$

where $k = 2\pi/\lambda$ is the wavenumber and λ is the wavelength. It is important to highlight that the above response from the array structure corresponds to the ideal scenario without mutual coupling effects, and the phase performance directly depends on the geometrical relation between the impinging wave and the antenna element position within the array

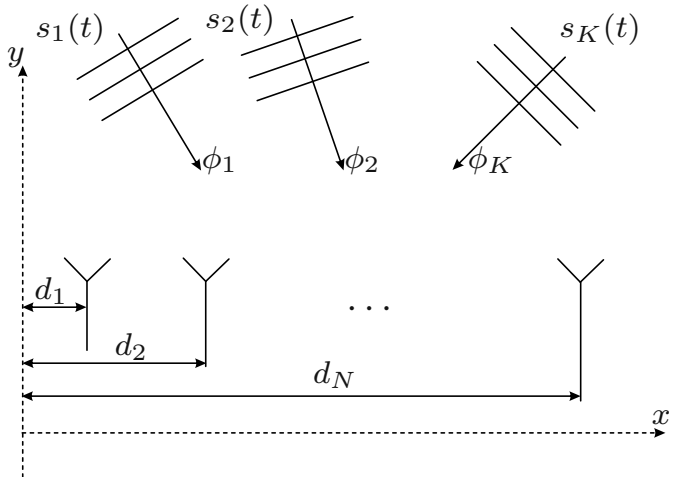

Figure 2.6: Visualization of linear array geometry and the impinging sources.

structure. Under these conditions, most AoA estimation algorithms are capable of accurately computing the impinging signals directions [17, 83–88]. However, the array response is usually quite different in practical scenarios, since the array model described above will deviate from the ideal model due to mutual coupling effects between the array elements. In other words, radiation occurs when an illuminating source induces a current on the surface of each array element, and a portion of the radiated signal impacts the performance of the remaining array elements. If the mutual coupling effects are not accounted for, they ultimately degrade the performance of the AoA estimation algorithms.

2.4.1 Mutual Coupling Mitigation Techniques in AoA Measurements

Over the years, a considerable amount of literature has investigated various techniques for mitigation of mutual coupling effects in AoA estimation, where some early techniques can be found in [89–95]. The work in [89] proposes an eigenstructure technique to estimate the angle of arrivals under the gain, phase uncertainties, and mutual coupling of the array sensors. In [91], a closed-form expression based on the array impedance matrix is investigated to integrate mutual coupling effects in linear arrays. A procedure to correct the voltage matrix based on the terminal impedance derived from the method of moments of impedance matrix is proposed to account for mutual coupling effects in [92]. In [93], the authors propose an algorithm for estimation of the calibration matrix comprising unknown gain, phase, mutual coupling coefficients, and the sensor locations by using a set of calibration sources in different known locations. Based on the relation between the entries of the method of moment voltage vector, [95] developed a square matrix equation to eliminate the mutual coupling effects in adaptive antenna arrays.

Recent works in mutual coupling mitigation for AoA measurements are discussed, e.g., in [96–104]. A method of moment mutual coupling compensation technique in AoA using circular arrays is presented in [96]. The work in [97] proposed a mutual coupling compensation technique that treats the coupling effects of the surrounding antennas as excitation sources and introduces a mutual impedance to compute the effects due to the excitation sources. In [101], a subspace-based blind calibration method is proposed for AoA estimation using Uniform Circular Arrays (UCAs) under mutual coupling effects. The work in [103]

proposes an algorithm that reduces the mutual coupling in AoA estimation, by restricting the sensors to be on the boundary of a uniform rectangular array to act as auxiliary sensors. In [104], and algorithm based on generalized eigenvalues utilizing signal subspace eigenvectors is proposed for AoA measurements using linear array structures in the presence of mutual coupling.

Other recent works focusing on mutual coupling mitigation are presented in [105–116]. The work [107] uses the receiving mutual impedance method to account for mutual coupling in closely spaced arrays. In other words, array structures with an inter-element spacing smaller than $\lambda/2$. A generalized iterative solution is used to estimate the AoA of unknown mutual coupling, based on the subspace auto-calibration technique in [108]. Super-nested arrays with reduced mutual coupling are presented in [110]. In [111], the authors discuss AoA estimation under direction-dependent mutual coupling. A machine-learning approach is presented in [112]. The study in [113] proposes an AoA estimation technique for a Uniform Circular Array (UCA) in the presence of mutual coupling. In [114], a phase center contour model combined with a novel algorithm is used to improve AoA measurements in the presence of mutual coupling.

While the above-discussed solutions represent significant advances in mutual coupling mitigation when performing AoA measurements, it is essential to highlight that most of the above mutual coupling mitigation techniques are not discussed for arrays comprising closely inter-spaced elements, therefore, such space requirements are challenging for AoA estimation in many modern IoT platforms, e.g., on-body devices. It should also be noted that most of these techniques rely on iterative algorithms and calibration methods. *As a result, these mutual coupling compensation techniques often require additional processing time, due to the calibration or complexity of the implemented algorithms and experience increased power consumption.* Those are strong disadvanates when considering their integration into compact resource-constrained IoT systems.

2.4.2 AoA with Compact Antennas

To perform AoA measurements from size-constrained spaces, novel compact antennas have been proposed, e.g., in [115–124]. A transformation matrix approach using electrically small

tuned dipoles is investigated in [117]. The work in [118] introduces an AoA concept based on composite right/left-handed leaky wave antennas. Electronically steerable parasitic array radiators are used in [119], with the mutual coupling between the parasitic elements being exploited to realize beamforming characteristics. An Electrically Small Antenna (ESA) array comprising elements with diverse radiation patterns is combined with an amplitude-based algorithm for AoA estimation in [121]. The proposed method included a calibration procedure to acquire the antenna responses and the parasitic effects of the closely spaced array elements.

Another approach involving compact antennas for AoA estimation is investigated in [115, 116, 122]. The authors in [115], investigate how using decoupling and matching networks improves the accuracy of AoA measurements in compact circular arrays. The study highlighted that it is possible to measure the AoA using a fixed aperture size array with different coupling levels and element arrangements. Further miniaturization was demonstrated in [116], where high permittivity scatterer and matching networks are used in a two-element array to allow a 0.05λ inter-element spacing.

Recently, the concept of multi-mode antennas has been applied to perform AoA estimation using compact antennas, e.g., in [123–129]. In [123], the authors propose a hemispherical spiral antenna with various radiation patterns to replace array structures in AoA measurements. In [124], a planar multi-mode antenna is proposed for AoA estimation. The design exploits different sets of characteristic modes on the same antenna element. To separate multiple impinging signals the solution relies on the array interpolation technique and the wavefield modeling method. The work in [127] proposes an AoA estimation method that weights coefficients of the characteristic modes supported by a cubic antenna structure.

The above-discussed methods offer significant advances in AoA performance, e.g., relatively compact designs, low power consumption, and low complexity. *However, it is essential to highlight that size constraint is still an issue because some solutions include parasitic elements, which require separation to produce sufficient phase variation needed for AoA measurements [118, 119].* Besides, switching between different antenna configurations requires additional time for the AoA estimation, which can be a significant problem when considering multiple moving sources [118, 119]. Additionally, *some methods produce*

increased ohmic losses, require scatterer-loaded systems, have a non-planar design, lack scalability for an increased number of array elements, and do not provide an easy manufacturing process [115, 116, 122, 123]. The multi-mode designs in [115, 122, 123], *still require matching networks.* Additionally, solutions like the one presented in [124, 125] rely on *accurate modeling methods to provide AoA estimations, which may result in measurement inaccuracies for separating multiple impinging signals.* Lastly, the methods in [124–127, 129] *require complex and computationally expensive AoA estimators and feeding networks.*

The above limitations place several constraints on the integration of AoA solutions in small IoT devices, i.e., as will be demonstrated in Chapter 4 *the current advances of multi-mode antennas for AoA estimation still have drawbacks related to the increased power consumption of the system, multiple signal separation, low complexity, simple feeding network, and size constraints*, highlighting that the problem of enabling localization using compact IoT systems is still a challenging one.

2.5 Summary

This chapter reviewed the basic theory of antennas and provided a literature review of DM and AoA estimation technologies. A comprehensive definition of the main parameters used to describe the performance of the antennas discussed in the thesis has been presented. Likewise, the main antenna configuration used in the thesis, i.e., circular microstrip patch and its cavity model analysis, have been introduced. Finally, a literature review was presented, highlighting the critical advances in the DM security approach and AoA estimation. More specifically, the review outlined the main challenges that still limit the implementation of these techniques in emerging compact IoT devices.

3 Spherical Modes Beamforming

Spherical Modes Beamforming (SMB)

In this chapter, the concept of *spherical modes* is introduced. The chapter provides the theoretical framework necessary to understand the beamforming concept discussed throughout this thesis. Therefore, starting from Maxwell's equation, a complete formulation of the *spherical modes* theory is presented. Next, a method based on the *spherical modes* analysis is proposed to realize advanced beamforming characteristics from a given constrained space of antenna installation. Lastly, the chapter investigates a compact multi-port antenna design to demonstrate the capabilities of the proposed beamforming technique. Moreover, an initial analysis of the beamforming characteristics, efficiency, and bandwidth limitations related to the proposed principle will also be discussed. The antenna presented in this chapter was published in the IEEE Internet of Things Magazine [130].

3.1 Spherical Modes Theory

Spherical modes, spherical waves, or vector spherical harmonics are solutions of the vector wave equation. They were introduced by W. W. Hansen [131], who presented a technique for generating solutions to the vector wave equation in any coordinate system where the scalar wave equation can be separated. A comprehensive formulation can be found in the work of J. A. Stratton [132]. J. E. Hansen [133] has provided a more contemporary treatment of the subject in relation to spherical near-field measurements, and his notation is adopted in this thesis.

Assuming $e^{-i\omega t}$ time-dependency, Maxwell's equation for the electromagnetic field in a linear, isotropic, and homogeneous medium can be expressed as follows

$$\nabla \times \vec{E} = i\omega\mu\vec{H} - \vec{M}, \tag{3.1}$$

$$\nabla \times \vec{H} = -i\omega\epsilon\vec{E} + \vec{J}, \tag{3.2}$$

$$\nabla \cdot \vec{E} = \frac{\rho}{\epsilon}, \tag{3.3}$$

$$\nabla \cdot \vec{H} = 0, \tag{3.4}$$

where $\vec{E}$ and $\vec{H}$ are the electric and magnetic field vectors, ρ is the electric charge density, ω is the angular frequency, μ and ϵ are the permeability and permittivity of the medium, respectively. $\vec{J}$ and $\vec{M}$ are the assumed electric and magnetic current density sources. Within a closed domain from which the sources have been excluded, Maxwell's equations (3.1) and (3.2) imply that both $\vec{E}$ and $\vec{H}$ satisfy the vector wave equation

$$\nabla \times (\nabla \times \vec{C}) - k^2\vec{C} = 0, \tag{3.5}$$

where $\vec{C}$ represents either the electric or magnetic fields, and $k = \omega\sqrt{\mu\epsilon}$ is the wave number. Additionally, (3.3) and (3.4) imply that the homogeneous Helmholtz equation is satisfied by $\vec{E}$ and $\vec{H}$ in source free region

$$\nabla^2\vec{C} + k^2\vec{C} = 0. \tag{3.6}$$

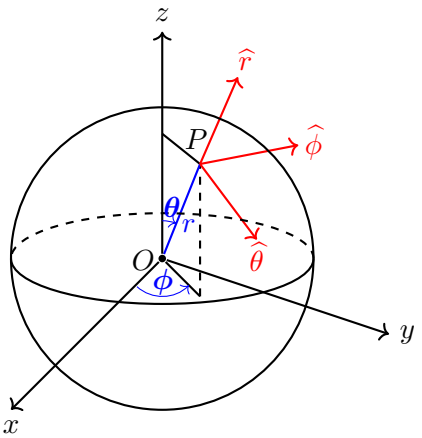

Figure 3.1: Cartesian (x, y, z) and spherical coordinate systems (r, θ, ϕ) with unit vectors $\widehat{r}, \widehat{\theta}, \widehat{\phi}$.

The *spherical modes* are defined in the spherical coordinates (r, θ, ϕ) with unit vectors $(\widehat{r}, \widehat{\theta}, \widehat{\phi})$ as shown in Fig. 3.1. For reference, cartesian coordinates (x, y, z) are also included with unit vectors $(\widehat{x}, \widehat{y}, \widehat{z})$. To solve (3.6) in spherical coordinates, a *generating function* $f(r, \theta, \phi)$ is obtained by solving the scalar wave equation

$$(\nabla^2 + k^2)f = 0. \tag{3.7}$$

It can be shown that the solution of (3.7) [132], allows to define two vector functions $\vec{m}$ and $\vec{n}$ given as

$$\vec{m} = \nabla f \times \vec{r}, \tag{3.8}$$

$$\vec{n} = k^{-1}\nabla \times \vec{m}, \tag{3.9}$$

In addition, the two functions $\vec{m}$ and $\vec{n}$ form an orthogonal and complete basis on which the electromagnetic field $(\vec{E}, \vec{H})$ in any spherical source-free region of space can be decomposed. The *generating function* for $\vec{m}$ and $\vec{n}$ can then be obtained by the separation of variables as [132]

$$f^{(c)}_{mn^{e}_{o}}(r, \theta, \phi) = z^{(c)}_n(kr)P^m_n(\cos\theta)^{\cos}_{\sin}m\phi, \tag{3.10}$$

where $n = 1, 2, 3, \cdots$ and $m = 0, 1, 2, \cdots, n$; e and o indicate even and odd in relation to the choice of the trigonometric function in the ϕ-dependence, respectively. $P^m_n(\cos\theta)$ is the associated Legendre function of nth degree and mth order describing the θ-dependence [132, 133]. $z^{(c)}_n(kr)$ is a radial function specified by an upper index (c) as one of the functions

$$z_n^{(1)} = j_n(kr), \qquad \text{spherical Bessel function} \tag{3.11a}$$

$$z_n^{(2)} = n_n(kr), \qquad \text{spherical Neumann function} \tag{3.11b}$$

$$z_n^{(3)} = h_n^{(1)}(kr) = j_n(kr) + in_n(kr), \qquad \text{spherical Hankel function of the first kind} \tag{3.11c}$$

$$z_n^{(4)} = h_n^{(2)}(kr) = j_n(kr) - in_n(kr), \qquad \text{spherical Hankel function of the second kind} \tag{3.11d}$$

where $c = 1$ and $c = 2$ indicate standing waves, while $c = 3$ and $c = 4$ represent outward and inward travelling waves, respectively.

Using the *generating function* (3.10) in (3.8) and (3.9), the solutions to the vector wave equation become

$$\vec{m}_{mn_o^e}^{(c)}(r,\theta,\phi) = \mp z_n^{(c)}(kr)\frac{mP_n^m(\cos\theta)}{\sin\theta}\begin{matrix}\sin\\ \cos\end{matrix} m\phi\widehat{\theta} - z_n^{(c)}(kr)\frac{\mathrm{d}P_n^m(\cos\theta)}{\mathrm{d}\theta}\begin{matrix}\cos\\ \sin\end{matrix} m\phi\widehat{\phi} \tag{3.12}$$

$$\begin{aligned}\vec{n}_{mn_o^e}^{(c)}(r,\theta,\phi) = {} & \frac{n(n+1)}{kr} z_n^{(c)}(kr) P_n^m(\cos\theta)\begin{matrix}\cos\\ \sin\end{matrix} m\phi\widehat{r} + \frac{1}{kr}\frac{\mathrm{d}}{\mathrm{d}(kr)}\{kr z_n^{(c)}(kr)\}\frac{\mathrm{d}P_n^m(\cos\theta)}{\mathrm{d}\theta}\begin{matrix}\cos\\ \sin\end{matrix} m\phi\widehat{\theta} \\ & \mp \frac{1}{kr}\frac{\mathrm{d}}{\mathrm{d}(kr)}\{kr z_n^{(c)}(kr)\}\frac{mP_n^m(\cos\theta)}{\sin\theta}\begin{matrix}\sin\\ \cos\end{matrix} m\phi\widehat{\phi}.\end{aligned} \tag{3.13}$$

For use in relation to the far-field definitions, the asymptotic form of the $\vec{m}$ and $\vec{n}$ functions, with $c = 3$ as kr tends to infinity, are used in (3.12) and (3.13). This is obtained by replacing the radial functions with the large argument approximations valid for $kr \gg n$

$$z_n^{(3)} \to (-i)^{n+1}\frac{e^{ikr}}{kr} \quad (kr \to \infty) \tag{3.14}$$

$$\frac{1}{kr}\frac{\mathrm{d}}{\mathrm{d}(kr)}\{kr z_n^{(3)}(kr)\} \to (-i)^n\frac{e^{ikr}}{kr} \quad (kr \to \infty). \tag{3.15}$$

3.1.1 Power Normalized Spherical Modes

A more compact notation is obtained by introducing a new symbol $\vec{f}_{smn}^{(c)}$ to designate $\vec{m}$ and $\vec{n}$, where $s = 1$ indicates the $\vec{m}$-function while $s = 2$ represents the $\vec{n}$-function, and using a slightly different *generating function* [134]

$$g_{mn}^{(c)}(r, \theta, \phi) = z_n^{(c)}(kr) P_n^{|m|}(\cos\theta) e^{im\phi}, \tag{3.16}$$

where $n = 1, 2, 3, \cdots$, and now $m = -n, -n+1, \cdots, 0, \cdots, n-1, n$. Note that using $e^{im\phi}$ factor instead of cosine and sine in (3.10) is more convenient in relation to the *spherical modes* rotation [133]. The power normalized *spherical modes generating function* such that a single $c = 3$ *spherical mode* of amplitude 1 radiates a power of $\frac{1}{2}$ watt, is then given as

$$F_{mn}^{(c)}(r, \theta, \phi) = \frac{1}{\sqrt{2\pi}} \frac{1}{\sqrt{n(n+1)}} \left(-\frac{m}{|m|}\right)^m z_n^{(c)}(kr) \bar{P}_n^{|m|}(\cos\theta) e^{im\phi}, \tag{3.17}$$

where $\bar{P}_n^{|m|}(\cos\theta)$ is the normalized associated Legendre function [135] and the $\left(-\frac{m}{|m|}\right)^m$ factor ensures that the phases of the modes follow the phase of spherical harmonics [136]. Inserting the *generating function* (3.17) into the right-hand side of (3.8) defines the *spherical mode* function

$$\begin{aligned} \vec{F}_{1mn}^{(c)}(r, \theta, \phi) &= \nabla F_{mn}^{(c)}(r, \theta, \phi) \times \vec{r} \\ &= \frac{1}{\sqrt{2\pi}} \frac{1}{\sqrt{n(n+1)}} \left(-\frac{m}{|m|}\right)^m \left\{ z_n^{(c)}(kr) \frac{im\bar{P}_n^{|m|}(\cos\theta)}{\sin\theta} e^{im\phi} \widehat{\theta} \right. \\ &\left. - z_n^{(c)}(kr) \frac{\mathrm{d}\bar{P}_n^{|m|} \cos\theta}{\mathrm{d}\theta} e^{im\phi} \widehat{\phi} \right\}. \end{aligned} \tag{3.18}$$

Then by using $\vec{F}_{1mn}^{(c)}$ in the right-hand side of (3.9) we have

$$\begin{aligned}\vec{F}^{(c)}_{2mn}(r,\theta,\phi) &= k^{-1}\nabla \times F^{(c)}_{1mn}(r,\theta,\phi) \\ &= \frac{1}{\sqrt{2\pi}}\frac{1}{\sqrt{n(n+1)}}\left(-\frac{m}{|m|}\right)^m \left\{\frac{n(n+1)}{kr} z^{(c)}_n(kr)\bar{P}^{|m|}_n(\cos\theta)e^{im\phi}\widehat{r}\right. \\ &+ \frac{1}{kr}\frac{\mathrm{d}}{\mathrm{d}(kr)}\{krz^{(c)}_n\}\frac{\mathrm{d}\bar{P}^{|m|}_n\cos\theta}{\mathrm{d}\theta}e^{im\phi}\widehat{\theta} \\ &+ \left.\frac{1}{kr}\frac{\mathrm{d}}{\mathrm{d}(kr)}\{krz^{(c)}_n\}\frac{im\bar{P}^{|m|}_n(\cos\theta)}{\sin\theta}e^{im\phi}\widehat{\phi}\right\}.\end{aligned} \tag{3.19}$$

The expressions (3.18) and (3.19) are the dimensionless power-normalized *spherical modes* functions adopted in this work. The electric field in a source-free region can then be written as a weighted sum of the *spherical modes* functions as

$$\vec{E}(r,\theta,\phi) = \frac{k}{\sqrt{\eta}}\sum_{csmn} Q^{(c)}_{smn}\vec{F}^{(c)}_{smn}(r,\theta,\phi), \tag{3.20}$$

where η is the specific impedance of the medium, and the index s is used to distinguish between two different functions. One of the two wave functions, i.e., $\vec{F}^{(c)}_{1mn}$ has no radial component. Therefore, it represents the part of a (magnetic or electric) field that is transverse with respect to the radial coordinate r. The magnetic field of a Transverse Magnetic (TM) wave is proportional to $\vec{F}^{(c)}_{1mn}$, whereas the associated electric field is proportional to $\vec{F}^{(c)}_{2mn}$. This is reversed for the Transverse Electric (TE) waves, i.e., the electric field is proportional to $\vec{F}^{(c)}_{1mn}$, while the associated magnetic field is represented by $\vec{F}^{(c)}_{2mn}$.

3.1.2 Far-field Radiation Patterns Expressed by Spherical Modes

The electric field $\vec{E}$ of a general outgoing wave field is given as

$$\vec{E}(r,\theta,\phi) = \frac{k}{\sqrt{\eta}}\sum_{smn} Q^{(3)}_{smn}F^{(3)}_{smn}(r,\theta,\phi). \tag{3.21}$$

To obtain the far-field expressions, the asymptotic form of the $\vec{F}^{(3)}_{smn}$ functions as kr tends to infinity are employed. They are obtained by replacing the radial functions entering $\vec{F}^{(3)}_{smn}$ by their large argument approximation [see (3.14) and (3.15)]. For the electric field at a

large distance, the following expression is used

$$\vec{E}(r,\theta,\phi) \rightarrow \frac{k}{\sqrt{\eta}} \sum_{smn} Q^{(3)}_{smn} \vec{F}^{(3),a}_{smn}(r,\theta,\phi), \quad \text{as,} \quad kr \rightarrow \infty, \tag{3.22}$$

where the superscript shows the insertion of the asymptotic form of the radial functions entering the *spherical mode* function. For ease of computation, more convenient expressions can be obtained by introducing a function describing the far-field in terms of the angular variables only. To this end, the far-field patterns $\vec{K}_{smn}(\theta,\phi)$ are defined as

$$\vec{K}_{smn}(\theta,\phi) = \lim_{kr\rightarrow\infty} \left[\sqrt{4\pi} \frac{kr}{e^{ikr}} \vec{F}^{(3)}_{smn}(r,\theta,\phi) \right]. \tag{3.23}$$

The expressions for the far-field pattern functions can then be defined explicitly as

$$\vec{K}_{1mn}(\theta,\phi) = \sqrt{\frac{2}{n(n+1)}} \left(-\frac{m}{|m|}\right)^m \mathrm{e}^{im\phi}(-i)^{n+1} \left\{ \frac{im\bar{P}^{|m|}_n(\cos\theta)}{\sin\theta} \vec{e}_\theta - \frac{\mathrm{d}\bar{P}^{|m|}_n(\cos\theta)}{\mathrm{d}\theta} \vec{e}_\phi \right\}. \tag{3.24}$$

$$\vec{K}_{2mn}(\theta,\phi) = \sqrt{\frac{2}{n(n+1)}} \left(-\frac{m}{|m|}\right)^m \mathrm{e}^{im\phi}(-i)^{n} \left\{ \frac{\mathrm{d}\bar{P}^{|m|}_n(\cos\theta)}{\mathrm{d}\theta} \vec{e}_\theta + \frac{im\bar{P}^{|m|}_n(\cos\theta)}{\sin\theta} \vec{e}_\phi \right\}. \tag{3.25}$$

In terms of $\vec{K}_{smn}(\theta,\phi)$ the electric field at large distance is given by

$$\vec{E}(r,\theta,\phi) \rightarrow \frac{k}{\sqrt{\eta}} \frac{1}{\sqrt{4\pi}} \frac{e^{ikr}}{kr} \sum_{smn} Q^{(3)}_{smn} \vec{K}_{smn}(\theta,\phi). \tag{3.26}$$

3.2 Spherical Modes Beamforming

Let us assume that within an enclosing sphere of radius r_0 (see Fig. 3.2), a number of omnidirectional *spherical modes* of type $s = 1$ are radiated so that indices n and m of each mode are linked by the following relation

$$m = \pm n, \tag{3.27}$$

where $n \geq 2$, i.e., the radiation of the fundamental mode ($n = 1$) is implicit and the relation (3.27) is only valid for high-order omnidirectional *spherical modes*.

The radiation patterns of the modes satisfying the (3.27) condition have omnidirectional amplitudes as shown in Fig. 3.2, and they can be expressed as $\vec{K}_{s,m,n} = \vec{K}_{1,\pm N,N}$, where $n = 2, 3, 4, \cdots, N$. The term $\pm N$ indicates that the excited modes have their azimuthal phase changing in two opposite directions $\pm N, \pm(N-1), \cdots, \pm 3, \pm 2$, where the " $+$ " sign indicates clockwise rotation, and the " $-$ " sign denotes counter-clockwise rotation. To realize beamforming across the entire azimuth plane ($xy-$plane in Fig. 3.2), a multi-port antenna is designed to excite all omnidirectional *spherical modes* of order $N, N-1, \cdots, 1$, that can be supported within the enclosing sphere of radius less than or equal to r_0. The beamforming towards a desired ϕ_d direction is then realized using

$$D_{\max}(\theta, \phi_d) = w_1 \vec{K}_{1,0,1}(\theta, \phi_d) + \sum_{n=2}^{N} w_n \vec{K}_{1,\pm n,n}(\theta, \phi_d), \tag{3.28}$$

where $D_{\mathbf{max}}(\theta, \phi_d)$ denotes the maximum directivity for a desired ϕ_d direction in a given θ-cut plane, $w_n = |A_n| e^{j\Delta\psi_n}$ term is a weighting coefficient applied at the port exciting the respective omnidirectional *spherical mode*, and $|A_n|$ and $\Delta\psi_n$ are the amplitude and phase shift, respectively. $\vec{K}_{1,0,1}$ represents the fundamental mode (with $m = 0$), i.e., a constant phase across the entire $xy-$plane. Because of the uniform performance of the fundamental mode across the azimuthal plane, it is selected as the reference mode when computing the

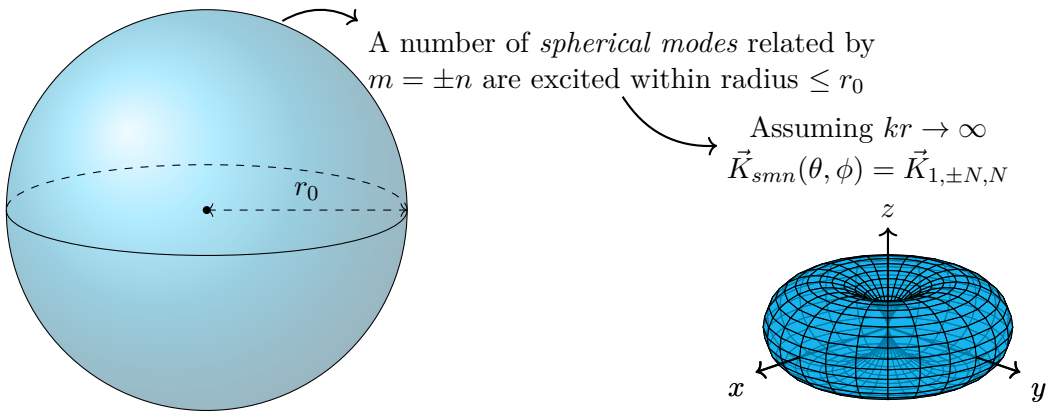

Figure 3.2: Visualization of the enclosing sphere of radius r_0 and exemplar amplitudes of omnidirectional phase-varying *spherical modes*, where the azimuthal phase and order of the excited modes are related by $m = \pm n$.

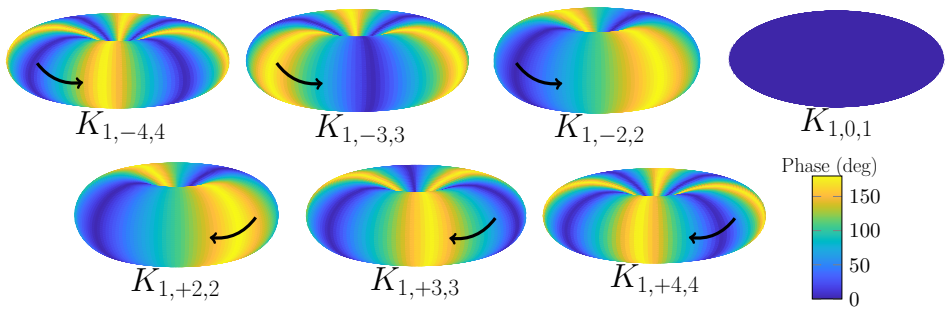

Figure 3.3: Color-coded phase of the radiation pattern for the first few $\vec{K}_{1,m,n}$ omnidirectional *spherical modes*.

phase shift required by each mode to steer the beam to the ϕ_d direction using (3.28). The phase shift is computed using

$$\Delta\psi_n = \psi_{\vec{K}_{1,0,1}}(\phi_d) - \psi_{\vec{K}_{1,\pm n,n}}(\phi_d), \tag{3.29}$$

where $\psi_{\vec{K}_{1,0,1}}(\phi_d)$ represents the phase value of the fundamental mode at the desired angle ϕ_d, and $\psi_{\vec{K}_{1,\pm n,n}}(\phi_d)$ is the phase value of the corresponding phase-varying mode.

For completeness, Fig. 3.3 shows the first few modes of interest for the proposed *Spherical Modes Beamforming (SMB)* principle. It can be seen that except for the fundamental mode, all the modes of order $n \geq 2$ have their phase changing in two opposite directions.

There are few advantages related to using the proposed *SMB* principle, while those will be discussed throughout the thesis, it is important to highlight a few critical aspects at this point. First, the beamforming concept is fundamentally different to that of classical arrays, because the required phase shifts to steer the antenna main beam is generated by the different phase distribution of the *spherical modes*. In contrast, classical arrays rely on the phase characteristics obtained by exciting the same antenna element, that is inter-spaced at uniform or non-uniform distances. Because no inter-spacing is needed in the *SMB* principle, co-located and/or concentric annular ring strcutures can be used to realize a beamforming antenna, while allowing for compact dimensions compared to classical arrays. Lastly, when an antenna is designed to excite a given number of omnidirectional *spherical modes*, the phase characteristics of these modes can be explored to generate different types of radiation (e.g., bi-directional, unidirectional) patterns depending on the number of their phase variations around the azimuthal plane, i.e., value m in Fig. 3.3.

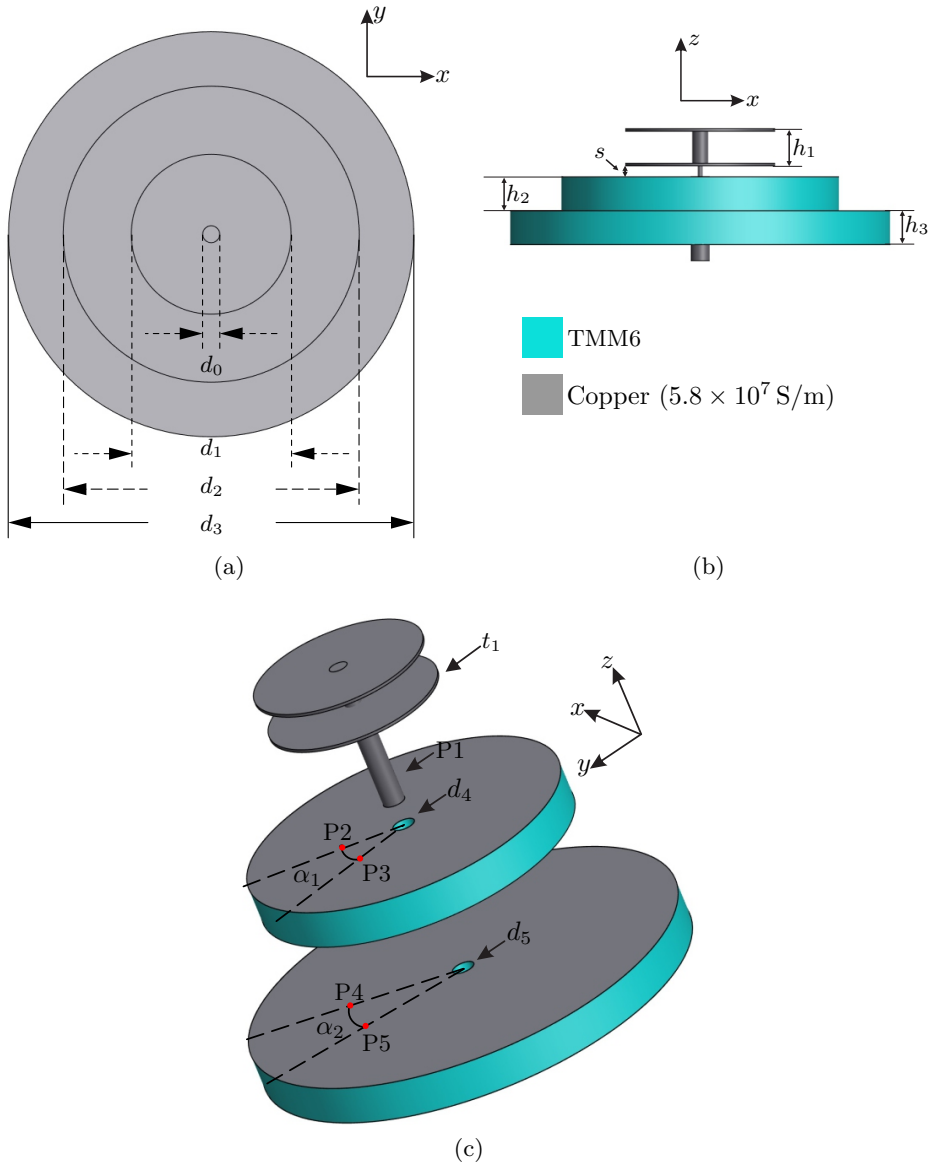

Figure 3.4: Proposed *SMB* antenna. (a) Top view showing each layer's diameter. (b) Front view highlighting each layer's thickness. (c) Exploded view outlining the ports arrangements. All dimensions in mm: $d_0 = 3, d_1 = 28.4, d_2 = 53.25, d_3 = 72, d_4 = 3.6, d_5 = 3.8, s = 2.5, h_1 = 7, h_2 = h_3 = 6.35, h_4 = 0.5, \alpha_1 = 45°, \alpha_2 = 30°$. Feeding ports distance from the center of the substrate, P1 is center-fed, P2=P3=17 mm, and P4=P5=22 mm.

3.3 SMB Performance Evaluation

3.3.1 Antenna Design

To evaluate the *SMB* performance, a multiport co-located antenna radiating omnidirectional *spherical modes* of up to order $n = 3$ is investigated in this section. The antenna is designed to operate near 2.36 GHz and the configuration is shown in Fig. 3.4, comprising

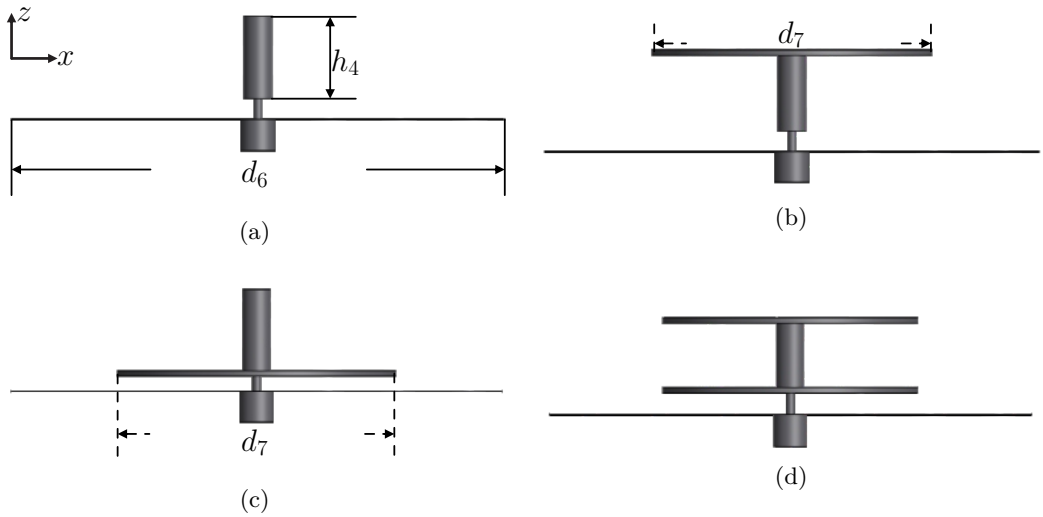

Figure 3.5: Miniaturization steps of the $\lambda/4$ monopole. (a) Ant-A. (b) Ant-B. (c) Ant-C. (d) Ant-D. Dimensions: $h_4 = 8\,\text{mm}$, and $d_7 = 30\,\text{mm}$.

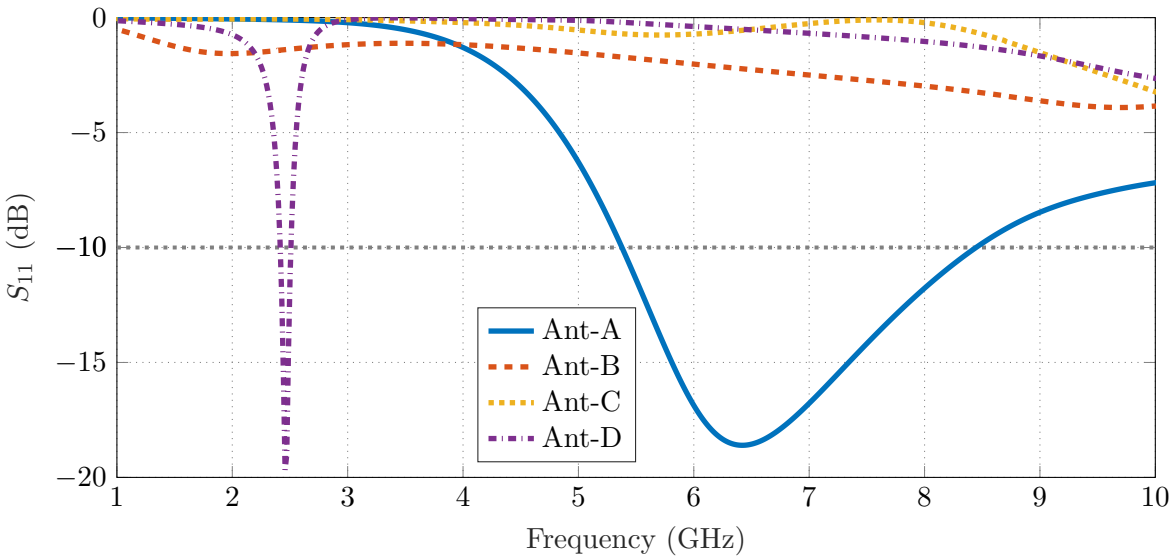

Figure 3.6: S-parameters of the four investigated configurations of the monopole antenna.

three co-located layers: a top-loaded monopole (as the top layer) and two circular patch antennas (as the middle and bottom layers).

Excitation of the Fundamental Mode

The top-loaded monopole excites the fundamental $\vec{K}_{1,0,1}$ mode. It is made of a copper rod with diameter $d_0 = 3\,\text{mm}$ and height $h_1 = 7\,\text{mm}$. For antenna miniaturization, two disks of thickness $t_1 = 0.5\,\text{mm}$ and diameter $d_1 = 28.5\,\text{mm}$ are attached at the extremities of the

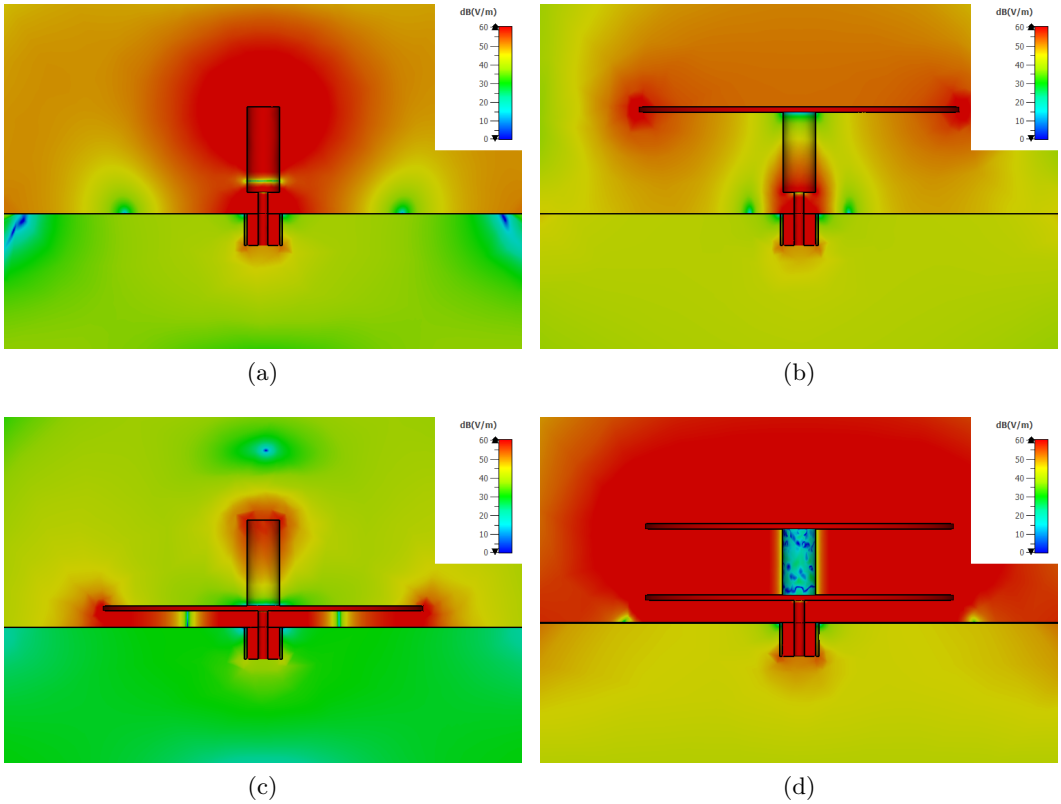

Figure 3.7: $\vec{E}$ distribution of the four investigated monopole antenna configurations in the xz-plane. (a) Ant-A (at 6.41 GHz). (b) Ant-B (at 2 GHz). (c) Ant-C (at 6 GHz). (d) Ant-D (at 2.46 GHz).

copper rod (see Fig. 3.4a and Fig. 3.4b) [137]. The miniaturization steps of the top-loaded monopole antenna are shown in Fig. 3.5, and Fig. 3.6 shows the corresponding S-parameters for each configuration.

Fig. 3.5a shows antenna A (Ant-A), a monopole design of length $h_4 = 8\,\text{mm}$, and diameter= 3 mm. The monopole is mounted on a ground plane of $d_6 = 53\,\text{mm}$ diameter, with the feed located $s = 2\,\text{mm}$ above the ground for impedance matching. The reflection coefficient ($|S_{11}|$) of Ant-A is shown in solid lines in Fig. 3.6. It can be seen that the antenna resonates near 6.41 GHz, and the corresponding $\vec{E}$ distribution is shown in Fig. 3.7a highlighting strong $\vec{E}$ along the copper rod.

Because at $f_0 = 2.36\,\text{GHz}$ the monopole height is 0.062λ (i.e., $h_4 \ll \lambda/4$), a metalic disk is inserted in a follow-up design step, that forms Ant-B (Fig. 3.5b) in order to increase antenna's capacitance [138]. The disk diameter is $d_7 = 30\,\text{mm}$ with 0.5 mm thickness [130], and as shown in Fig. 3.5b the disk is loaded at the top extremity of the rod. A $|S_{11}| < -1.5\,\text{dB}$ can be seen near 2 GHz (red curves in Fig. 3.6), the corresponding $\vec{E}$ distribution is shown

in Fig. 3.7b, where strong fields are seen along the disk. For completeness, Fig. 3.5c shows Ant-C, where the disk is loaded at the copper rod's lower extremity. The $\vec{E}$ distribution at 6 GHz, where $|S_{11}| < -0.5$ dB (see Ant-C in Fig. 3.6) is shown in Fig. 3.7c. While a strong $\vec{E}$ is seen at the disk, the resonance is at significantly higher frequency of 6 GHz due to the height of the loaded disk. To further reduce the capacitive reactance and increase the radiation resistance [130], the monopole is loaded with two disks at both extremities (see Fig. 3.5d). This also achieves a resonance near the desired f_0 with good matching characteristics (see $|S_{11}|$ values for Ant-D in Fig. 3.6). The corresponding $\vec{E}$ distribution is shown in Fig. 3.7d, highlighting strong fields on and between the two disks.

Excitation of Phase-Varying Modes

The middle layer of the co-located *SMB* antenna comprises a circular patch made of copper with 35 μm thickness and for miniaturization it is supported by a TMM6 substrate ($\epsilon_r = 6.3$ and $\tan\delta = 0.0023$) with $h_2 = 6.35$ mm thickness (see Fig. 3.4). This patch is used to excite the $\vec{K}_{1,\pm2,2}$ omnidirectional *spherical modes*, which are obtained by exciting two orthogonal TM_{21} modes fed in-quadrature to enforce the required azimuthal phase variations. The

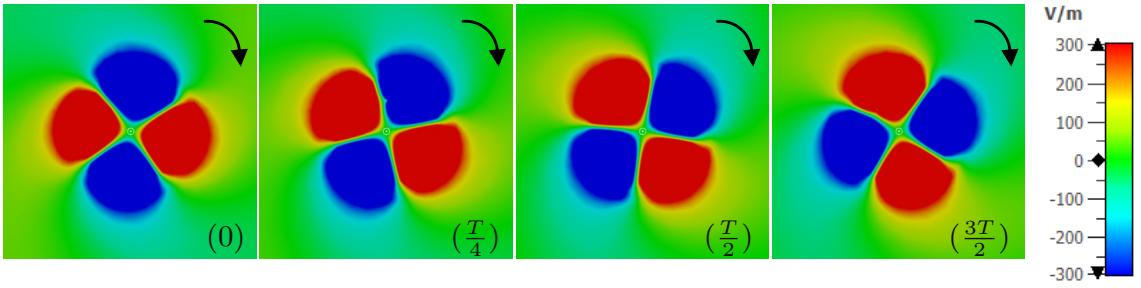

(a)

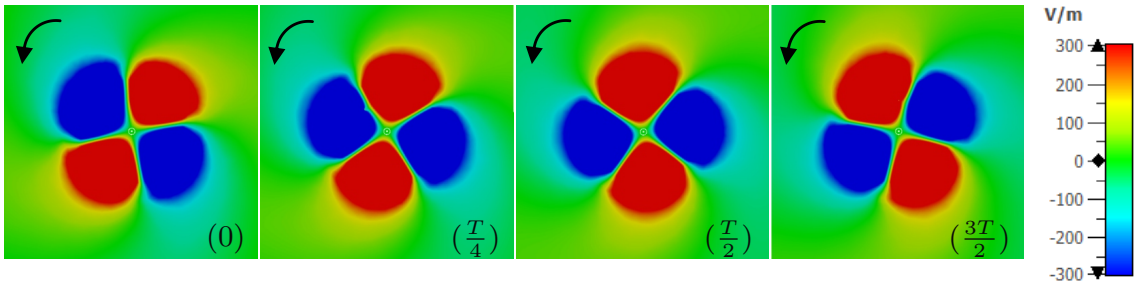

(b)

Figure 3.8: $\vec{E}$ distribution in the middle layer (z-components) at different time points. (a) P2. (b) P3.

patch diameter ($d_2 = 52.6\,\text{mm}$) is therefore approximated using (2.17). The feeding ports P2 and P3 are rotated by $\alpha_1 = 45°$ to ensure orthogonality between the two excited modes of the same order. P2 and P3 are discrete ports located at 17 mm from the center and use the bottom layer patch as the ground plane.

To allow for the feeding of the top-loaded monopole, a center hole of diameter $d_4 = 3.6\,\text{mm}$ is introduced on the patch and substrate of the middle layer (see Fig. 3.4c). Because the modes radiated by this patch are omnidirectional, the presence of the hole has little impact on the properties of the excited $\vec{K}_{1,\pm2,2}$ modes. Lastly, the $\vec{E}$ distribution of the two orthogonal modes excited within the patch are shown in Fig. 3.8. The fields are depicted at different time points to highlight the required phase rotation around the azimuth plane, i.e., a clockwise rotation is seen for P2 (Fig. 3.8a). In contrast, a counter-clockwise rotation is observed for P3 (Fig. 3.8b).

The bottom layer includes a circular patch antenna made of a 35 μm thick copper with diameter $d_3 = 72\,\text{mm}$ and supported by a 6.35 mm thick TMM6 substrate (see Fig. 3.4). The bottom layer patch has the largest diameter in the proposed *SMB* antenna, therefore, the final antenna dimensions are 72 mm × 72 mm × 22.3 mm, or correspondingly $0.56\lambda \times$

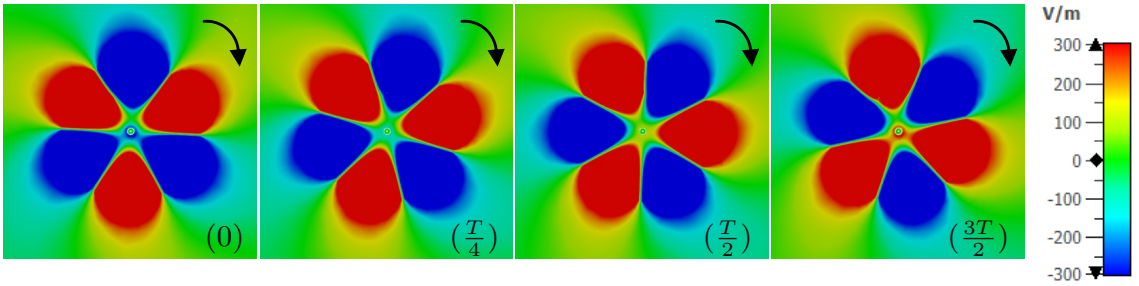

(a)

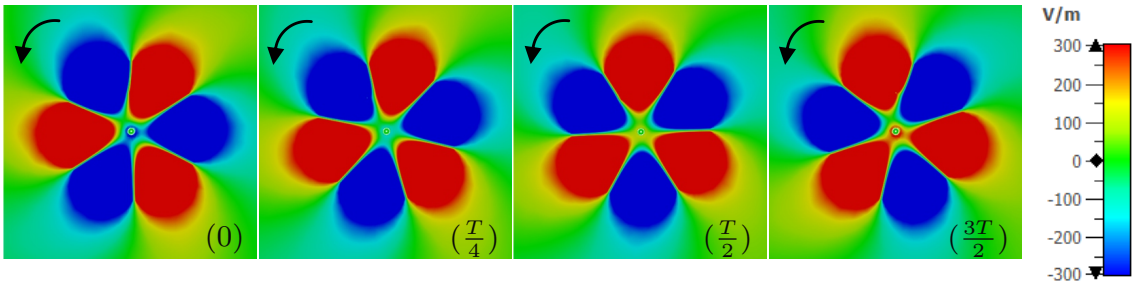

(b)

Figure 3.9: $\vec{E}$ distribution in the bottom layer (z-components) at different time points. (a) P4. (b) P5.

$0.56\lambda \times 0.17\lambda$ for $f_0 = 2.36\,\text{GHz}$.

The bottom patch is used to excite the $\vec{K}_{1,\pm3,3}$ modes, which are generated by exciting two orthogonal TM_{31} modes fed in-quadrature. The feeding ports (P4 and P5) are rotated by $\alpha_2 = 30°$ to ensure orthogonality between the two modes of the same order. Note that this layer also includes a center hole (of diameter $d_5 = 3.8\,\text{mm}$) to enable the feeding of the top-loaded monopole through a $50\,\Omega$ semi-rigid coaxial cable as shown in Fig. 3.4. Lastly, Fig. 3.9 shows the electric field distribution of the two excited orthogonal modes. In this case, too, it can be seen that the fields rotate in two opposing directions, clockwise rotation for P4 (Fig. 3.9a) and counter-clockwise for P5 (Fig. 3.9b).

3.3.2 Beamforming Discussion

The antenna S-parameters are shown in Fig. 3.10. It can be seen that the antenna center frequency is at 2.36 GHz, and the overlapping $-10\,\text{dB}$ impedance bandwidth between all the ports is 5.8 MHz. Note that this bandwidth is mainly limited by the bottom and middle layers, which excite the higher order modes $\vec{K}_{1,\pm2,2}$ (P2 and P3 with 14.8 MHz bandwidth) and $\vec{K}_{1,\pm3,3}$ (P4 and P5 with 5.8 MHz bandwidth). In contrast, the fundamental $\vec{K}_{1,0,1}$ mode (excited using P1) has the largest bandwidth of around 144 MHz.

At the antenna center operating frequency, the isolation between all the antenna ports

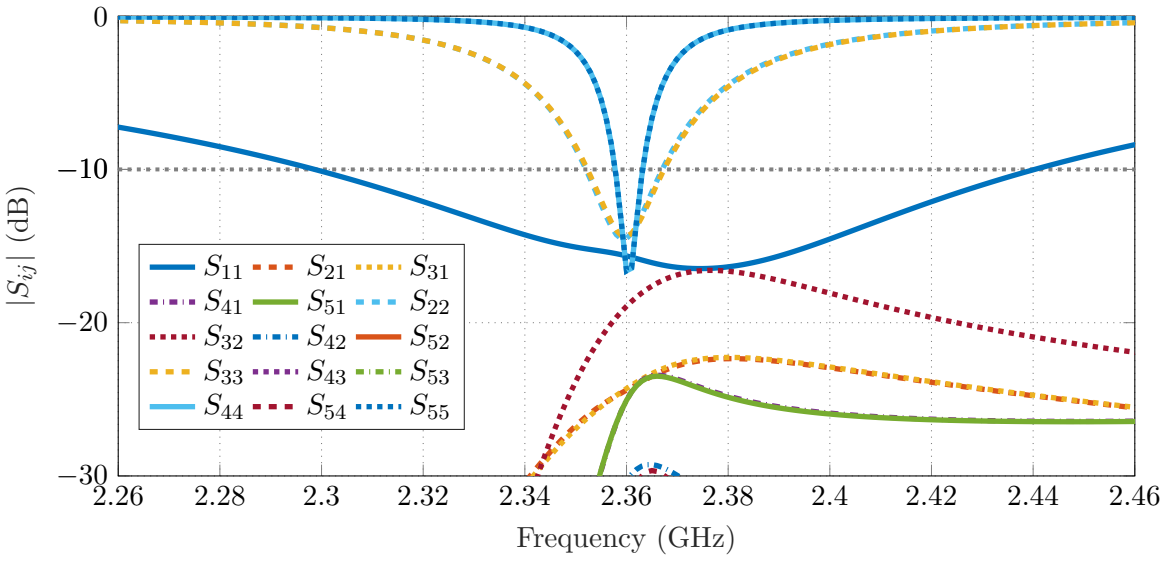

Figure 3.10: S-parameters of the proposed *SMB* antenna, port index $i, j = 1, 2, 3, 4,$ and 5.

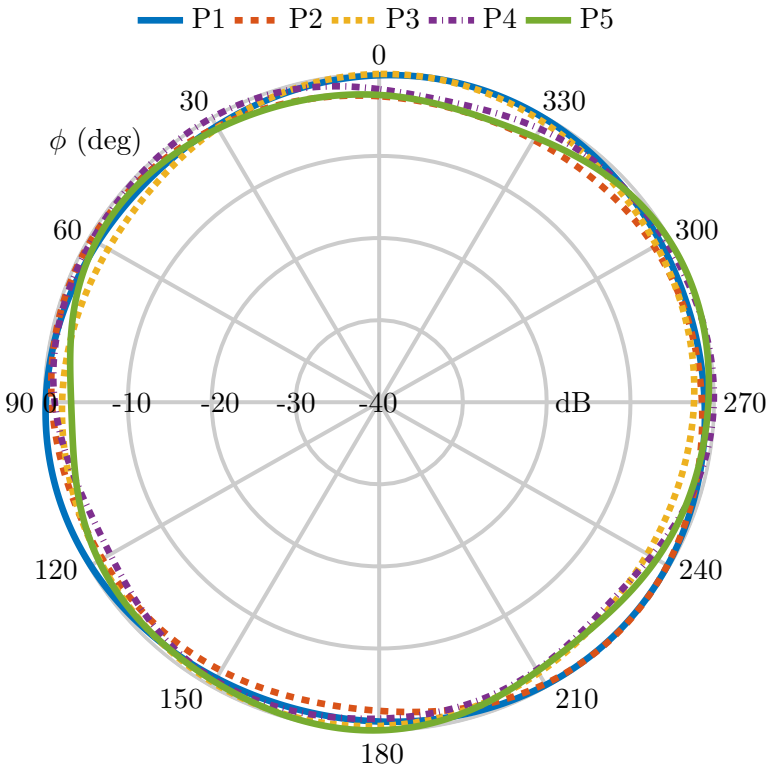

Figure 3.11: Normalized radiation pattern of each port of the proposed *SMB* antenna in the xy-plane ($\theta = 90°$).

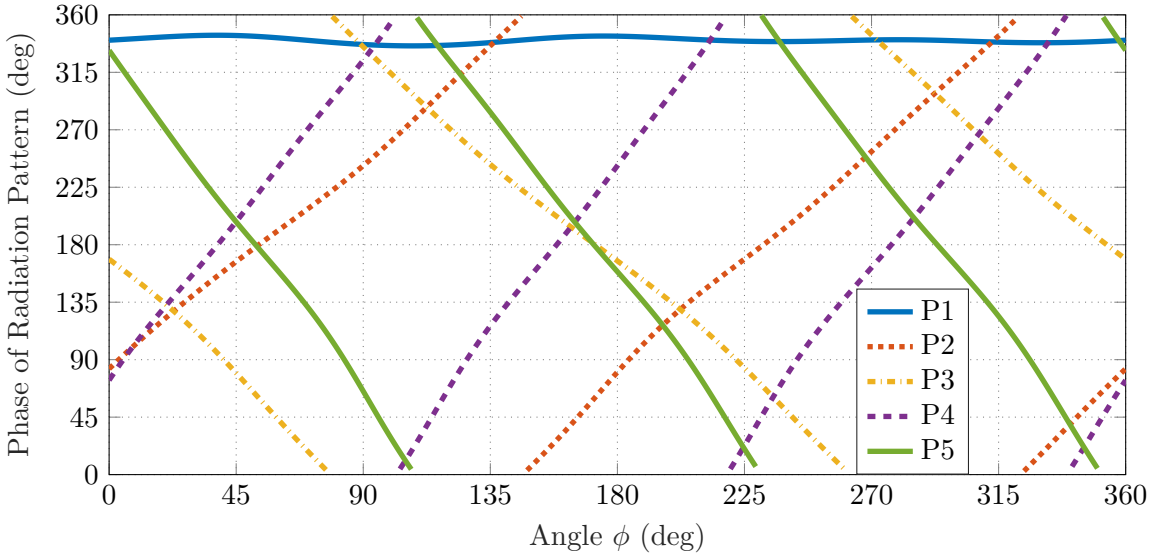

Figure 3.12: Phase of the radiation pattern of each port of the *SMB* antenna in the xy-plane.

is better than 18.9 dB, and it stays above 17.8 dB across the entire −10 dB impedance bandwidth region. The antenna total efficiency at f_0 = 95% for P1, 79% for P2 and P3,

43% for P4 and P5. These values shohw that the total efficiency decreases for the higher-order modes, as they require a much larger diameter to support the phase variations around their perimeter, i.e., dual-phase variations for the $\vec{K}_{1,\pm2,2}$ modes and triple-phase variations for the $\vec{K}_{1,\pm3,3}$ modes.

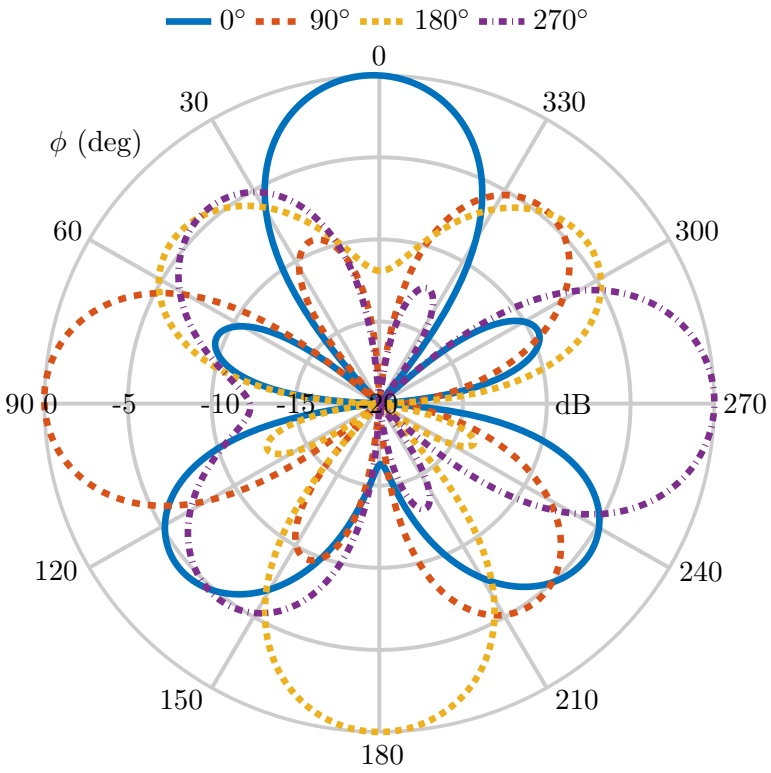

Figure 3.13: Normalized radiation patterns (xy-plane) of the proposed antenna. The antenna main beam is steered in four different directions separated by 90° to cover the entire horizontal plane.

Fig. 3.11 shows the normalized radiation patterns of all the modes excited in the proposed *SMB* antenna. In general, it can be seen that the required omnidirectional patterns are achieved in all five ports. The corresponding phase of the radiation pattern for each excited mode is shown in Fig. 3.12. It can be seen that the mode excited by P1 follows the characteristics of the fundamental $\vec{K}_{1,0,1}$ mode, i.e., it has a constant phase across the entire azimuthal plane. In contrast, the modes excited by P2 and P3 have the characteristics of the $\vec{K}_{1,\pm2,2}$ modes, i.e., their phase changes twice across the azimuthal plane in two opposite directions (clockwise direction for P2 and counter-clockwise for P3). Lastly, P4 and P5 excite the $\vec{K}_{1,\pm3,3}$ modes, as shown by their triple phase variations across the horizontal plane. The modes also change in two opposite directions, clockwise direction for

Table 3.1: Excitation Values for the co-located *SMB* Antenna.

ϕ_d	$\lvert A_1\rvert$	$\Delta\psi_1$	$\lvert A_2\rvert$	$\Delta\psi_2$	$\lvert A_3\rvert$	$\Delta\psi_3$	$\lvert A_4\rvert$	$\Delta\psi_4$	$\lvert A_5\rvert$	$\Delta\psi_5$
0°	1	0°	1	264°	1	177°	1	274°	1	14°
90°	1	0°	1	99°	1	7°	1	17°	1	281°
180°	1	0°	1	270°	1	181°	1	105°	1	189°
270°	1	0°	1	91°	1	1°	1	180°	1	99°

$\lvert A_n\rvert$ (amplitude), and $\Delta\psi_n$ (phase shift) for the nth port.

P4 and counter-clockwise for P5.

Fig. 3.13 shows the beamsteering performance of the proposed design. The antenna main beam is steered into four directions separated by 90° to cover the entire horizontal plane, i.e., $\phi_d = 0°, 90°, 180°$, and 270°. The beamsteering is achieved using (3.28), the required phase compensations in each antenna port to steer the main beam towards the desired direction are computed using (3.29), and are outlined in Table 3.1. As shown in Fig. 3.13, a unidirectional beamforming performance is realized across the entire horizontal plane, the antenna is vertical linearly polarized, and the Side Lobe Level (SLL) of the generated patterns is below −4 dB. The achieved realized gain varies within 4 to 4.4 dBi, and the Half-Power BeamWidth (HPBW) changes from 40.7° to 42.9°.

3.4 Summary

This chapter presented the fundamental concepts of the *spherical modes* theory. Building on the theoretical formulation of the *spherical modes*, a beamforming concept was proposed to exploit the different phase characteristics of the omninidirectional *spherical modes* excited within a constrained antenna size. To validate the proposed beamforming principle, a five-port co-located *SMB* antenna operating at 2.36 GHz with 0.56λ diameter and 0.17λ profile was designed. It was demonstrated that the antenna excites different omnidirectional *spherical modes*, which enable to realize continuous unidirectional beamforming with vertical linear polarization across the entire azimuthal plane. Initial analysis of the beamforming characteristics demonstrated that a realized gain of up to 4.4 dBi with a HPBW within 40.7° to 42.9° can be achieved across the desired plane.

4 SMB Driven AoA Estimation

SMB Driven AoA Estimation

This Chapter analyzes the feasibility of the *Spherical Modes Beamforming* (*SMB*) antennas to enable Angle of Arrival (AoA) estimation in size-constrained Internet of Things (IoT) devices. Based on the characteristics of each excited omnidirectional *spherical mode*, a system model is formulated and numerically validated using the Multiple Signal Classification (MUSIC) algorithm. The Chapter further discusses the challenges of performing AoA estimation with classical arrays, by investigating the issue of mutual coupling effects in AoA estimation of arrays comprising electrically small and closely spaced antenna elements. As an alternative model to perform AoA estimation in small platforms, this Chapter highlights the different AoA measurement characteristics that can be generated with the proposed *spherical modes* concept, by investigating the implementation of two *SMB* antennas. Moreover, to quantify the performance of the proposed solution, benchmarking with classical arrays are also demonstrated, and to highlight the efficacy of the proposed method, location estimations based on triangulation are presented. The results emanating from this chapter were published at the IEEE Internet of Things Magazine [130], IEEE Sensors Letters [139], and the 2022 International Workshop on Antenna Technology [140].

4.1 Suitability of SMB Antennas for AoA Estimation

To address the difficulties related to miniaturization of classical arrays, *SMB* antennas offer an alternative solution to enhance the performance of small IoT devices. As demonstrated in Chapter 3, such antennas exploit the different phase distributions of all the omnidirectional *spherical modes* excited within a given antenna volume. In other words, the *SMB* principle derives a multi-modal antenna structure. This is different from classical arrays, where an

antenna element radiates a single mode and it is then inter-spaced by a given distance d, and the phase difference of the signal as it impinges at these elements is used to compute the AoA.

The *SMB* antennas then offer significant advantages compared to classical arrays. For instance, the antenna discussed in Section 3.3 uses co-located structures with no inter-spacing d, between the elements. Therefore, compared to an array using the same number of antenna elements, the *SMB* design occupies a much smaller diameter. As will be demonstrated, these properties make it suitable for integrated compact IoT devices.

4.1.1 System Model

A few assumptions are made in this Chapter, in order to model and fairly compare both the proposed *SMB* antennas and reference classical arrays. First, the source signals are considered to be narrowband, and far-field radiation is assumed, i.e., the distance between the sources and the antenna is considered to be larger than the Rayleigh distance $2R^2/\lambda$, where R is the antenna's largest dimension. This implies that the radiation impinging on the antennas consists of a set of planar wavefronts, as demonstrated in Fig. 4.1. Moreover, the waves are assumed to be verically linear polarized.

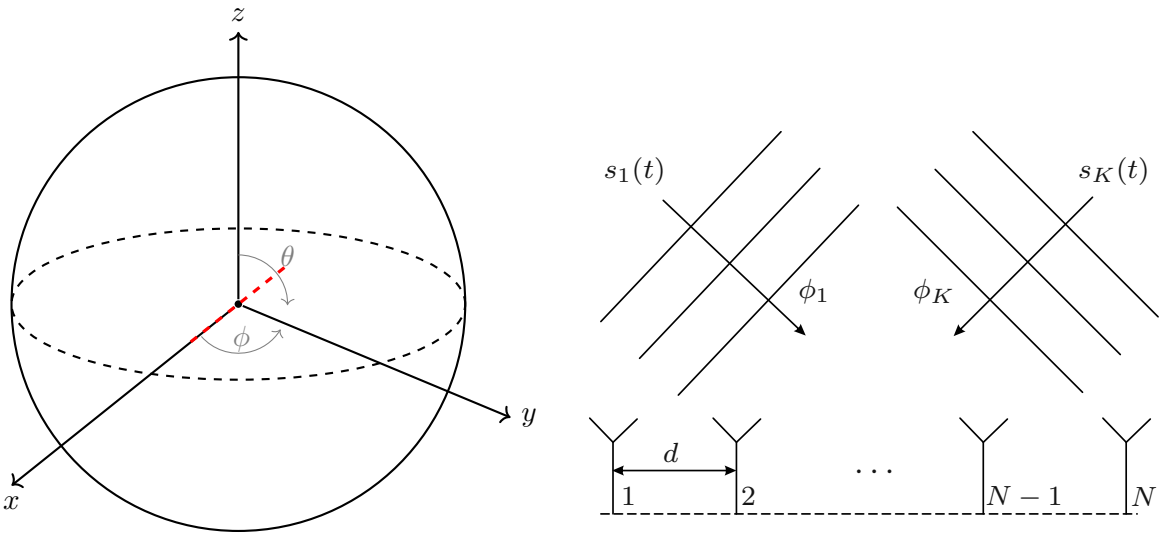

Figure 4.1: The left image shows the AoA measurements coordinates, i.e., xy-plane. The antennas are centrally located and for the linear array the elements are inter-spaced along the x-axis (dashed red). The right image demonstrate the planar wavefronts impinging on array comprising N elements.

A number of $s_k(t), k = 1, 2, 3, \cdots, K$ source signals impinge on the N elements/modes of the antennas with wavelength λ at time t. Additionally, the sources and the antennas are assumed to be in the same horizontal plane (xy-plane in Fig. 4.1), and for simplicity, the elevation angles are fixed at $\theta = 90°$. The antenna response is then sampled over a grid of azimuth angles defined as ϕ_i, and the response from directions $\phi_1, \phi_2, \cdots, \phi_K$ is a complex matrix $\boldsymbol{A}(\phi) \in \mathbb{C}^N$ comprised of steering vectors $\vec{a}_m(\phi_i)$ given by

$$\vec{a}_m(\phi_i) = [w_1, w_2, w_3, ..., w_K] \tag{4.1}$$

where w_i with $i \in [1, \cdots, K]$ are the weighting components of the steering vector to point the main beam in the desired ϕ_i direction. The steering vectors for arrays were defined in (2.19) and for *SMB* antennas they are are obtained from (3.28). Assuming that L snapshots are observed for the i^{th} beam, the input signal vector $\vec{x}(t)$ for the m^{th} port of the *SMB* antenna or reference array is then given as

$$\vec{x}_m(t) = \sum_{i=1}^{K} \vec{a}_m(\phi_i) s_i(t) + v_m(t) \tag{4.2}$$

where $m = 1, 2, 3, \cdots, N$, $\vec{x}_m \in \mathbb{C}^{N \times L}$, i indicates the beam pointing to the direction ϕ_i, i.e., the AoA of the i^{th} impinging wave, and $\vec{a}_m(\phi_i)$, $s_i(t)$, and $v_m(t)$ correspond to the steering vector, the complex waveform, and the complex white Gaussian noise of the m^{th} antenna port, respectively. The noise is assumed to be spatially uncorrelated with the source signals, and the antenna signal model is defined as

$$\boldsymbol{X}(t) = \boldsymbol{A}(\phi)\vec{s}(t) + \vec{v}(t) \tag{4.3}$$

where $\boldsymbol{X}(t) = [\vec{x}_1(t), ..., \vec{x}_N(t)]^{\mathrm{T}} \in \mathbb{C}^{N \times 1}$ represents the received signals, $[.]^{\mathrm{T}}$ denotes the transpose operation. $\boldsymbol{A}(\phi) = [\vec{a}_1(\phi_i), ..., \vec{a}_m(\phi_K)] \in \mathbb{C}^{N \times K}$ is the array response matrix. $\vec{s}(t) = [s_1(t), ..., s_N(t)]^{\mathrm{T}} \in \mathbb{C}^{N \times 1}$ is the vector of the impinging signals, and $\vec{v}(t) = [v_1(t), ..., v_N(t)]^{\mathrm{T}} \in \mathbb{C}^{N \times 1}$ is the additive white Gaussian noise. The impinging signal covariance matrix is given by

$$\boldsymbol{R}_X = \mathbb{E}\{\boldsymbol{X}(t)[\boldsymbol{X}(t)]^{\mathrm{H}}\} = [\boldsymbol{A}(\phi)]^{\mathrm{H}}\boldsymbol{R}_s\boldsymbol{A}(\phi) + \boldsymbol{R}_v \tag{4.4}$$

where $\boldsymbol{R}_s = \mathbb{E}\{\vec{s}(t)[\vec{s}(t)]^{\mathrm{H}}\}$ is the signal covariance matrix and $\boldsymbol{R}_v = \mathbb{E}\{\vec{v}(t)[\vec{v}(t)]^{\mathrm{H}}\} = \sigma^2\boldsymbol{I}$ is the noise covariance matrix, σ^2 is the noise variance, $[.]^{\mathrm{H}}$ denotes Hermitian operation. $\boldsymbol{I}$ is the $N \times N$ unitary matrix and $\mathbb{E}\{.\}$ denotes statistical expectation. In practical scenarios, the matrix $\boldsymbol{R}_X$ is estimated from a limited set of received data, therefore, the sample covariance matrix $\widehat{\boldsymbol{R}}$, extracted from L snapshots is given by

$$\widehat{\boldsymbol{R}} = \frac{1}{L}\sum_{r=1}^{L}\boldsymbol{X}(r)\boldsymbol{X}^{\mathrm{H}}(r) \tag{4.5}$$

4.1.2 AoA Estimation

To evaluate the AoA performance of the *SMB* antennas and the classical arrays, the MUltiple SIgnal Classification (MUSIC) algorithm is used [141], as it offers higher AoA estimation performance [142]. MUSIC is a subspace method based on the eigen-decomposition of the output covariance matrix. In the classical implementation of the MUSIC algorithm, for an array comprised of N elements/modes, it is assumed that the number of impinging signals K is known a priori and $K < N$. The covariance matrix is then divided into signal subspace $\boldsymbol{Q_S} \in \mathbb{C}^{K\times N}$ and noise subspace $\boldsymbol{Q_N} \in \mathbb{C}^{K\times(N-K)}$. From the signal modeling of the investigated antennas, the output covariance is given in (4.5). The MUSIC spectrum function is then derived as [141]

$$P_{MUSIC}(\phi_i) = \frac{1}{[\vec{a}_m(\phi_i)]^{\mathrm{H}}\boldsymbol{Q_N}\boldsymbol{Q_N}^{\mathrm{H}}\vec{a}_m(\phi_i)} \tag{4.6}$$

where the peak values of the $P_{MUSIC}(\phi_i)$ spectrum function corresponds to the AoA.

The AoA estimation performance for all the investigated antennas in this thesis is summarized as follows

1. The data matrix covariance (4.5) for the MUSIC algorithm is extracted from complex radiation patterns of the investigated antennas. For simulation, the CST Studio

Suite is used. For measurements, the matrix is obtained from radiation patterns measured in an anechoic chamber.

2. The MUSIC algorithm implementation is done in MATLAB, and the estimated AoA is extracted as the peak value of the MUSIC spectrum function (4.6).
3. The performance accuracy is evaluated in terms of Mean Absolute Error (MAE) between the MUSIC algorithm estimated angle and the actual incident angle using $N_{mc} = 1000$ Monte Carlo runs as

$$\phi_i^{error} = \frac{1}{N_{mc}} \sum_{k=1}^{N_{mc}} |\phi_i^{MUSIC} - \phi_i^{incident}| \tag{4.7}$$

4. The incident angles for all the evaluated antennas are swept in the horizontal plane ϕ_i with 0.1° resolution.
5. Because the classical MUSIC algorithm is implemented in this thesis, it is assumed that the number of signals is smaller than the number of elements/modes in the antenna, i.e. $N > K$. Therefore, a maximum of four simultaneous impinging signals can be separated in the *SMB* antenna discussed in Chapter 3.

4.2 Limitations of Arrays for AoA Estimation

As discussed in Section 2.4, classical arrays require inter-element spacing, which minimizes the mutual coupling effects between antenna elements. This is necessary because the presence of mutual coupling results in changes in the radiators' current distribution, which leads to changes in antenna impedance, radiation of distorted antenn patterns, and reduced radiation efficiency, among other issues. To limit the above effects, an inter-element separation of typically $\lambda/2$ (where λ is the wavelength at the array's center operating frequency) is used. This separation generally allows for a coupling level which is $\leq -10\,\text{dB}$, since for relatively compact antennas, this level has little effect on the overall antenna array performance. However, because of this separation, the array becomes over-sized for compact integrated IoT devices operating at sub-6 GHz frequency bands.

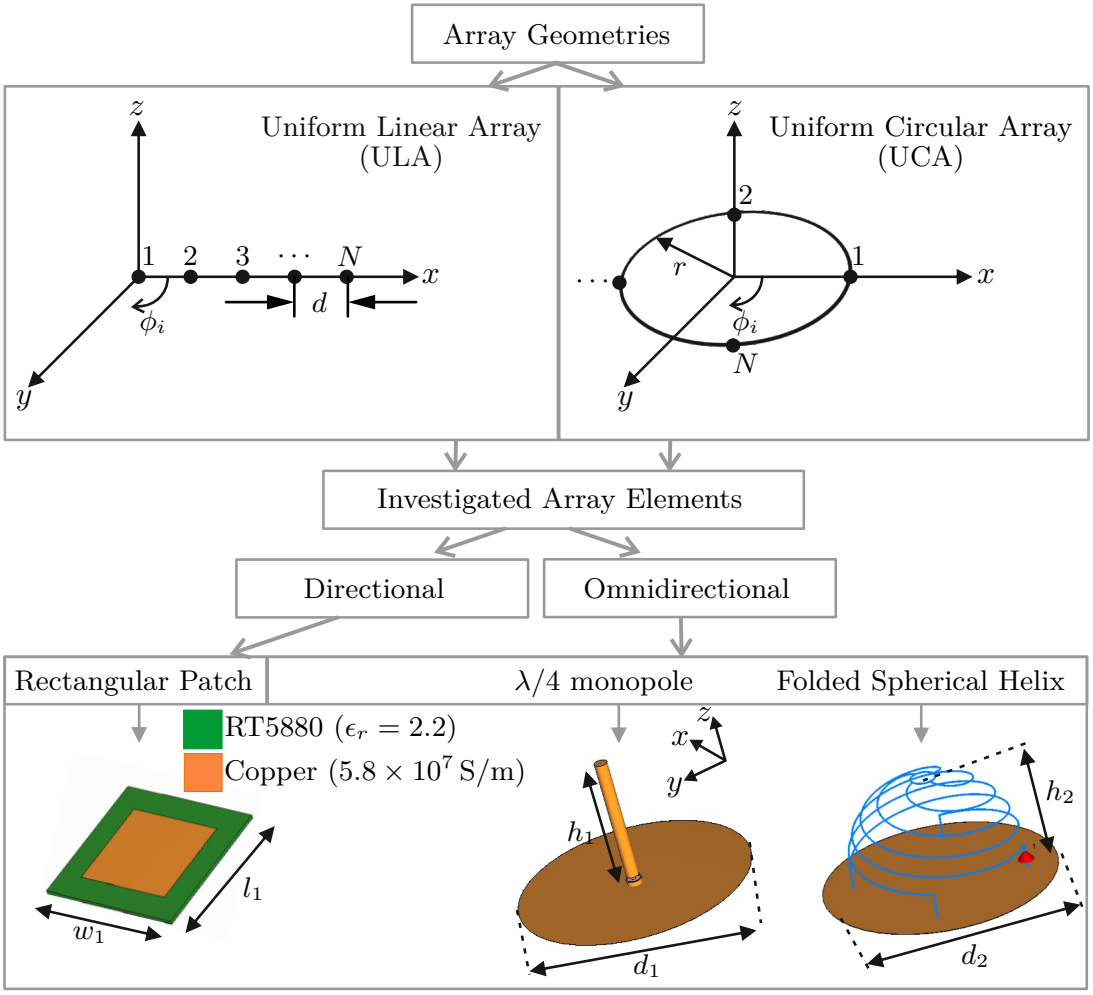

Figure 4.2: Schematic outlining the investigated array elements. The top part shows the array geometries used for AoA estimation, namely Uniform Linear Array (ULA) (top left) and Uniform Circular Array (UCA) (top right). Each of the proposed geometries is then tested with a directional (rectangular patch) and omnidirectional [$\lambda/4$ monopole and FSH antennas]. Note that the copper wires of the FSH antenna are shown in blue for visualization. All the antennas operate at the center frequency of 2.4 GHz, and the corresponding dimensions are in mm: $w_1 = 60, l_1 = 62, d_1 = 44, h_1 = 28, d_2 = 17.2$, and $h_2 = 8$.

4.2.1 Investigated Arrays

To demonstrate the limitations of classical arrays for AoA measurements, this section investigates the miniaturization performance of uniform linear arrays. The schematic in Fig. 4.2 outlines antennas studied in this Chapter. Note, however, that for this section only linear arrays comprising omnidirectional elements will be investigated, i.e., a $\lambda/4$ monopole, and for further miniaturization, an electrically small omnidirectional antenna is used – the Folded Spherical Helix (FSH) monopole antenna proposed by Best in [143].

As shown in Fig. 4.2, uniform linear arrays constitute the simplest array geometry, comprising identical antennas equally placed over a straight line [16]. For an impinging signal incoming from angle ϕ_i, the separation between the array elements creates a phase shift proportional to the cosine of the angle. This means the signals in each direction will differ in phase, which can be used for AoA measurements. It is important to point out that linear arrays employing omnidirectional antennas face front-back ambiguity, as the mirrored signals impinging from two sides of the line containing the array elements, will eventually produce the same signal at antenna ports. For this reason, in this thesis, a directional antenna (rectangular patch) is used to eliminate this ambiguity. However, the linear array's field of view is still limited to $0° - 180°$. Another issue of linear arrays is that the beamwidth is known to broaden near end-fire directions [16, 144], which practically limits the AoA performance to a field of view of around $120°$ $(30° - 150°)$ [144].

For completeness the uniform circular array structures (shown on the top-right of Fig. 4.2) comprise identical elements that are equally spaced on the circumference of a circle with radius r. Such structures offer a $360°$ field of view across the azimuthal plane. Moreover, if a suitable directional antenna element is utilized, electronic beamforming can be obtained by simply shifting the complex excitation coefficient around the circular ring. This, therefore, enables the circular array to have a more uniform beam pattern across the entire horizontal plane. For this reason the performance of circular arrays will be benchmarked against the unidirectional *SMB* antenna in Section 4.3.

Table 4.1: Comparison of Coupling Effects on AoA using ULAs

$\lvert S_{12}\rvert, \lvert S_{32}\rvert$ (dB)	Inter-element spacing (d)		Half-power beamwidth		Coverage with MAE $< 1°$	
	$\lambda/4$ monopole	FSH	$\lambda/4$ monopole	FSH	$\lambda/4$ monopole	FSH
-13.5	$\lambda/2$	$\lambda/2$	$37.1°$	$37.2°$	$155°$	$155°$
-10	0.36λ	0.36λ	$47.7°$	$48.1°$	$146°$	$146°$
-8	0.28λ	0.3λ	$62°$	$63.3°$	$138°$	$141°$
-6	0.17λ	0.21λ	$112°$	$84.3°$	$109°$	$117°$

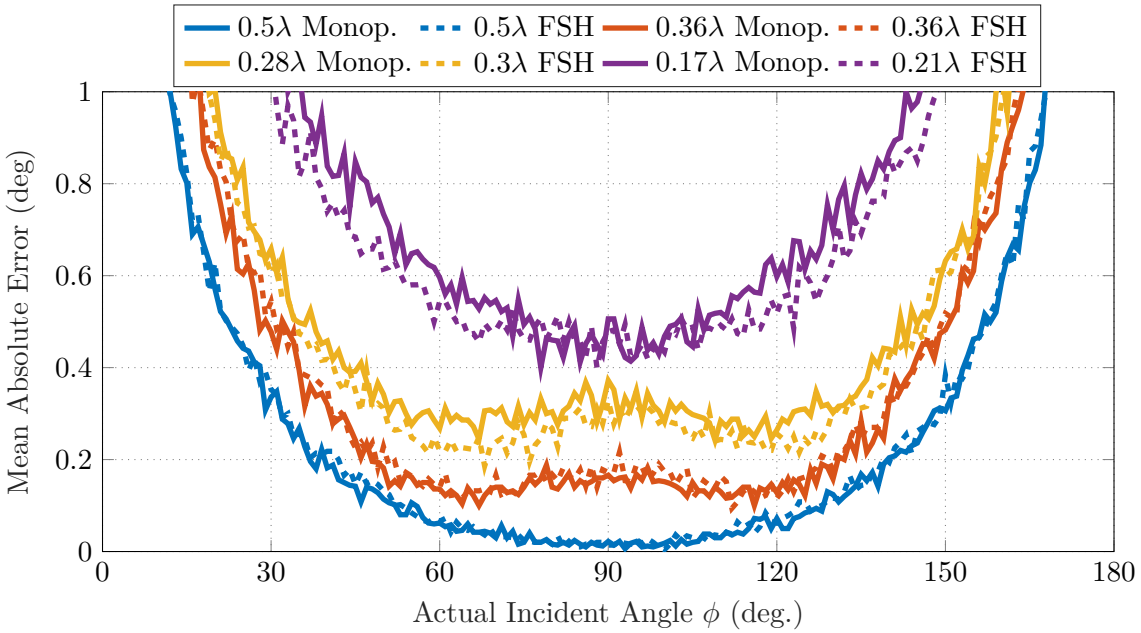

Figure 4.3: Comparison of MUSIC performance of $\lambda/4$ monopole and ultra-small FSH antenna for different inter-element spacing using 10 dB SNR and 100 snapshots.

4.2.2 AoA Estimation from Miniaturized Arrays

To discuss the effects of mutual coupling in AoA measurements, the system modeling and AoA performance evaluation method outlined in previous sections, are used to compare the performance of two Uniform Linear Arrays (ULAs) comprising three omnidirectional elements. The first array utilizes a $\lambda/4$ monopole antenna, and the second array uses ultra-small FSH monopole with a radius of 0.13λ. Table 4.1 outlines the inter-element spacing required by each configuration to have the mutual coupling between each adjacent element, i.e., $|S_{12}|$ and $|S_{32}|$ of -13.5, -10, -8 and -6 dB.

From the results shown in Table 4.1, it can be seen that as the inter-element spacing is decreased, the mutual coupling level between the antenna elements increases. The increase of mutual coupling translates into degradation in the AoA measurements. As shown in Fig. 4.3, a $\lambda/2$ inter-element spacing realizes lower Mean Absolute Errors (MAEs) compared to smaller inter-element spacing.

The results in Table 4.1 further detail that the Field of View (FoV) with MAE $< 1°$ for $\lambda/2$ inter-element spacing (where a -13.5 dB coupling is achieved) for both arrays is 155° (12° − 167°). However, when the coupling level increases to -6 dB (0.17λ inter-element

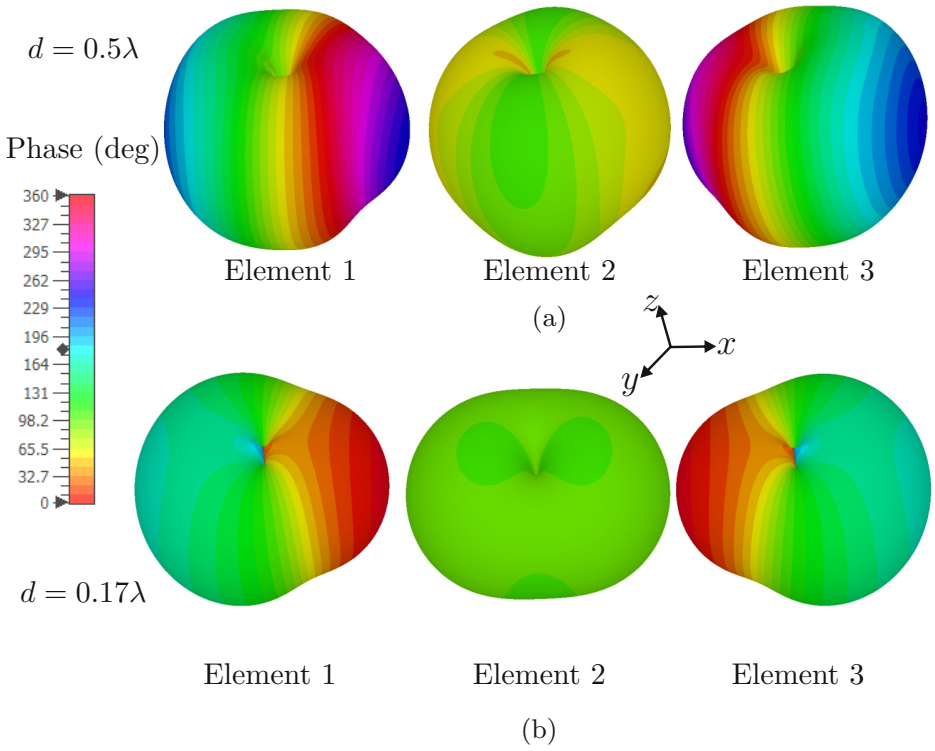

Figure 4.4: Mutual coupling analysis for 3-element uniform linear array comprising $\lambda/4$ monopoles. (a) 3D radiation patterns with a color-coded phase of the monopole antennas within the linear array using 0.5λ inter-element spacing. (b) 3D radiation patterns with color-coded phase for the array comprising the same elements, but with 0.17λ inter-element spacing. Note that the patterns with an inter-element spacing of 0.17λ exhibit smaller phase variation, and their amplitudes differ significantly from that of omnidirectional patterns.

spacing for $\lambda/4$ monopole and 0.21λ inter-element spacing for the FSH), this coverage decreases to around 109° (36° − 145°) and 117° (31° − 148°) for the $\lambda/4$ monopole and ultra-small FSH, respectively. Note that, the $\lambda/4$ monopole array shows a lower FoV (for −8 and −6 dB) as the inter-spacing between its elements is smaller than that of the ultra-small FSH for a similar level of coupling. The performance deterioration in both arrays occurs because of the increased similarity of the phase of the radiation patterns. This is highlighted in Fig. 4.4a and Fig. 4.4b, where it can be seen that as the inter-element spacing decreases, the phase variations diminish and the omnidirectional patterns of the elements also become increasingly distorted. Another factor that contributes to the degradation of the AoA performance for miniaturized arrays is the fact that the beam broadens as the array inter-spacing is lowered. As shown in Table 4.1, the Half-Power BeamWidth (HPBW) increases from 37.1° to 112° for the array comprising $\lambda/4$ monopole and from 37.2° to 84.3°

for the array using the ultra-small FSH antennas.

Lastly, the results also indicate that as the inter-element spacing is decreased, the mutual coupling for electrically small antennas (ultra-small FSH) degrades much faster as compared to the mutual coupling of the antennas not subject to any miniaturization, i.e., $\lambda/4$ monopole. This is seen from Table 4.1, where the element spacing of the array comprising $\lambda/4$ monopoles can be reduced to 0.17λ for a $-6\,\text{dB}$ coupling. However, the array using ultra-small FSH antennas cannot be reduced to less than 0.21λ for the same coupling level. The significance of this finding is that the use of arrays comprising Electrically Small Antenna (ESA) elements does not directly solve the problem of AoA measurements in compact IoT devices. This is because the highly miniaturized elements will experience increased mutual coupling when compared to designs not subject to miniaturization. It is also important to point out that the increased mutual coupling for electrically small antennas, occurs for very small inter-element spacing values. For the FSH antenna investigated in this Chapter, the effect is not noticeable for values greater than 0.36λ.

4.3 AoA Estimation from SMB Antennas

To address the limitations of classical arrays, this section studies the suitability of *SMB* antennas for AoA measurements. To this end, the antenna proposed in Chapter 3 is used for the AoA studies. This is the co-located *SMB* antenna shown in Fig. 4.5b. The antenna excites $\vec{K}_{1,0,1}$, $\vec{K}_{1,\pm2,2}$, and $\vec{K}_{1,\pm3,3}$ modes, i.e., a total of five *spherical modes* are generated, hence it is denoted as penta-modal antenna. As demonstrated in Section 3.3 the design, offers unidirectional beamforming characteristics across the entire horizontal plane. For completeness, the AoA performance of a structure exciting the first combination of modes capable of beamforming in the horizontal plane, the $\vec{K}_{1,0,1}$ and $\vec{K}_{1,\pm2,2}$ modes, hence denoted tri-modal antenna is also analyzed and is shown in Fig. 4.5a.

As depicted in Fig. 4.5a, the tri-modal antenna includes three ports and has a total diameter of 53.25 mm (0.41λ). This antenna then comprises the first two layers of the penta-modal design, i.e., the top-loaded monopole and the middle layer, for the excitation of the $\vec{K}_{1,0,1}$ and $\vec{K}_{1,\pm2,2}$ *spherical modes*. The corresponding simulated S-parameters are shown

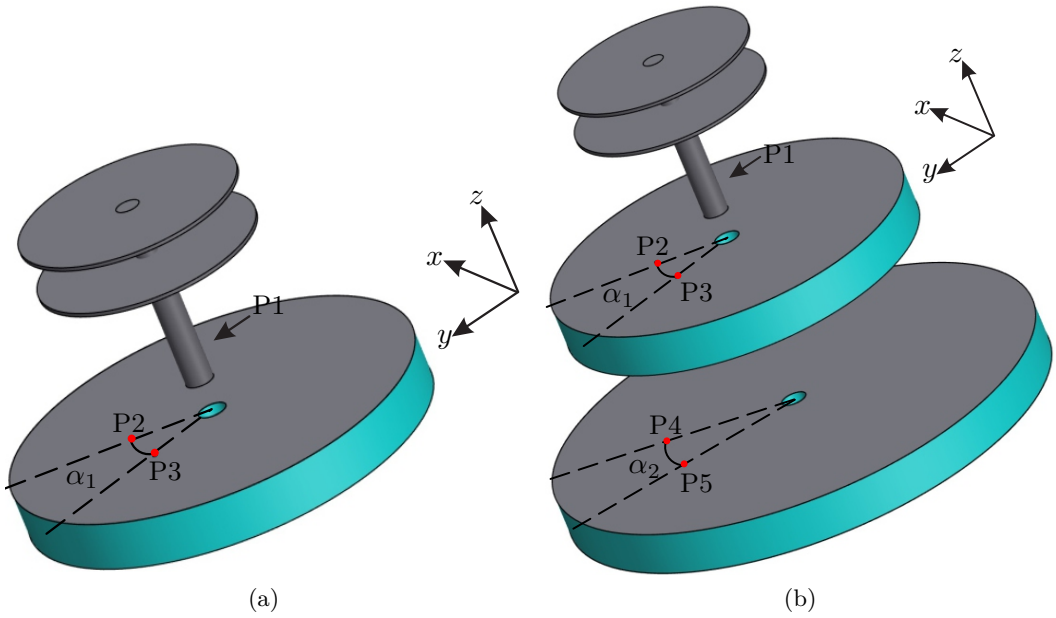

Figure 4.5: Perspective views of the proposed *SMB* antenna. (a) Tri-modal antenna. (b) Penta-modal. $\alpha_1 = 45°, \alpha_2 = 30°$. Feeding ports distance from the center, P1 is center-fed, P2 = P3 = 17 mm, and P4 = P5 = 22 mm. Except for the top disk of the tri-modal design (radius = 14.8 mm), all dimensions follow the penta-modal dimensions as given in Section 3.3.

in Fig. 4.6a. The antenna center-frequency is $f_0 = 2.33$ GHz, the impedance bandwidth is 14.8 MHz, and the isolation is better than 16 dB at the center operating frequency. The penta-modal design (Fig. 4.5b) has a total of five ports, and as shown in Fig. 4.6b it operates at $f_0 = 2.36$ GHz, with an impedance bandwidth of 5.8 MHz, and an isolation better than 18.7 dB at the center frequency.

The beamforming characteristics of the two antennas are compared in Fig. 4.7 by steering the main beam of both structures to the $\phi_d = 270°$ direction. It can be seen that the tri-modal design offers the first type of beamforming characteristics, which is a bi-directional antenna pattern, i.e., a second main beam is always located at $\phi_d + 180°$. This is mainly due to the use of low number of omnidirectional *spherical modes*, i.e., only $\vec{K}_{1,0,1}$ and $\vec{K}_{1,\pm2,2}$ modes are used. While the use of these modes helps to realize a smaller structure of $0.41\lambda \times 0.41\lambda \times 0.12\lambda$, however, the generated pattern can limit the use of the antenna for applications requiring single-beam coverage across the entire horizontal plane.

To obtain a unidirectional radiation pattern, $\vec{K}_{1,\pm3,3}$ modes are excited in the penta-modal antenna. While the antenna total size increases to $0.56\lambda \times 0.56\lambda \times 0.17\lambda$, it can be seen that the generated beam has a much sharper characteristic, where the main beam

points to only one direction, also with a smaller HPBW of 41.5°, a realized gain of 4.1 dBi, as compared to the tri-modal design, which shows a HPBW of 68.5° and a realized gain of 2.24 dBi.

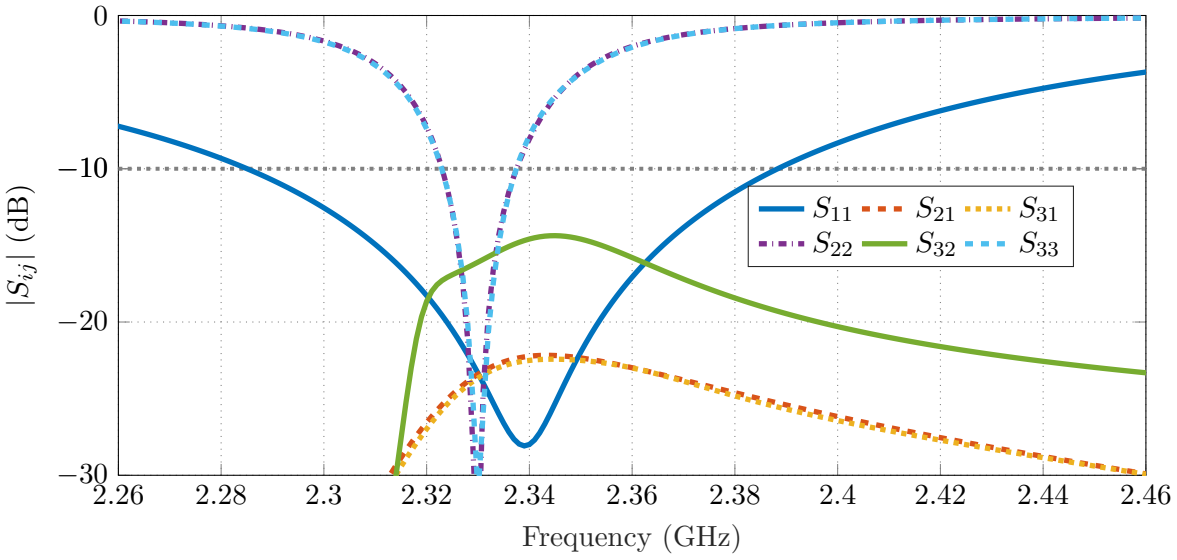

(a)

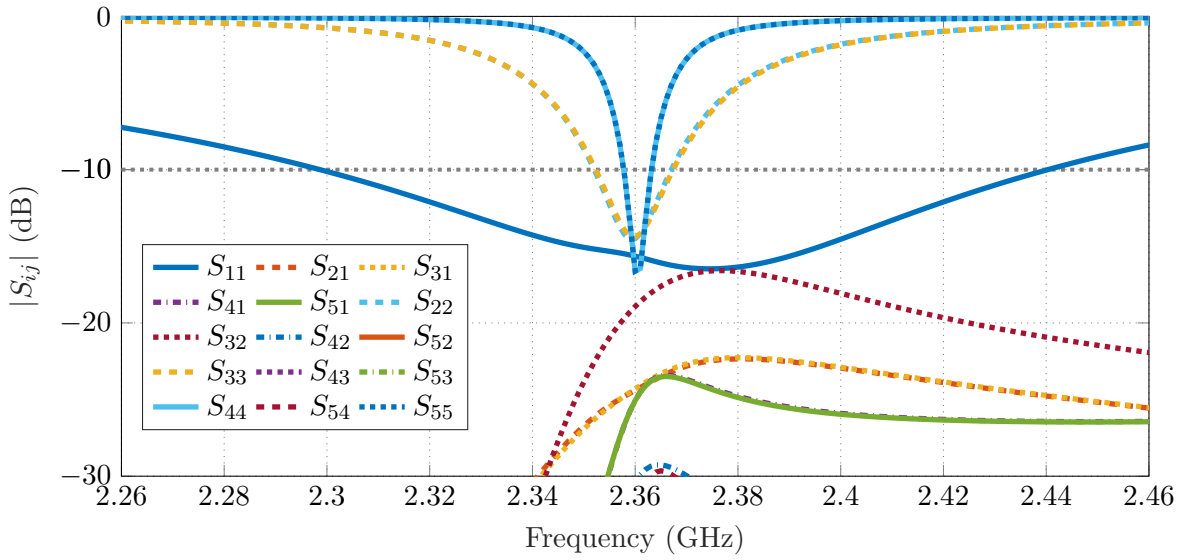

(b)

Figure 4.6: Simulated S-parameters of the investigated *SMB* antennas. (a) Tri-modal antenna. (b) Penta-modal antenna.

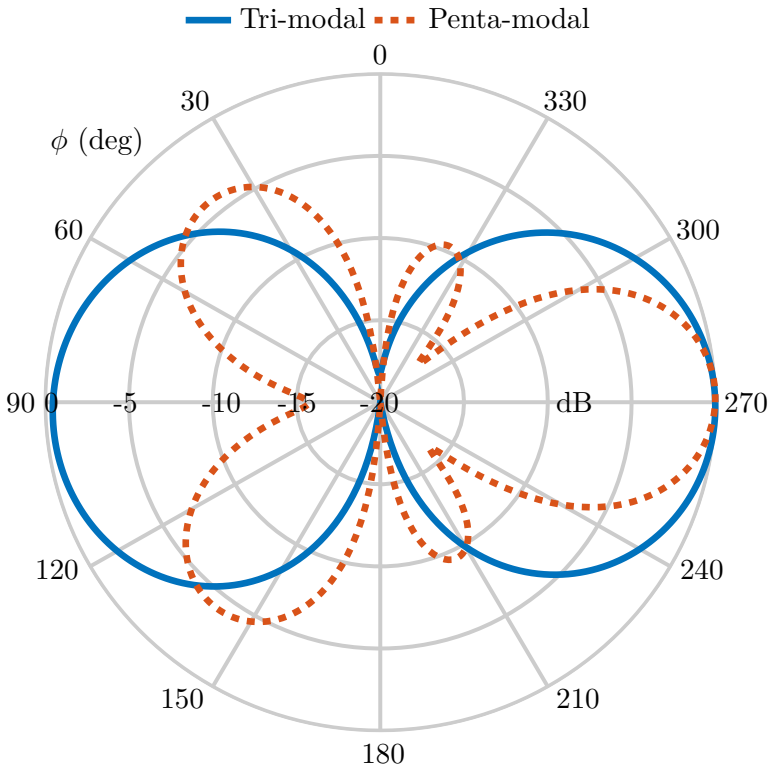

Figure 4.7: Normalized radiation patterns (xy-plane cut) highlighting the beamsteering performance of the proposed antennas for the main beam steered towards $\phi_d = 270°$.

4.3.1 AoA Estimation from Tri-Modal Antenna

Fig. 4.8 shows the AoA performance of the tri-modal antenna. For benchmarking, the ULAs comprising the elements outlined in Fig. 4.3 are used. This is due to the AoA estimation ambiguity in linear arrays and the tri-modal antenna, which constrains the AoA estimation between 0° and 180°. Note that the inter-spacing between each element within the arrays is chosen so as to provide the highest miniaturization, while still ensuring at least 10 dB isolation between each adjacent antenna element. The Mean Absolute Error (MAE) is computed using 100 snapshots and different Signal-to-Noise Ratio (SNR) levels. It can be seen that for 10 dB SNR, the FoV with MAE $< 0.4°$ is $125°(26° - 151°)$, $114°(34° - 148°)$, for the 3-element linear arrays comprising the rectangular patch, and the FSH monopole antennas, respectively. The results also show that the MAE of the ULAs increases towards the end-fire directions. However, this does not occur in the tri-modal antenna, which exhibits a more uniform MAE within the entire investigated plane, i.e., MAE is $< 0.4°$ within

the $0° - 180°$ interval. From Fig. 4.8, it can also be seen that for the broadside directions, the arrays show better performance, with 95° coverage where MAE $< 0.1°$. However, the proposed tri-modal antenna still achieves MAE $< 0.38°$ over the entire evaluated range.

To further validate the AoA performance, the SNR level is increased to 15 dB. In this case the coverage with MAE $< 0.4°$ increases from 125° to 155° for the array comprising rectangular patches, and from 114° to 143° for the array using FSH antennas. For the same SNR level, the tri-modal antenna realizes a MAE $< 0.056°$ across the entire interval of $0° - 180°$. It can be seen that for this SNR level, the MAE still increases for end-fire directions of the linear arrays, and an increasing number of elements or a much higher SNR level would be required to limit the AoA performance degradation. Note, however, that the arrays still outperform the tri-modal design in the broadside directions. This is because a much larger aperture, which is $\geq 0.97\lambda$ is used, compared to 0.56λ for the proposed antenna.

Lastly, Table 4.2 highlights that the performance of the tri-modal antenna is realized using a structure occupying only 0.41λ diameter (53.25 mm at 2.33 GHz) compared with linear arrays of size $1.36\lambda \times 0.38\lambda \times 0.012\lambda$ (rectangular patch array), and $0.97\lambda \times 0.13\lambda \times 0.065\lambda$ (FSH monopole array). This implies that the proposed *SMB* solution offers comparable

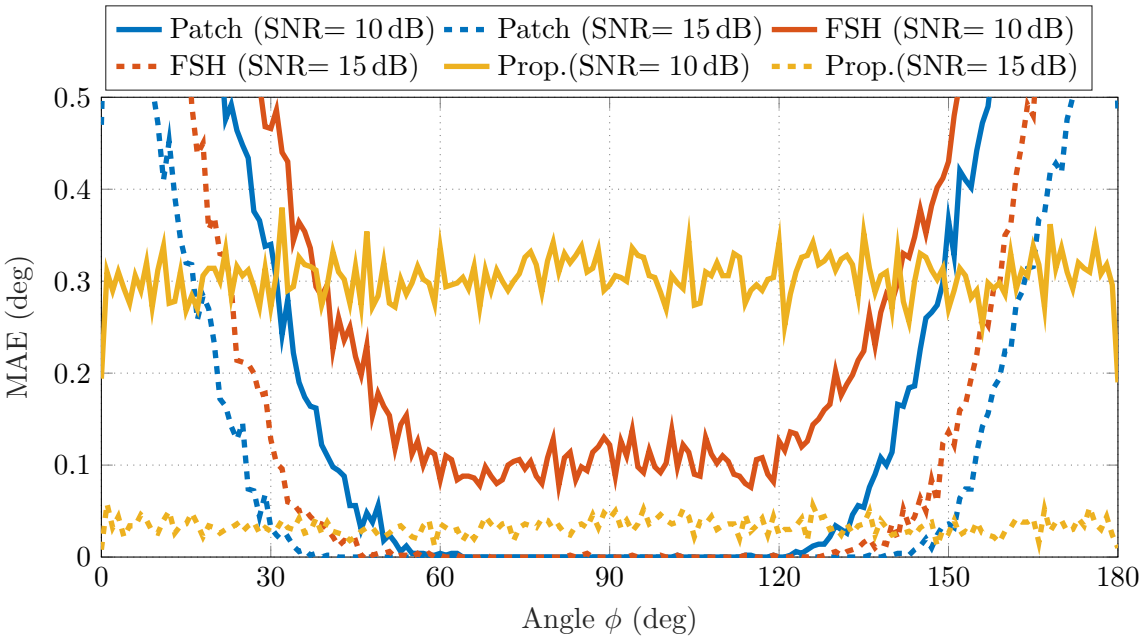

Figure 4.8: MUSIC performance comparison between ULAs and tri-modal antenna. The results are calculated using 100 snapshots for 10 and 15 dB SNR levels.

Table 4.2: Size Comparisons Between the Investigated Antennas

Antenna	Element size (λ^2) total size (λ^3)	3-element linear arrays		5-element circular arrays	
		$d(\lambda)$	Total size(λ^3)	$d(\lambda)$	Total size(λ^3)
FSH	0.14×0.065	0.42	$0.97 \times 0.13 \times 0.065$	0.47	$0.94 \times 0.94 \times 0.065$
Patch	0.32×0.35	0.43	$1.36 \times 0.38 \times 0.012$	0.42	$0.93 \times 0.93 \times 0.5$
Tri-m.	$0.41 \times 0.41 \times 0.12$	Miniaturization up to 70%		-	
Penta-m.	$0.56 \times 0.56 \times 0.17$	-		Miniaturization up to 40%	

if not better AoA estimation performance, while using a structure that is up to 3.3 times smaller (miniaturization up to 70%) when compared to the investigated linear arrays comprising directional antennas, and up to 2.4 times smaller (miniaturization up to 57%) when compared to linear arrays comprising ultra-small FSH monopole antenna elements.

4.3.2 AoA Estimation from Penta-Modal Antenna

The penta-modal antenna is shown in Fig. 4.5b, and is capable of generating a unidirectional radiation pattern across the entire horizontal plane. This property expands the FoV of the tri-modal antenna to the full 360°. Note that because linear arrays do not offer a 360° field of view across the horizontal plane, for fair and unbiased comparison studies, 5-element Uniform Circular Arrays (UCAs) are used in this section.

Fig. 4.9 compares the AoA estimation between the UCAs comprising directional (rectangular patch) and omnidirectional (FSH monopole) antennas and the proposed penta-modal antenna. The comparisons are conducted using 100 snapshots, and for 10 dB SNR level, it can be seen that the penta-modal antenna achieves MAE $< 0.126°$ across the entire horizontal plane. The circular array comprised of directional patch antennas reaches the lowest errors (MAE $< 0.05°$) around 20°, 92°, 164°, 236° and 308°, as those angles are the broadside angles of each directive antenna element. For any other angle, the proposed penta-modal antenna outperforms all the other investigated arrays. Additionally, it can be seen that while the circular array comprising omnidirectional elements (ultra-small FSH) shows the worst AoA performance, nevertheless, its estimated MAE is still smaller than 0.2° across the entire investigated plane.

From Fig. 4.9 it can also be seen that the AoA performance of all the investigated

antennas improves for high SNR levels. For the case where SNR = 15 dB, against 100 snapshots, all the antennas achieve MAE$<0.08^\circ$ across the entire azimuthal plane. Lastly, as outlined in Table 4.2, the penta-modal design occupies a total diameter of 0.56λ, therefore when compared to the UCA comprising rectangular patches (diameter = 0.93λ with an inter-element spacing of 0.43λ) and the UCA comprising ultra-small FSH (diameter = 0.94λ with an inter-element spacing of 0.47λ), the proposed *SMB* antenna achieves AoA estimation performance comparable with UCAs while providing miniaturization of up to 40%.

Multiple incoming signals

As outlined in the system modeling discussions (see Section 4.1.1), the number of signals that can be simultaneously separated by the classical MUSIC algorithm is limited to $N-1$, where N is the total number of antenna inputs, i.e., the number of elements or modes. This means that for the proposed penta-modal antenna, a maximum of four simultaneous impinging signals can be separated. However, the resolution of this separation significantly depends on the antenna performance. To improve the accuracy of the AoA estimation of the proposed antenna, the numerical studies are conducted using 200 snapshots, and the

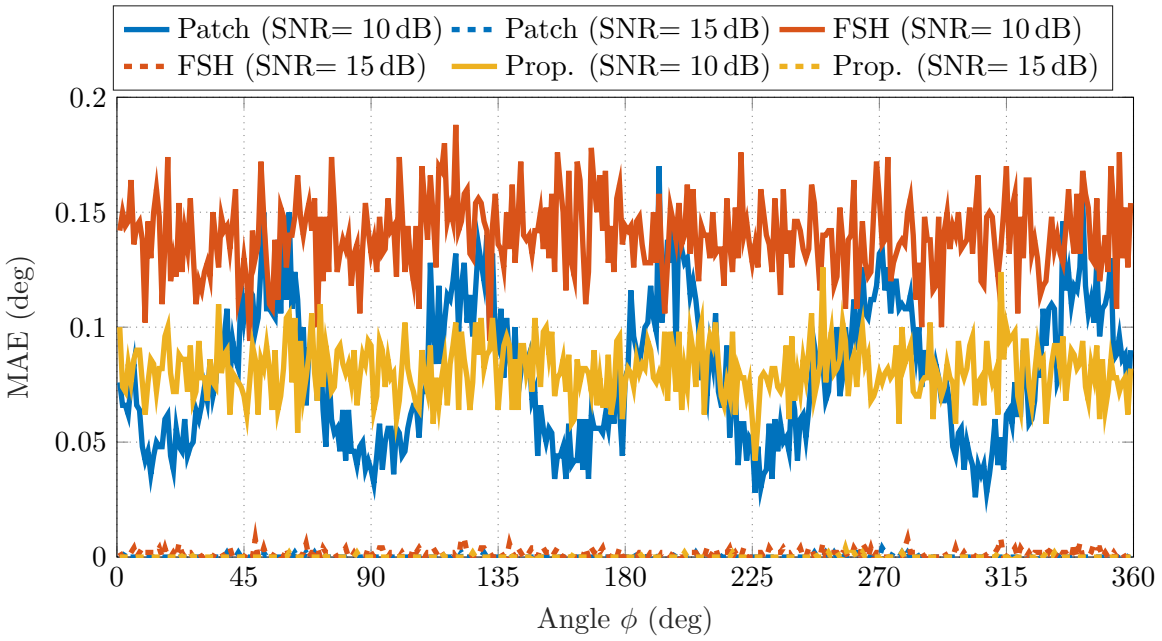

Figure 4.9: MUSIC performance comparison between UCAs and penta-modal antenna. The results are calculated using 100 snapshots, for 10 and 15 dB SNR levels.

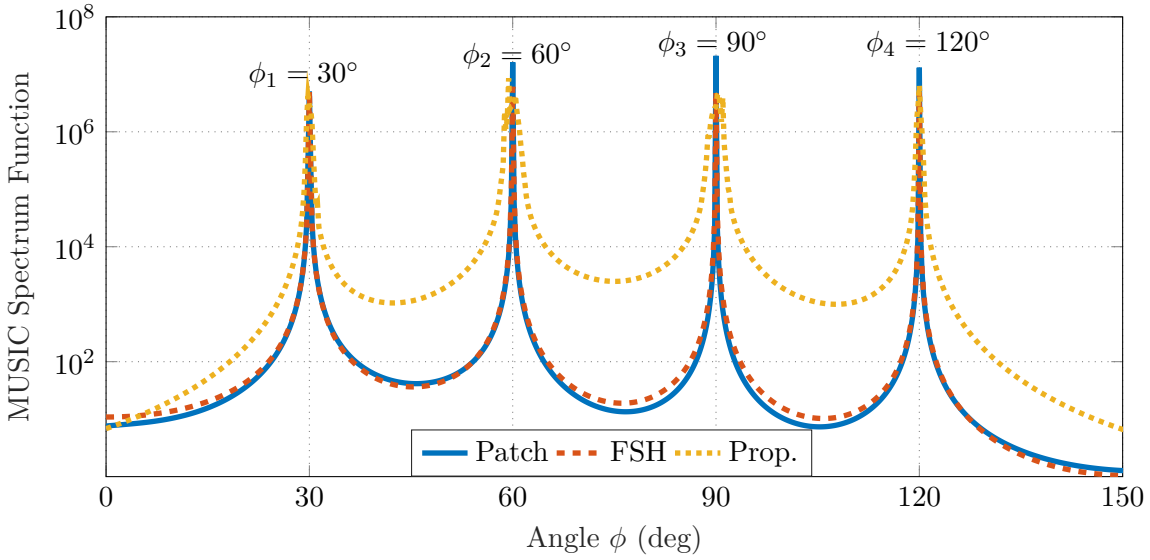

Figure 4.10: Comparison between MUSIC resolution of the proposed penta-modal antenna and UCAs, for 200 snapshots and 10 dB SNR with 30° angular separation: $\phi_1 = 30°, \phi_2 = 60°, \phi_3 = 90°$, and $\phi_4 = 120°$.

SNR level is set to 10 dB.

Fig. 4.10 depicts the MUSIC spectrum function for the investigated UCAs and the penta-modal antenna. The performance is tested for four simultaneous arriving signals with different angular separations and the minimum angular separation that still provides four clear peaks is a 30° separation between each adjacent signal. The actual incident angles of the four signals for this case are: $\phi_1 = 30°$, $\phi_2 = 60°$, $\phi_3 = 90°$, and $\phi_4 = 120°$. The MUSIC spectrum results illustrate clear distinctive peaks in the directions of the actual impinging signals, therefore, indicating good multiple simultaneous signals separation.

To further validate the performance of the proposed antenna, different separations of signals were tested as shown in Fig. 4.11 and Fig. 4.12. As was demonstrated in Fig. 4.10, both arrays generate very similar MUSIC spectrum functions. Therefore, to simplify the discussion on multiple signals separation, only the circular array comprising the directional elements is investigated.

Fig. 4.11a illustrates the MUSIC spectrum of the proposed antenna and the circular array for three simultaneous impinging signals. It can be seen that when the number of arriving signals is lowered, the capability to detect closely spaced signals is significantly improved. As shown in Fig. 4.11a, compared to the resolution of four simultaneous sig-

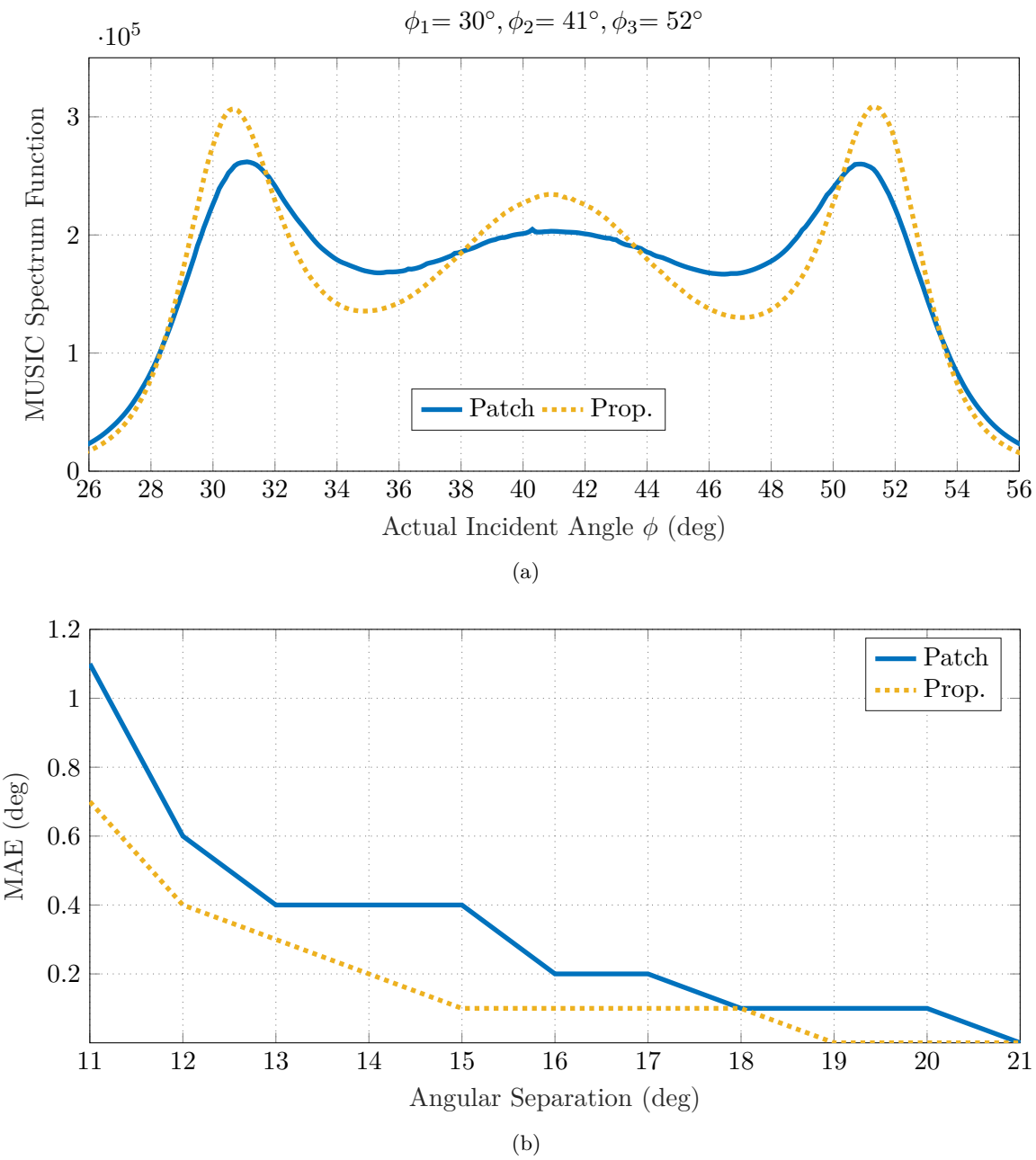

Figure 4.11: MUSIC resolution of the penta-modal antenna and UCA for 200 snapshots, 10 dB SNR, when separating three signals. (a) MUSIC spectrum function for three arriving signals with 11° angular separation. (b) MAE as a function of angular separation.

nals separation, which is 30° in Fig. 4.10, the resolution improves to 11° for three signals separation. The three estimated directions in the penta-modal antenna are $\phi_1 = 30.6°$, $\phi_2 = 40.9°$ and $\phi_3 = 51.4°$, which gives a peak MAE of 0.6°. The estimated signals for the circular array are: $\phi_1 = 31.1°$, $\phi_2 = 40.9°$ and $\phi_3 = 50.9°$, translating into a peak MAE of 1.1°. Fig. 4.11b depicts the peak MAE as a function of the angular separation for the case of three arriving signals. It can be observed that the proposed *SMB* antenna achieves

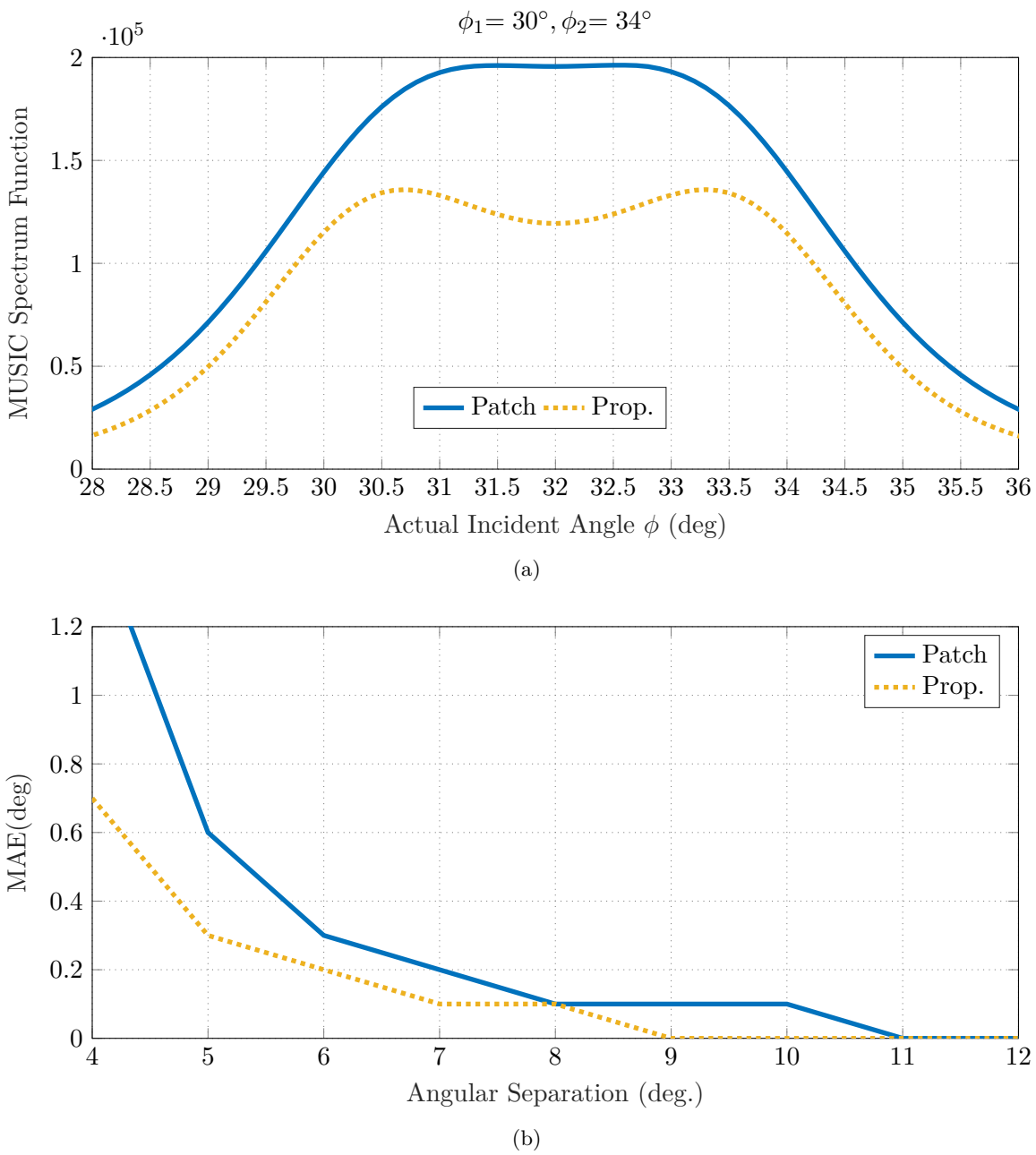

Figure 4.12: MUSIC resolution between the penta-modal antenna and UCA for 200 snapshots, 10 dB SNR when separating two signals. (a) MUSIC spectrum for two arriving signals with 4° angular separation. (b) MAE as a function of angular separation.

smaller MAE. For instance, to achieve a MAE of 0.1°, the angular separation needs to be at least 15° for the proposed antenna, while the UCA requires a larger angular separation of at least 18°.

The resolution for two signals separation is shown in Fig. 4.12. The results in Fig. 4.12a depict the MUSIC spectrum for two arriving signals with a 4° angular separation. The

actual incident angles are $\phi_1 = 30°$ and $\phi_2 = 34°$, and the estimated angles for the penta-modal antenna are $\phi_1 = 30.7°$ and $\phi_2 = 33.3°$. This translates into a peak MAE of 0.7°. In contrast, for the UCA the signals are detected at angles $\phi_1 = 31.5°$ and $\phi_2 = 32.6°$, showing an increase in the peak MAE which becomes 1.5°. Fig. 4.12b shows the MAE as a function of angular separation for the case of two arriving signals. In this case too, it is observed that the proposed *SMB* concept achieves better resolution as compared to classical arrays. Overall, it can be seen that the proposed antenna needs 7° angular separation to achieve MAE of at most 0.1°, while the circular array needs 8°.

The above discussed performance demonstrate that the use of different omnidirectional *spherical modes* to realized beamforming functionality is a promising compact IoT solution for AoA estimation, showing better resolution compared to the circular arrays while still offering up to 40% miniaturization as highlighted in Table 4.2.

4.4 Localization Performance

To demonstrate the practical application of the proposed principle within an IoT framework, this section explores the *SMB* driven AoA estimation capabilities to perform localization.

Fig. 4.13 depicts a planar scenario integrating the penta-modal antenna. The localiza-

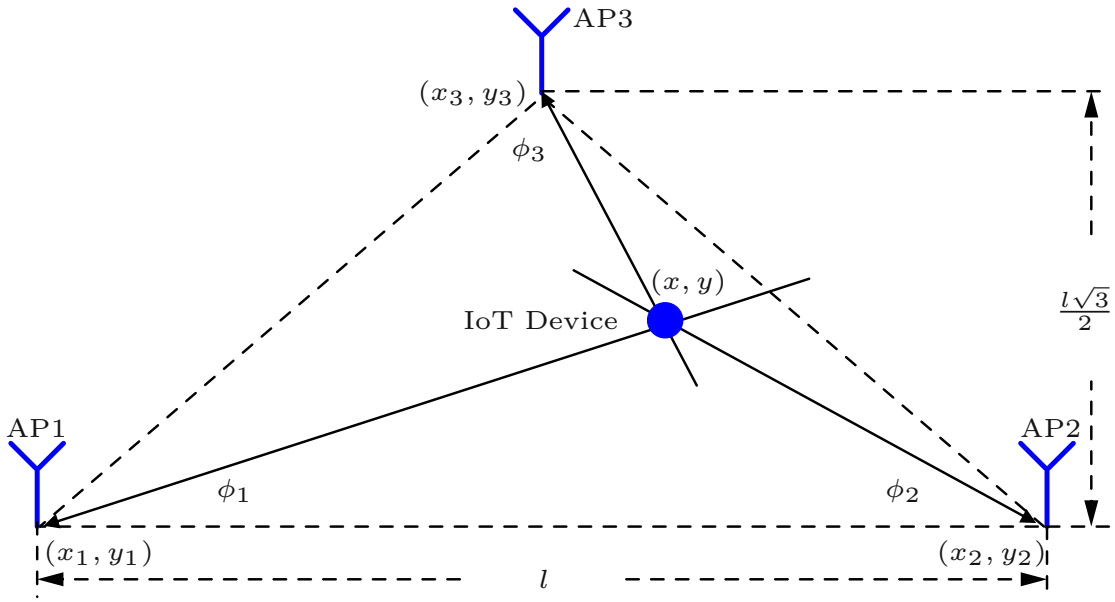

Figure 4.13: Investigated Line of Sight (LoS) localization scenario using AoA technique.

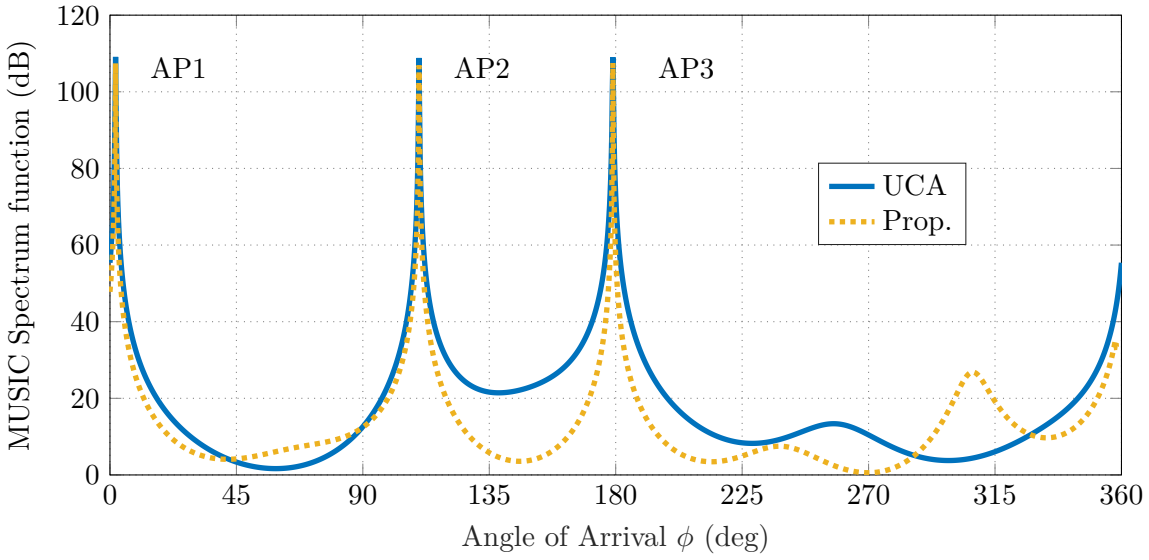

Figure 4.14: Comparison between resolution of the penta-modal antenna and the UCA for the three access points (AP1 = 2°, AP2 = 110°, and AP3 = 179°).

tion problem is analyzed based on triangulation from the AoA estimation. The system is assumed to be narrowband, in a planar scenario, and a LoS channel with three fixed Access Points (APs). The APs serve as localization anchors, and are located at (x_i, y_i) expressed in meters: AP1 at $(0, 0)$, AP2 at $(l, 0)$, and AP3 at $(\frac{l}{2}, \frac{l\sqrt{3}}{2})$, and the angles of arrival are ϕ_1, ϕ_2, and ϕ_3. In the analyzed scenario, the proposed IoT device attempts to localize itself with respect to the APs. Therefore, at least two AoA estimation from two different APs are required to retrieve the position of the IoT device [83]. The coordinates (x, y) are then computed using

$$x = \frac{l \tan \phi_2}{\tan \phi_2 - \tan \phi_1} \tag{4.8a}$$

$$y = \frac{l \tan \phi_2 \tan \phi_1}{\tan \phi_2 - \tan \phi_1} \tag{4.8b}$$

The required signals to perform triangulation are detected using the MUSIC algorithm, tested with a UCA (comprising the directional rectangular patch antennas) or the proposed penta-modal antenna. The MUSIC spectrum functions generated from 200 snapshots and 10 dB SNR for AP1, AP2, and AP3 located at three exemplar directions, i.e., 2°, 110°, and 179° are shown in Fig. 4.14. These results highlight that both investigated antennas have three clear and distinct peaks at the desired AoA directions of the three APs, and the two

systems are capable of accurately performing localization, where for $l = 10\,\text{m}$ the (x, y) coordinates are computed as $(9.87\,\text{m}, 0.344\,\text{m})$. It should be noted that when the AoA of the APs are closely spaced, the localization performance of the circular array comprising patch antennas will deteriorate much faster as compared to that of the proposed *SMB* antenna. This was illustrated in the simultaneous separation of three arriving signals in Fig. 4.11, where it was shown that the array has a peak error of 1.1° when the separation of the signals is increased to 11°, while the proposed design has a lower peak error of 0.7°.

Lastly, because the UCA requires a 0.93λ diameter to achieve the demonstrated AoA estimation and localization performances, such sizes are challenging for many emerging size-constrained IoT devices. In contrast, the *spherical modes* solution requires only 0.56λ diameter to deliver comparable AoA and localization performances, making it suitable for packaging within emerging small IoT systems. This advance is therefore a potential solution for IoT applications like beacon technology used for access point identification in indoor navigation and tracking systems.

4.5 Summary

This Chapter investigated the suitability of the *SMB* antennas for AoA estimation applications. By analysis of the AoA performance of arrays comprising electrically small, closely spaced antennas, it was highlighted that the mutual coupling effects are still a challenging issue for compact applications requiring accurate AoA measurements. To validate the performance of the proposed *SMB* concept, two antennas were investigated, a tri-modal antenna (exciting $\vec{K}_{1,0,1}$ and $\vec{K}_{1,\pm2,2}$ modes for a bi-directional beamforming) and a penta-modal design (with unidirectional beamforming via the additional excitation of $\vec{K}_{1,\pm3,3}$ modes). Through benchmarking with classical arrays, it was demonstrated that the *spherical modes* principle realizes an AoA estimation performance comparable to linear arrays but with up to 70% miniaturization. In addition, when benchmarked with circular arrays, a comparable single signal separation performance, and better multiple signal separation resolution were demonstrated with up to 40% miniaturization. The obtained results, therefore, offer a very promising compact solution for AoA-based localization in many emerging and size-constrained IoT systems.

5 SMB Driven Directional Modulation

SMB Driven Directional Modulation

This Chapter presents the implementation of *Spherical Modes Beamforming (SMB)* concept for Directional Modulation (DM) technology. The DM performance of the proposed *spherical modes* principle is demonstrated using a penta-modal antenna comprising only stacked-patch structures to allow for antenna profile reduction. Through Bit Error Rate (BER) calculations it is demonstrated that the penta-modal antenna is capable of unique steerable secure transmissions across the entire horizontal plane while offering up to 35% diameter miniaturization and 75% profile reduction, when compared to classical Uniform Circular Arrays (UCAs). The finding presented in this chapter are published on the IEEE Antennas and Wireless Propagation Letters [145], and the 2023 IEEE International Symposium on Antennas and Propagation [146].

5.1 Methodology for Bit Error Rate Calculation

To investigate the suitability of *SMB* antennas for DM technology, the Quadrature Phase-Shift Keying (QPSK) is used in this Chapter. The transmitted symbol – represented as a complex number is then denoted using $g \in \{1; j; -1; -j\}$. The directionally modulated transmitted signal towards the desired secure direction,i.e., ϕ_{secure} is expressed as

$$DM_z = \frac{\vec{p}}{\vec{K}_{1,m,n}(\phi_{\text{secure}})}, \tag{5.1}$$

where $\vec{K}_{1,m,n}$ represents the complex patterns of the z^{th} excited omnidirectional *spherical mode* ($z = 1, 2, \cdots, Z$), and $\vec{p}$ is a complex modulation vector given as

$$\vec{p} = [(g + l_1), (g + l_2), \cdots, (g + l_Z)]^T, \tag{5.2}$$

where $\vec{l}$ is a Z-element vector utilized to disperse the modulation constellations. The elements of $\vec{l}$ are obtained from random permutations of the elements of $\vec{l'}$ and its negation $\neg\vec{l'}$. The $\vec{l'}$ vector comprises $\frac{Z}{2}$ elements drawn from the uniform distribution of the real and imaginary elements of g [i.e., $(-1; 1)$ and $(-j; j)$], which ensures maximal feasible randomness, which protects from possible attacks by eavesdroppers. This then gives

$$\sum_{z=1}^{Z} \vec{l}_n = 0, \tag{5.3}$$

therefore ensuring that at the desired ϕ_{secure} angle, the artificially generated contribution from random noise will be canceled out for the direction of legitimate receiver, i.e., ϕ_{secure}.

To evaluate the DM performance BER computations are conducted using MATLAB. The complex patterns of the excited $\vec{K}_{1,m,n}$ omnidirectional *spherical modes* (obtained through full-wave simulations or anechoic chamber measurements) are imported into MATLAB, and a message is then generated for transmission. In this thesis, a total of 10^5 symbols are transmitted with the Signal-to-Noise Ratio (SNR) at the intended receiver configured to 10 and 12 dB. Additive White Gaussian Noise (AWGN) is assumed to be independent for each transmission location, and the BER results are obtained by comparing the flipped bits between the demodulated signal and the original transmitted one.

5.2 Low-Profile SMB Antenna

5.2.1 Design Configuration

To obtain a low-profile *SMB* antenna with unidirectional beamforming in the horizontal plane, a stacked-patch design is investigated. As demonstrated in Section 3.3 a structure exciting the fundamental $\vec{K}_{1,0,1}$ mode, and the phase-varying $\vec{K}_{1,\pm2,2}$ and $\vec{K}_{1,\pm3,3}$ modes is required for unidirectional beamforming across the entire horizontal plane. However, unlike the design using the top-loaded monopole (see Fig. 4.5b), in this Chapter a low-

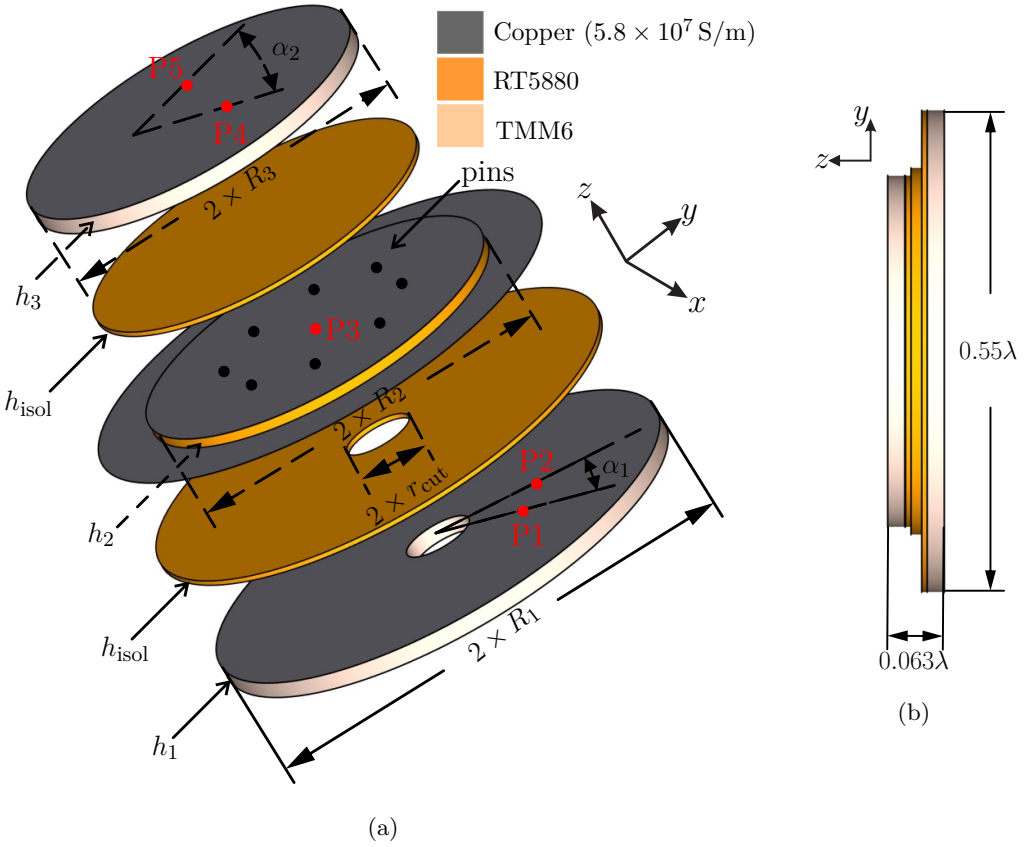

Figure 5.1: Proposed low-profile antenna. (a) Exploded view. (b) Side view highlighting antenna diameter and thickness. All dimensions (in mm): $R_1 = 36.9$, $R_2 = 28$, $R_3 = 26.9$, $r_{cut} = 5.25$, $h_1 = h_3 = 2.54$, $h_2 = 1.58$, $h_{\text{isol}} = 0.79$, $\alpha_1 = 30°$, $\alpha_2 = 225°$. Feed points from the center, P1 = P2 = 16.5, P3 = 0, P4 =P5 = 9.5.

profile configuration is realized by exciting the $\vec{K}_{1,0,1}$ mode using a circular patch antenna. Fig. 5.1 shows the configuration of the proposed stacked-patch antenna.

The antenna operates at the center frequency $f_0 = 2.24\,\text{GHz}$ and comprises three layers. As depicted in Fig. 5.1a, the bottom and top layers incorporate antennas supported by a TMM6 substrate ($\epsilon_r = 6.3$ and $\tan\,\delta = 0.0023$), with a thickness of $h_1 = h_3 = 2.54\,\text{mm}$. The radius of the bottom patch is $R_1 = 36.9\,\text{mm}$ and it is used for the excitation of the $\vec{K}_{1,\pm3,3}$ phase-varying omnidirectional *spherical modes*. To allow the feeding of the middle layer, a circular hole of radius $r_{\text{cut}} = 5.25\,\text{mm}$ is drilled at the center of the bottom layer. The radius of the top layer is $R_3 = 26.9\,\text{mm}$, and the circular patch of this layer is used to excite the $\vec{K}_{1,\pm2,2}$ omnidirectional *spherical modes*.

At this point is important to outline the feeding configuration to excite a given phase-varying omnidirectional *spherical mode*, i.e., the modes following $m = \pm n$ relation in (3.27),

as discussed in Section 3.2. To excite phase-varying $\vec{K}_{1,\pm m,n}$ modes, a feed point can be placed at a radial value (i.e. feed location) that allows for a $50\,\Omega$ impedance matching. If the feed point excites $+m/-m$ azimuthal phase-varying mode, the orthogonal *spherical mode* of the same order $-m/+m$ can then be excited by rotating the feed location by $\alpha = 90°/n(1+2k)$, where $k = 0, 1, 2, 3, \cdots$. In Fig. 5.1a the $\vec{K}_{1,\pm 3,3}$ omnidirectional *spherical modes* are obtained by using P1 and P2 oriented by $\alpha_1 = 30°$ and at a distance of 16.5 mm from the disk center, exciting TM_{31} modes. The $\vec{K}_{1,\pm 2,2}$ modes are generated from P4 and P5 located at 9.5 mm from the disk center and oriented by $\alpha_2 = 225°$, obtaining TM_{21} modes. To enforce the azimuthal phase variations required within the *SMB* concept, the feeding pairs of the bottom and top patches are fed in-quadrature. Therefore, the phase of the mode excited using P4 rotates in a clockwise direction, while the P5 rotates in a counter-clockwise direction.

The middle layer includes a patch supported by a RT5880 substrate ($\epsilon_r = 2.2$, $\tan\delta = 0.0009$), with a thickness $h_2 = 1.58$ mm, and radius $R_2 = 28$ mm (see Fig. 5.1a). As highlighted in Section 3.3, when two different *spherical modes* are excited using the same substrate material with no additional miniaturization steps, the *spherical modes* of higher-order will require a larger diameter compared to the lower order modes. This is mainly related to the fact that higher-order modes present increased phase variation, and a larger diameter is required to support these variations. From the above, the conclusion is that, once the diameter of the highest order *spherical mode* is determined, the overall efficiency of the antenna ports' exciting lower-order modes can be further improved by using a substrate material with a lower permittivity. For this case, the RT5880 substrate (with $\epsilon_r = 2.2$ as compared to $\epsilon_r = 6.3$, which is used in the bottom and top layers) is employed to excite the $\vec{K}_{1,0,1}$ mode in the middle layer.

The configuration of the middle layer is shown in Fig. 5.2. It can be seen that to excite the $\vec{K}_{1,0,1}$ omnidirectional *spherical mode*, the patch is shorted to its ground using eight pins of radius $r_{\text{pin}} = 0.25$ mm, which are rotated by 45° with respect to the disk center. The pins are placed at a distance d_{pins} from the center of the disk. Note that the total number of shorting pins (n_{pins}) and their location (d_{pins}), are two critical parameters to tune the center operating frequency and the impedance of the middle patch design.

Fig. 5.3 shows how the matching and isolation change for different n_{pins} with fixed $d_{\text{pins}} = 15\,\text{mm}$. Because of the S-parameters symmetry between the pairs (P1, P2) and (P4, P5), only the isolation of one of the ports is shown for each pair, i.e., $|S_{13}|$ and $|S_{43}|$. As depicted in Fig. 5.3, due to the pins' inductance, the resonance frequency increases as the number of pins (n_{pins}) increases. It can also be seen that the matching improves for higher n_{pins} values. For this case, good matching and better isolation characteristics are realized for $n_{\text{pins}} = 8$.

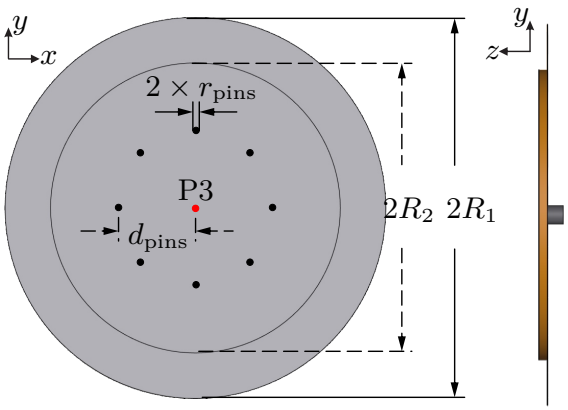

Figure 5.2: Top view (right) and side view (left) of the middle layer. All dimensions (in mm): $R_1 = 36.9$, $R_2 = 28$, $r_{\text{pins}} = 0.25$, $d_{\text{pins}} = 15$.

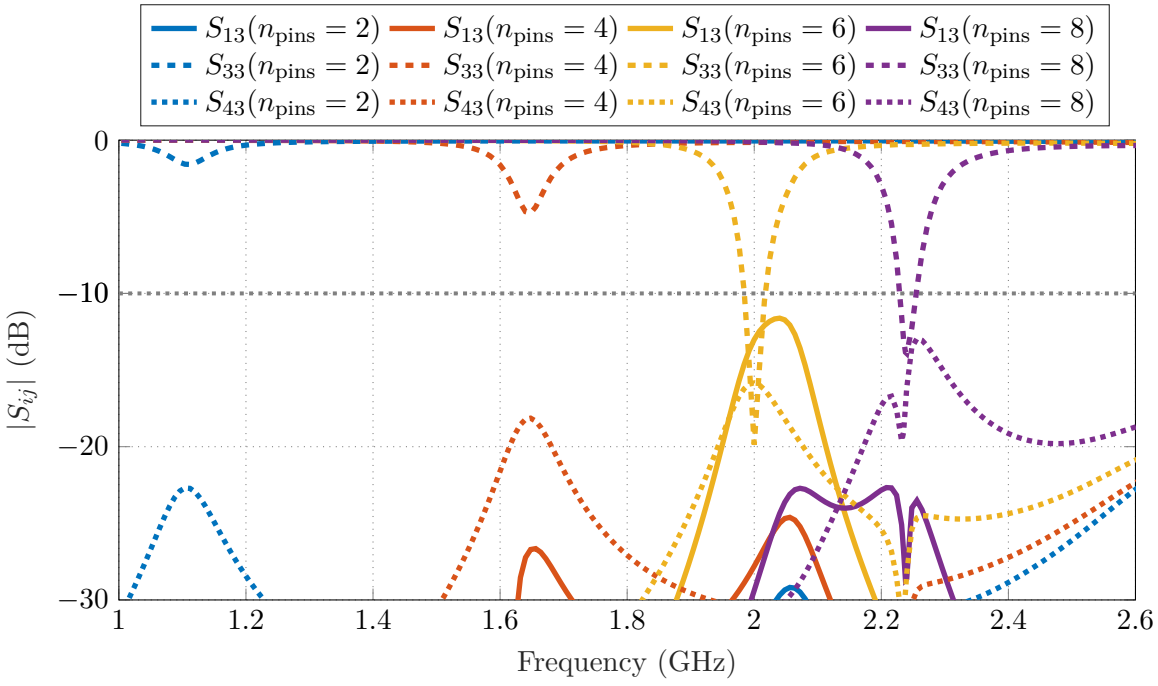

Figure 5.3: S-parameters results for different number of pins (n_{pins}) with fixed $d_{\text{pins}} = 15\,\text{mm}$.

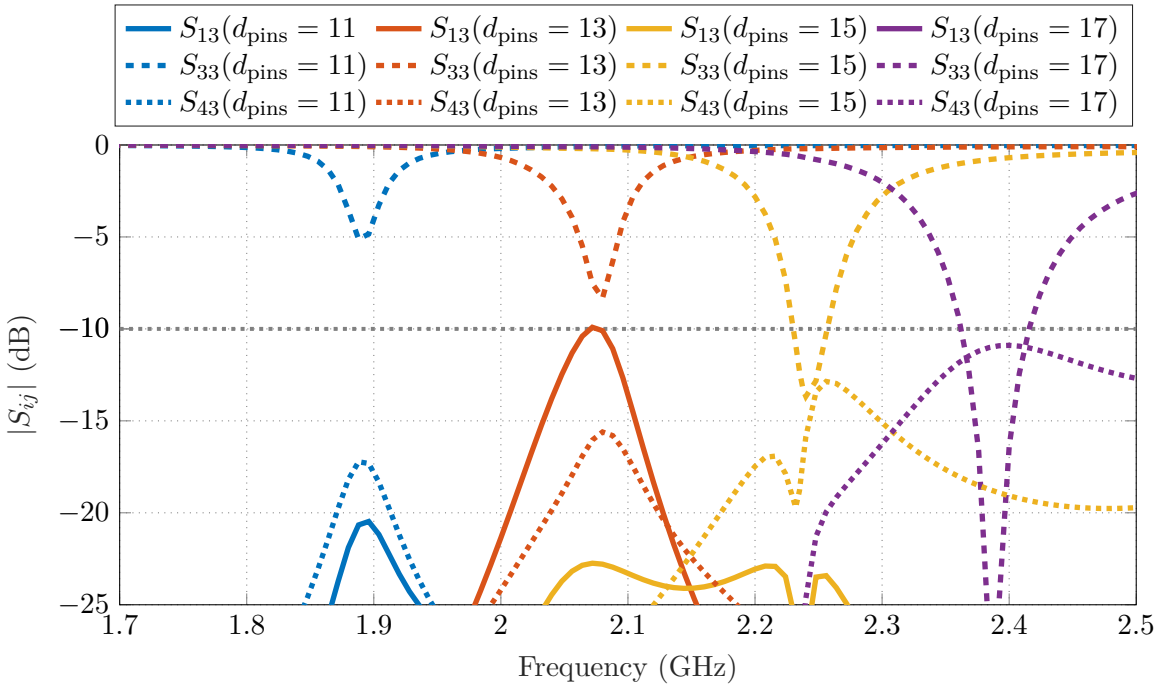

Figure 5.4: S-parameter results for different d_{pins} values with fixed $n_{\text{pins}} = 8\,\text{mm}$.

Fig. 5.4 shows how the matching and isolation vary for different d_{pins} values with fixed $n_{\text{pins}} = 8$. As illustrated in this figure, the resonance frequency increases as the value d_{pins} is increased. While better matching characteristics are realized for $d_{\text{pins}} = 17\,\text{mm}$ the isolation is much lower for this case, i.e., $|S_{ij}| < 10.5\,\text{dB}$ at the center frequency. Therefore, the final design uses $d_{\text{pins}} = 15\,\text{mm}$, where $|S_{ij}| > 15\,\text{dB}$ is realized at the desired center frequency of 2.24 GHz.

Next, to separate the three stacked patches, two layers made of RT5880 substrate, with a thickness of $h_{\text{isol}} = 0.79\,\text{mm}$, are used to isolate the middle patch structure from the bottom and top patches. It is important to mention that different substrate materials with other thicknesses are also feasible to be used as isolation between the three patches. However, this may require further tuning of the antenna parameters. The antenna final dimensions are $73.8\,\text{mm} \times 73.8\,\text{mm} \times 8.45\,\text{mm}$ or $0.55\lambda \times 0.55\lambda \times 0.063\lambda$ in terms of wavelength for the center frequency of 2.24 GHz.

Finally, for benchmarking, classical array technology is used. The array configuration is shown in Fig. 5.5. It is a 5-elements Uniform Circular Array (UCA) comprising $\lambda/4$ monopole antennas. The array's final dimensions are $106\,\text{mm} \times 106\,\text{mm} \times 30.6\,\text{mm}$ or correspondingly $0.84\lambda \times 0.84\lambda \times 0.24\lambda$ with respect to center frequency of 2.4 GHz, where

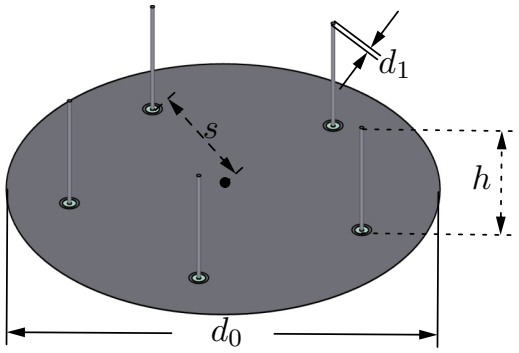

Figure 5.5: UCA comprising 5-elements $\lambda/4$ monopole antennas. All dimensions (in mm): $d_0 = 106$, $R_2 = 28$, $d_1 = 1.0$, $s = 38$, and $h = 30.6$.

the isolation is better than 11.9 dB, and the impedance bandwidth is 605 MHz.

5.2.2 Experimental Results

To validate the performance of the proposed antenna, the design was manufactured and tested. The fabricated prototype is shown in Fig. 5.6a, and for performance comparisons, the UCA is also manufactured and is shown in Fig. 5.6b.

The antenna simulated S-parameters results are shown in Fig. 5.7a. In measurements the S-parameters are tested using a four-port VNA(Rohde & Schwarz ZVA40) and are shown in Fig. 5.7b. It can be seen that in simulations the antenna center operating frequency is $f_0 = 2.24$ GHz, where the isolation is better than 17.5 dB. The -10 dB impedance bandwidth overlapping between all the ports is 8.2 MHz, and it is mainly limited by the higher-order $\vec{K}_{1,\pm3,3}$ modes excited using P1 and P2. In measurements, the center frequency is 2.238 GHz, where the antenna isolation decreases to 11.6 dB as compared to 17.5 dB achieved in the simulated case (see Fig. 5.7a). The impedance bandwidth also reduces from 8.2 MHz in simulations to 5 MHz in measurements. It is also important to note that the observed isolation, bandwidth, freqeuncy shifts, among other discrepancies are most likely due to manufacturing inaccuracies, assembly tolerances, possible misalignment between the stacked layers, and the impact of the polyamide hot melt utilized to assemble the antenna layers.

(a)

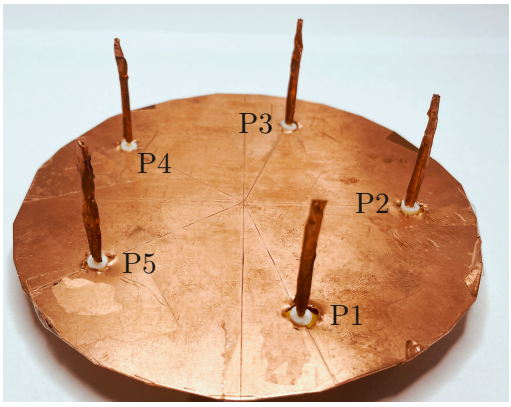

(b)

Figure 5.6: Images of the manufactured prototypes. (a) Prototype of the *SMB* antenna. (b) Prototype of the UCA.

5.2.3 Beamforming Performance

The amplitudes of all the excited modes are shown in Fig. 5.8. It can be seen that all the modes achieve the required omnidirectional property. Fig. 5.9a shows the phase of the radiation patterns of each mode. The results demonstrate that the phase characteristics needed to realize beamforming is achieved by all the antenna ports, i.e., a constant phase is seen for P3, which excites the $\vec{K}_{1,0,1}$ mode, while the phase changes twice in two opposite directions for the $\vec{K}_{1,\pm 2,2}$ modes excited using P4 and P5, and changes thrice also in two opposite directions for $\vec{K}_{1,\pm 3,3}$ modes excited using P1 and P2.

To demonstrate different patterns that can be generated, we investigated the beamforming performance when the main beam is directed to $\phi_d = 180°$ while using the following combinations: $\vec{K}_{1,0,1}$ and $\vec{K}_{1,\pm 2,2}$; $\vec{K}_{1,0,1}$ and $\vec{K}_{1,\pm 3,3}$; and finally the combination of all the excited modes. Using (3.29), the phase shifts required for each phase-varying mode are computed, and Fig. 5.9b shows the phase patterns obtained after introducing the phase

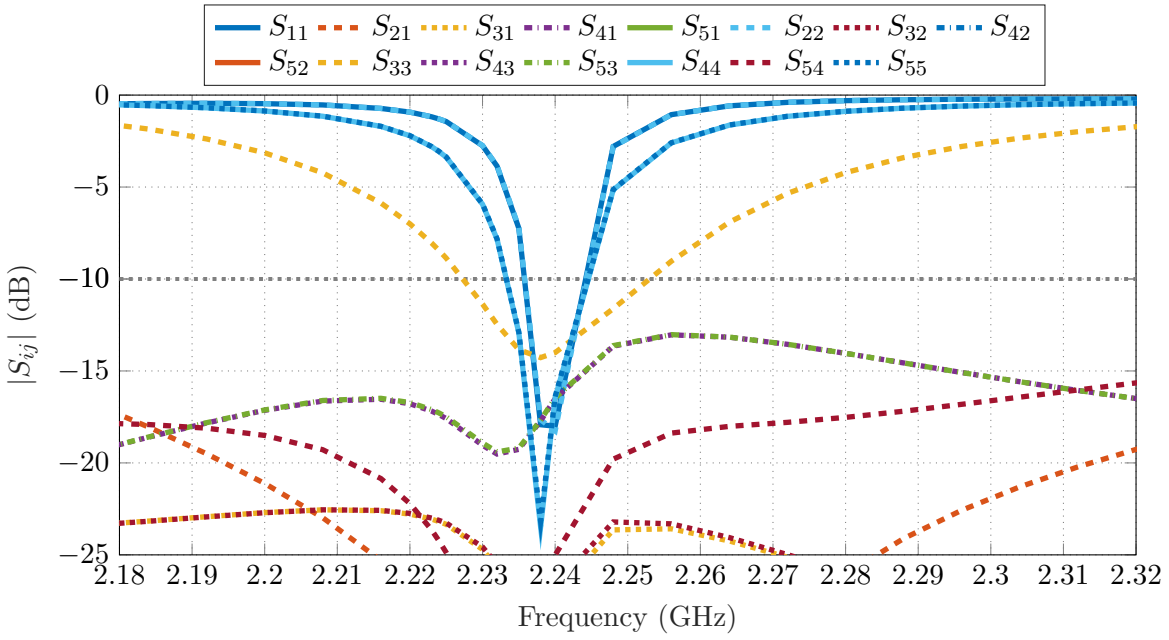

(a)

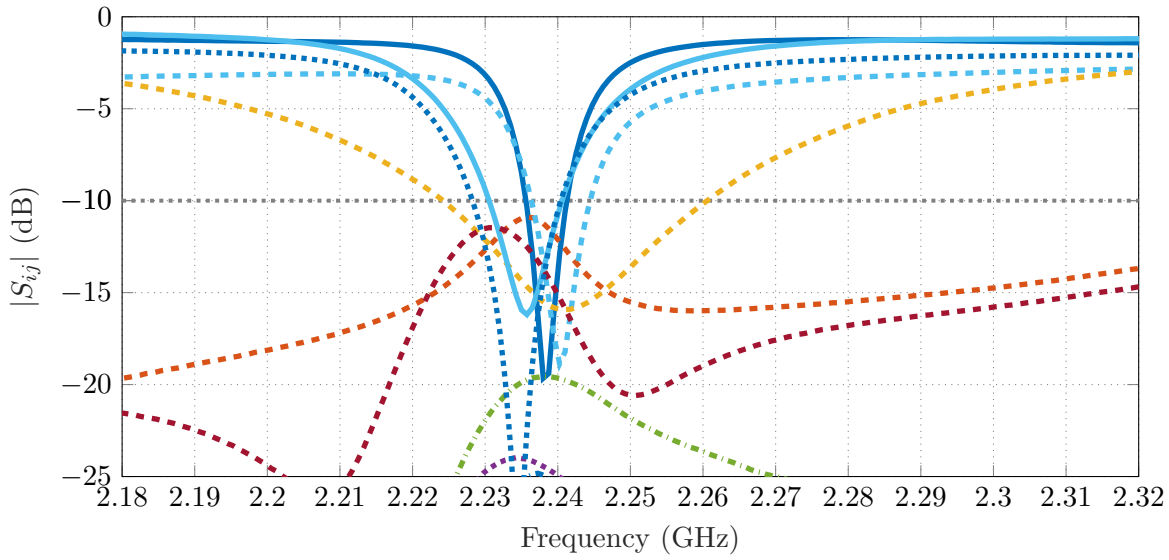

(b)

Figure 5.7: S-parameters of the proposed antenna. (a) Simulations. (b) Measurements.

shifts in each port. It can be seen that all the ports are in phase for the desired direction, allowing to synthesize different beam shapes around the azimuthal plane as shown in Fig. 5.10. As shown in previous chapters the $\vec{K}_{1,0,1}$ and $\vec{K}_{1,\pm2,2}$ combination produces the first type of beamforming, a bi-directional pattern, where the second beam is always located at $\phi_d + 180°$ and has the largest Half-Power BeamWidth (HPBW) of 59° and a realized gain of 2 dBi.

The pattern generated by $\vec{K}_{1,0,1}$ and $\vec{K}_{1,\pm3,3}$ modes produces three main beams, where the first is always located at $|\phi_d - 120°|$ and the second one at $\phi_d + 120°$ if $\phi_d \geq 120°$, and for the case where $\phi_d < 120$, the first beam will be located at $\phi_d + 120°$, while the second one is at $\phi_d + 240°$. Note that the $\vec{K}_{1,0,1} + \vec{K}_{1,\pm3,3}$ combination has a half-power beamwidth of 46.4° and a realized gain of 1.82 dBi.

The best antenna pattern is obtained by the combining all the five modes, which produces a unidirectional radiation pattern with the lowest HPBW of 45° and the largest realized gain of 3 dBi. Note that the proposed penta-modal antenna, uses the minimum number of modes required to generate a unidirectional beamforming across the horizontal plane. However, theoretically, an infinite number of omnidirectional *spherical modes* can be excited to provide better pattern control at the cost of size, profile, and feeding system complexity. This can be explained by the larger diameter needed to support the increased azimuthal phase-variations for higher-order *spherical modes* (e.g., for the proposed antenna, the $\vec{K}_{1,\pm3,3}$ *spherical modes* require a $R_1 = 36.9$ mm diameter, while the dual-phase varying

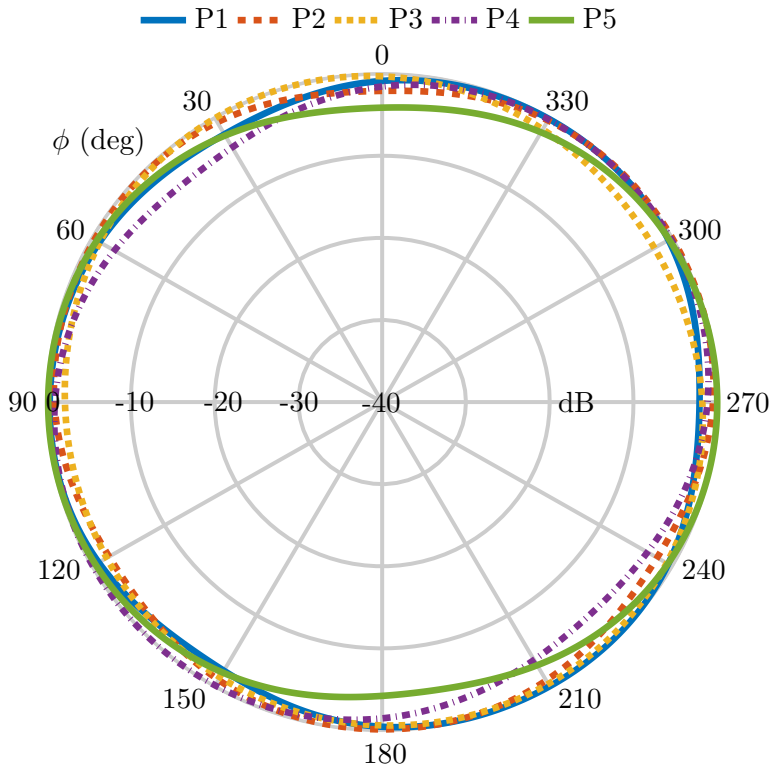

Figure 5.8: Normalized radiation patterns of the penta-modal antenna in the xy-plane ($\theta = 90°$).

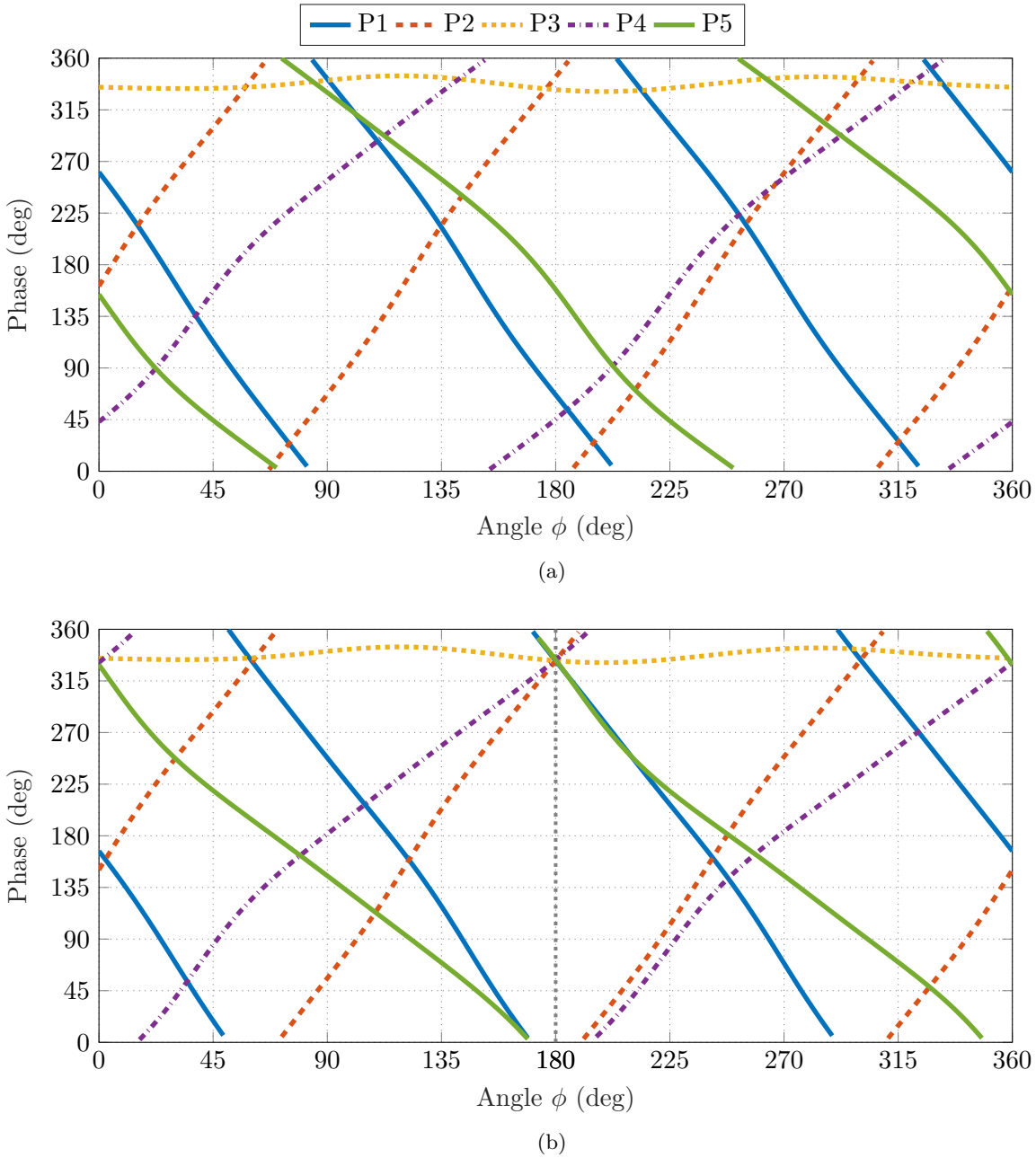

Figure 5.9: Phase of the radiation pattern of the penta-modal antenna. (a) Without phase shifts. (b) With phase shifts to steer the beam towards $\phi_d = 180°$.

$\vec{K}_{1,\pm2,2}$ modes are excited using $R_3 = 26.9\,\text{mm}$).

Lastly, Fig. 5.11 shows the anechoic chamber measurement setup used to experimentally validate the proposed antenna beamforming performance. The measured phase of the radiation patterns of each port is depicted in Fig. 5.12. It can be observed that despite a few asymmetries, the required phase properties of each mode are generally achieved, i.e., changing thrice for the $\vec{K}_{1,\pm3,3}$ modes excited using P1 and P2, constant for the $\vec{K}_{1,0,1}$

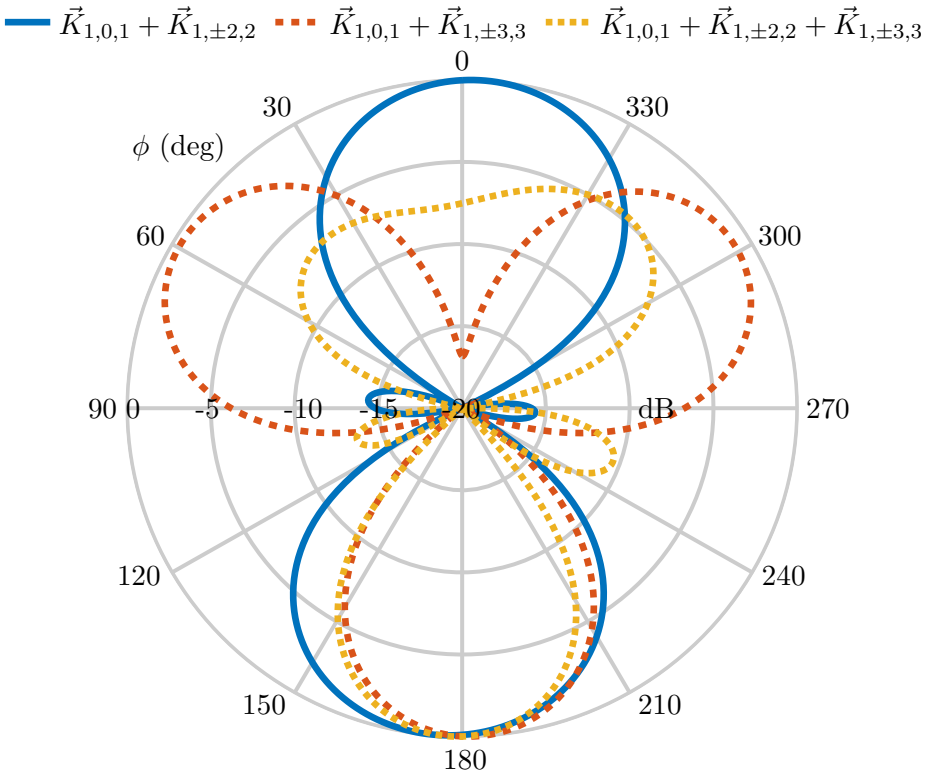

Figure 5.10: Normalized radiation patterns showing the beamforming of the proposed antenna.

mode excited using P3, and changing twice for the $\vec{K}_{1,\pm2,2}$ modes excited using P4 and P5. To demonstrate the best beamforming performance, i.e., unidirectional beamforming characteristics with vertical polarization, the main beam is steered into two different directions $\phi_1 = 110°$ and $\phi_2 = 300°$, where the required phase compensations are computed using (3.29). The generated beams are shown in Fig. 5.13, highlighting good beamforming performance across the horizontal plane.

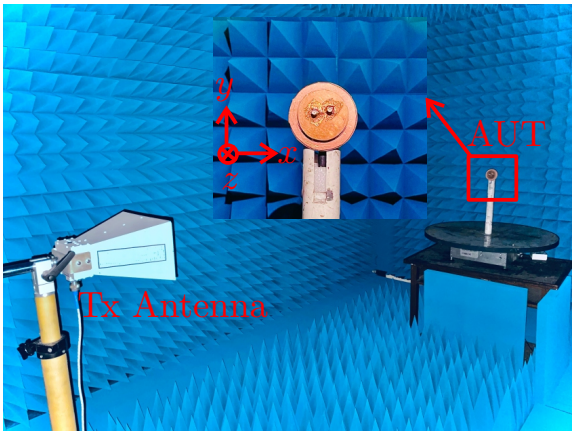

Figure 5.11: Images of the anechoic chamber measurement setup showing the Transmitter (Tx) antenna and the Antenna Under Test (AUT), i.e., the proposed antenna.

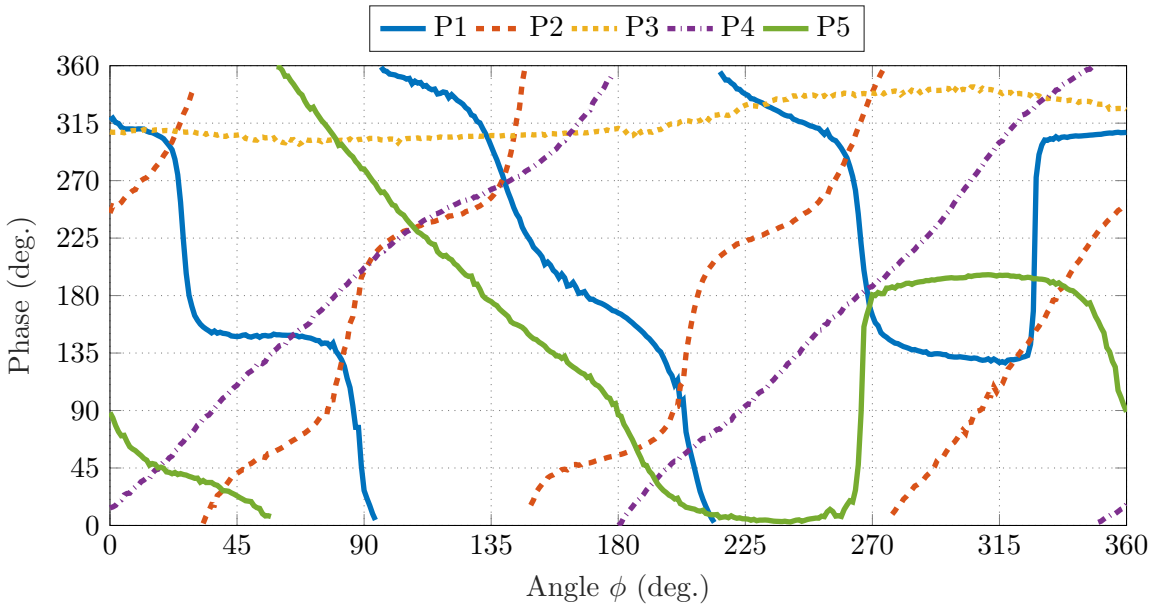

Figure 5.12: Phase of the radiation pattern of each port of the proposed design.

5.3 Directional Modulation Analysis

To investigate the beamforming performance of the proposed *SMB* antenna for DM, the method outlined in Section 5.1 is used. In the following discussion, the complex patterns of the *SMB* and UCA antennas are obtained from anechoic chamber measurements as outlined in Fig. 5.11. Two secure transmission directions $\phi_{\text{secure}_1} = 90°$ and $\phi_{\text{secure}_2} = 270°$, are selected around the horizontal plane to be the angles of the intended legitimate receiver and BER calculations are conducted using SNR = 10 and 12 dB. The obtained performance for the SNR = 10 dB is shown in Fig. 5.14a. It can be seen that at the desired location of

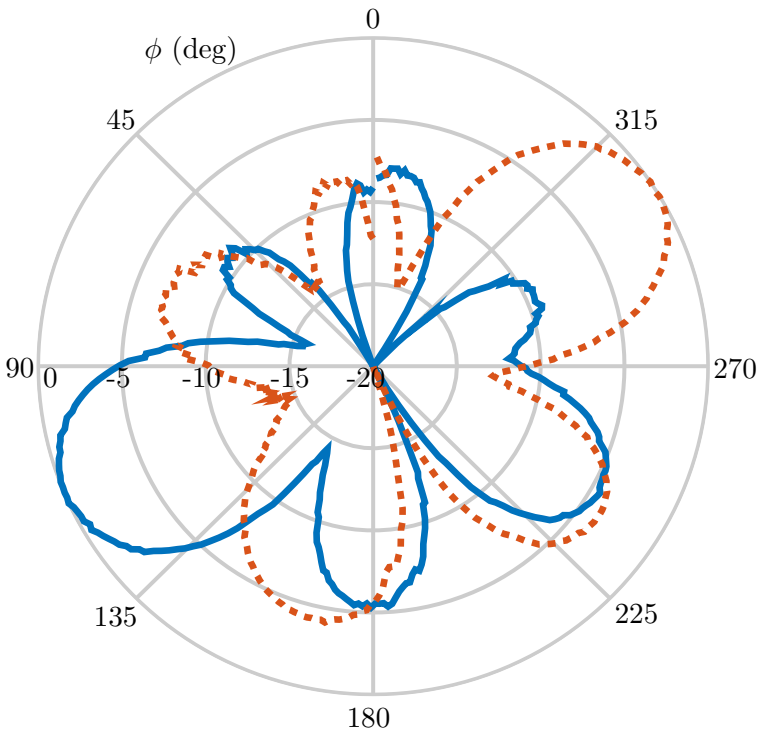

Figure 5.13: Normalized radiation pattern showing the measured beamforming performance of the proposed antenna in the xy-plane ($\theta = 90°$) for two different directions: 110° (solid lines) and 300° (dashed lines).

the legitimate user, low BER values better than 10^{-3} are realized for both the proposed penta-modal antenna and the UCA, while for all other directions, high error values of up to 0.46 are observed. It can also be seen that the proposed *spherical modes* solution achieves a much narrower 10^{-2} beamwidth as compared to the beamwidth obtained using the UCA, i.e., 18° as compared to 46.5° for the array. This may be explained by the relatively low beamwidth of the *SMB* antennas as compared to classical arrays (please see Chapter 4).

Fig. 5.14b shows the bit error rate computations for the SNR = 12 dB level. These results demonstrate that lower errors are achieved for both structures as the SNR level increases. For this case, lower BER values better than 10^{-4} are realized at the intended direction of the legitimate user. For this case too, it can also be observed that the beamwidth of the *SMB* antenna is narrower compared to that of the array, i.e., 22° as compared to 57°. As the *SMB* antenna realizes a smaller beamwidth, this translates into a much more secure directional modulation performance as compared to classical arrays, since the QPSK

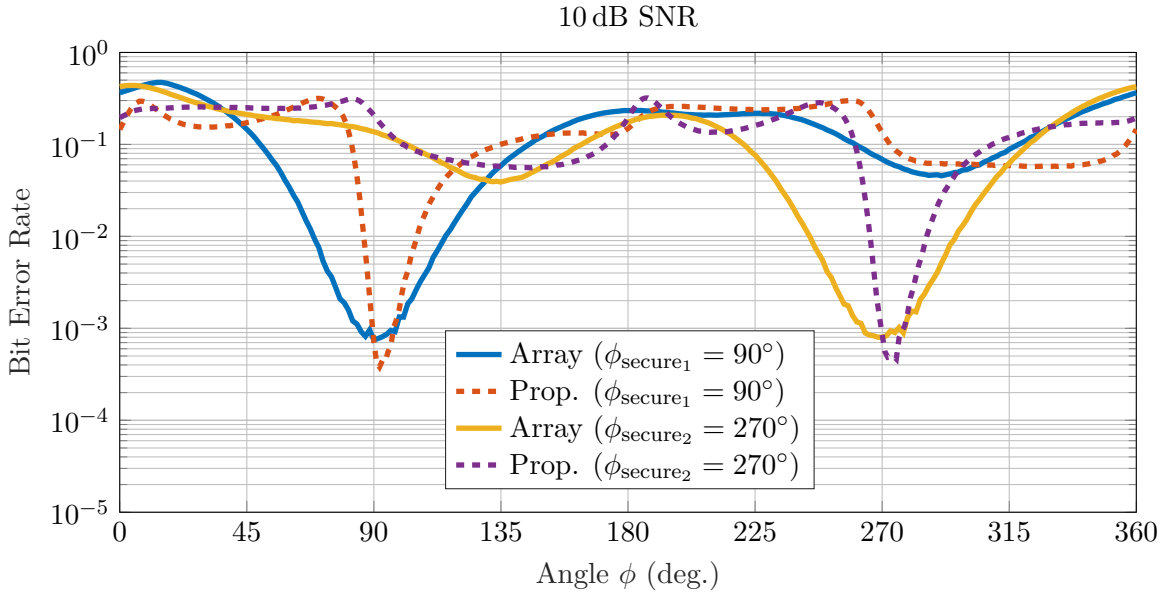

(a)

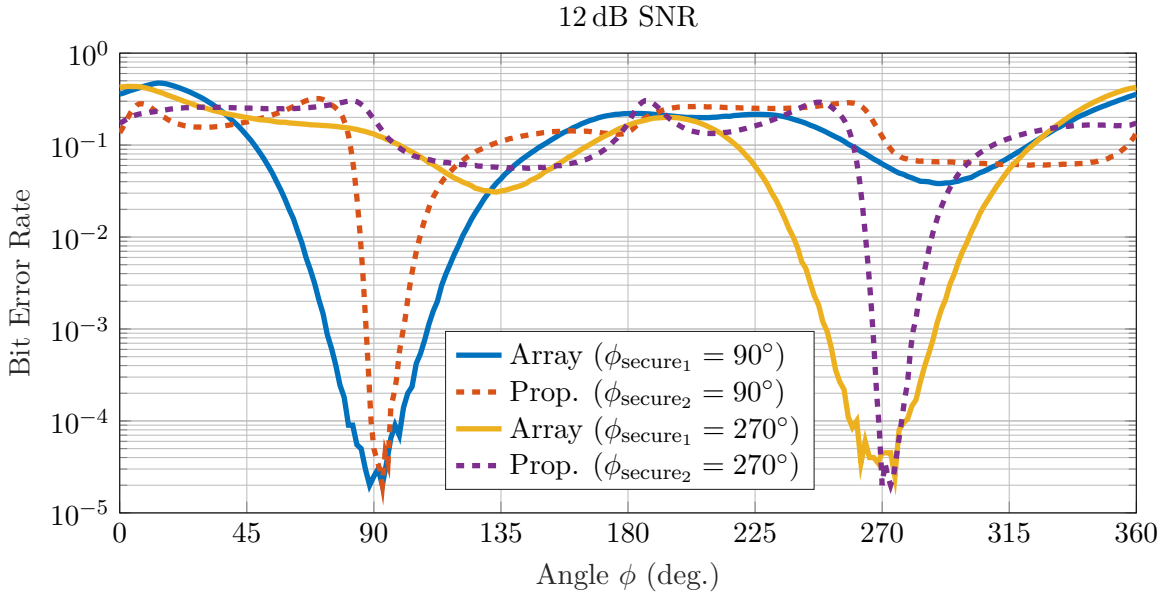

(b)

Figure 5.14: BER performance comparison between the UCA and the proposed antenna for two different transmission directions separated by 180°. (a) 10 dB SNR level. (b) 12 dB SNR level.

constellations are transmitted in a much smaller region. More importantly, the proposed *spherical modes* design needs only a diameter of 0.55λ and a profile of 0.063λ, while the UCA occupies a diameter of 0.84λ and 0.24λ profile. This means that the proposed concept offers diameter miniaturization of up to 35% and a 73% profile reduction.

To further validate the DM performance of the penta-modal antenna, Fig. 5.15 show the

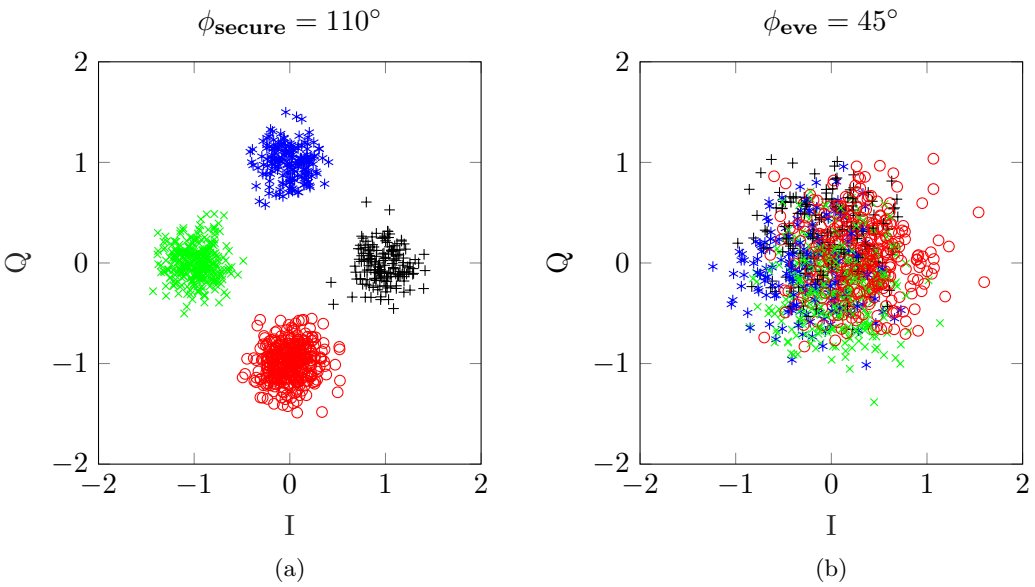

Figure 5.15: Color-coded QPSK constellations:'00' (black), '01' (red), '11' (green), '10' (blue). (a) QPSK constellations for the desired direction of the legitimate receiver at $\phi = 110°$. (b) QPSK constellations shown for the undesired eavesdropper at $\phi = 45°$.

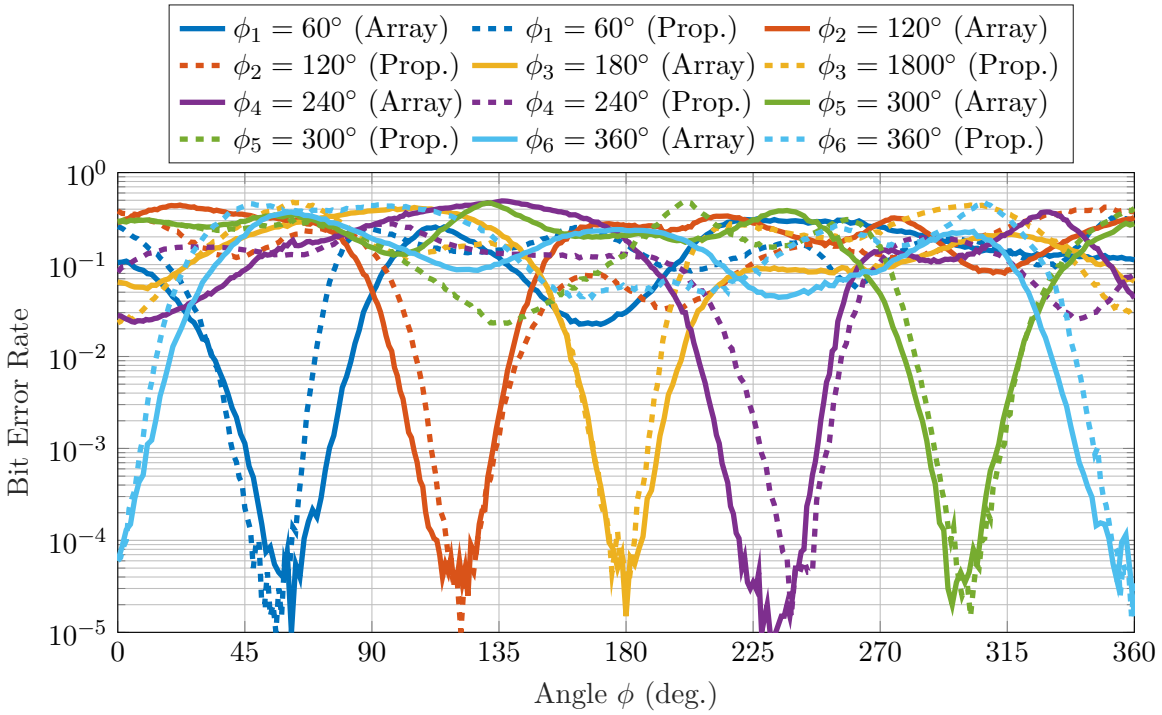

Figure 5.16: BER performance comparison between the UCA and the *SMB* antenna using 12 dB SNR for six different transmission directions separated by 60°.

In-phase and Quadrature (IQ) constellations patterns when the desired secure transmission direction is located at $\phi_{secure} = 110°$. As depicted in Fig. 5.15a, four clear clusters are obtained in the IQ plane, denoting correct transmissions in the desired secure direction

of the legitimate user. In contrast, for other eavesdroppers' locations, e.g., $\phi_{eve} = 45°$ shown in Fig. 5.15a, the constellations are scrambled, therefore, making it challenging for an illegitimate user to access the transmitted data.

To further highlight the unique steerable DM performance of the proposed antenna, six different transmission directions are tested, and the angles are separated by 60° to cover the entire horizontal plane. The BER calculations are computed using a SNR = 12 dB level for 10^5 transmitted symbols, and the obtained performance is shown in Fig. 5.16. It can be seen that a unique secure transmission direction is realized in all six directions of the legitimate receiver without leakage to other undesired eavesdroppers directions. At the desired secure angles of the legitimate receiver, very low BER values better than 10^{-4} are realized in all transmission directions. At the same time, outside the desired region, a high error rate of 10^{-1} is achieved. The largest beamwidth region with BER$< 10^{-2}$ is 44° for the measured *SMB* antenna and 61.5° for the array structure. These results further validate that the *SMB* antenna outperforms the UCA, as it achieves a narrower beamwidth where the transmitted QPSK constellations are decipherable.

5.4 Summary

This Chapter discussed the efficacy of *SMB* antennas as an alternative solution to large classical arrays for DM applications. At first, theoretical formulation for the implementation of *SMB* principle in DM technology were outlined. Next, a low-profile penta-modal antenna capable of unidirectional beamforming with vertical polarization across the entire horizontal plane was proposed and its performance is experimentally validated through BER computations. In general, it was demonstrated that the principle is capable of unique steerable DM transmissions wihtout leakage into undesired eavesdroppers directions. It was highlighted that using a SNR of 12 dB will enable the legitimate user to experience very low BER better than 10^{-4}, while high error rates will be observed outside the desired secure directions. Such performance was achieved while offering significant size and profile reductions when compared to classical arrays, enabling the implementation of DM security approach in emerging compact Internet of Things (IoT) applications.

6 Dual-Plane Directional Modulation

Dual-Plane Directional Modulation

A drawback of the previous *SMB* antennas is the fact that the beamforming capability is limited solely to the azimuthal plane. Therefore, such solutions cannot be utilized to realize secure transmissions if the legitimate user is located in the elevation plane. To address this limitation, this Chapter presents a Directional Modulation (DM) principle to allow for dual-plane steerable secure transmissions using a Three-Dimensional (3D) beamforming antenna. The DM performance is validated through Bit Error Rate (BER) analysis across the horizontal and elevation planes. This Chapter further addresses the size limitations of the proposed *(SMB)* antennas by investigating an Electrically Small Antenna (ESA) design with beamforming characteristics that still allow for dual-plane DM. The findings discussed in this chapter are published in the 2021 and 2022 IEEE International Symposium on Antennas and Propagation [147, 148], and the 17th European Conference on Antennas and Propagation [149].

6.1 Stacked-Patch 3D Beamforming Antenna

The antenna proposed for 3D beamforming is shown in Fig. 6.1. The system is designed to operate near the center frequency of 2.4 GHz. It comprises four stacked-patch antennas loaded with a TMM6 substrate ($\epsilon_r = 6.3$, $\tan\delta = 0.0023$ and thickness $H = 6.35\,\text{mm}$). In the proposed antenna, each metallic patch is made of 35 μm thick copper. The top structure (Layer L1) excites two orthogonal broadside TM_{11} modes. It has a radius $R1 = 16.1\,\text{mm}$ and is fed using port 6 and port 7 rotated by 90° to ensure the orthogonality between the two excited broadside modes. Port 6 is then located at $d_6 = (x, y) = (12\,\text{mm}, 0\,\text{mm})$, and the feed of port 7 is at $d_7 = (0\,\text{mm}, 12\,\text{mm})$.

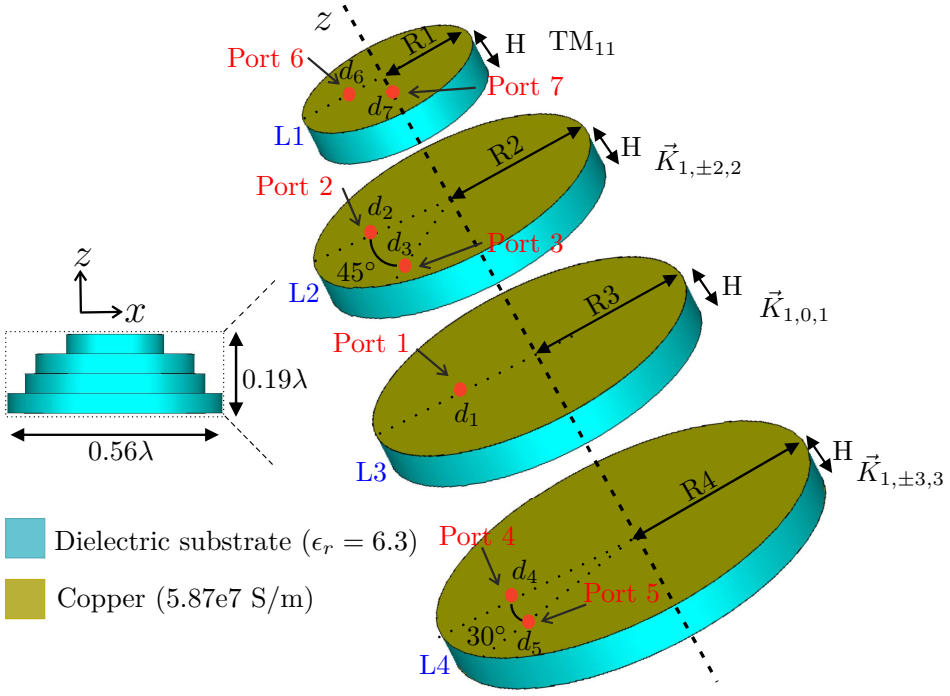

Figure 6.1: Exploded view of the proposed 3D beamforming antenna.

Layer L2 has radius $R2 = 26\,\text{mm}$, is fed using ports 2 and 3. The feed of port 2 is located at $d_2 = (13\,\text{mm}, 0\,\text{mm})$ and the port 3 feed is at $d_3 = (12\,\text{mm}, 12\,\text{mm})$, i.e., the ports are rotated by 45°. This layer is used to excite the $\vec{K}_{1,\pm2,2}$ omnidirectional *spherical modes*, generated by exciting TM_{21} modes fed in-quadrature to enforce the required dual-phase variations around the horizontal plane. The patch antenna in L3 layer has radius $R3 = 29.8\,\text{mm}$, it is fed using port 1 located at $d_1 = 7\,\text{mm}$. This patch is used to excite the $\vec{K}_{1,0,1}$ omnidirectional *spherical modes*.

The bottom patch (in layer L4) has radius $R4 = 35.08\,\text{mm}$, and is fed using ports 4 and 5. Port 4 is located at $d_4 = (15.5\,\text{mm}, 0\,\text{mm})$ and the feed location of port 5 is at $d_5 = (17.2\,\text{mm}, 10\,\text{mm})$, i.e., the ports are rotated by 30°. The L4 patch is used to excite the $\vec{K}_{1,\pm3,3}$ omnidirectional *spherical modes*, obtained by exciting TM_{31} modes fed in-quadrature to realize the required triple-phase variation around the horizontal plane. The final antenna dimensions are $70.16\,\text{mm} \times 70.16\,\text{mm} \times 25.6\,\text{mm}$, or correspondingly $0.56\lambda \times 0.56\lambda \times 0.19\lambda$ with respect to the center frequency of 2.39 GHz.

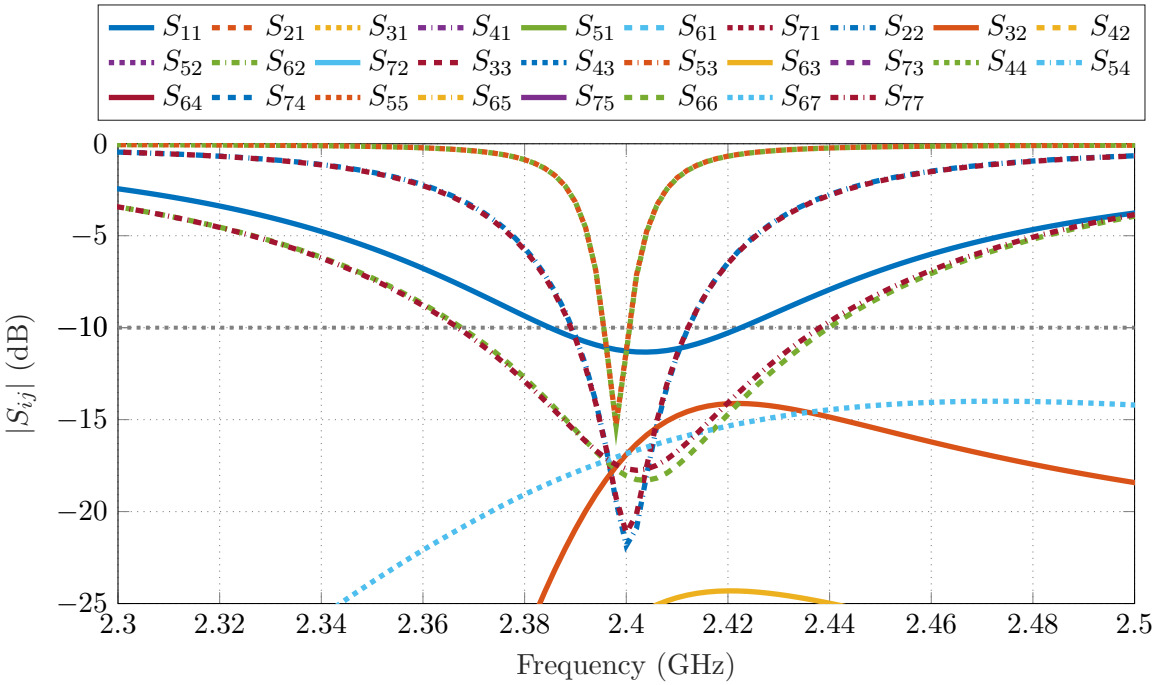

Figure 6.2: S-parameters of the proposed 3D beamforming antenna.

6.1.1 Beamforming Performance

The antenna simulated S-parameters results are shown in Fig. 6.2. The center operating frequency is $f_0 = 2.39\,\text{GHz}$, where the isolation between all antenna ports is better than 17 dB. The impedance bandwidth overlapping between all antenna ports is 5 MHz. The antenna total efficiency for ports P1, P2, P3, P4, P5, P6 and P7 at f_0 is 67%, 72%, 72%, 19%, 19%, 90% and 90%, respectively. The relatively low total efficiency for P4 and P5 is due to the use high dielectric substrate for the excitation of $\vec{K}_{1,\pm3,3}$ higher-order *spherical modes*, which present triple phase-variation while using a relatively small antenna volume. It can also be seen that the antenna overlapping bandwidth between all ports is limited by the ports exciting the $\vec{K}_{1,\pm3,3}$ modes. In contrast, the broadside radiating modes have the highest total efficiency and a bandwidth of 75 MHz.

6.1.2 Azimuth Plane Beamforming

The beamforming in the azimuth plane is based on the *SMB* principle discussed in previous Chapter. The phases of the radiation patterns of the *spherical modes* (Layers L2, L3, and L4) are shown in Fig. 6.3. It can be seen that the required phase properties are achieved,

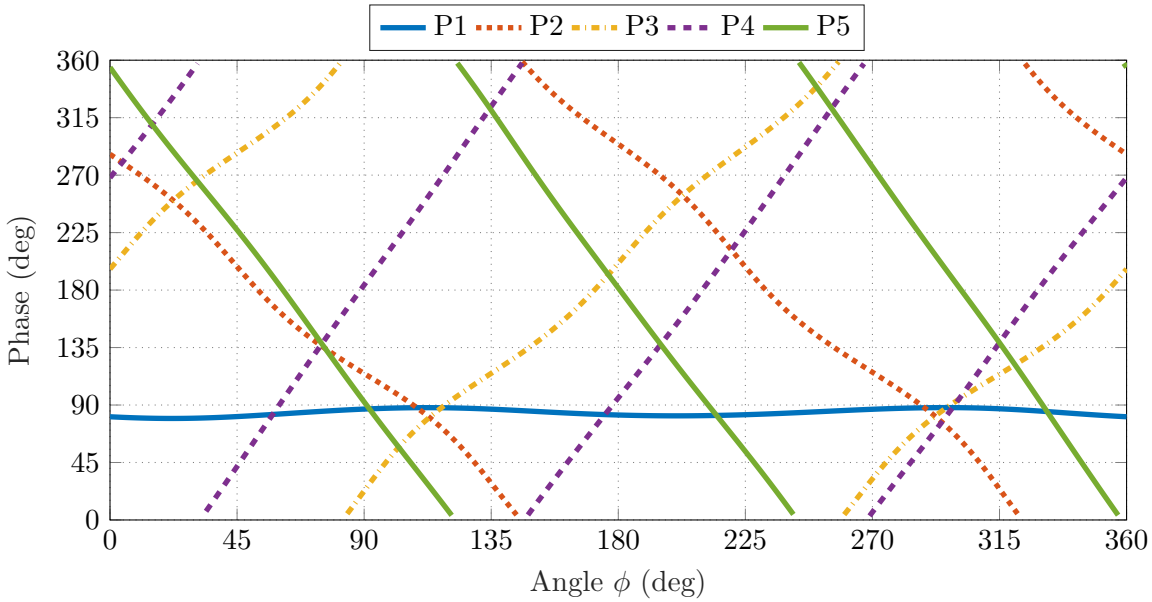

Figure 6.3: Phase of the radiation pattern of each port radiating an omnidirectional *spherical mode*.

i.e., constant phase for P1, dual-phase variations for P2 and P3, and lastly, triple-phase variations for P4 and P5. Using (3.29) and (3.28), the main beam is directed into four different directions separated by 90° to cover the entire horizontal plane. The generated beams are shown in Fig. 6.4 and are all vertically polarized, demonstrating that the antenna is capable to steer its main beam across all the desired directions in the horizontal plane. The realized gain across this plane is within $4.54\,\text{dBi} - 4.98\,\text{dBi}$, and the Half-Power BeamWidth (HPBW) stays around 42.5°.

6.1.3 Elevation Plane Beamforming

To extend the beamforming characteristics to cover the upper hemisphere, the broadside modes radiated by the top layer are used. Fig. 6.5 shows the radiation patterns of the broadside radiating modes excited using P6 and P7 for the xz and yz-planes. The results show that by exciting either P6 or P7 without any additional phase or amplitude control, the antenna main beam can be direceted to the broadside direction ($\theta = 0°$). To steer the main beam away from the $\theta = 0°$ direction, P6 and P7 are combined with a phase-varying *spherical mode*, as excited through P1 to P5.

Fig. 6.6a highlights the beamscanning performance in the xz-plane. It can be seen that the beamforming in this plane can be realized by using a broadside radiating mode

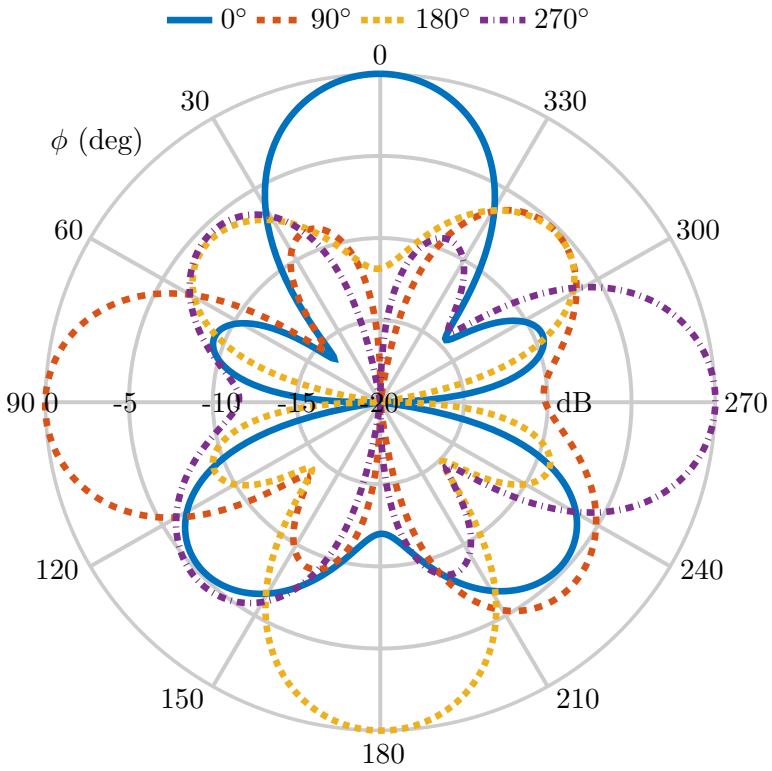

Figure 6.4: Normalized radiation patterns demonstrating the xy-plane ($\theta = 90°$) beamforming performance of the proposed antenna.

and the dual-phase varying omnidirectional modes $\vec{K}_{1,\pm 2,2}$. By simultaneously exciting P6 and P3 without any additional phase compensations in both ports the main beam is steered towards $\theta_+ = 35°$. To direct the antena main beam to the opposite direction, i.e., $\theta_- = -35°$, a phase inversion of 180° is introduced into the broadside mode or the phase-varying mode. By simultaneously exciting P7 and P2, beam tilting in the xz-plane can also be obtained. For the case where no additional phase compensations are introduced between P7 and P2, the main beam will be at $\theta_+ = 35°$. Correspondingly, when exciting the two ports simultaneously with a 180° phase shift in P7, the main beam will be steered towards $\theta_- = -31°$.

Fig. 6.6b outlines the beamforming performance in the yz-plane. It can also be seen that by combining a broadside radiating mode and a dual-phase varying mode, beamforming capabilities can be realized across this plane. From the simultaneous excitation of P6 and P2 without any phase compensations the antenna main beam is steered to $\theta_+ = 29°$. To direct the beam to the opposite direction $\theta_- = -32°$, P7 and P3 are simultaneously excited

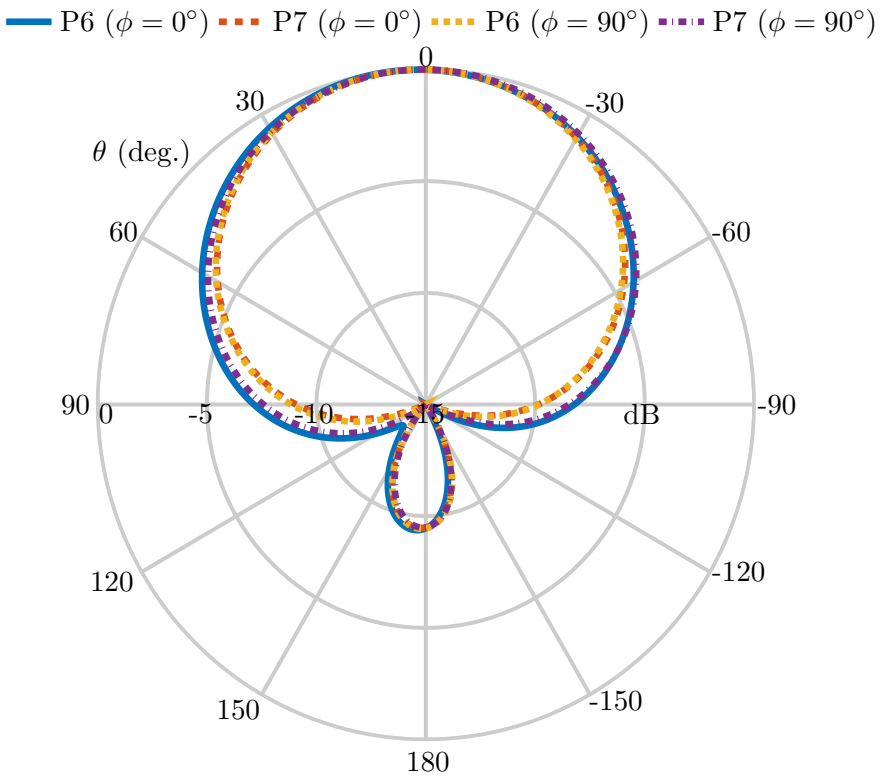

Figure 6.5: Normalized radiation patterns of the broadside modes of the proposed antenna for different cut planes xz-plane ($\phi = 0°$) and yz-plane ($\phi = 90°$).

with no phase shifts. For this plane, too, it is seen that when the antenna main beam is at a given θ_+ direction a phase inversion in the broadside or phase-varying modes steers the main beam towards the opposite direction θ_-. This is highlighted in the radiation patterns generated by P6 (excited with 180° phase shift) along with P2 (without any phase shift), which directs the beam to $\theta_- = -34°$, as opposite to the $\theta_+ = 29°$ direction obtained when no phase compensation is introduced in the two ports. A similar behaviour is seen in the $\theta_- = -32°$ direction (obtained by exciting P7 and P3 with no phase shifts), where the main beam is then steered towards $\theta_+ = 37°$ when a 180° phase inversion is introduced to P7. Overall, the above discussions demonstrate good 3D beamforming capabilities of the proposed antenna across the upper hemisphere, where the realized gain stays within $4.73 - 5.3\,\text{dBi}$.

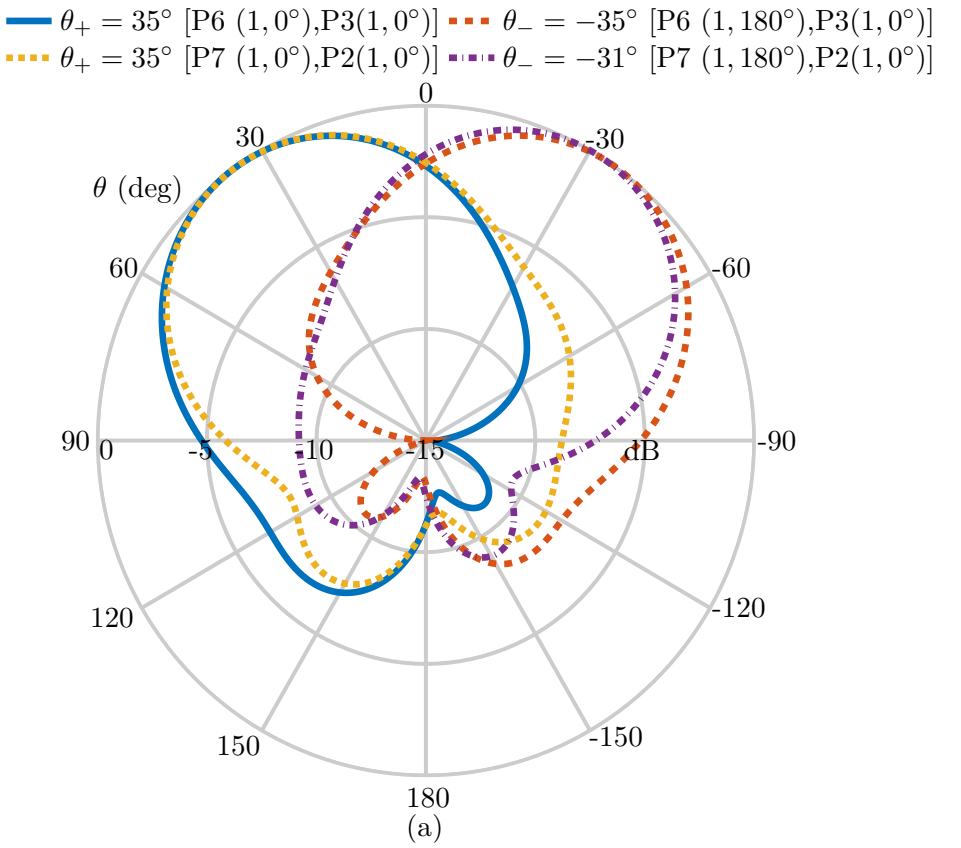

(a)

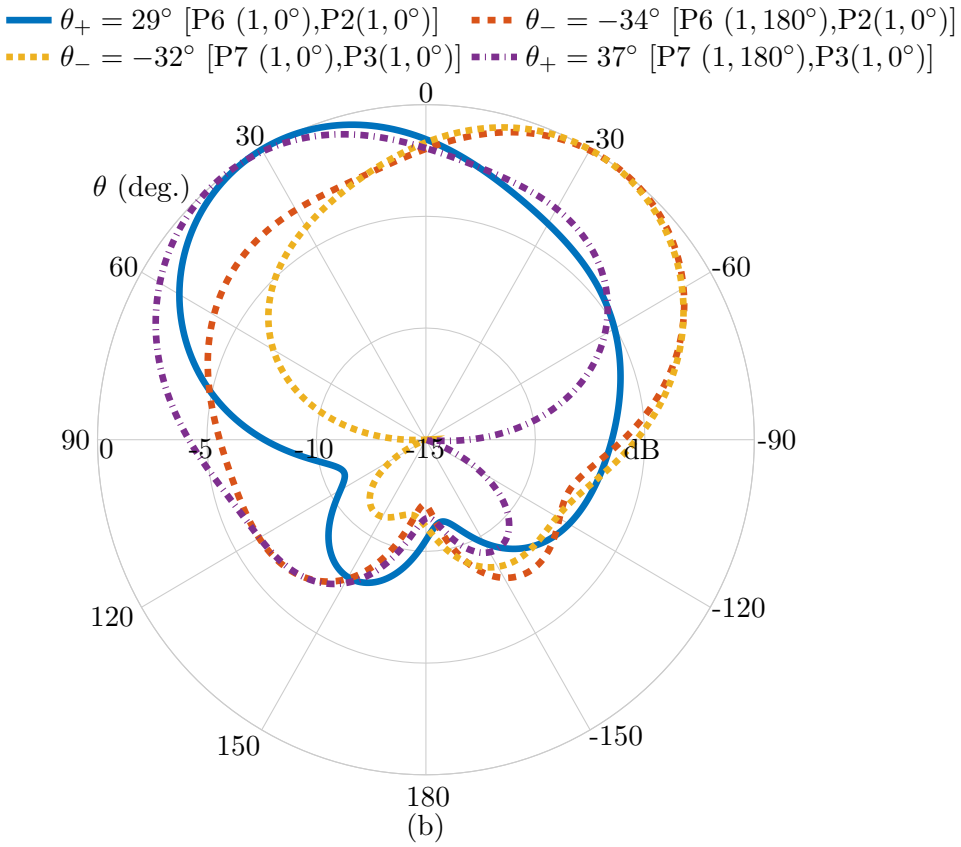

(b)

Figure 6.6: Normalized antenna patterns showing beamforming in (a) xz-plane and (b) yz-plane.

6.1.4 Dual-Plane Directional Modulation Analysis

To realize DM in the azimuthal or elevation planes the proposed 3D beamforming antenna is used and the directionally modulated signals are given by

$$DM_{\text{azimuth}} = \frac{\vec{p}}{\vec{K}_{1,m,n}(\phi_{\text{Bob}})} \tag{6.1a}$$

$$DM_{\text{elevation}} = \frac{\vec{p}}{P_j(\theta_{\text{Bob}}) + \vec{K}_{1,m,n}(\theta_{\text{Bob}})} \tag{6.1b}$$

where DM_{plane} denotes the transmitted signal in the desired plane, $\vec{K}_{1,m,n}(\phi_{\text{Bob}})$ is the complex radiation pattern of the nth omnidirectional *spherical mode* at the desired secure direction of the legitimate receiver, i.e., ϕ_{Bob} in the azimuth; and $P_j(\theta_{\text{Bob}})$ denotes the complex pattern of the jth antenna port that radiates a broadside mode (P6 or P7) at the desired θ_{Bob} secure direction; $\vec{p}$ is a complex modulation vector, as defined in (5.2).

The DM performance of the proposed antenna is shown in Fig. 6.7. The results are obtained using Quadrature Phase-Shift Keying (QPSK), with the BER calculations conducted using a data stream of 10^5 transmitted symbols, and a 12 dB SNR. Fig. 6.7a shows the DM performance in the azimuthal plane, tested for the desired secure direction of the legitimate user at $\phi_{\text{Bob}} = 120°$. It can be seen that secure data transmission is realized without leakage into other undesired directions, where very low bit errors below 10^{-4} are realized in the direction of the legitimate user, moreover for this plane very narrow beamwidth of 33° are realized for BER level of $< 10^{-2}$.

The BER computations for the elevation plane are shown in Fig. 6.7b, the intended receiver is assumed to be at $\theta_{\text{Bob}} = 120°$. For this case, too, it can be seen that secure data transmission is achieved without leakage into undesired eavesdroppers directions and the beamwidth with BER $< 10^{-2}$ is 50°. Overall, this performance demonstrate that by using a compact antenna structure requiring only 0.56λ diameter and 0.19λ profile, secure data transmission can be realized in both the azimuthal and elevation planes.

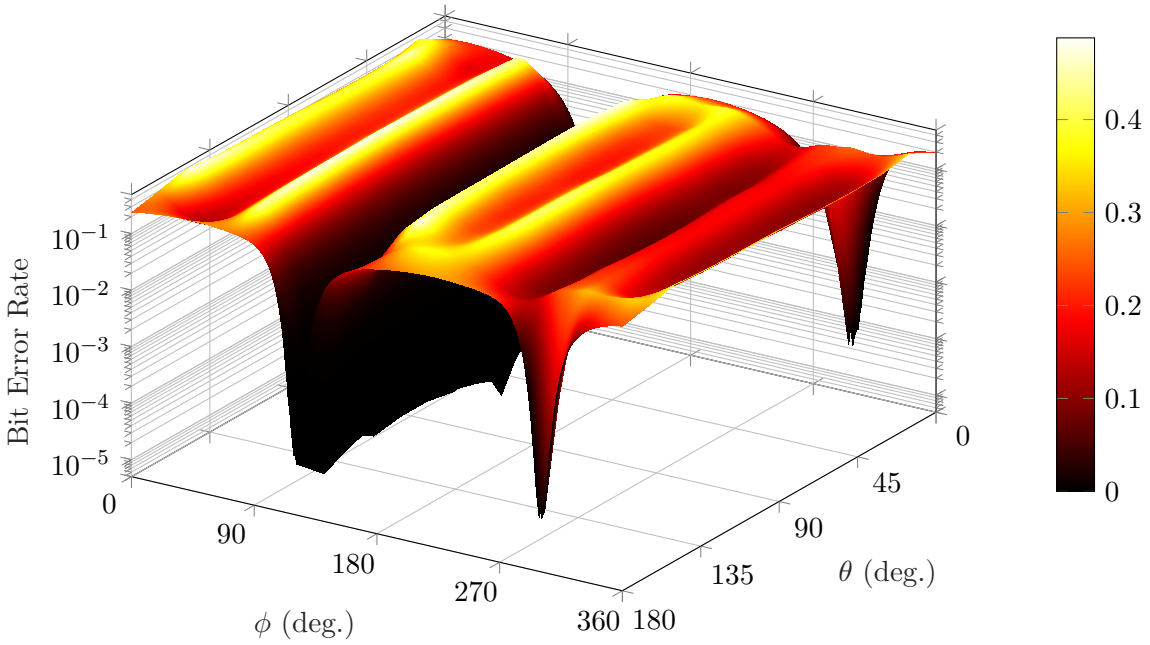

(a)

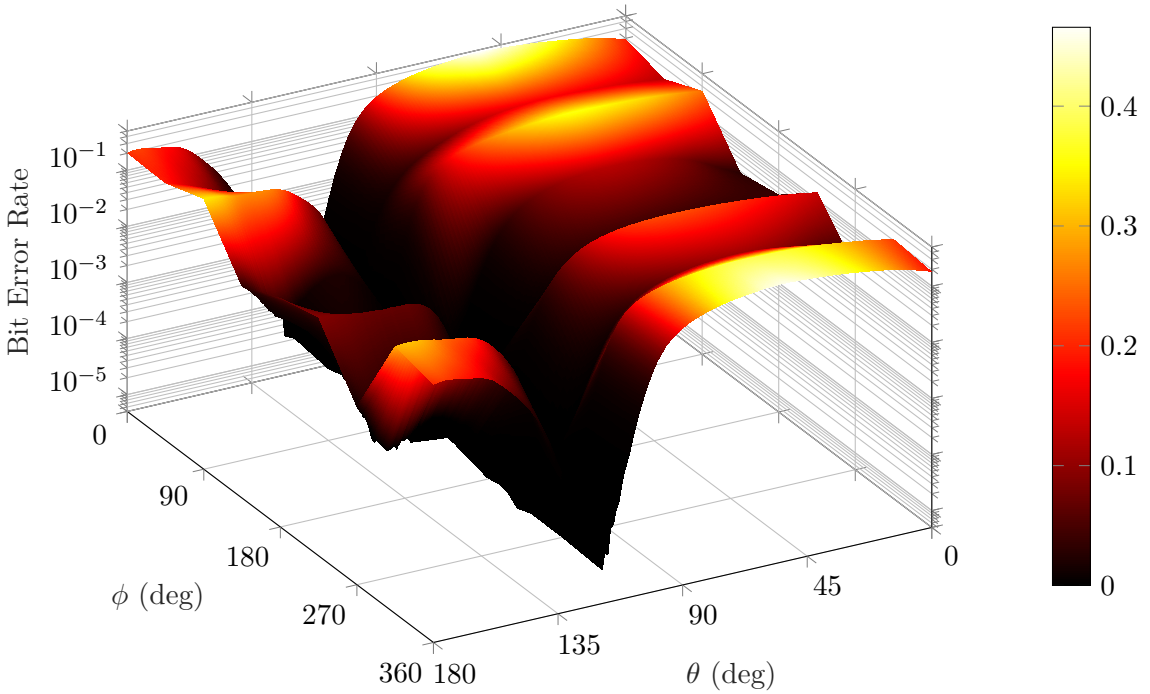

(b)

Figure 6.7: BER calculations using Signal-to-Noise Ratio (SNR) = 12 dB. (a) Azimuth plane DM performance for the legitimate receiver at $\phi = 120°$. (b) Elevation plane performance for the legitimate receiver at $\theta = 120°$.

6.2 Electrically Small 3D Beamforming Antenna

While the aforementioned antenna is capable to realize beamforming across the upper hemisphere, it uses a total of four stacked-patch structures excited through seven ports. Therefore, the design still presents challenges for practical integration in size and energy constrained Internet of Things (IoT) devices, as the profile is still relatively large and an increased number of ports is used. To address this issue, a new antenna was designed to allow similar performance from a low-profile structure.

6.2.1 Antenna Design

The proposed electrically small 3D beamforming antenna is depicted in Fig. 6.8. It consists of two layers, a top-layer denoted L1 with diameter $d_1 = 50\,\text{mm}$, thickness $h_1 = 1.57\,\text{mm}$, and a bottom layer represented using L2 with diameter $d_1 = 50\,\text{mm}$ and $h_2 = 2.54\,\text{mm}$ thickness.

As shown in Fig. 6.8b, the L1 layer comprises a centrally located circular patch antenna of diameter $d_3 = 21\,\text{mm}$ and a concentric shorted pin ring antenna, as shown in Fig. 6.8b. Both structures are supported by a TMM6 substrate ($\epsilon_r = 6.3$ and $\tan\delta = 0.0023$). The shorted pin antenna excites the $\vec{K}_{1,\pm2,2}$ omnidirectional *spherical modes*, obtained through excitation of TM_{21} modes fed using ports P4 and P5, rotated by $\alpha = 135°$ and located at (x, y) P4$(5.5\,\text{mm}, 13.5\,\text{mm})$ and P5$(5.5\,\text{mm}, -13.5\,\text{mm})$. A total of 24 shorting pins ($d_{\text{vias}} = 0.5\,\text{mm}$) rotated by 15° and located 0.6 mm from the edges of the inner diameter $d_2 = 22\,\text{mm}$, are loaded in the ring for enhanced frequency tuning and isolation improvements. Moreover, eight double T-shaped slits rotated by 45° are introduced in the concentric ring for miniaturization [149], and their locations follows the current distribution of the $\vec{K}_{1,\pm2,2}$ *spherical modes* as discussed in Chapter 3. In the double T-shaped slits, the top T-shaped slit has length $l_1 = 11\,\text{mm}$, while the bottom one has length $l_2 = 16\,\text{mm}$, while they both have a similar width of $w_3 = 0.6\,\text{mm}$.

The centrally located patch antenna (see Fig. 6.8b) excites two orthogonal TM_{11} broadside modes. This patch is fed using P1 and P2 oriented by 90°, and located at P1(2 mm,0 mm) and P2$(0\,\text{mm}, 2\,\text{mm})$. To increase the current path, four triple T-shaped slits rotated by

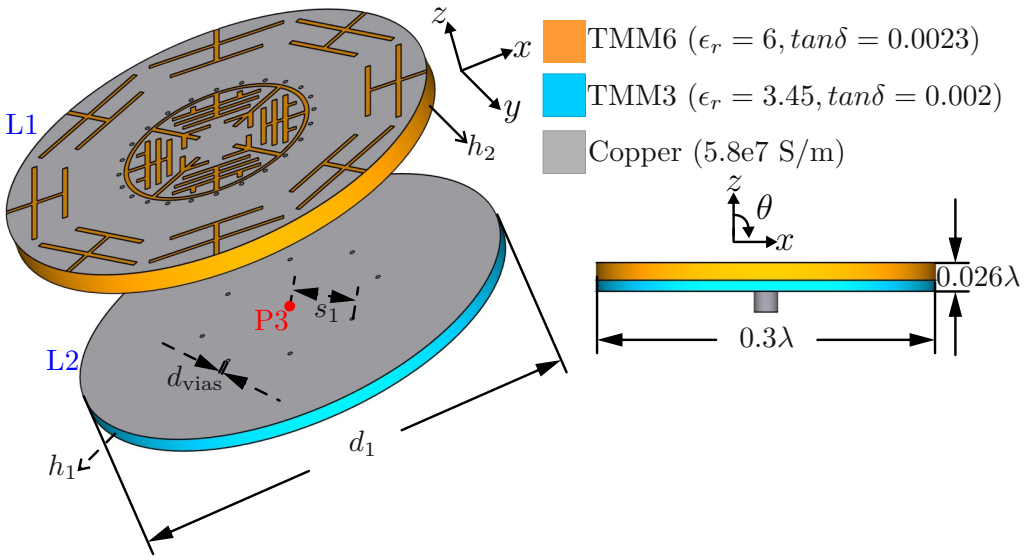

(a)

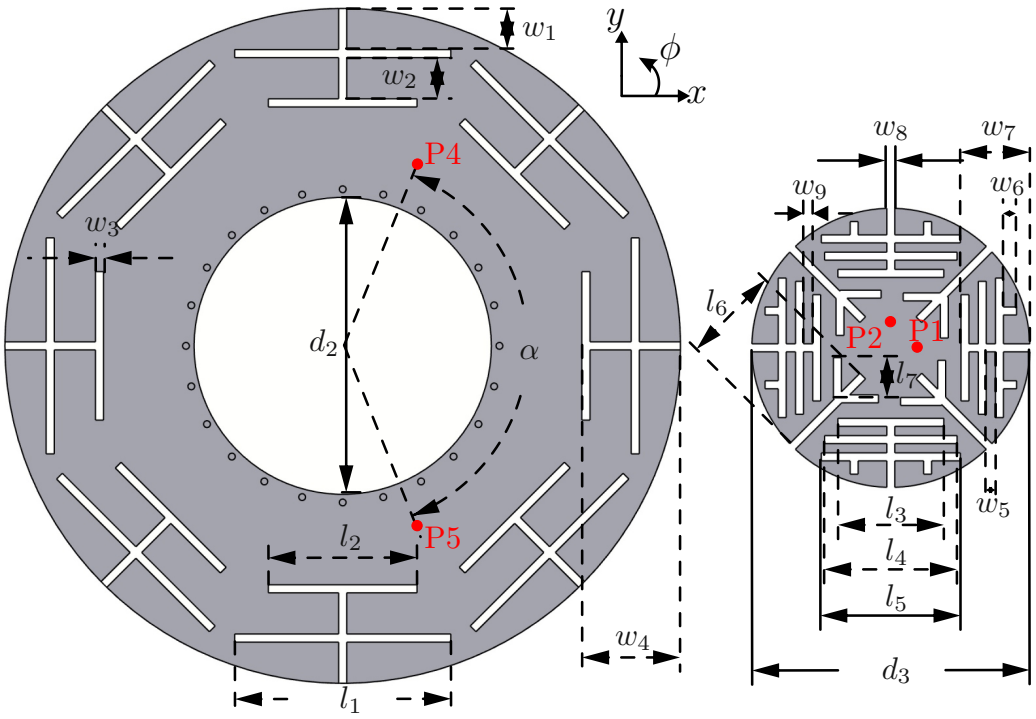

(b)

Figure 6.8: Proposed 3D beamforming ESA. (a) Exploded view showing the two stacked layers and the configuration of the bottom layer. The right image shows the front view highlighting antenna diameter and thickness. (b) Top view of the shorted-ring patch with port arrangement. The right image shows the top view of the central patch. Antenna dimensions (all in mm): $a_1 = 10.4$, $d_1 = 50$, $d_2 = 22$, $d_3 = 21$, $d_{\text{vias}} = 0.5$, $h_1 = 1.57$, $h_2 = 2.54$, $l_1 = 11$, $l_2 = 16$, $l_3 = 8$, $l_4 = 10$, $l_5 = 10.5$, $l_6 = 7.5$, $l_7 = 2.8$, $w_1 = 3.05$, $w_2 = 3.05$, $w_3 = 0.6$, $w_4 = 7.3$, $w_5 = 0.7$, $w_6 = 1$, $w_7 = 5.2$, $w_8 = 0.6$, $w_9 = 0.7$, $\alpha = 135°$. Feed locations from the disk center (in mm): P1 = P2 = 2, P3 = 0, P4 = P5 = 3.5.

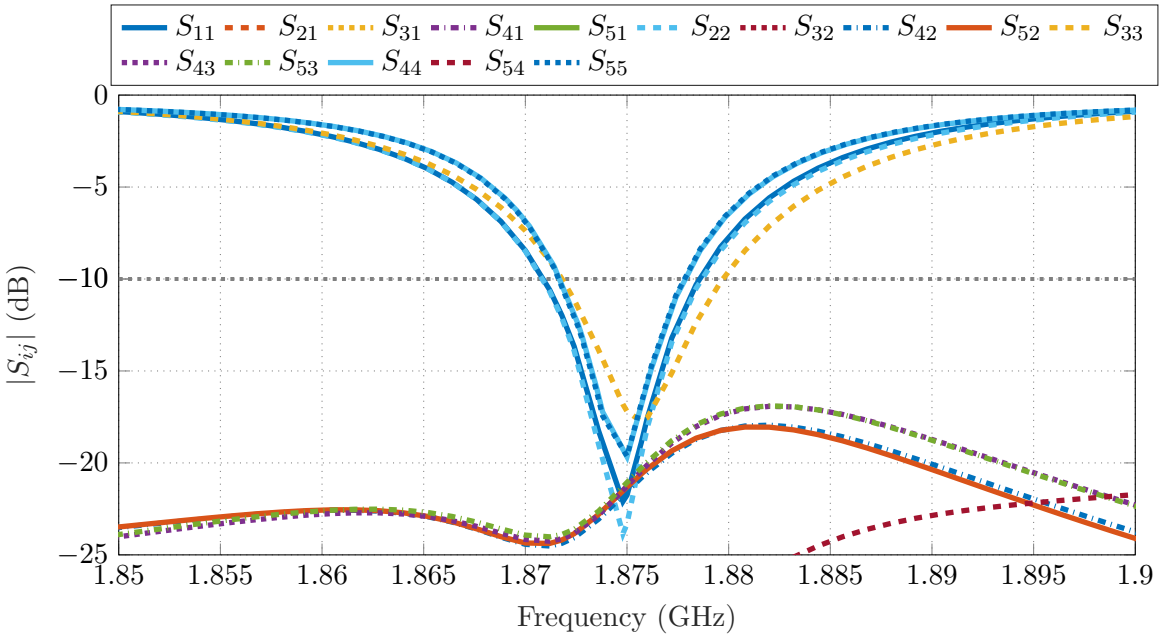

Figure 6.9: Simulated S-parameters of the proposed electrically small 3D beamforming antenna.

90° are introduced in the patch structure [149]. All the triple T-shaped slits have the same width $w_8 = 0.6\,\text{mm}$ and they have different lengths, $l_3 = 8\,\text{mm}$ for the top slit, $l_4 = 10\,\text{mm}$ for the middle slit, and finally $l_5 = 10.5\,\text{mm}$ for the bottom slit. Furthermore, this central patch also includes four rectangular slits with a V-shaped ends for miniaturization. These slits have length $l_6 = 7.5\,\text{mm}$, width of 0.6 mm, with V-shaped ends of length $l_7 = 2.8\,\text{mm}$ and width 0.6 mm. The four slits are placed diagonally across the patch, i.e., at $45°, 135°, 225°, \text{and}, 315°$.

Lastly, the L2 layer comprises a shorted pin circular patch antenna of diameter $d_1 = 50\,\text{mm}$. This patch is used to excite the $\vec{K}_{1,0,1}$ omnidirectional *spherical mode*, and is supported by a TMM3 substrate ($\epsilon_r = 3.45$ and $\tan\delta = 0.002$). The patch is centrally fed using P3. In addition, a total of eight pins, rotated by 45° and located at $a_1 = 10.4\,\text{mm}$ from the disk center, are loaded in the patch for frequency tuning and isolation enhancement. The antenna final dimensions are $50\,\text{mm} \times 50\,\text{mm} \times 4.21\,\text{mm}$ or correspondingly $0.3\lambda \times 0.3\lambda \times 0.026\lambda$, where λ is the wavelegnth at $f_0 = 1.875\,\text{GHZ}$. The design, therefore, presents a very small electrical size of $ka = 0.98$, where $k = 2\pi/\lambda$ is the wavenumber and a is the radius of the smallest sphere that can fully enclose the proposed antenna ($a = 25\,\text{mm}$), also with a very low profile of 0.026λ.

The simulated S-parameters are shown in Fig. 6.9. It can be seen that at $f_0 = 1.875\,\text{GHz}$, $|S_{ij}| < 20\,\text{dB}$, and the impedance bandwidth 6 MHz. The antenna total efficiency at the center freequency is 15% for P4 and P5, 30% for P1 and P2, and 55% for P3. It is important to note that the relatively low total efficiency of the ports P4 and P5 is due to the higher levels of miniaturization, since a substrate with high dielectric constant is sued to enable the excitation of the higher-order $\vec{K}_{1,\pm2,2}$ modes, which present a more complex pattern, i.e., dual-phase variations and therefore require a much larger diameter to support these phase characteristics [150].

6.2.2 Beamforming Analysis

The principle discussed in Chapter 3 is used to realize beamforming in the azimuthal plane. Fig. 6.10a shows the phase of the radiation pattern (without any phase shifts) of each port required to realize the azimuthal plane beam scanning, i.e., P3, P4, and P5.

Fig. 6.10b depicts the phase patterns when the desired direction is $\phi_{\text{dir}} = 45°$, where the phase shifts are computed using (3.29). It can be observed that by introducing the phase compensations all the three ports can be made to operate in-phase at the desired direction. The exemplary generated radiation pattern is shown in Fig. 6.11. Note, however, that because a second in-phase state is also observed around $\phi_{\text{dir}} = 225°$ (see the black ellipses in Fig. 6.10b), a bi-directional radiation pattern is generated. It should be mentioned that this beamforming performance is not unique to $\phi_{\text{dir}} = 45°$. In other words, the second main beam will also be observed for all the steering angles across the entire horizontal plane, and will always be seen at $\phi_{\text{dir}} + 180°$ direction. To further illustrate the horizontal plane beamforming performance, the main beam is steered into three additional directions: $0°, 90°$, and $135°$. The characteritics of all four generated beams in this plane is shown using 3D plots in Fig. 6.12, where it can be observed that all the four cases realize the desired beamforming performance. The required phase shifts of all the omnidirectional *spherical modes* are outlined in Table 6.1.

The beamforming in the elevation plane is obtained by combining only the modes excited by the layer L1, this is, the $\vec{K}_{1,\pm2,2}$ omnidirectional *spherical modes* excited using the shorted pin patch (P4 and P5), and the broadside TM_{11} modes excited by the circular patch (P1

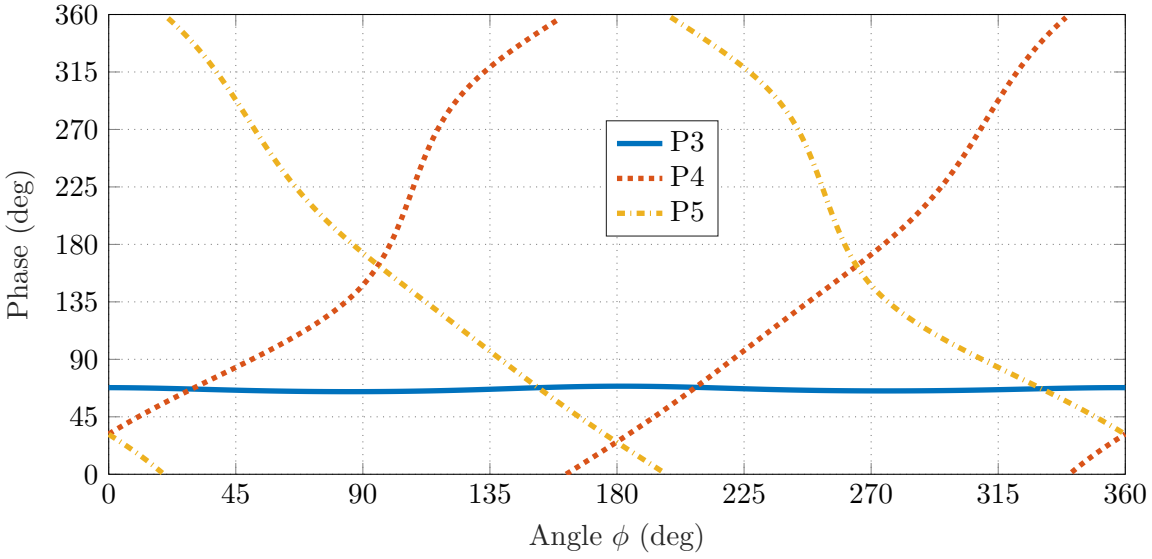

(a)

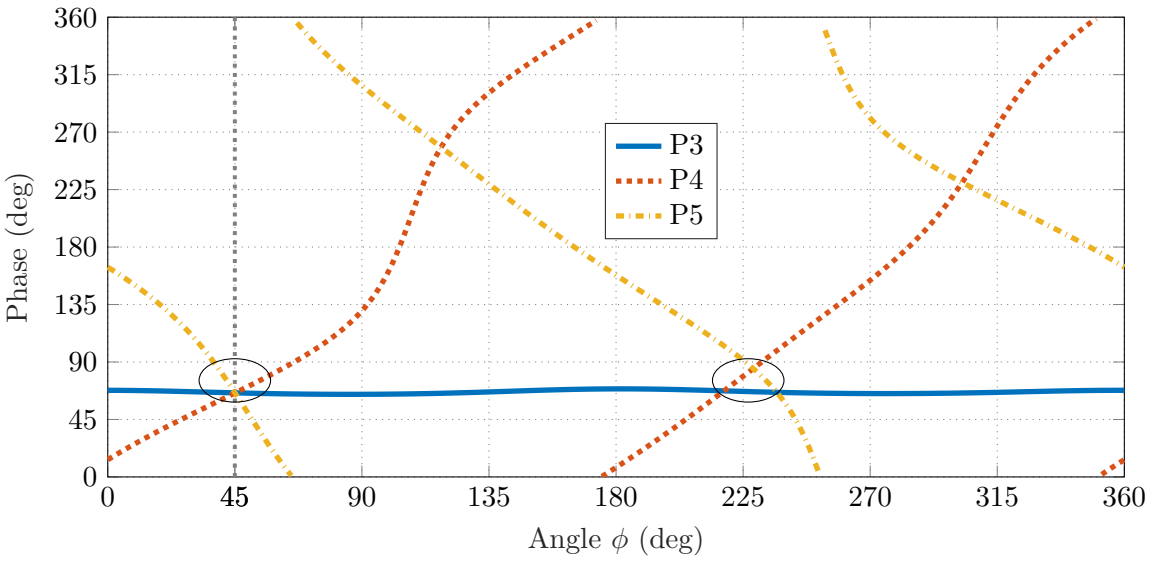

(b)

Figure 6.10: Phase of the radiation pattern of the modes used for beamforming in the horizontal plane. (a) Patterns without additional phase shift. (b) Patterns where phase compensations are introduced in P4 and P5 for beamforming towards $\phi_{\text{dir}} = 45°$. Note that a constructive phase interference is also seen near $\phi_{\text{dir}} + 180°$, which results in a second main beam.

and P2). Fig. 6.13 shows the beamforming performance for four different directions: xz-plane $\theta = 22°$ obtained by combining P1 and P4 (Fig. 6.13a), xz-plane $\theta = -22°$ generated from P1 and P5 (Fig. 6.13c), yz-plane $\theta = 28°$ (Fig. 6.13b) obtained from P2 and P5, and yz-plane $\theta = -28°$ generated using P2 and P4 (Fig. 6.13d). It is important to note that the above configurations do not require any additional phase compensations in any of the two excited ports.

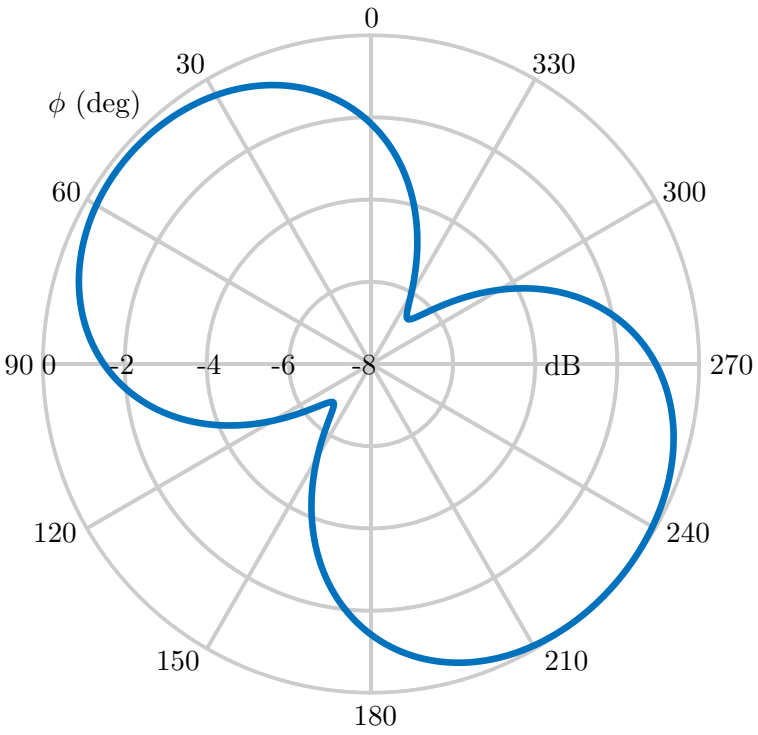

Figure 6.11: Normalized radiation pattern showing the beam steered towards $\phi_{\text{dir}} = 45°$, obtained using P3, P4, and P5 (for xy-plane). Note that this method produces a bi-directional pattern, where the second main beam is at $\phi_{\text{dir}} + 180° = 225°$.

Table 6.1: Excitations for Azimuthal Plane Beamforming

Beam direction	$\lvert A_3\rvert$	$\Delta\psi_3$	$\lvert A_4\rvert$	$\Delta\psi_4$	$\lvert A_5\rvert$	$\Delta\psi_5$
$\phi = 0°/180°$	1	0°	1	37°	1	37°
$\phi = 45°/225°$	1	0°	1	342°	1	132°
$\phi = 90°/270°$	1	0°	1	277°	1	252°
$\phi = 135°/335°$	1	0°	1	108°	1	331°

6.2.3 Azimuthal Plane Unidirectional Beamforming

The proposed ESA is capable of a unidirectional beamforming in the elevation plane, however, it only realizes a bi-directional beamforming in the horizontal plane. This performance can compromise the secrecy of the transmitted data because unwanted users may exploit the second main beam location to retrieve the transmitted information.

To enhance the bi-directional beamforming performance, the omnidirectional *spherical*

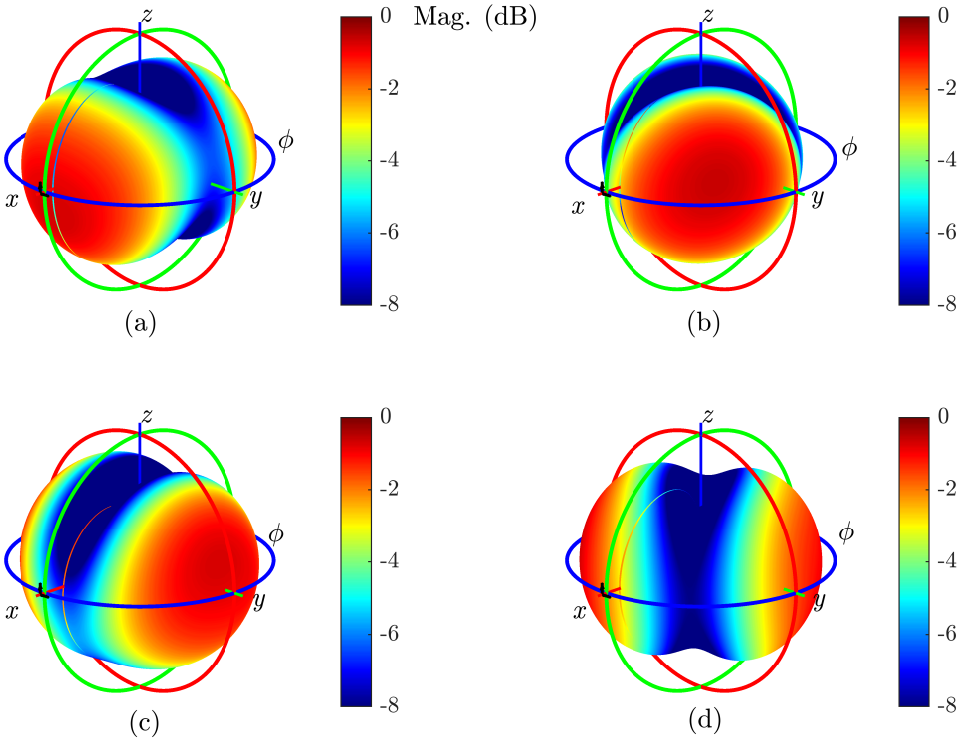

Figure 6.12: Horizontal plane beamforming obtained using P3, P4, and P5 for four different directions covering the entire plane. (a) 0°/180°. (b) 45°/225°. (c) 90°/270°. (d) 135°/315°.

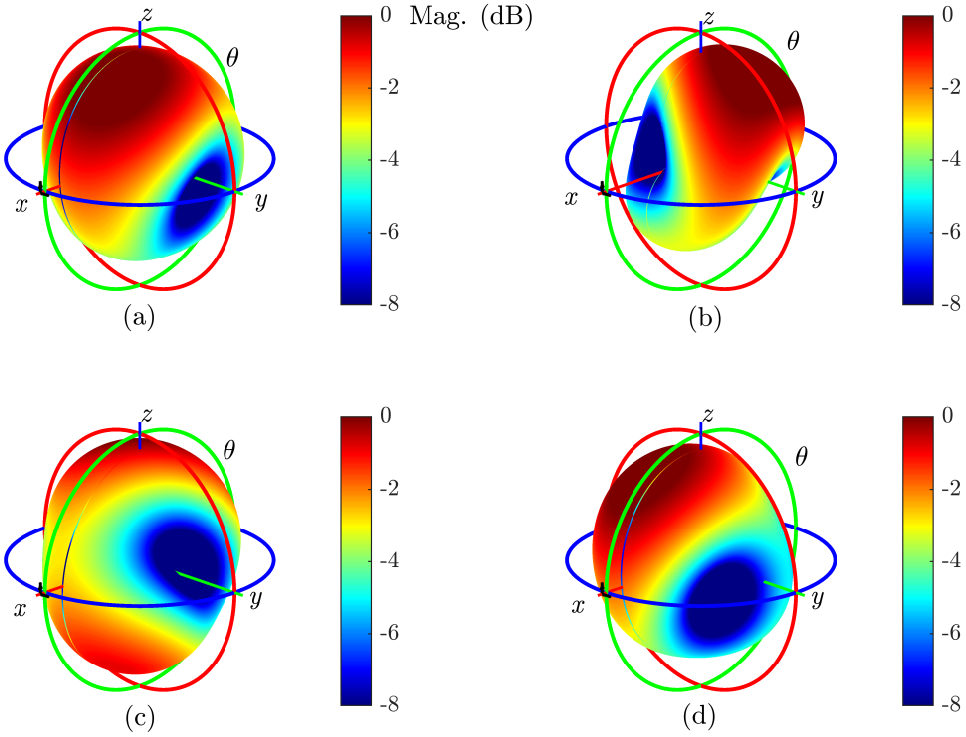

Figure 6.13: $xz(\phi = 0°)$ and $yz(\phi = 90°)$-planes beamforming obtained by combining P1, P2, P4, and P5 shown for four different directions. (a) $\phi = 0°, \theta = 22°$. (b) $\phi = 90°, \theta = 28°$. (c) $\phi = 0°, \theta = -22°$. (d) $\phi = 90°, \theta = -28°$.

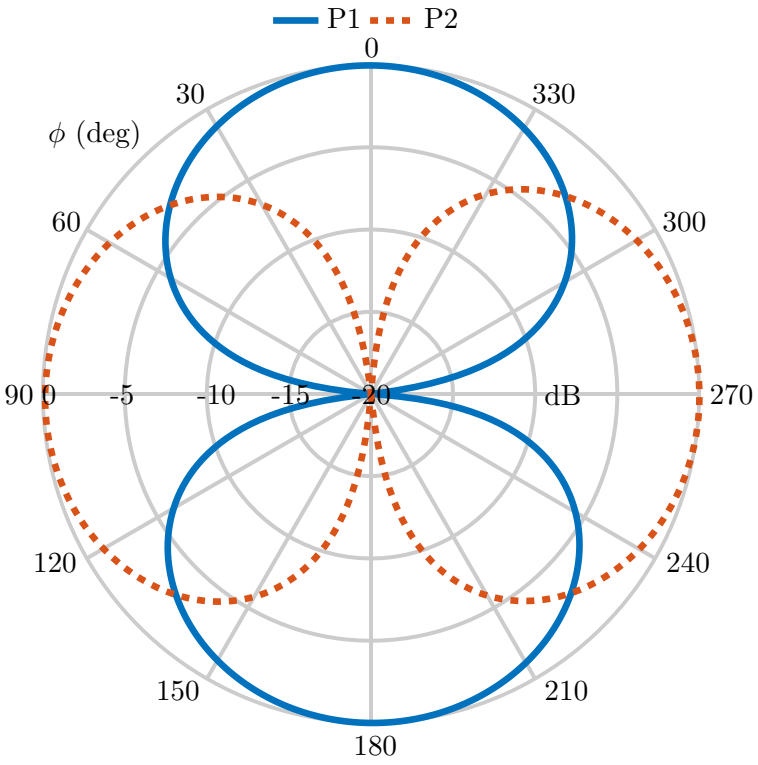

Figure 6.14: Normalized radiation pattern xy-plane ($\theta = 90°$) for the broadside modes excited using P1 and P2.

modes (P3, P4 and P5) and a broadside mode (P1/P2) are simultaneously excited. A unidirectional radiation pattern, can then be obtained by also exciting a broadside mode chosen according to the desired ϕ_{dir} angle. This means that, the selected mode will have a strong contribution towards the desired ϕ_{dir} direction (see Fig. 6.14). Next, different amplitude values are used for the selected broadside mode (P1/P2), this is necessary to control the Side Lobe Level (SLL) and to ensure that the maximum directivity is still across the horizontal plane.

Fig. 6.15 depicts the performance of the proposed directivity enhancement method. The methodology is demonstrated for two different directions $\phi_{\text{dir}} = 90°$ and $\phi_{\text{dir}} = 180°$. By analyzing the patterns given in Fig. 6.14, P1 should be used when ϕ_{dir} is located within $(0° - 50°)$, $(135° - 220°)$ and $(320° - 360°)$. The remaining ϕ_{dir} angles, i.e., $(51° - 134°)$, $(221° - 319°)$ are covered using P2. Following the above configurations, to steer the beam towards $\phi_{\text{dir}} = 90°$, the pattern generated by P2 is used to reduce the magnitude of the second main beam located at $\phi_{\text{dir}} + 180° = 270°$. The performance is tested using different

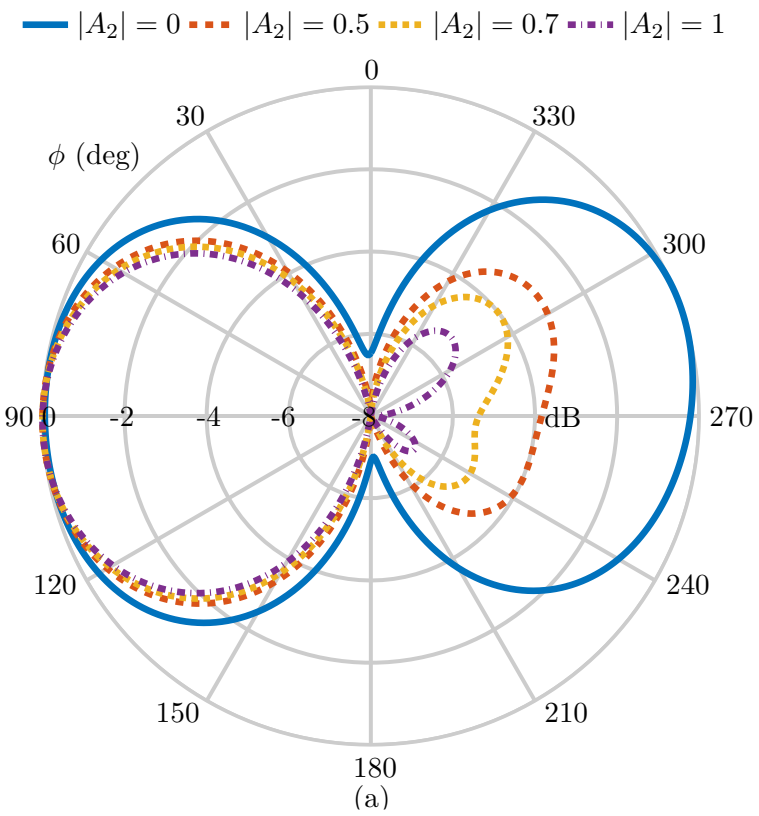

(a)

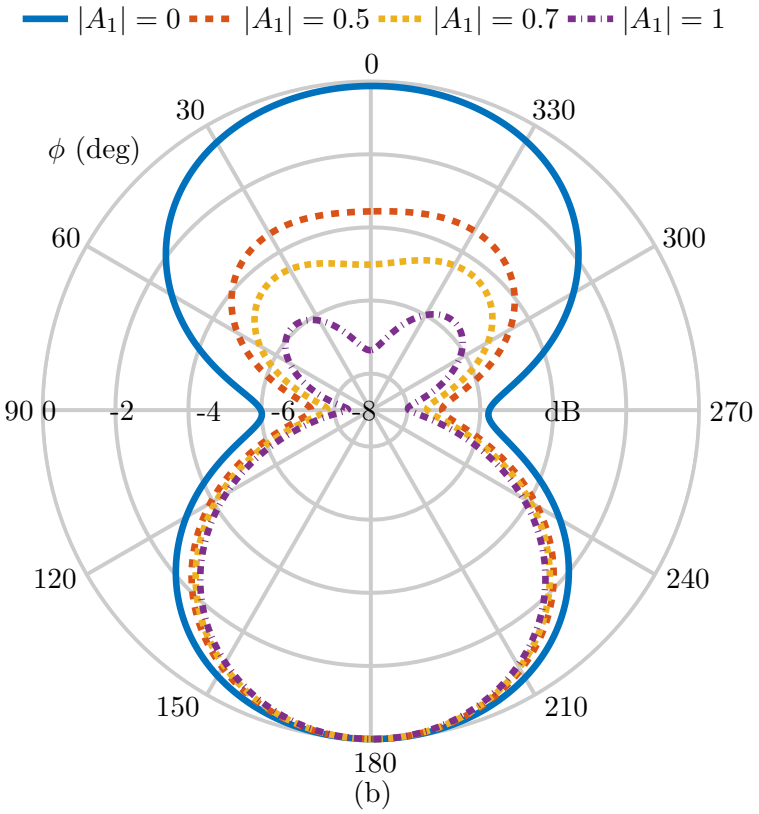

(b)

Figure 6.15: Unidirectional beamforming across the horizontal plane using different amplitude values ($|A_2|$ or $|A_1|$). (a) $\phi_{\text{dir}} = 90°$. (b) $\phi_{\text{dir}} = 180°$

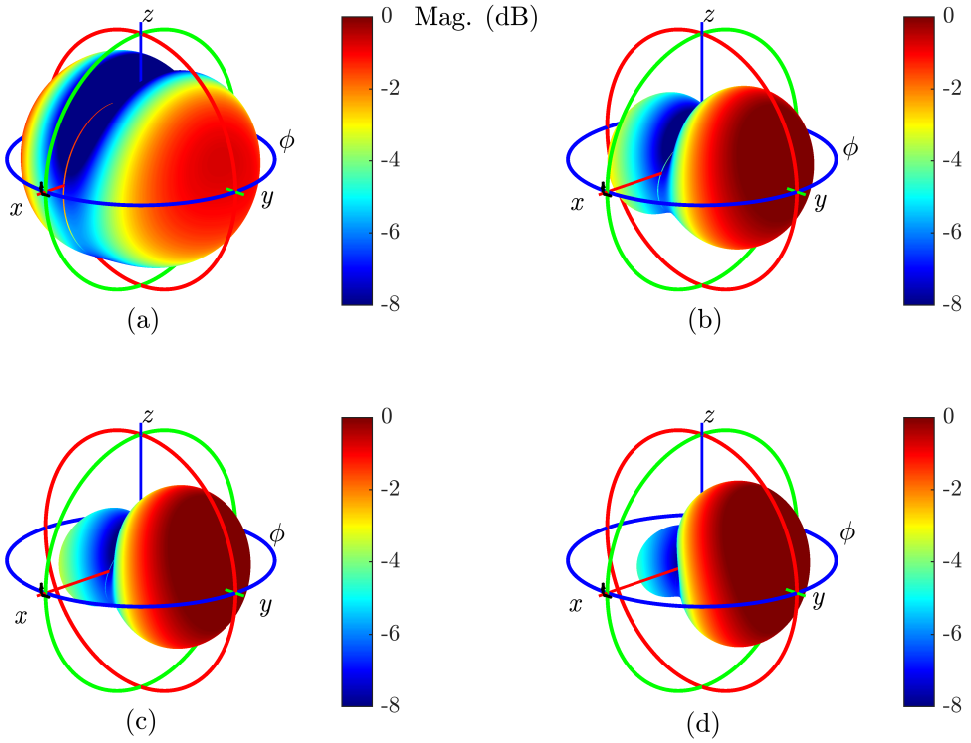

Figure 6.16: 3D plots showing the unidirectional beamforming for $\phi_{\text{dir}} = 90°$ direction shown in Fig. 6.15: (a) $|A_2| = 0$. (b) $|A_2| = 0.5$. (c) $|A_2| = 0.7$. (d) $|A_2| = 1$.

amplitude values of P2, i.e., $|A_2|$ and is shown in Fig. 6.15a. It can be seen that higher $|A_2|$ values provide better reductions of the $\phi_{\text{dir}} + 180°$ beam magnitude. To further highlight the directivity enhancement of the proposed method Fig. 6.16 shows the 3D plots of each $|A_2|$ value.

Fig. 6.15b outlines the performance of the proposed method for $\phi_{\text{dir}} = 180°$ direction. For this angle, the mode excited using P1 will have stronger contribution towards the desired beamforming direction $\phi_{\text{dir}} = 180°$. For this case, too, different amplitude values $|A_1|$ are tested and the generated patterns are shown in Fig. 6.15b, also demonstrating that the second main beam magnitude is reduced at $\phi_{\text{dir}} + 180° = 0°$.

6.2.4 Directional Modulation Analysis

To investigate the DM performance of the proposed electrically small 3D beamsteering antenna the method described in Section 6.1.4 is used. The performance is tested using QPSK, and BER calculations are executed using 10^5 transmitted symbols and 12 dB SNR at the intended receiver. The BER calculations are done for two different transmissions

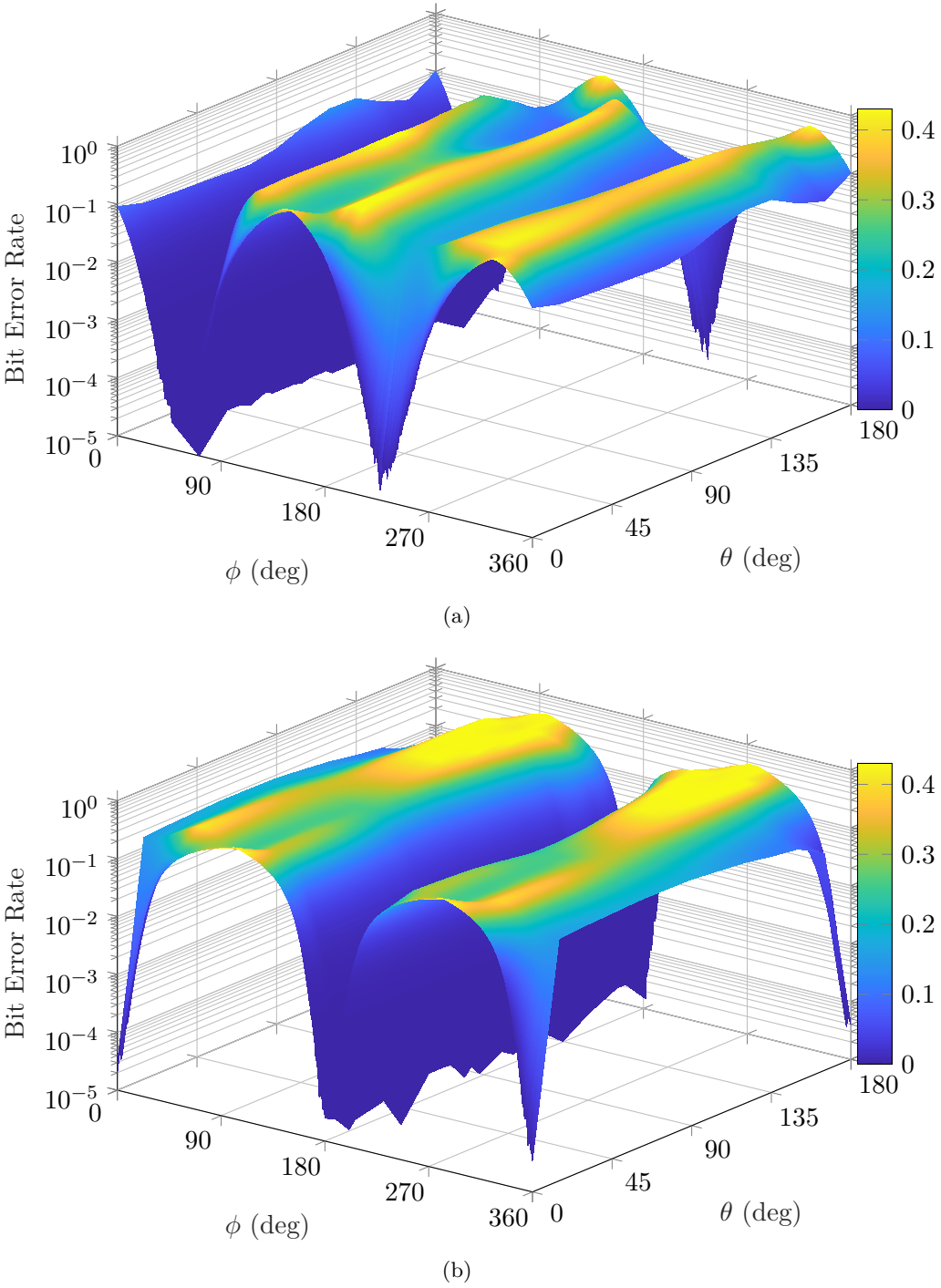

Figure 6.17: BER computations for 12 dB SNR depicting the directional modulation performance in the horizontal plane plane. (a) $\phi_{\text{Bob}} = 50°$. (b) at $\phi_{\text{Bob}} = 180°$.

directions in each given plane.

The BER results for the azimuth plane are shown in Fig. 6.17a and Fig. 6.17b for $\phi_{\text{Bob}} = 50°$ and $\phi_{\text{Bob}} = 180°$ directions, respectively. It can be seen that the method realizes steerable transmissions with low BER towards the desired angle ϕ_{Bob}, without

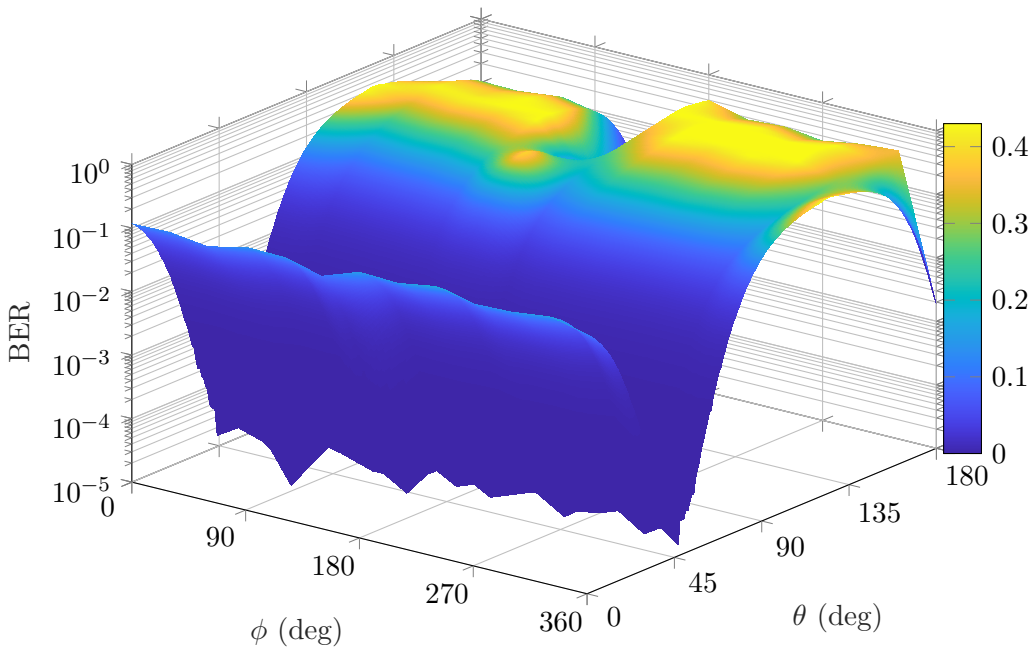

(a)

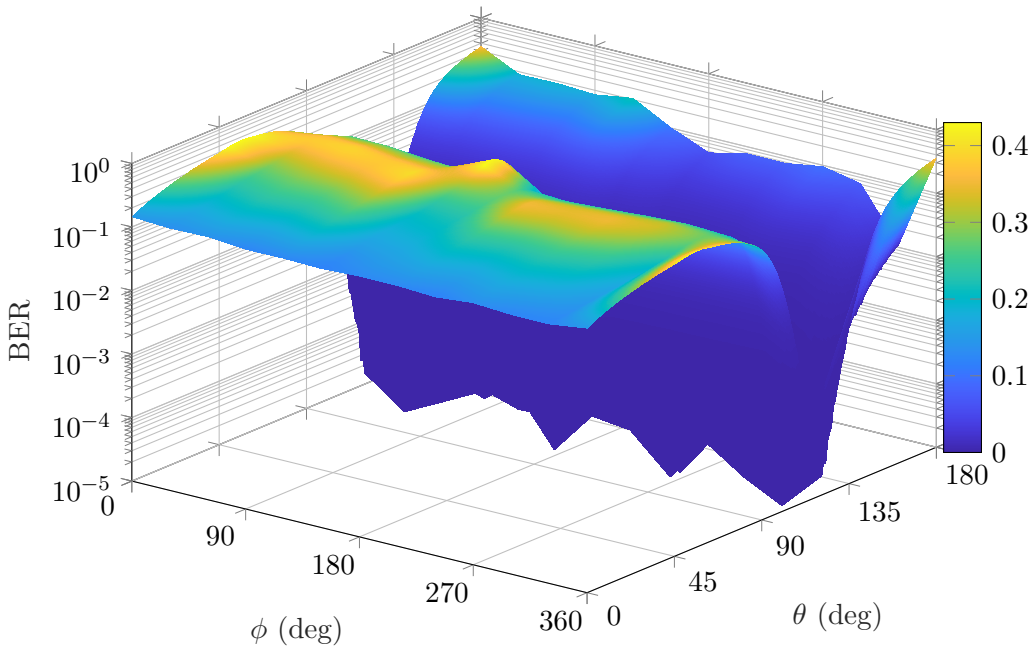

(b)

Figure 6.18: BER results calculated using 12 dB SNR highlighting the directional modulation performance in the elevation planes. (a) Receiver located at $\theta_{\text{Bob}} = 50°$. (b) Intended receiver at $\theta_{\text{Bob}} = 120°$.

leakage into undesired eavesdroppers' locations in the same plane. Very low BER values below 10^{-4} are obtained at the desired directions of the legitimate user, and the beamwidth with BER smaller than 10^{-2} is 55°. To validate the DM performance in the elevation plane two θ_{Bob} directions are also investigated: $\theta_{\text{Bob}} = 50°$ (see Fig. 6.18a) and $\theta_{\text{dir}} = 120°$ (shown

in Fig. 6.18b). It can also be observed that very low BER values below 10^{-4} are also realized in the two investigated cases, where the 10^{-2} BER beamwidth is 58°. Overall, the results demonstrate that secure data transmission can be realized while using highly miniaturized antennas, therefore, highlighting the suitability of the proposed concept in enhancing the security of data transmission within many emerging size-constrained IoT systems.

6.3 Summary

This Chapter discussed dual-plane DM for size-constrained IoT devices. To realize the proposed dual-plane DM characteristics, 3D beamforming antennas were investigated. These properties were achieved via the excitation of broadside radiating modes, which are used to extend the horizontal *SMB* principle. Overall, it was demonstrated that unique steerable DM transmissions are realized in both planes wihtout leakage into undesired eavesdroppers directions. It was observed that the desired receiver experience very low BER better than 10^{-4} across the two planes, while high error rates will be observed outside the desired secure directions. To further address the increasing demand of highly miniaturized antennas for IoT applications, an ESA capable of 3D beamforming across the azimuth and elevation planes is proposed and the dual-plane DM performance was also validated through BER calculations. It was also demonstrated that the proposed ESA realizes unique steerable directionally modulated transmissions without leakage into eavesdroppers directions.

7 On-Body Analysis of SMB Antennas

On-Body Analysis of SMB Antennas

This chapter studies *SMB* principle for emerging on-body Internet of Things (IoT) applications. The analysis is based on a stacked-patch design capable of unidirectional beamforming with vertical polarization across the entire horizontal plane. The impact of the human body is investigated using a multi-layer forearm phantom, and its effects on the antenna efficiency, matching, and beamforming are thoroughly examined. To adhere to the established standards of electromagnetic exposure in human tissue, Specific Absorption Rate (SAR) analyses are conducted for both wrist-worn and next-to-the-mouth conditions. Next, the on-body performance of Directional Modulation (DM) and Angle of Arrival (AoA) estimation techniques are also analyzed in detail. Lastly, it is essential to highlight that the chapter aims to provide preliminary analyses on the suitability of *SMB* concept for on-body applications. Therefore, all the results are based on rigorous full-wave simulations. The experimental validations are presented in the following chapters, using advanced models with lower profile and enhanced beamforming characteristics. Lastly, part of the results presented in this chapter were published at the 16th European Conference on Antennas and Propagation [151] and the 2022 International Workshop on Antenna Technology [140].

7.1 Antenna Design

The proposed antenna is shown in Fig. 7.1. It comprises three stacked layers made of patch antennas. Each patch is made of a $35\,\mu$m thick copper supported by a substrate of H = 3.81 mm thickness. Similar to the design discussed in Section 5.2, to realize unidirectional beamforming across the entire horizontal plane, a total of five omnidirectional *spherical modes* are excited within the three patch structures. However, unlike the design

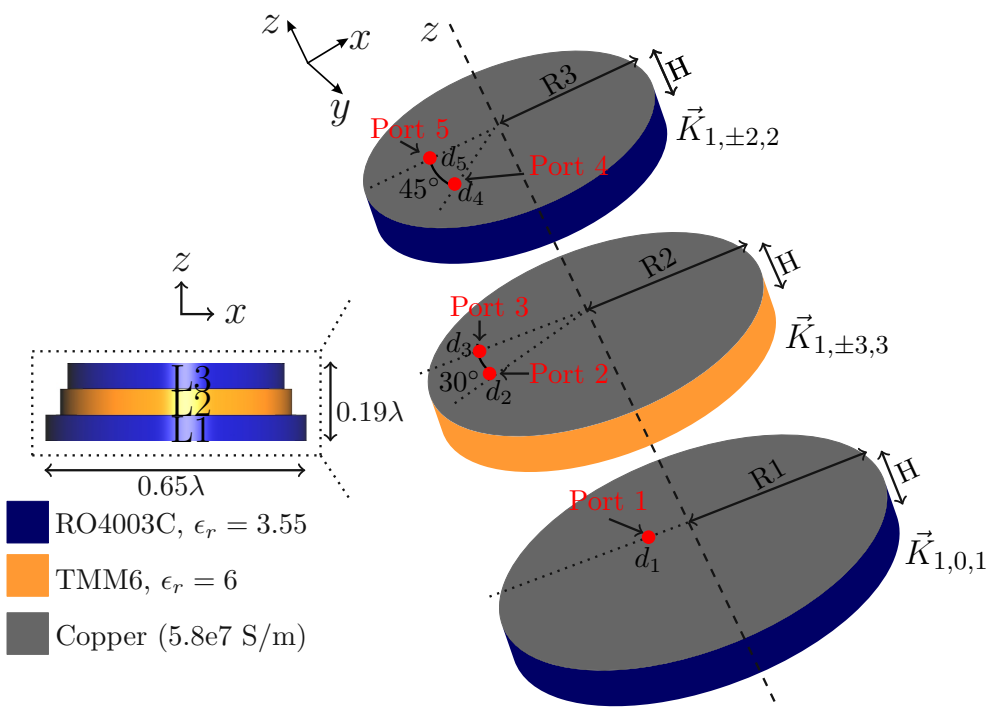

Figure 7.1: Proposed antenna. Front view highlighting the antenna diameter and thickness is shown on the left and exploded view outlining each layer feeding arrangements is depicted on the right.

in Section 5.2, here, the bottom layer (L1) excites the fundamental $\vec{K}_{1,0,1}$ mode and no shorting pins are included in the design. Note that the placement of the fundamental mode as the bottom layer is related to its total efficiency performance, since the mode is of the lowest possible order, it has highest possible efficiency among all modes. Therefore its placement is closest to the lossy tissue, i.e., the $\vec{K}_{1,0,1}$ mode is excited using the bottom layer. As will be demonstrated the port exciting the $\vec{K}_{1,0,1}$ mode will have the highest efficiency deterioration, however, this is still above 50%, which would not be the case if the higher-order *spherical modes* were excited using the bottom patch [151]. The remaining layers, i.e., middle (L2) and top (L3) respectively excite the $\vec{K}_{1,\pm3,3}$ and $\vec{K}_{1,\pm2,2}$ phase-varying *spherical modes*.

The antenna operate at $f_0 = 5\,\text{GHz}$. The layer L3 patch has radius R3 = 16.2 mm, is supported by RO4003C substrate ($\epsilon_r = 3.55$ and $\tan\delta = 0.0027$). This layer excites the $\vec{K}_{1,\pm2,2}$ modes, obtained through the excitation of two orthogonal TM_{21} modes fed using ports 4 and 5 that are fed in-quadrature. Port 5 is located at $d_5(x, y) = (10\,\text{mm}, 0\,\text{mm})$ and port 4 is located at $d_4(x, y) = (7\,\text{mm}, 7\,\text{mm})$, i.e. the ports are rotated by 45°.

Table 7.1: Dielectric Properties of the Multi-Layer Forearm Phantom at $f_0 = 5\,\text{GHz}$ and the Corresponding Volume Porpotions

Layer	ϵ_r	Conductivity (σ) S/m	Volume
Skin	35.77	3.06	Skin + Fat = 15%
Fat	5.02	0.24	-
Muscle	49.54	4.04	72.1%
Bone	16.05	1.81	12.9%

The layer L2 is used to excite the $\vec{K}_{1,\pm3,3}$ *spherical modes*. Because these modes require a larger antenna diameter to support the triple-phase variations, a higher relative permittivity substrate TMM6 ($\epsilon_r = 6.3$ and $\tan\delta = 0.0023$) is used for miniaturization, resulting in radius R2 = 17.3 mm. The *spherical modes* are then obtained by exciting two orthogonal TM_{31} modes fed using ports 2 and 3, with the two ports fed in-quadrature. Port 3 is located at $d_3(x, y) = (9.5\,\text{mm}, 0\,\text{mm})$, and port 2 is located at $d_2(x, y) = (8.2\,\text{mm}, 4.8\,\text{mm})$, i.e., rotated by 30°.

Lastly, the bottom-patch has radius R1 = 19.5 mm, it uses the RO4003C substrate, and is fed using port 1 located at $d_1(x, y) = (5\,\text{mm}, 0\,\text{mm})$. This patch excites the fundamental omnidirectional *spherical mode*. The antenna final dimensions are: 39 mm × 39 mm × 11.6 mm or correspondingly $0.65\lambda \times 0.65\lambda \times 0.19\lambda$, where λ is the wavelength at the antenna center operating frequency , i.e., $f_0 = 5\,\text{GHz}$, and the generated patterns are vertically polarized.

7.1.1 Multi-Layer Forearm Phantom

To investigate the influence of the human forearm on the proposed *SMB* antenna, a multilayer forearm phantom is used in simulation. The phantom is shown in Fig. 7.2, with a total thickness of $h = 36\,\text{mm}$, length $l = 200\,\text{mm}$, and width $w = 60\,\text{mm}$. The phantom comprises four layers, namely skin, fat, muscle and bone, where the respective volume proportions are obtained from the computed tomography results observed in [152] and are outlined in Table 7.1. Additionally, the dielectric properties of each layer at $f_0 = 5\,\text{GHz}$ are obtained from [153], and shown in Table 7.1.

The proposed antenna is placed at the phantom's center, where the ground plane is in

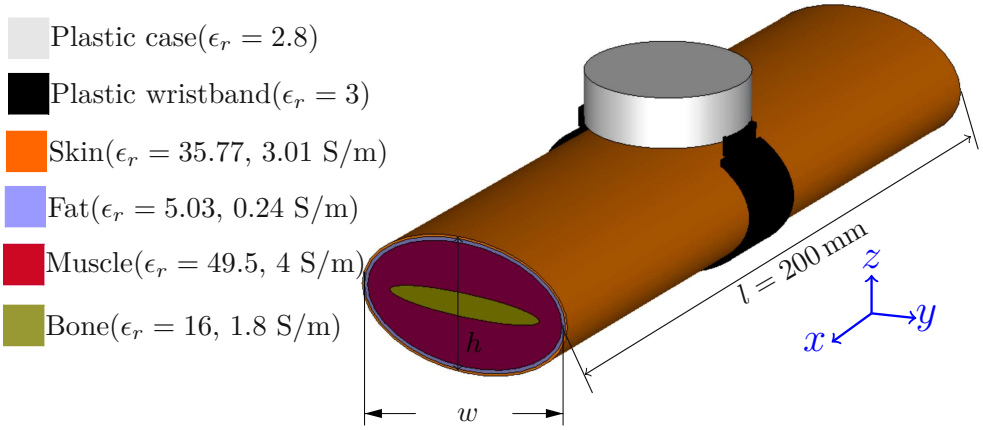

Figure 7.2: Proposed multi-layer forearm phantom. Note that the antenna is placed on the phantom's center, enclosed by a plastic case and its ground plane is in direct contact with the skin layer.

direct contact with the skin layer. To simulate practical wearable IoT devices, the antenna enclosing case is simulated by a plastic material of $\epsilon_r = 2.8$, $\tan\delta = 0.01$, with a 1 mm spacing between the antenna and the plastic case. A wall thickness of 1 mm is ensured between the case and the antenna, and the total diameter and height of the case are then 42.98 mm and 13.57 mm, respectively. A plastic wristband ($\epsilon_r = 3$), with width = 20 mm and thickness = 3 mm is attached at two opposite edges of the plastic case, surroundding the phantom's skin-layer.

7.2 On-Body Performance

The simulated S-parameters results in free space and with the multilayer phantom are shown in Fig. 7.3a and Fig. 7.3b, respectively. It can be seen that in free space all the excited ports of the antenna operate at $f_0 = 5$ GHz, where the isolation is better than 17 dB, and the impedance bandwidth is 18.5 MHz. As shown in Fig. 7.3b, when the phantom is included the center frequency is shifted toward lower values, and the matching along with isolation characteristics deteriorate. Note, however, that for $f_0 = 4.98$ GHz, the isolation increases to 13.7 dB and the impedance bandwidth overlapping is 23.5 MHz.

The phantom impacts on the antenna total efficiency is plotted in Fig. 7.4 and also detailed in Table 7.2. At f_0 of the free space case the antenna total efficiency is better than

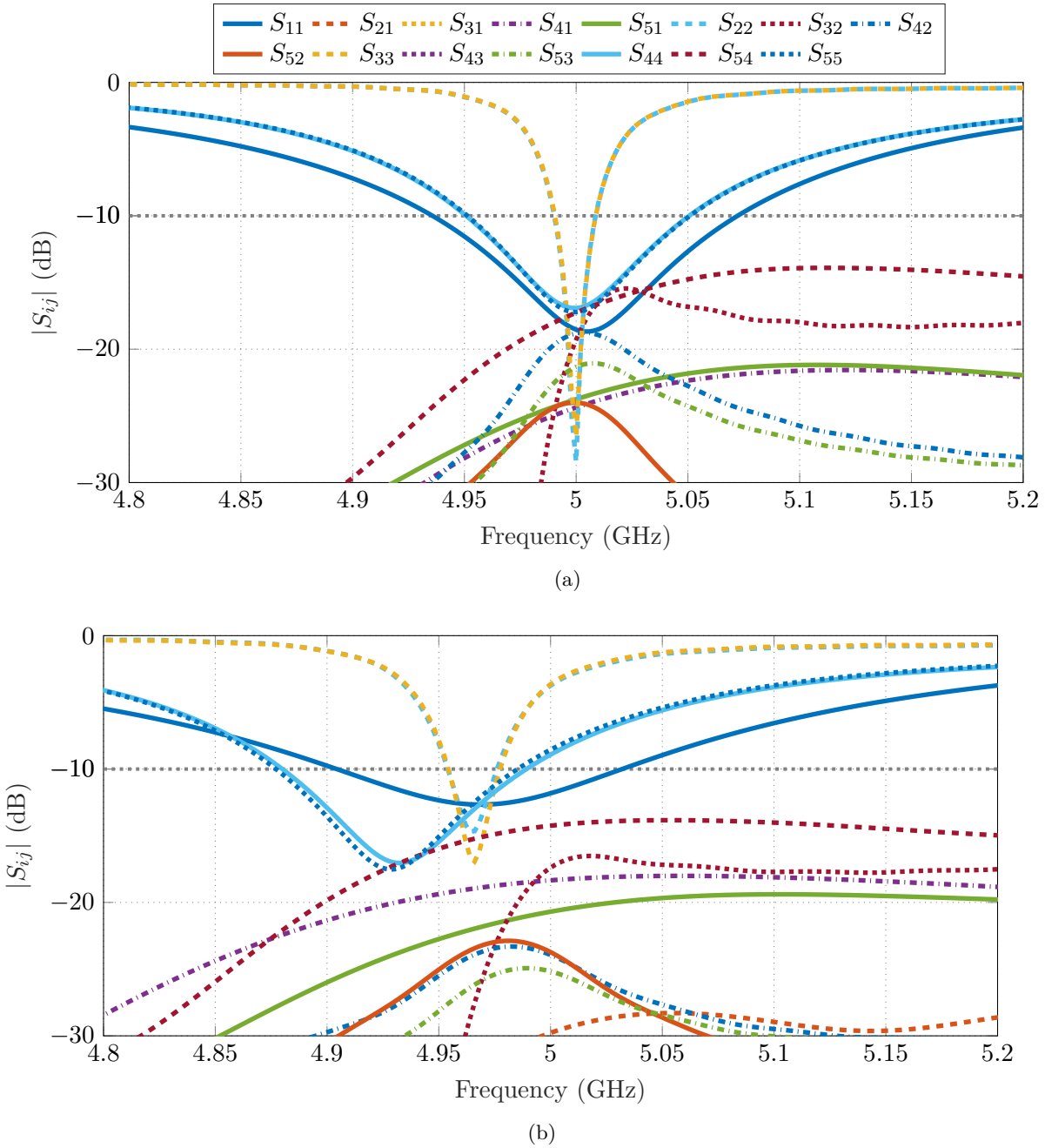

Figure 7.3: Simulated S-parameters results. (a) S-parameters wihtout phantom. (b) S-parameters including the phantom.

49% in all the five ports, dropping to 37.5% for the case including the phantom. Note that this antenna efficiency is limited by the higher order *spherical modes* $\vec{K}_{1,\pm3,3}$ which uses a substrate with a higher dielectric constant, since these modes require much larger diameter to support the triple-phase variations around their perimeter. As for the $\vec{K}_{1,\pm2,2}$ their ports total efficiency is better than 87%. The largest value of the antenna total efficiency is seen

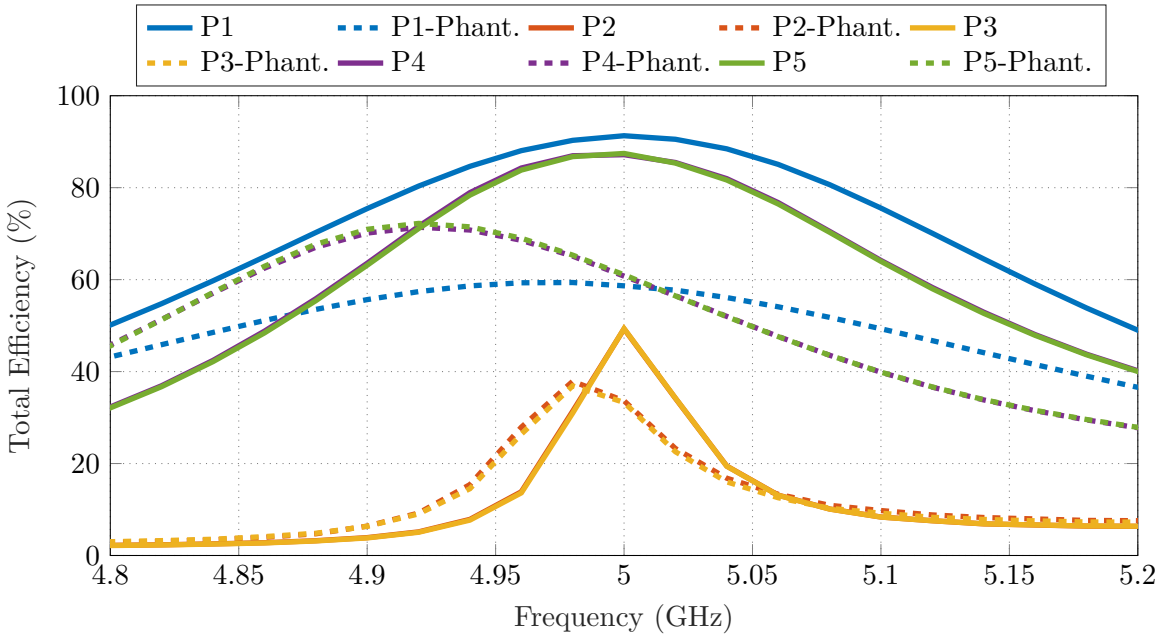

Figure 7.4: Simulated total efficiency of the proposed *SMB* antenna operating in free space (solid lines) and including phantom (dashed lines).

Table 7.2: Total Efficiency at $f_0 = 5\,\text{GHz}$ (Free Space) and $f_0 = 4.98\,\text{GHz}$ (with Phantom)

Total Efficiency	Antenna Ports				
	Port 1	Port 2	Port 3	Port 4	Port 5
Free space	91%	49%	49%	87%	87%
With Forearm Phantom	59.3%	37.5%	36.5%	65%	65%

for port 1, which excites the fundamental $\vec{K}_{1,0,1}$ mode. Fig. 7.4 also highlights that the largest efficiency deterioration occurs for port 1, where the value drops from 91% (free space) to 59.3% (including phantom). It is important to note that this significant drop can be explained by the bottom patch close proximity to the multi-layer phantom, as it is placed 0 mm away from the groundplane, i.e., it is in direct contact with the phantom's skin-layer. However, the layer still realizes a total efficiency better than 55%.

7.3 Beamforming Performance

Fig. 7.5a shows the normalized radiation patterns of the proposed antenna when operating in free space. In general, the required omnidirectional properties are realized in all excited *spherical modes*. Fig. 7.5b highlights the radiation patterns of each port when the forearm phantom is integrated. The obtained patterns present some shoulderings and dips, especially along the 0° and 180° angles. This may be explained by the fact that those locations are along the phantom's length, therefore, increased dips are observed as compared to those directions that lie within the angles that are orthogonal to the phantom's length, i.e., 90° and 270°, as around these directions the impact of the phantom on the antenna main beam is minimal.

Fig. 7.6 outlines the phase of the radiation pattern of each excited mode. It can be seen that in both cases (free space and including phantom) the required phase characteristics are achieved. In other words, despite some minor phase discrepancies within $(0° - 40°)$ and $(320° - 360°)$ for port 1, and $(138° - 220°)$ for ports 1, 2 and 3, a constant phase is still realized by port 1 (exciting $\vec{K}_{1,0,1}$ mode), changing twice in two opposing directions for ports 4 and 5 (exciting the $\vec{K}_{1,\pm 2,2}$ modes), and lastly the phase changes thrice also in two opposing for ports 2 and 3 (exciting the $\vec{K}_{1,\pm 3,3}$ modes).

The proposed antenna beamforming is obtained using the principle discussed in Section 3.3. The realized performance is shown in Fig. 7.7 for the two evaluated cases, free space operation and the performance including the phantom effects. The beamforming is tested for the following steering directions: $0°, 30°, 60°, 90°, 270°, 300°$ and $330°$. It can be seen that the antenna achieves unidirectional beamforming across the entire horizontal plane. Moreover, slight beam tilts and beamwidth changes occur when the forearm phantom is included in the simulations. The main-beam direction has a maximum tilt of 9°. These tilts are more noticeable within the beams steered towards $(15° - 70°)$, $(120° - 170°)$, $(190° - 230°)$ and $(295° - 350°)$. This may be explained by the dips seen on the phase patterns of port 1 (see Fig. 7.6) and on the amplitudes changes observed when the phantom effects are included (see Fig. 7.5b). Note that the phase patterns and amplitudes for the phantom-case are less uniform compared to the free space case, consequently beam tilts

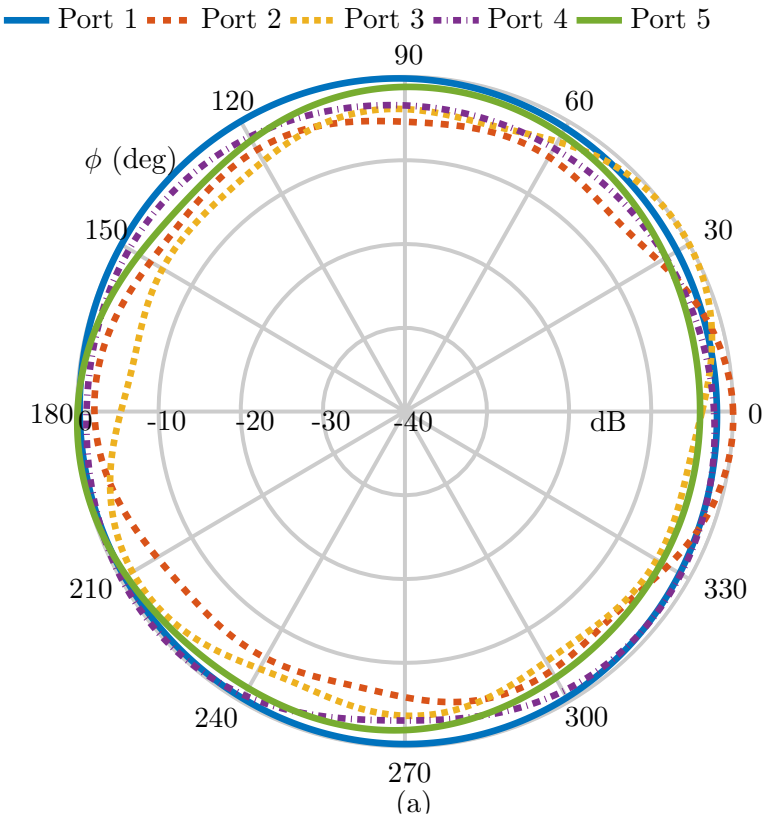

(a)

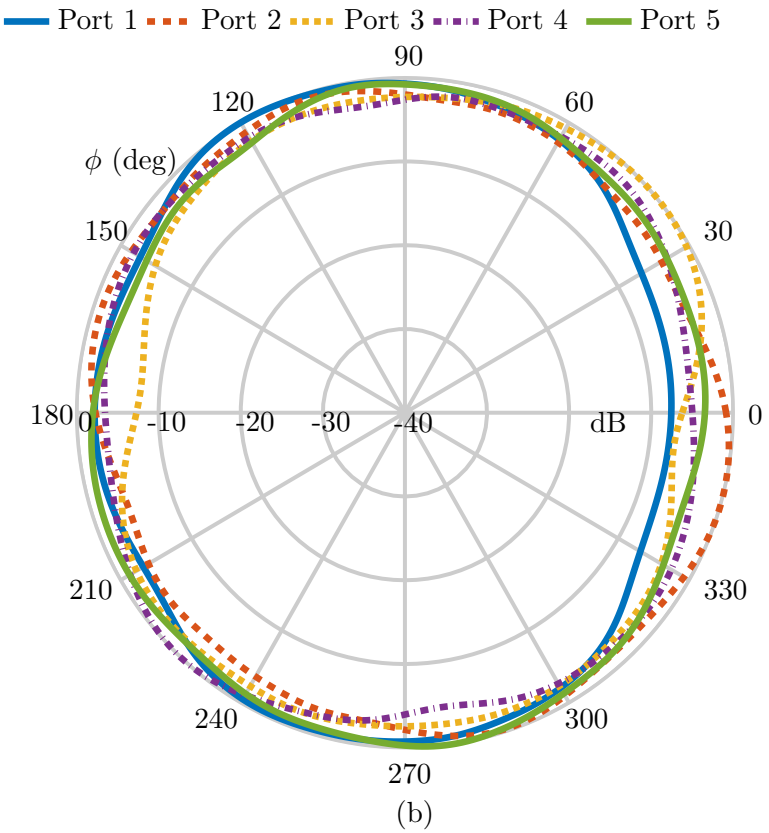

(b)

Figure 7.5: Normalized radiation patterns showing the amplitudes in the xy-plane ($\theta = 90°$) for each port of the proposed antenna. (a) Free space. (b) Including forearm phantom.

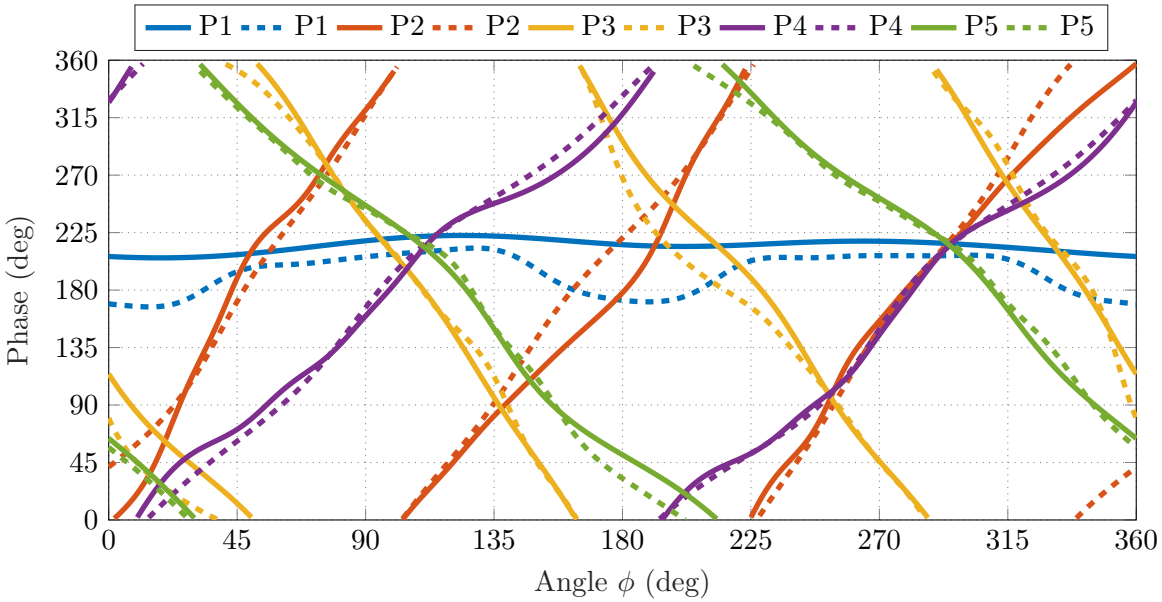

Figure 7.6: Simulated phase of the radiation pattern of the proposed *SMB* antenna operating in free space (solid lines) and including phantom (dashed lines).

effect on the phantom patterns will be observed. Nevertheless, phase-corrections may be added to further adjust the desired beamforming direction.

From Fig. 7.7 it can also be seen that the main beam direction of the generated patterns is little affected when the beam is directed towards 0°. This may be explained by the fact that this direction falls exactly at the phantom's center, and the generated beam wil be positioned in a symetrical way with respect to the phantom, i.e., equal from both $-y$ and $+y$ directions. While this has little impact on the main beam direction, however, due to the phantom's surface reflections, for $\theta = 90°$ cut-plane, a significant drop of 3.1 dBi occurs on the realized gain, i.e., from 4.2 dBi in free space to 1.1 dBi when including the phantom. Note that similar behaviour occurs when the main beam is directed towards 180°.

Lastly, it is important to mention that for directions near 90° and 270°, the beamforming including phantom effects, shows minimal tilts and very small realized gain drops. This may be explained by the fact that these directions lie in the orthogonal plane (yz-plane) with respect to the phantom's length, and hence are less exposed to the phantom's effects. Therefore, experiencing high realized gain of up to 4.3 dBi. Overall, the abover results highlight that the proposed *SMB* solution still offers good unidirectional performance when operating with a multilayer forearm phantom.

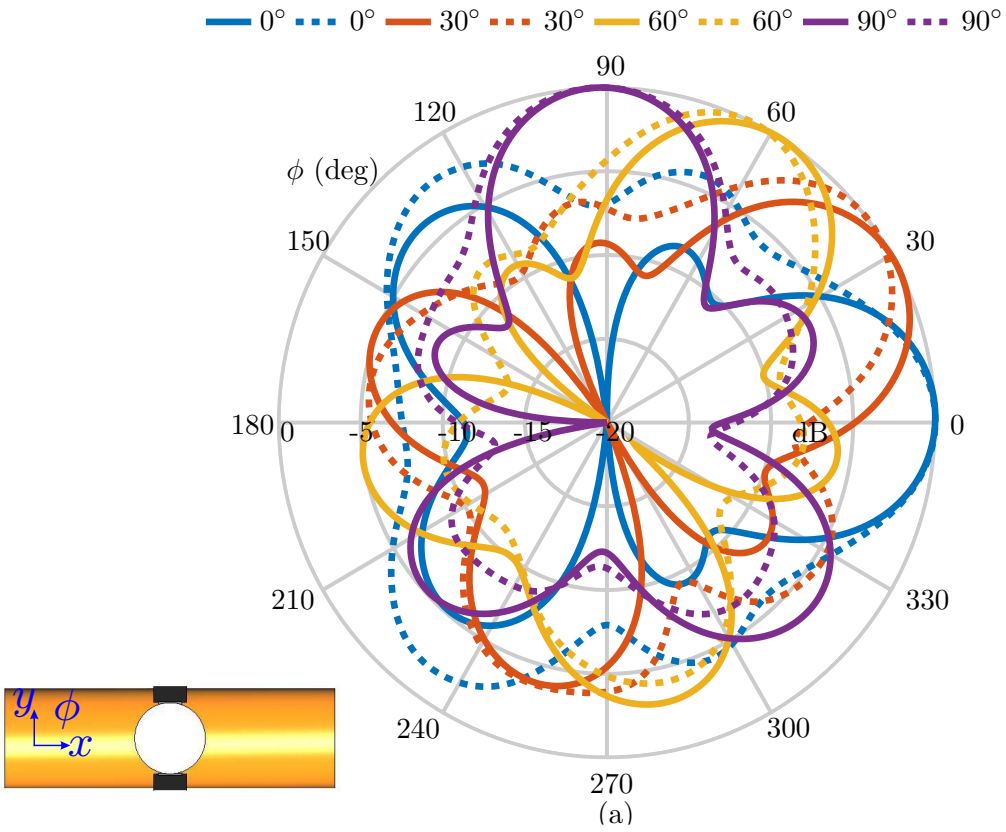

(a)

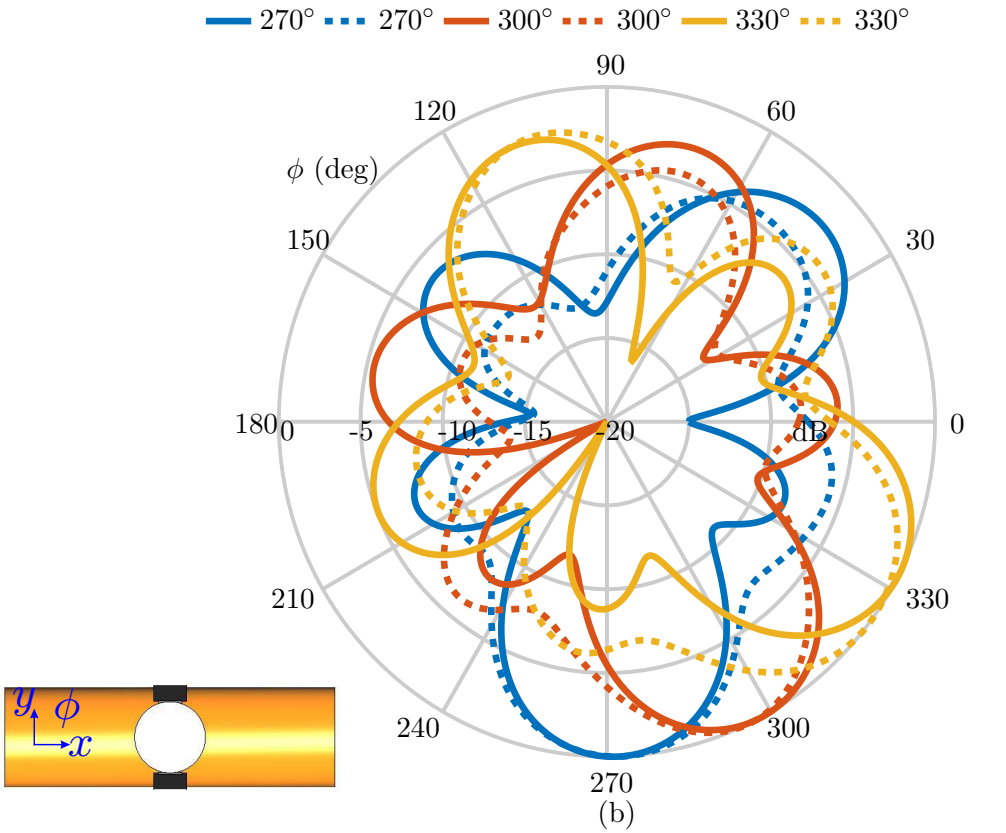

(b)

Figure 7.7: Normalized gain in free space (solid lines) and including the phantom (dashed lines). (a) 0°, 30°, 60°, and 90° directions. (b) 270°, 300°, and 330° directions.

7.4 Specific Absorption Rate

Because the antenna is proposed for on-body applications this section investigates the electromagnetic field exposure when exciting each antenna port. These analyses were done by computing the SAR using [154]

$$SAR = \frac{\sigma |E|^2}{\rho} \tag{7.1}$$

where σ and ρ respectively represent the electrical conductivity (S/m) and mass density (kg/m^3) of the evaluated tissue, and E is the root mean square magnitude of the $\vec{E}$ strength (V/m) in the same tissue. To obtain the SAR values, the validation setup for this work follows the Federal Communications Comission (FCC) guidelines under two conditions [155], namely wrist worn setup and the next-to-the-mouth setup for devices supporting voice-over communications (see Fig. 7.8). For the wrist worn case, the antenna is placed in direct contact with a block filled with human hand tissue, and the tissue averaged over 10 g. In the next-to-the-mouth setup, the antenna is placed 10 mm away from a block filled with human head tissue and the tissue is averaged over 1 g. For both investigated cases, the SAR computations were done using an input power of 100 mW for each port.

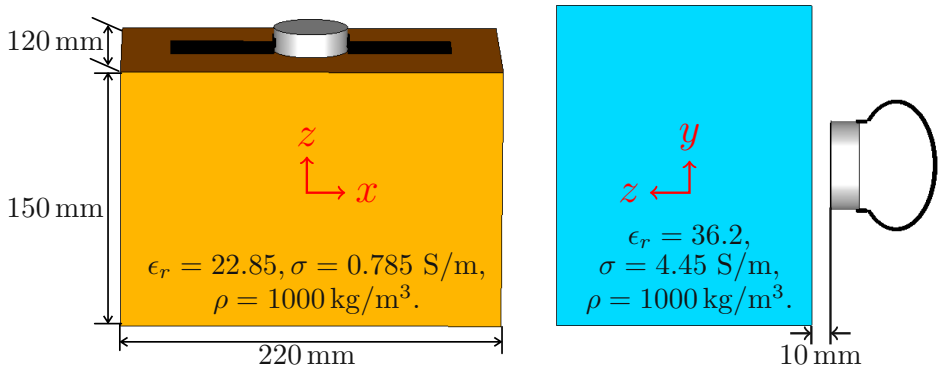

Figure 7.8: Proposed setups to evaluate the SAR performance of the *SMB* antenna. The left image shows the FCC wrist worn validation setup, while the next-to-the-mouth setup is shown on the right image. Note that the dielectric properties of the two block tissues are given for $f_0 = 4.98$ GHz.

7.4.1 Wrist-worn Setup

The wrist worn setup simulated SAR results are shown in Fig. 7.9. The performance of port 1 (exciting $\vec{K}_{1,0,1}$ omnidirirectional *spherical modes*) is shown in Fig. 7.9a and has a peak of 0.3 W/kg. The SAR values of higher order $\vec{K}_{1,\pm3,3}$ modes are shown in Fig. 7.9b and Fig. 7.9c, where port 2 has a peak of 0.49 W/kg and port 3 has a peak value of 0.4 W/kg. Fig. 7.9d and Fig. 7.9e show the SAR values for the $\vec{K}_{1,\pm2,2}$ modes, for this case port 4 has a peak SAR of 0.24 W/kg and port 5 has a peak of 0.18 W/kg. Note that the peak SAR values between the five ports is observed for the higher order modes $\vec{K}_{1,\pm3,3}$ and for the $\vec{K}_{1,0,1}$ mode, which may be explained by the higher absorption due to their close proximity to the phantom. Nevertheless, in all five cases the SAR level is well below the FCC limit of 4 W/kg.

7.4.2 Next-to-the-mouth Setup

Fig. 7.10 highlights the SAR analysis for the next-to-the-mouth validation setup. The port exciting the fundamental $\vec{K}_{1,0,1}$ mode has a peak SAR value of 0.57 W/kg. Ports 2 and 3 exciting the $\vec{K}_{1,\pm3,3}$ modes have a peak SAR below 0.33 W/kg. Ports 4 and 5 used to excite the $\vec{K}_{1,\pm2,2}$ modes both have a SAR value around 1.42 W/kg. It is important to note that the relatively high SAR values of ports 4 and 5, can be explained by the fact that these ports are used to feed the top layer's patch. Since in the next-to-the-mouth setup the antenna is positioned facing the head block tissue, as a result the top layer exciting the $\vec{K}_{1,\pm2,2}$ modes is closer to the block as compared to the other layers, therefore, resulting in higher SAR levels. Nevertheless, the peak SAR for ports 4 and 5 is still below the FCC limit of 1.6 W/kg.

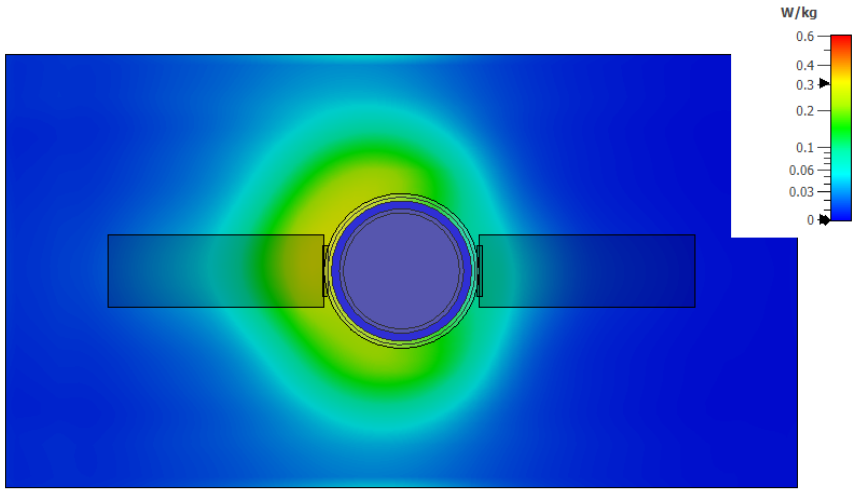

(a)

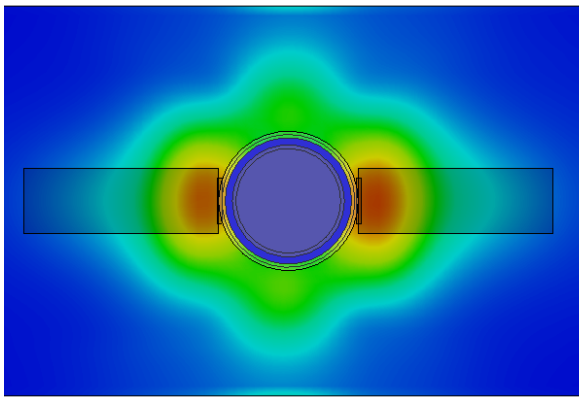

(b)

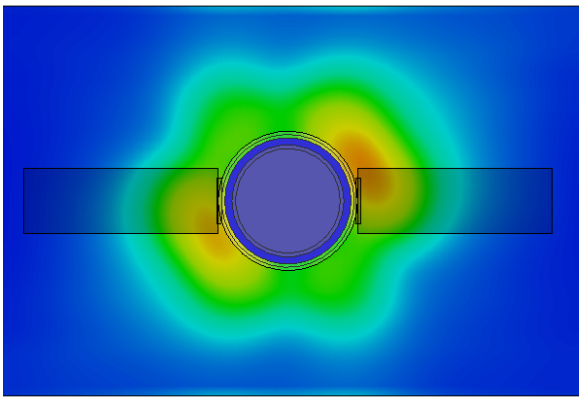

(c)

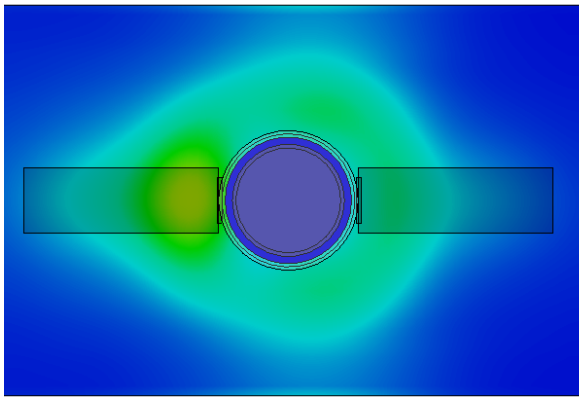

(d)

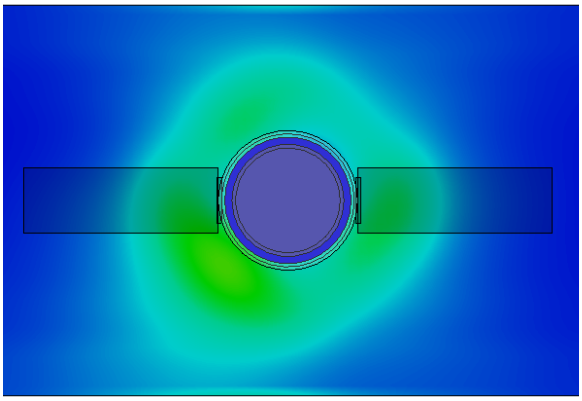

(e)

Figure 7.9: Simulated SAR results for the wrist worn setup at 4.98 GHz. (a) Port 1. (b) Port 2. (c) Port 3. (d) Port 4. (e) Port 5.

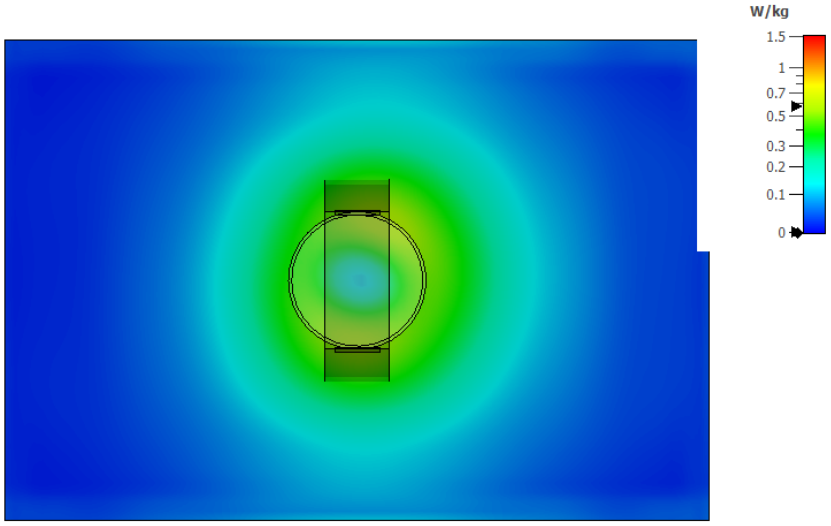

(a)

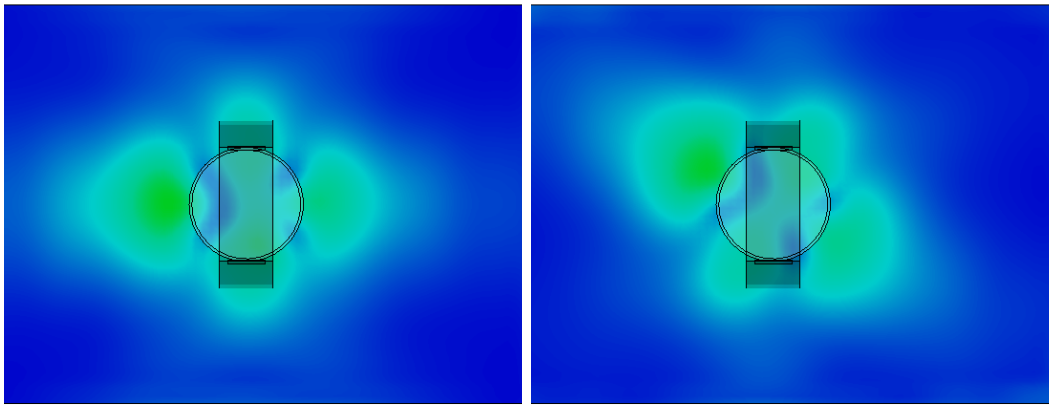

(b) (c)

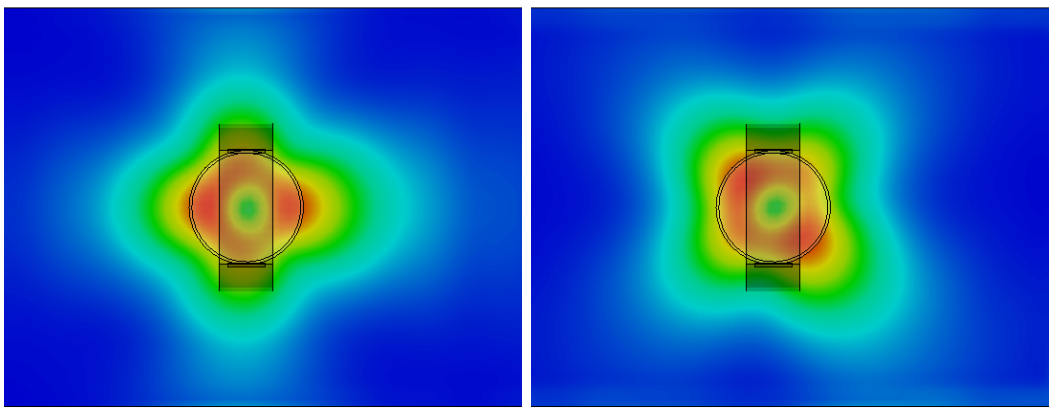

(d) (e)

Figure 7.10: Simulated SAR results for the next-to-the-mouth setup at 4.98 GHz. (a) Port 1. (b) Port 2. (c) Port 3. (d) Port 4. (e) Port 5.

7.5 On-Body Directional Modulation

To study the on-body DM performance of the proposed *SMB* antenna, narrowband transmissions are assumed, and Quadrature Phase-Shift Keying (QPSK) modulation is used. The Bit Error Rate (BER) is computed for different directions of the legitimate user across the azimuth plane using a data stream with 10^5 transmitted symbols. The required complex radiation pattern of each omnidirectional *spherical mode* is extracted from CST Studio Suite and the bit error rate calculations are conducted using MATLAB. Moreover, Signal-to-Noise Ratio (SNR) is set to 12 dB.

Fig. 7.11 highlights the BER performance in free space and including the phantom effects for width $w = 60$ mm. The results are shown for six different directions separated by 60° to cover the entire horizontal plane. In both cases the directionally modulated transmissions have comparable performance, i.e., the signals can be transmitted towards any ϕ direction across the horizontal plane without leakage into undesired eavesdroppers angles.

Fig. 7.12 shows the BER computations when the desired secure direction of the legitimate user is located at $\phi = 180°$ with the antenna operating in free space and including the forearm phantom tested with different widths. The beamwidth for BER $< 10^{-1}$ around the secure direction is within $44°(160° - 204°)$ in all the four investigated cases. It can also be observed that the beamwidth performance for the cases with phantom is slightly narrower than the free space case. This may be due to additional distortion of the radiation pattern, since the $\phi = 180°$ direction lies along the phantom's length. Also note that, while the beamwidth is narrower around the desired legitimate user direction, additional regions with BER smaller than 10^{-2} occur for the cases including the phantom. Overall, these results demonstrate that steerable secure transmissions are realized across the entire horizontal plane and the multi-layer phantom has little impact on the overall DM performance.

To further demonstrate the on-body DM performance, Fig. 7.13 and Fig. 7.14 show four exemplary QPSK constellations obtained using 12 dB when the antenna is operating in free space and when the phantom's effects of the largest investigated width ($w = 80$ mm) is used. Each transmitted data symbols is shown using different colors. Fig. 7.13a show the free space constellations for an eavesdropper located at $\phi_{\text{eve}} = 150°$, while Fig. 7.13b depicts

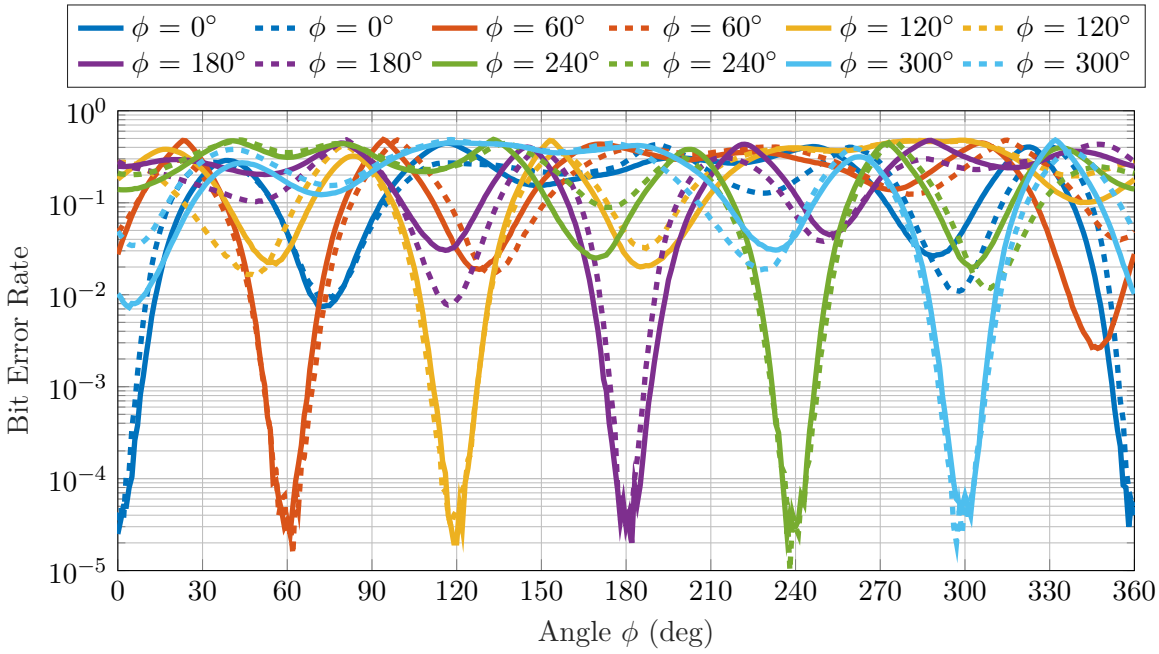

Figure 7.11: BER results for six different directions. The angles are separated by 60°, where the solid lines represent the free space results and the dashed lines indicate the phantom case.

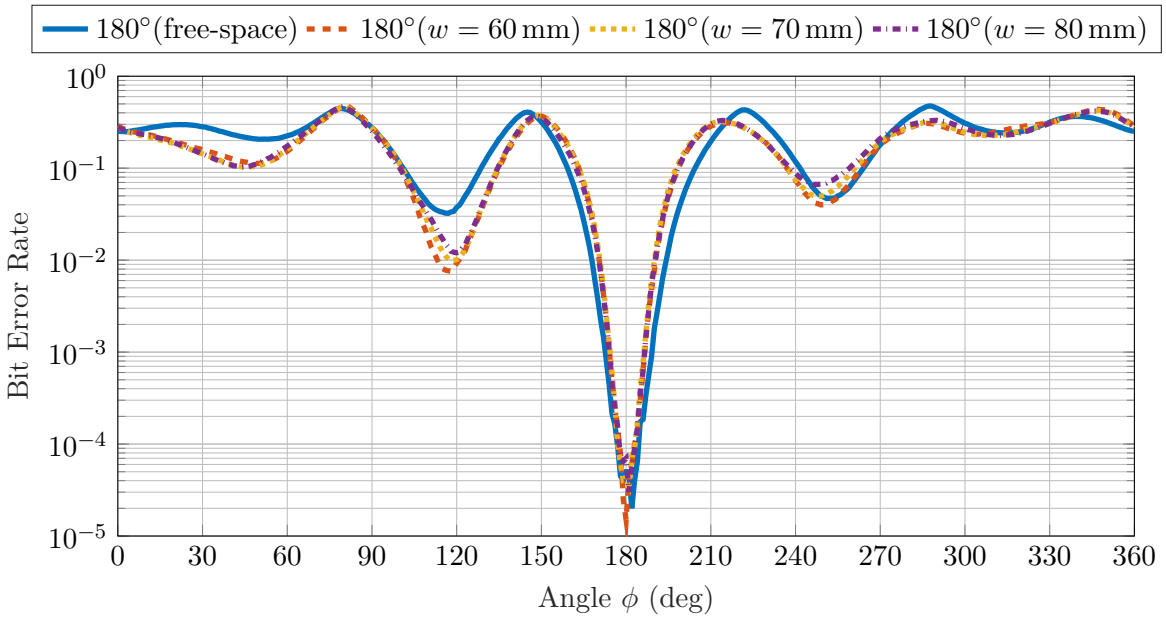

Figure 7.12: BER computations for the legitimate receiver at $\phi = 180°$ in free space and with different widths of the multilayer forearm phantom.

the free space constellations for a legitimate user located at a secure direction $\phi_{\text{secure}} = 180°$. It can be observed that for the desired location of the legitmate user, clear QPSK constellations are obtained, where each of the four clusters is only comprised by the same within cluster transmitted symbols. In contrast, for the undesired eavesdropper direction

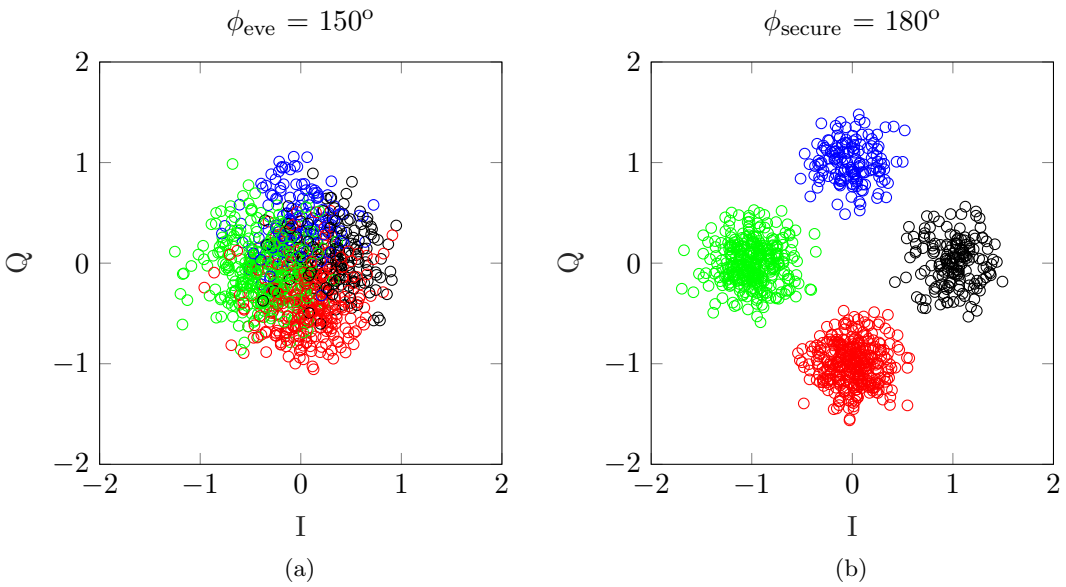

Figure 7.13: Color-coded QPSK constellations:'00' (black), '01' (red), '11' (green), '10' (blue). (a) Results for the undesired eavesdropper at $\phi_{\text{eve}} = 150°$. (b) Results for the legitimate receiver at $\phi_{\text{secure}} = 180°$.

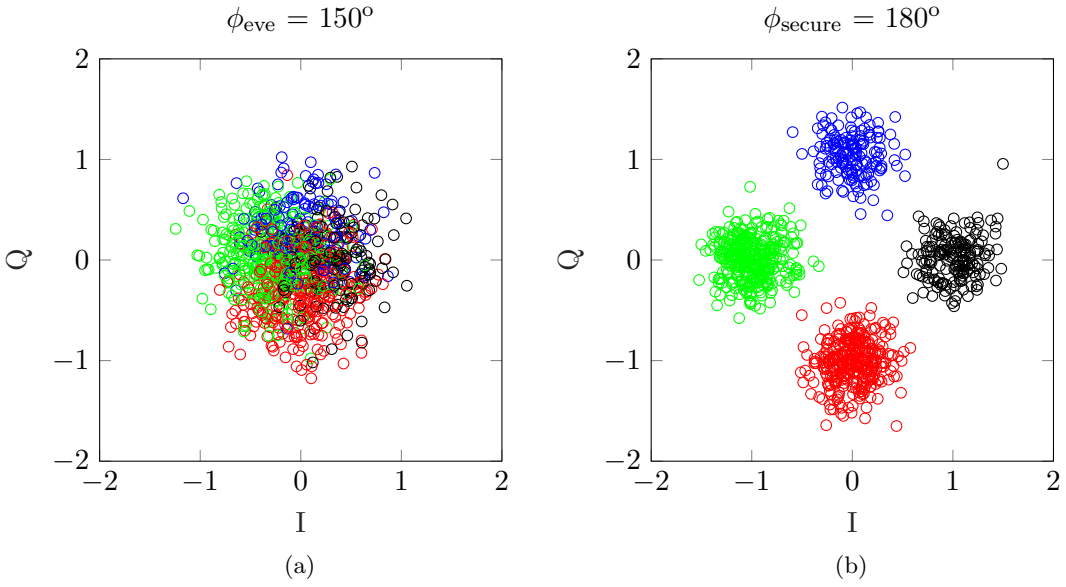

Figure 7.14: Color-coded QPSK constellations:'00' (black), '01' (red), '11' (green), '10' (blue). (a) Results for the undesired eavesdropper location at $\phi_{\text{eve}} = 150°$. (b) Results demonstrated for the secure direction $\phi_{\text{secure}} = 180°$.

($\phi_{\text{eve}} = 150°$), the symbols are scrambled making it challenging for the eavesdropper to correctly retrieve the transmitted symbolys. Fig. 7.14 shows QPSK constellations for the phantom case. It can be seen that clear clusters are still realized when the phantom effects are included. Therefore, in the directions other than that of the desired legitimate receiver,

i.e., $\phi_{\text{secure}} = 180°$, it is difficult for the eavesdropper receiver to correctly separate the transmitted symbols. This performance then highlights that the proposed *SMB* solution can enhance the secrecy and privacy of data transmission in on-body IoT devices.

7.6 On-Body AoA Estimation

To investigate the on-body AoA performance, the methodology outlined in Section 4.1.2 is used, where the Multiple Signal Classification (MUSIC) algorithm is implemented using MATLAB, and the performance is evaluated in terms of Mean Absolute Error (MAE) between the MUSIC estimated angle and the actual incident angle. The simulation setup investigated in Section 7.5 is also used for the AoA studies, i.e., the stacked-pacth antenna integrated with a multi-layer forearm phantom.

Fig. 7.15 highlights the MUSIC-based AoAperformance of the proposed *SMB* solution. The results are obtained using 10 dB SNR and 100 snapshots. The free space results are shown using solid lines, and it can be seen that the solution achieves MAE$< 0.3°$ across the entire horizontal plane. It can also be observed that the errors increase when the phantom's effects are included. To further investigate the impact of the phantom, the AoA estimation is tested using different widths (w) of the multi-layer forearm phantom. In general, it can be seen that a slight increment of the MAE is observed when the width is increased from 60 mm to 80 mm. However, in all the three investigated phantom cases, the computed errors stay below 0.45°.

The obtained AoA performance for different widths is also shown in Fig. 7.15. The MAE peaks when the phantom effects are included are relatively higher around $(35° - 65°)$, $(140° - 165°)$, $(215° - 230°)$, and $(310° - 345°)$. This can be explained by the increased beam tilts and asymmetries introduced by the phantom when the omnidirectional *spherical modes* are excited. Those are the asymmetries verified in the beamforming performance discussed in Section 7.3.

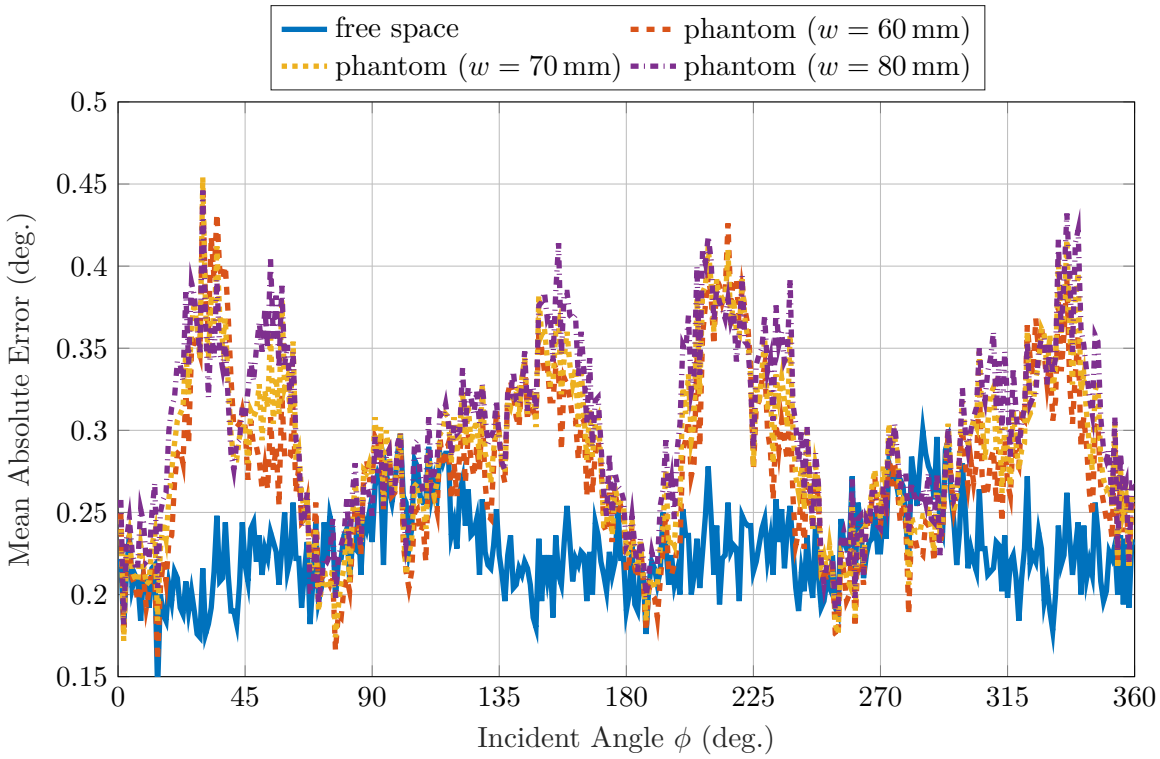

Figure 7.15: Comparisons of the AoA estimation performance using MUSIC algorithm for 10 dB SNR environment with 100 snapshots.

7.7 Summary

This Chapter discussed the performance of stacked-patch *SMB* for on-body applications. Using a three layer stacked-patch antenna good on-body beamforming performance was demonstrated across the entire horizontal plane. It was highlighted that the antenna still achieved a total efficiency better than 36.5% when tested with a multilayer phantom. Moreover, an isolation better than 13.7 dB with a 23 MHz bandwidth is still realized, while the computed specific absorption rate values are within the established limits. The on-body solution was tested with the DM technique, demonstrating comparable performance with the free space case, with unique steerable transmissions and very low BER performance below 10^{-5}. Lastly, on-body AoA estimation performance was also tested and validated through different phantom widths. Overall, good performance was demonstrated with the MAE staying below 0.45° across the entire horizontal plane.

8 Planar SMB Antennas

Planar SMB Antennas

This chapter presents the implementation of the proposed *Spherical Modes Beamforming (SMB)* principle to realize planar antenna models. The method is based on the excitation of different phase-varying omnidirectional *spherical modes* via the use of annular ring structures. At first, the principle is demonstrated for the azimuthal plane and then extended to cover the upper hemisphere. The proposed planar antenna's main advantage is its very thin profile, which allows its integration into on-body Internet of Things (IoT) devices. In this regard, on-body analyses are conducted to demonstrate the beamforming properties when the antenna operates in the vicinity of the human body. Additionally, experimental verifications are carried out to validate the performance of the proposed planar *SMB* antenna in free space and within an on-body scenario. The results emanating from this chapter were published at the 17th European Conference on Antennas and Propagation [156, 157], and the IEEE Transactions on Antennas and Propagation [158].

8.1 Azimuthal Plane SMB Antennas

8.1.1 Antenna Design

To implement the *SMB* principle using a planar design, a centrally located patch and concentric annular rings are used. The fundamental mode $\vec{K}_{1,0,1}$ is excited using a central circular patch, while the phase-varying omnidirectional modes are excited from concentric annular rings. Fig. 8.1 shows an evolution of the planar *SMB* principle, where each configuration excites $l = 1, 2, 3, \cdots L$ omnidirectional *spherical modes*. Each configuration is supported by a 1.52 mm thick RO4003C substrate ($\epsilon_r = 3.38$, $\tan\delta = 0.0027$) and operate at the center frequency $f_0 = 5.8$ GHz. The metallic layers are made of 35 μm thick copper

material ($\sigma = 5.8 \times 10^7$ S/m), and the shorting pins are also made of copper with 0.5 mm diameter.

Fig. 8.1a shows antenna A, which is a center-fed circular patch with 14 mm diameter. It is fed using P1 to excite the single fundamental omnidirectional *spherical mode* ($l = 1$). Four shorting pins, i.e., $n_{\text{pins}} = 4$ are located at $v_1 = 2.75$ mm from the center of the patch and

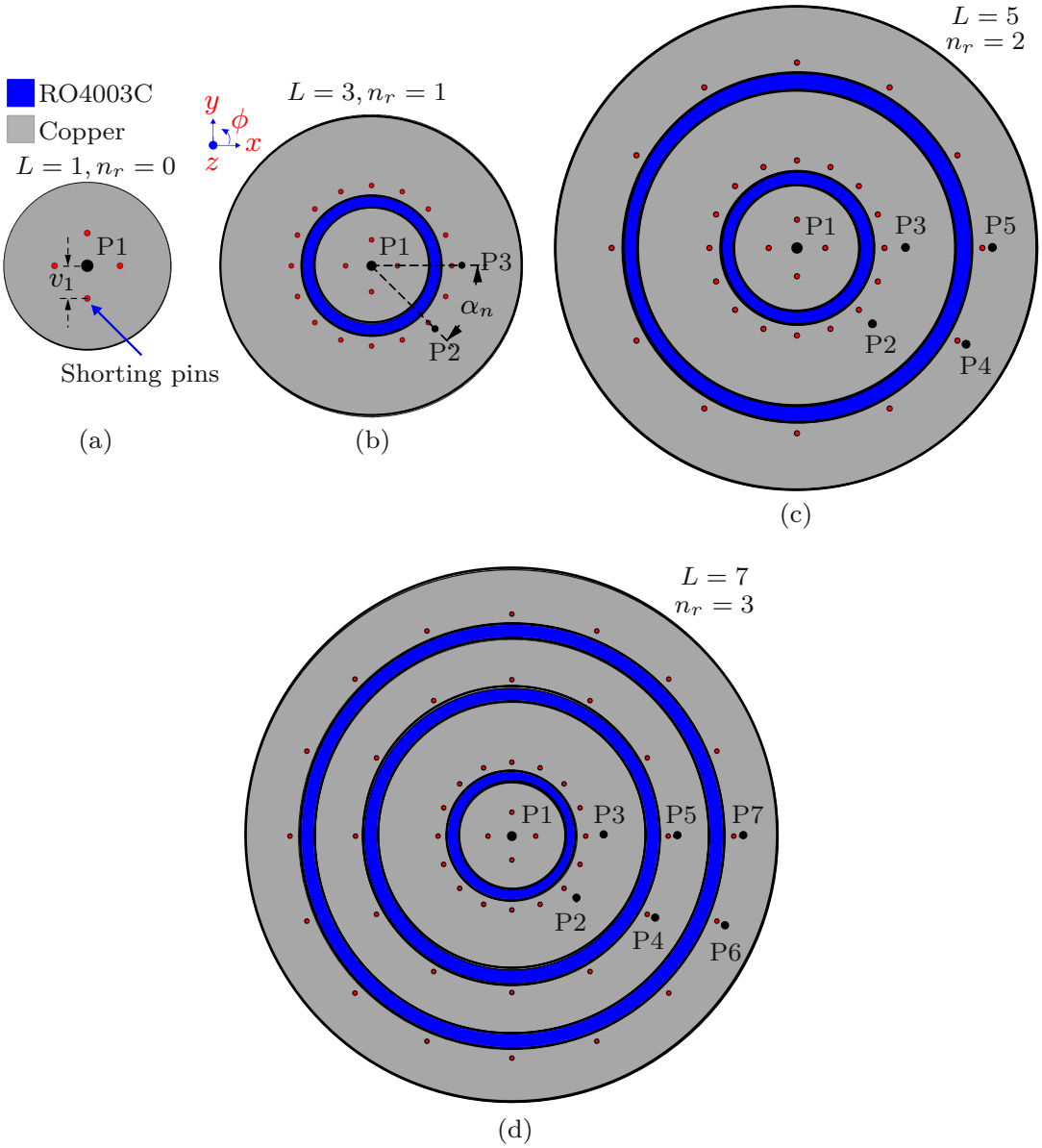

Figure 8.1: Evolution of the proposed compact and planar *spherical modes* based antennas for beamforming in the azimuthal plane. (a) Antenna A exciting the fundamental $\vec{K}_{1,0,1}$ mode. (b) Antenna B exciting the $\vec{K}_{1,\pm2,2}$ modes for bi-directional beamforming characteristics. (c) Antenna C exciting the $\vec{K}_{1,\pm3,3}$ modes for unidirectional beamforming. (d) Antenna D exciting the $\vec{K}_{1,\pm4,4}$ modes for unidirectional beamforming with enhanced directivity.

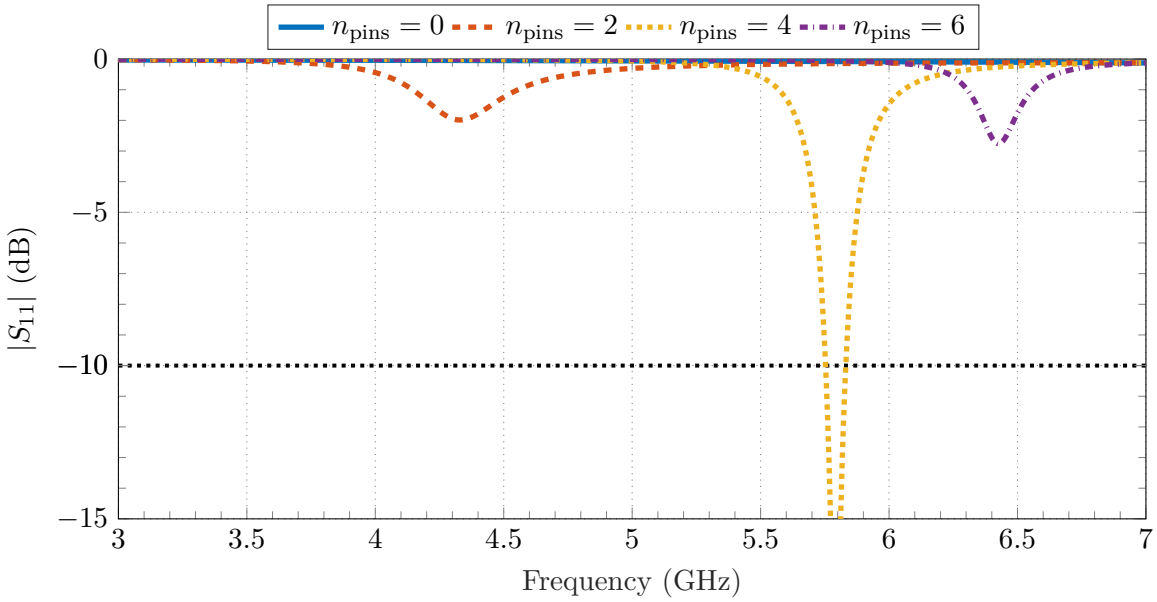

Figure 8.2: Parametric studies showing the effects of increasing the number of shorting pins in antenna A.

oriented 90° with respect to the disk center. Because without the shorting pins ($n_{\text{pins}} = 0$ case), the patch is out of resonance in the investigated frequency range, the inclusion of the shorting pins allows to have resonance at the desired center frequency. This is highlighted in Fig. 8.2, where the number of pins is increased from $n_{\text{pins}} = 0$ to $n_{\text{pins}} = 6$. It can be observed that within the investigated frequency range, the patch has non-zero resonance for $n_{\text{pins}} = 2, 4, \text{and}, 6$, along with good matching characteristics, i.e., $|S_{11}| < -15\,\text{dB}$ for the $n_{\text{pins}} = 4$ value. Additionally, due to the pins' inductance, an upward frequency shift is seen for an increased value of n_{pins}. Moreover, frequency adjustment and matching improvements can be obtained by tuning the shorting pins' distance, i.e., the v_1 value. These effects are shown in Fig. 8.3, where v_1 is increased from 2.5 mm to 3.25 mm. The frequency increases with v_1, and at for $v_1 = 2.75\,\text{mm}$ case, good matching characteristics are observed at $f_0 = 5.8\,\text{GHz}$.

Fig. 8.1b shows antenna B. In addition to the configuration of antenna A, a shorted pin annular ring structure is integrated to generate two additional omnidirectional *spherical modes*, these are the dual-phase varying *spherical modes* $\vec{K}_{1,\pm 2,2}$ excited using P2 and P3. Antenna B then includes a total of $n_r = 1$ ring, with an inner diameter of 15 mm and an outer diameter of 32 mm. The annular ring is fed using two ports, located 2 mm from the edges of the inner diameter of the ring and are rotated by $\alpha_2 = \pi/4$. The angular

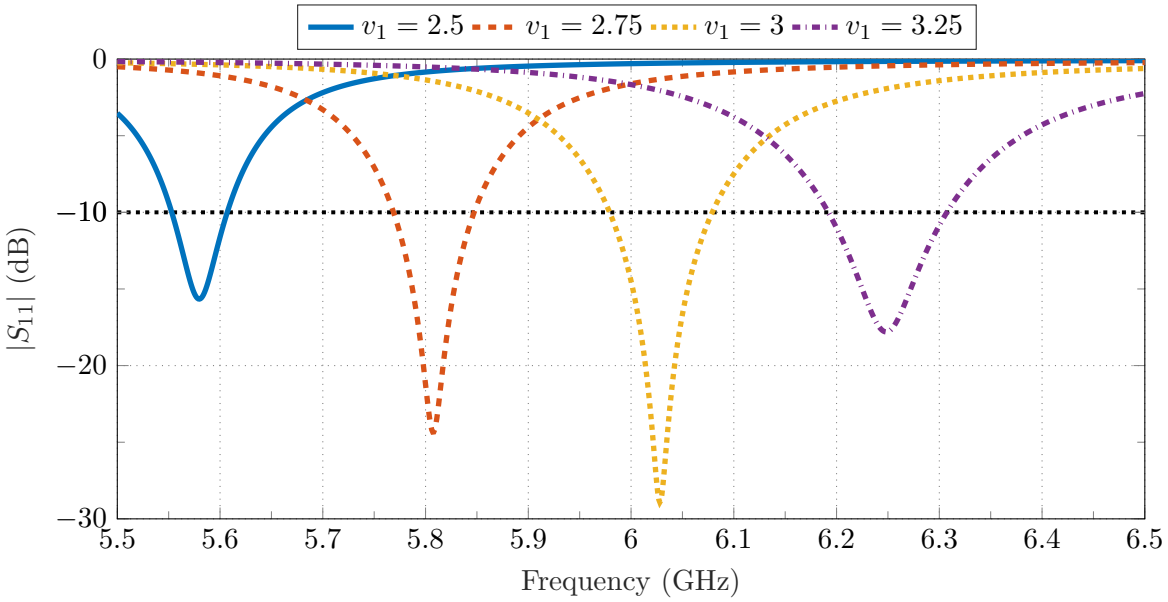

Figure 8.3: Parametric studies showing the effects of increasing v_1 value in antenna A.

arrangement of the ports to excite the corresponding omnidirectional *spherical mode*, is computed using

$$\alpha_n = \begin{cases} \frac{\pi}{2}(\frac{1}{n} + q), & n = 2, 4, 6, \cdots ;\ q = 0, 1, 2, 3, \cdots \\ \frac{\pi}{6}(\frac{3}{n} + 2q), & n = 3, 5, 7, \cdots ;\ q = 0, 1, 2, 3, \cdots \end{cases} \tag{8.1}$$

where n is the order of the excited omnidirectional *spherical mode*, and q is used to generate a complete set of values α_n that will also satisfy the angular port arrangement required for the excitation of the corresponding omnidirectional *spherical mode* of order n.

The ring also includes shorting pins, which are used to produce frequency tuning and isolation improvements. The total number of pins need to take into account the ports' position, as it is necessary to ensure symmetry between the two excited modes of the same order. For this thesis, the total number of pins in a given annular ring is calculated using

$$n_{\text{pins}} = \frac{2\pi}{\alpha_n} p \tag{8.2}$$

where $p = 1, 2, 3, \cdots$ is an integer that controls the total number of pins, and is optimized to ensure the desired center frequency, reflection and transmission coefficients $\leq -10\,\text{dB}$. Because of the pins' inductance, an increase in the center frequency will be observed for

larger values of p. For antenna B, $p = 2$ is used, and the total number of pins in the structure is $n_{\text{pins}} = 16$. The pins of this configuration are located 1 mm from the edges of the inner diameter of the ring and are rotated with respect to the center by $\alpha_{\text{pins}} = \pi/8$ obtained using

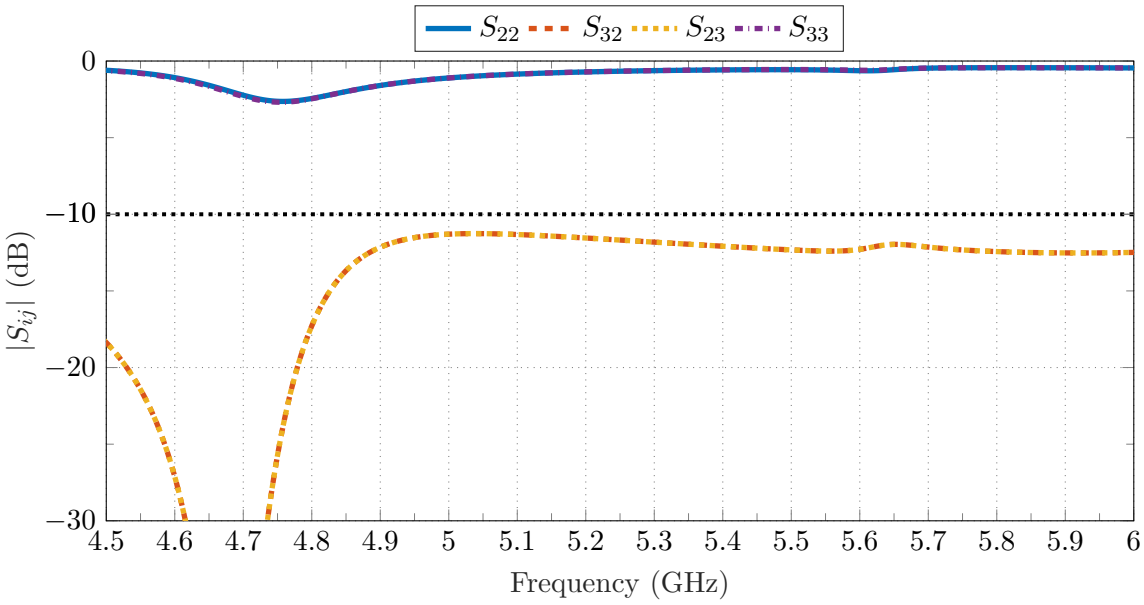

(a)

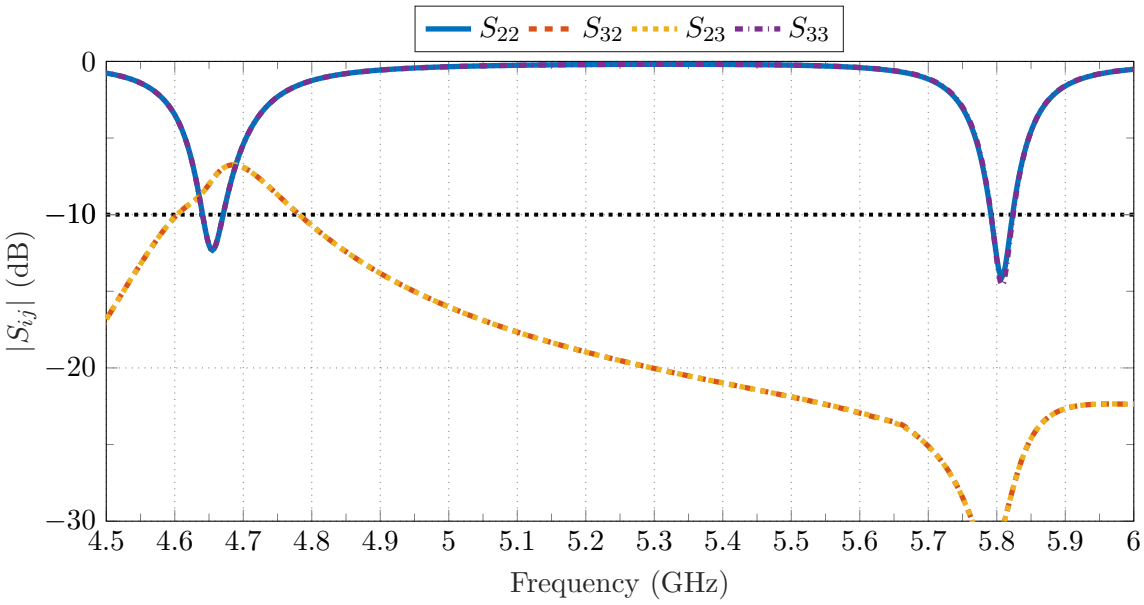

(b)

Figure 8.4: S-parameters of antenna B, port index $i, j = 2, 3$. (a) S-parameters of the annular ring without shorting pins. (b) S-parameters of the annular ring with shorting pins.

$$\alpha_{\text{pins}} = \frac{\alpha_n}{p} \tag{8.3}$$

Fig. 8.4 shows the effect of adding shorting pins into the ring structures, demonstrated for antenna B. Fig. 8.4a shows the case without any shorting pins, where it can be seen that while good isolation is obtained, the reflection coefficient of the two ports stays above $-2.5\,\text{dB}$. In contrast, when a total of 16 pins are added into the ring (see Fig. 8.4b), good isolation is obtained with an improvement on the matching (i.e., reflection coefficient $< -14\,\text{dB}$), while due to the pins' inductance, the center frequency shifts upwards towards the desired $f_0 = 5.8\,\text{GHz}$.

Fig. 8.1c shows antenna C, where a second annular ring is added to antenna B, i.e. the total number of rings in the configuration is $n_r = 2$. The ring has an inner diameter of 34 mm and outer one of 46.8 mm. It excites two omnidirectional *spherical modes* with their phase changing three times across the horizontal plane, i.e., $\vec{K}_{1,+3,3}$ and $\vec{K}_{1,-3,3}$ modes. The feed ports P4 and P5 are located 1.75 mm from the ring's inner diameter and are rotated by $\pi/6$ obtained from (8.1) is used. For this ring $n_{\text{pins}} = 12$ obtained from (8.2). The shorting pins are located 1 mm from the edge of the inner diameter and are rotated by $\pi/6$.

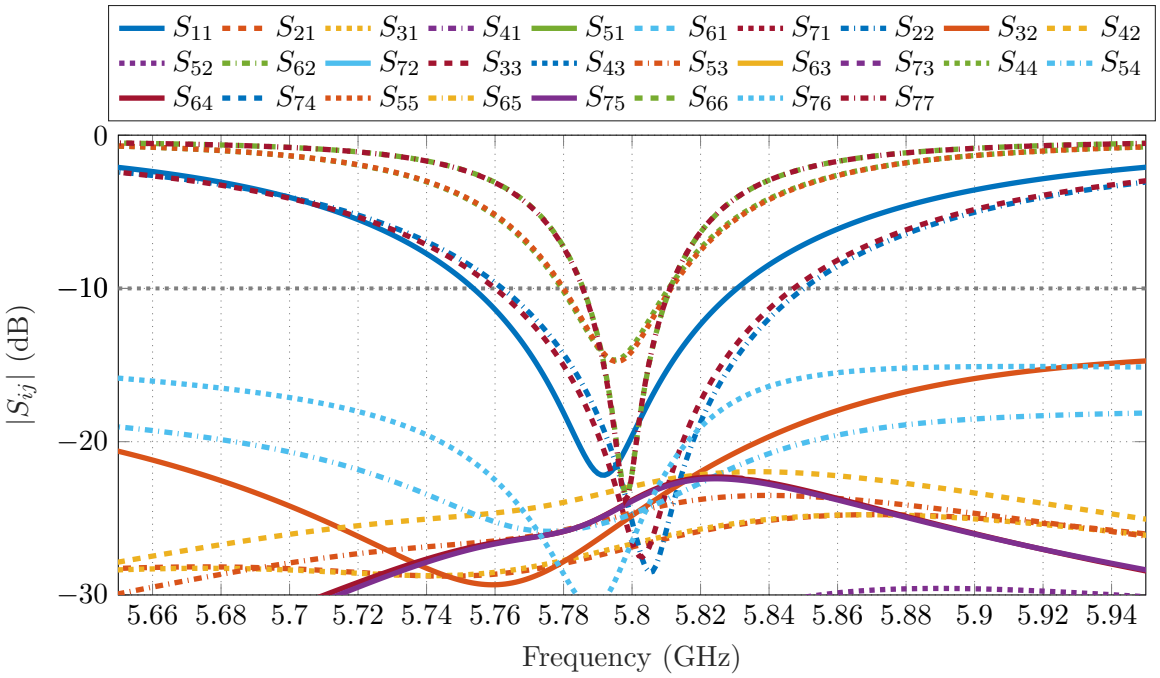

Figure 8.5: Simulated S-parameters of antenna B, port index $i, j = 1, 2, 3, 4, 5, 6, \text{and}, 7$.

Fig. 8.1d depicts antenna D. It is based on antenna C with the addition of a third annular ring, i.e., a total of $n_r = 3$ rings are included in the design. This ring generates the $\vec{K}_{1,\pm4,4}$ omnidirectional *spherical modes*, with their phases changing four-times across the azimuthal plane. It's outer diameter is 61.3 mm and is fed using P6 and P7. The ports are located 1.8 mm from the inner diameter, which has a value of 49.1 mm. The angular arrangement of the ports is $\alpha_3 = \pi/8$ and $n_{\text{pins}} = 16$. The pins are placed 1 mm from the inner diameter and rotated by $\alpha_{\text{pins}} = \pi/8$. The S-parameters of the antenna D are shown in Fig. 8.5, where it can be seen that the center frequency is at $f_0 = 5.8$ GHz, with isolation better than 23 dB.

8.1.2 Beamforming Performance

The beamforming performance is demonstrated by steering the antenna main beam towards $\phi_d = 90°$. The two ports located in the same ring are fed in-quadrature, and Fig. 8.6 shows the phase characteristics of the final design, i.e., antenna D. The desired phase properties of each mode are achieved: with P1 generating the fundamental $\vec{K}_{1,0,1}$ mode, to produce a constant phase across the entire azimuthal plane, P2 and P3 exciting the $\vec{K}_{1,\pm2,2}$ modes for dual-phase variations in two opposing directions, P4 and P5 generating the $\vec{K}_{1,\pm3,3}$ modes

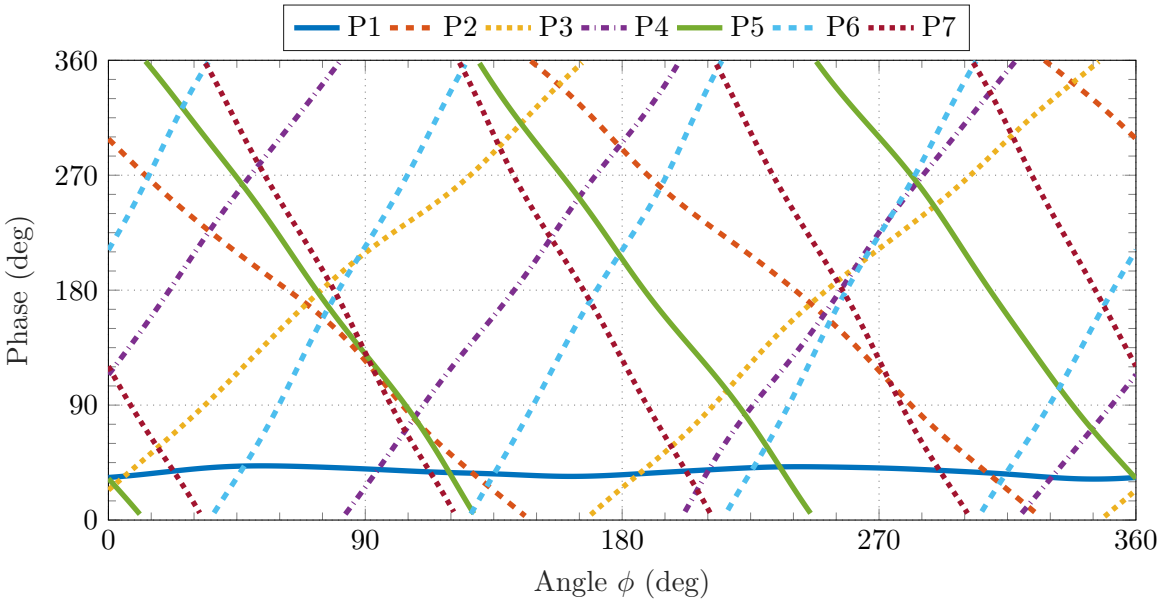

Figure 8.6: Phase of the radiation patterns for the modes excited in antennas A, B, C, and D. The phases are shown for antenna D as it excites the highest number of modes.

Table 8.1: Fig. 8.1 Antenna Excitation for $\phi_d = 90°$ direction.

l	Antenna	$\Delta\psi_n(°)$						
		P1	P2	P3	P4	P5	P6	P7
1	A	0	-	-	-	-	-	-
3	B	0	189	275	-	-	-	-
5	C	0	277	198	278	16	-	-
7	D	0	275	191	14	270	186	269

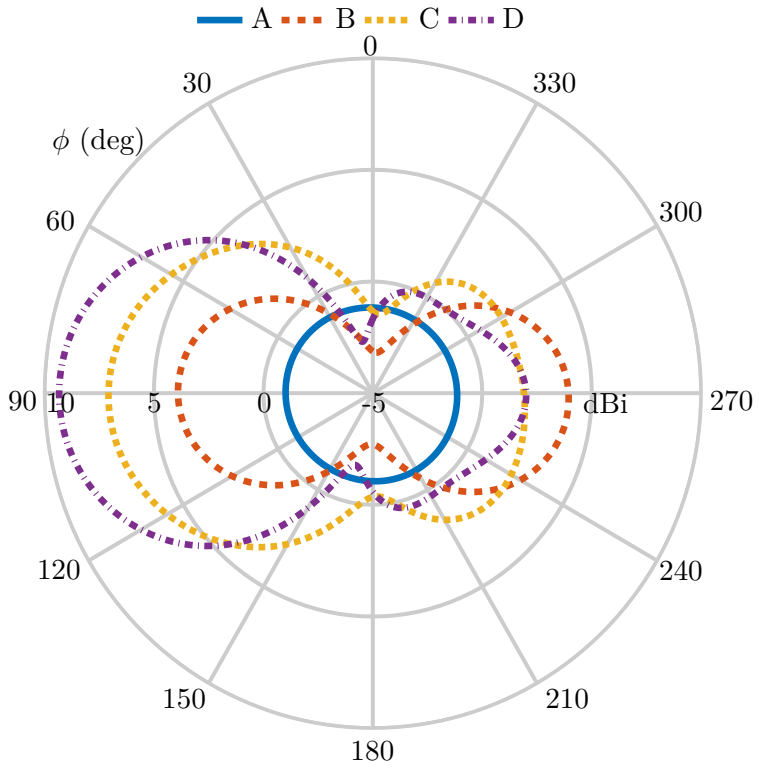

Figure 8.7: Beamforming performance of the azimuthal plane *SMB* antennas, for $\phi_d = 90°$.

with triple-phase variations in two opposing directions, and P6 and P7 exciting the $\vec{K}_{1,\pm4,4}$ modes for quad-phase variations also in two opposing directions. The required phase shifts in each port to steer the beam towards $\phi_d = 90°$ are shown in Table 8.1 and are computed using the principle described in Section 3.3, i.e., no phase shift is added to P1 (which excites the fundamental mode) and the phase shifts of the remaining ports are obtained by subtracting the phase value of the respective radiation pattern at $\phi_d = 90°$ and the phase of reference radiation pattern at the same $\phi_d = 90°$.

Table 8.2: Beaforming Comparisons Between Structures Shown in Fig. 8.1.

l	Antenna	Size (λ^3)	$-\lvert S_{ij}\rvert$ $i \neq j$(dB)	Tot. Eff.	IBW (MHz)	D_{max} (dBi)	HPBW (°)	SLL (dB)
1	A	$0.27^2 \times 0.038$	-	87%	81	-1	-	-
3	B	$0.62^2 \times 0.037$	31.2	73%	34	3.95	88.7	-
5	C	$0.9^2 \times 0.036$	23.2	55.8%	32	7.08	95.4	-4.8
7	D	$1.18^2 \times 0.036$	23	44.6%	27	9.33	71.3	-7.3

The generated patterns from each configuration are vertically polarized and are shown in Fig. 8.7, and the beam characteristics are detailed in Table 8.2. The results show that by increasing the number of excited modes in the planar configuration, a desired level of directivity can be realized. For instance, in the analyzed setups depicted in Fig. 8.1, it can be seen that a directivity ≥ 7 dBi is obtained by exciting a minimum of $l = 5$ modes, specifically through the use of antenna C. In relation to the beamforming characteristics, antenna B enables the first type of beamforming around the azimuthal plane, via the excitation of the fundamental and dual-phase varying modes. This pattern is similar to the one obtained in the previous chapters (i.e., using stacked-patch designs) and is a bi-directional radiation pattern, where a second main beam is always located at $\phi_d + 180°$, as shown in Fig. 8.7. Furthermore, it can be observed that to generate a unidirectional pattern in the azimuthal plane, at least $l = 5$ modes need to be excited, i.e., $\vec{K}_{1,0,1}, \vec{K}_{1,\pm2,2}$, and$\vec{K}_{1,\pm3,3}$ modes.

From Table 8.2 results, it can be seen that as a large number of *spherical modes* are excited, the bandwidth and the total efficiency will decrease, i.e., antenna C and D have the lowest bandwidth and total efficiency. This characteristics may be explained by the increased phase-variations of these higher-order *spherical modes*. This is because the modes need a much larger diameter to support the required phase changes around their perimeters. Lastly, while antenna D requires the largest dimension it allows to generate the most selective radiation pattern, with the lowest Half-Power BeamWidth (HPBW), highest directivity values, and lowest Side Lobe Level (SLL).

8.2 3D Beamforming Planar Antenna

To realize beamforming across the azimuthal and elevation planes, the following steps are used:

1. Selection of the desired beamforming characteristics in the azimuthal plane, i.e., bi-directional or unidirectional radiation pattern.
2. Excitation of the omnidirectional *sperical modes* necessary to obtain the radiation pattern selected in step one. This step is done following the principle presented in Section 8.1.
3. Addition of an annular ring for the excitation of two orthogonal broadside modes.

To implement the above steps this section uses the combination of the fundamental and dual-phase varying modes, since they are the first modes capable of producing beamforming in the azimuth plane. Because the omnidirectional *spherical modes* cannot control the beam outside of the azimuth plane. Therefore, the last step excites modes that have a main beam along the z-axis, with two modes corresponding to two orthogonal polarization covering four principal directions, i.e., $+x$, $+y$, $-x$, $-y$. Any intermediate direction can be covered by a superposition of those. Since a single broadside mode will allow the structure to cover $\theta = 0°$ without any phase and amplitude control. The beam can be steered towards other θ directions, e.g., within xz- and yz-planes, by combining the broadsisde mode with the omnidirectional phase-varying $\vec{K}_{1,\pm n,n}$ modes.

Fig. 8.8 shows the proposed Three-Dimensional (3D) beamforming antenna. It has a thickness $h = 1.59\,\text{mm}$, and it uses RO4003C substrate. For beamforming in the azimuthal plane, the antenna generates $\vec{K}_{1,0,1}$ mode (utilizing the center-fed circular patch), $\vec{K}_{1,2,2}$, and $\vec{K}_{1,-2,2}$ omnidirectional *spherical modes* (using the outer-most ring fed via P4 and P5). Two broadside modes are excited using ring 1, fed using P2 and P3 with the two ports orientated by 90° with respect to each other. Ring 1 includes 8 shorting pins located $v_2 = 1\,\text{mm}$ from the inner diameter and rotated by 45° with respect to the center. Note that this function and the generated patterns are different from the antenna B, here ring 1 is used to excite the broadside modes as they use a smaller diameter than the other modes. Therefore, the outer-most ring, i.e., ring 2 is used to excite the $\vec{K}_{1,\pm 2,2}$ modes. The final antenna

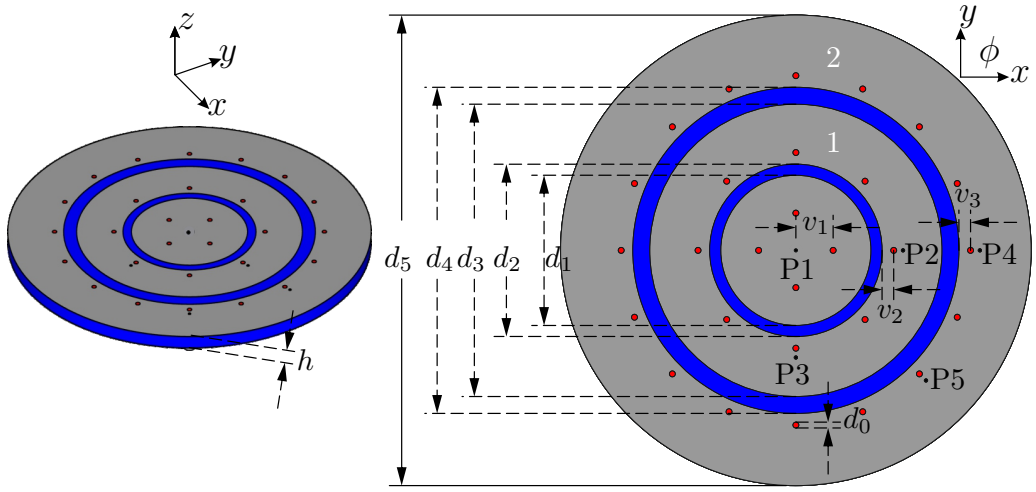

Figure 8.8: Proposed antenna: (left) perspective view, and (right) top view. Dimensions (all in mm): $d_0 = 0.5, d_1 = 12.9, d_2 = 14.8, d_3 = 25.1, d_4 = 28, d_5 = 40.4, v_1 = 3.2, v_2 = 1, v_3 = 1$; P2, P3, P4 and P5 feeding points are located 1.8 mm from the respective ring inner diameter.

dimensions are 40.4 mm × 40.4 mm × 1.59 mm, or correspondingly $0.77\lambda \times 0.77\lambda \times 0.03\lambda$ for $f_0 = 5.75$ GHz.

8.2.1 Free Space Performance

Fig. 8.9 shows the fabricated antenna, the top view is shown in Fig. 8.9a and the bottom views are depicted in Fig. 8.9b. The antenna feeding system consist of a 50 Ω semi-rigid coaxial cable, specifically the Taoglas CAB.058 cable [159]. The inner conductor of the cable has a diameter of 0.287 mm, while the outer conductor diameter is 1.193 mm.

Fig. 8.10 shows the simulated total efficiency for each port of the proposed antenna. At f_0, the total efficiency is 88%, 82.5%, 82.7%, 73%, and 73%, for P1, P2, P3, P4, and P5, respectively. The lowest efficiency is seen for the dual-phase varying modes, i.e. the $\vec{K}_{1,\pm 2,2}$ modes generated using P4 and P5. The simulated S-parameters and the counterpart measured results are shown in Fig. 8.11, where the reflection coefficient results are depicted in Fig. 8.11a, and the transmission coefficient values are given in Fig. 8.11b. The f_0 in both cases is at 5.75 GHz, where an isolation > 24 dB and a 42.2 MHz Impedance BandWidth (IBW) are obtained in the simulated case. These values decrease to 16 dB and 31 MHz for the measured case. The observed discrepancies may be due to manufacturing tolerances. Note that the antenna IBW and the total efficiency are limited by the dual-phase varying

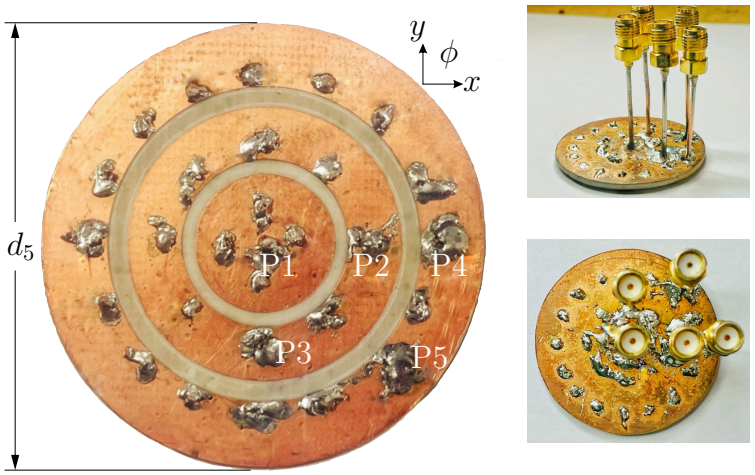

(a) (b)

Figure 8.9: Image of the manufactured planar beamforming antenna. (a) Top view. (b) Bottom views highlighting the feeding system.

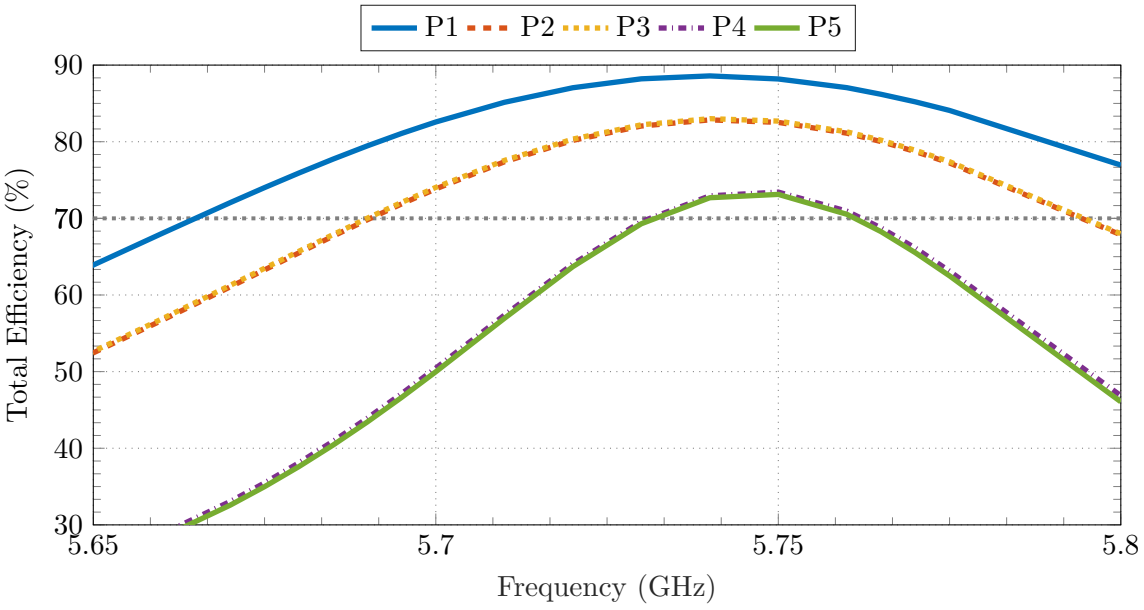

Figure 8.10: Simulated total efficiency of each port of the proposed antenna.

modes. These characteristics agree well with the performance highlighted in Section 8.1, where the IBW and total efficiency are limited by the higher order *spherical modes*.

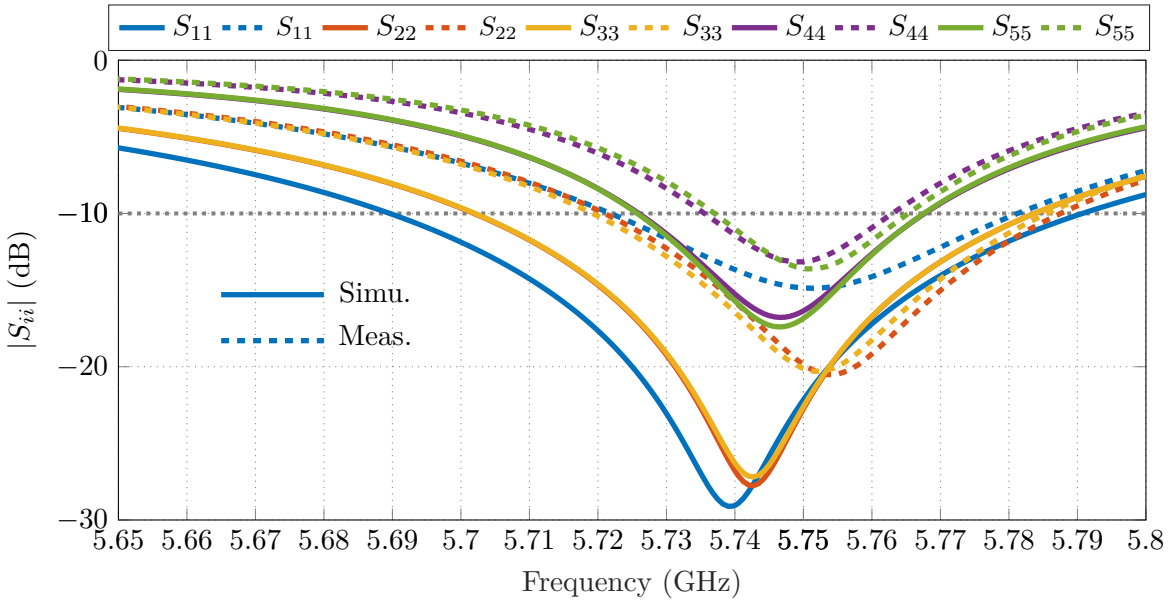

(a)

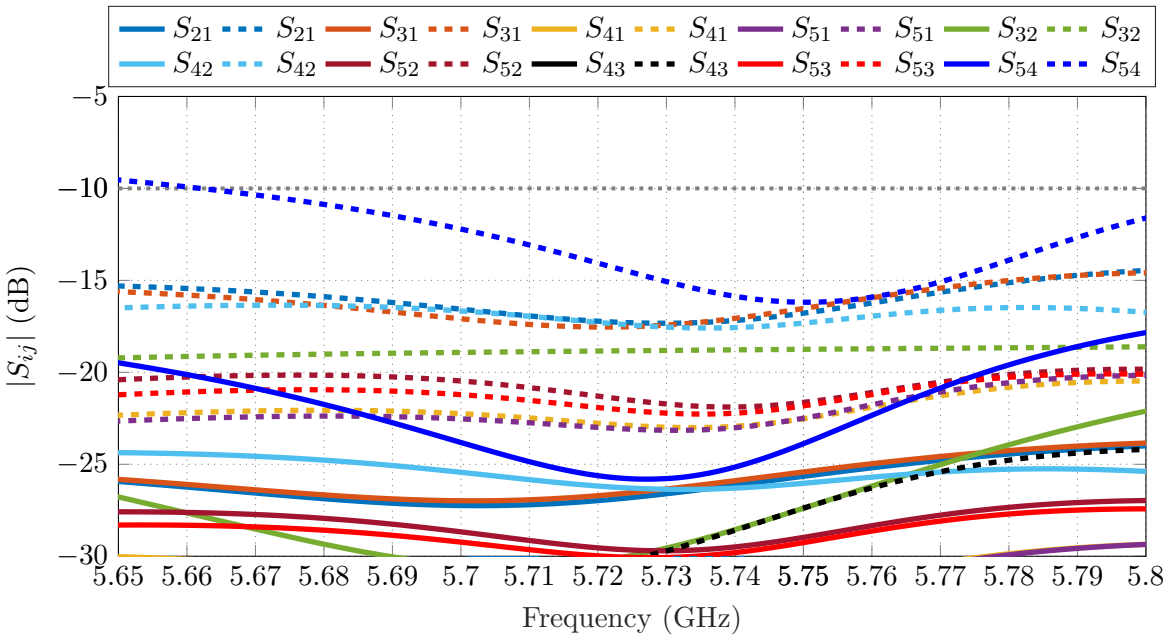

(b)

Figure 8.11: S-parameters results, solid lines indicate simulated values, while the dashed lines denote the measured ones, port index $i, j = 1, 2, 3, 4,$ and, 5. (a) Reflection coefficient $|S_{ii}|$. (b) Transmission coefficient $|S_{ij}|$ for $i \neq j$.

8.2.2 Free Space Beamforming Performance

Azimuthal Plane Beamforming

Fig. 8.12 shows the simulated and measured normalized radiation patterns of the ports used to generate the omnidirectional *spherical modes*. Good agreement is demonstrated and the required omnidirectional patterns are obtained. The simulated peak realized gain at 5.75 GHz is 2.1, 4.3 and 4.3 dBi for P1, P4 and P5, respectivelly. The measured values slightly decrease to 1.9, 3.5, and 3.4 dBi for P1, P4 and P5, respectively. It can be seen that the realized gain slightly deteriorates in the measured cases (especially for the ports exciting the dual-phase varying modes), where a discrepancy of up to 0.87 dBi is observed. The occurence of such variations maybe due to the substrate material tolerance and other manufacturing inaccuracies.

The phases of the radiation patterns are shown in Fig. 8.13 for the simulated and

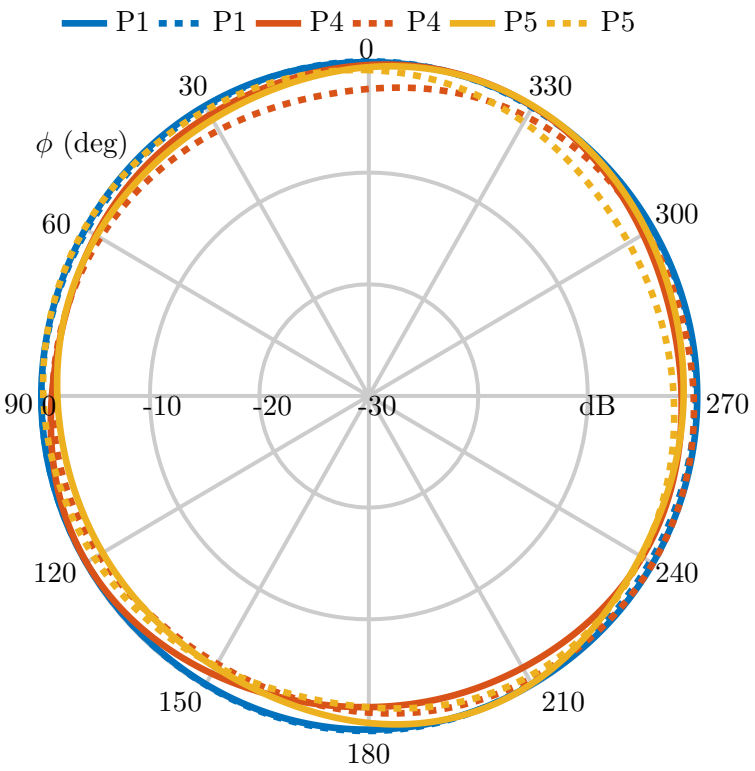

Figure 8.12: Normalized radiation patterns of the excited omnidirectional *spherical modes* (xy-plane), solid lines represent simulations, and dashed lines denote the measurements.

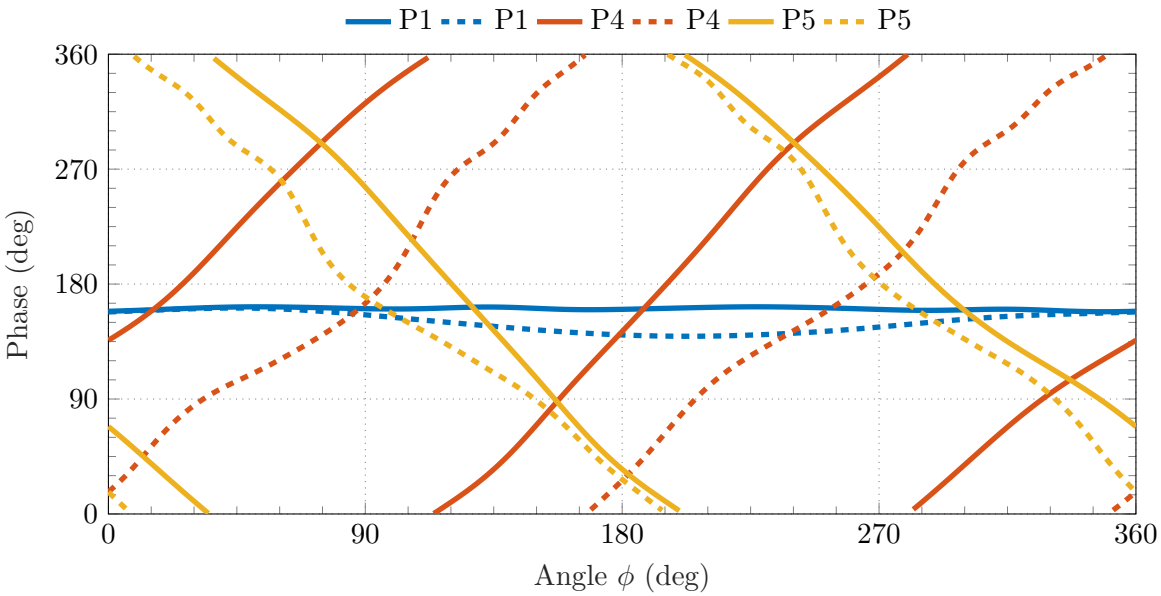

Figure 8.13: Free space phase of the radiation pattern for the omnidirectional *spherical modes*, where solid lines indicate the simulated resullts and dashed lines represent the measured values.

measured cases in the azimuth plane. In both cases, the patterns have the desired dual-phase variations, with the phase changing in two opposing directions for the $\vec{K}_{1,\pm 2,2}$ modes (P4 and P5), while P1 has a constant phase (as it is used to generate the fundamental $\vec{K}_{1,0,1}$ mode). The small discrepancies seen in the measured case may be the results of the manufacturing tolerances.

The antenna main beam was directed to four distinct directions spaced apart by 90°, to cover the entire azimuthal plane. Fig. 8.14 illustrates the achieved beamforming performance. In Fig. 8.14a, the beamforming for directions 0°/180° and 90°/270° is depicted, while Fig. 8.14b shows the beamforming for directions 45°/225° and 135°/315°. The required phase shifts to steer the antenna main beam towards the desired directions are computed based on the phase values shown in Fig. 8.13 and using (3.29). The computed phase shifts for the measured beamforming results are outlined in Table 8.3. A good agreement is realized between the measured and simulated cases, with the generated main beams covering the desired directions. The few discrepancies seen in the measured cases (beamwidth, shouldering, and dips) may be the resuls of the small phase dips in the measured values and other manufacturing tolerances.

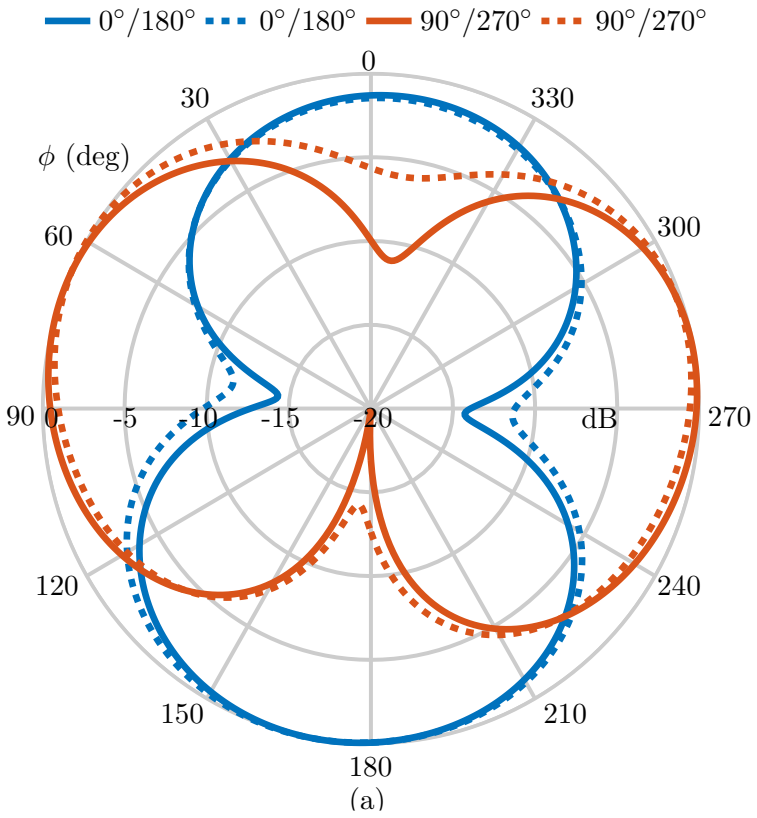

(a)

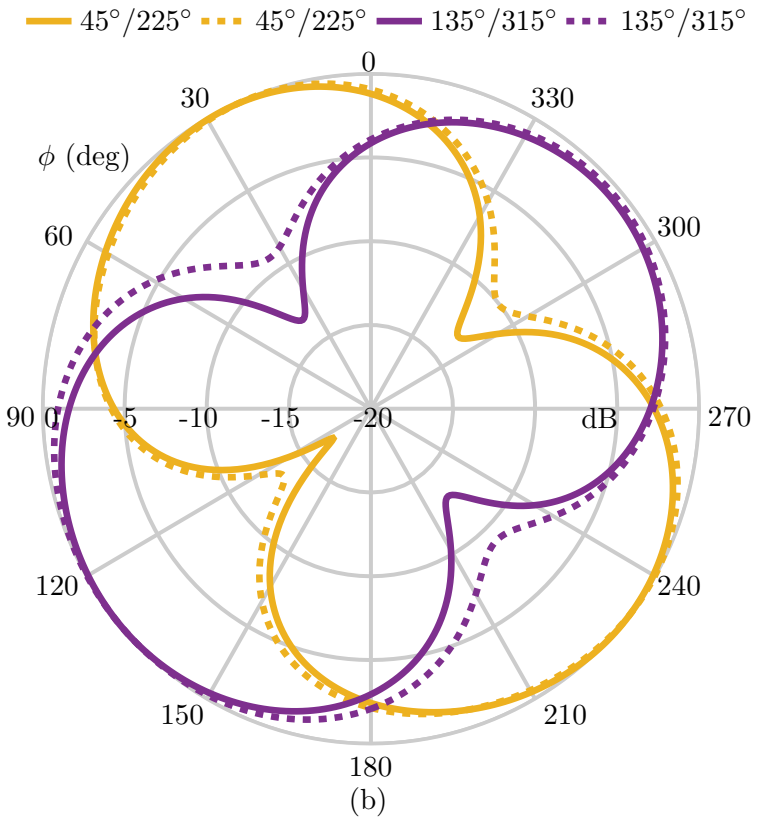

(b)

Figure 8.14: Normalized radiation patterns showing xy-plane beamforming, solid lines (simulations) and dashed lines (measurements). (a) 0°/180° and 90°/270°. (b) 45°/225° and 135°/315°.

Table 8.3: Excitations for Azimuth Plane Free Space Beamforming

Beam direction	$\lvert A_1\rvert$	$\Delta\psi_1$	$\lvert A_4\rvert$	$\Delta\psi_4$	$\lvert A_5\rvert$	$\Delta\psi_5$
$\phi = 0°/180°$	1	0°	1	135°	1	135°
$\phi = 45°/225°$	1	0°	1	45°	1	243°
$\phi = 90°/270°$	1	0°	1	359°	1	358°
$\phi = 135°/335°$	1	0°	1	219°	1	39°

Elevation Plane Beamforming

The radiation patterns of the broadside modes are depicted in Fig. 8.15 for both simulated and measured scenarios. The patterns exhibit their main beam directed towards $\theta = 0°$. At $f_0 = 5.75\,\text{GHz}$, the simulated peak realized gain is 8.58 dBi for P2 and 8.61 dBi for P3, while in measurements, these values decrease to 7.21 dBi for P2 and 7.15 dBi for P3. Such discrepancies in the realized gain and beamwidth may be the result of manufacturing tolerances and the influence of the antenna holder during measurements.

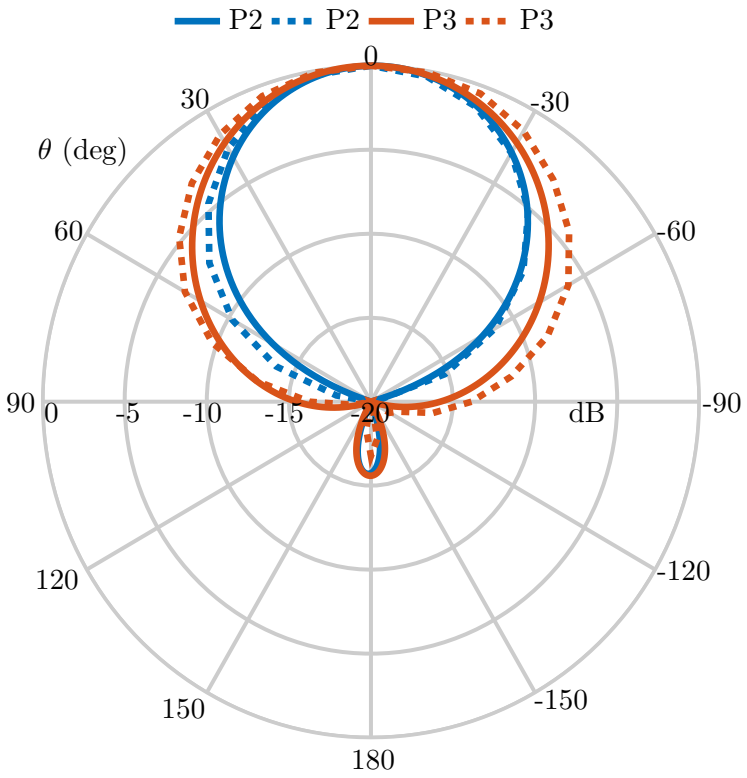

Figure 8.15: Normalized radiation patterns of the antenna excited broadside radiating modes (xz-plane), solid lines represent simulations, and dashed lines denote the measurements.

Table 8.4: Excitations for Elevation Plane Beamforming

Beam direction	$\lvert A_2\rvert$	$\Delta\psi_2$	$\lvert A_4\rvert$	$\Delta\psi_4$	$\lvert A_5\rvert$	$\Delta\psi_5$
$\phi = 0°, \theta = 22°$	1	0°	-	-	1	0°
$\phi = 0°, \theta = -22°$	1	0°	-	-	1	180°
$\phi = 90°, \theta = 20°$	1	0°	1	0°	-	-
$\phi = 90°, \theta = -22°$	1	0°	1	180°	-	-

In Fig. 8.16a, the beamforming in the xz-plane (cut at $\phi = 0°$) is illustrated, while Fig. 8.16b presents the results for beamforming in the yz-plane (cut at $\phi = 90°$). This performance is achieved by exciting one phase-varying omnidirectional *spherical mode* (using P4/P5) and one broadside radiating mode (excited via P2/P3). For completeness, Table 8.4 outlines the excitation used to generate the elevation plane beamforming, note that the same excitations are used for the simulation and measurement. Overall, a good agreement is obsrved between the simulated and measured cases, with slight discrepancy (of up to 2°) in the main beam direction for the measured cases in the yz-plane. Additionally, the slight increase in beamwidth of the measured cases may be attributed to the discrepancies highlighted in the measured broadside radiating modes and the phase characteristics of the omnidirectional *spherical modes* (P4 and P5). Finally, it is important to observe that when the main beam is directed towards a specific θ direction (e.g., $+\theta$), a phase inversion of 180° results in a shift of the main beam direction, meaning that the main beam will now be positioned at $-\theta$.

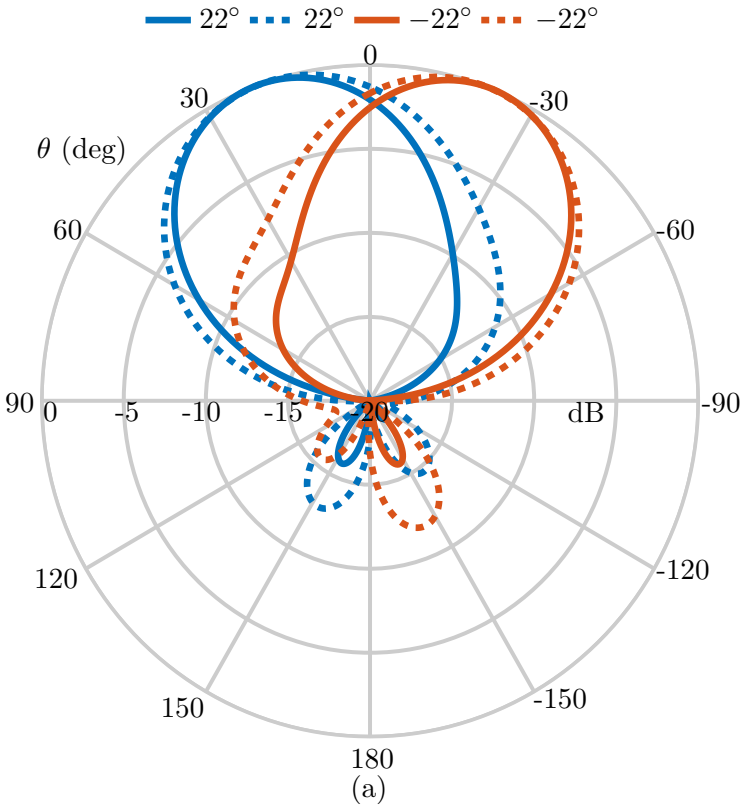

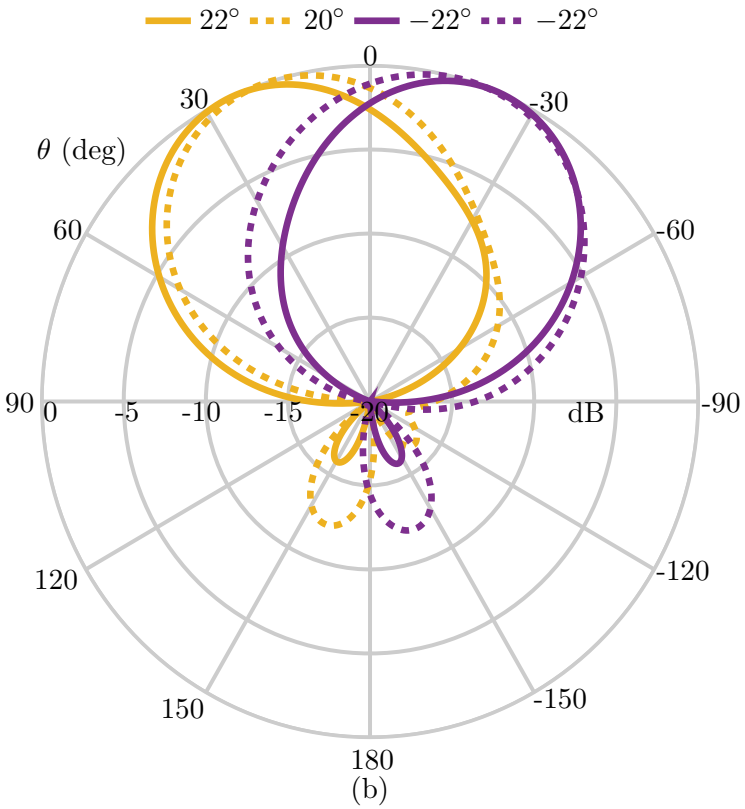

Figure 8.16: Normalized radiation patterns of the elevation plane beamforming, solid lines (simulations), and dashed lines (measurements). (a) xz-plane results. (b) $yz-$plane performance.

8.3 On-Body Performance

To assess the antenna performance in an on-body scenario, a multi-layer phantom, as depicted in Fig. 8.17a, is employed. The simulated phantom consists of three layers: a skin layer with a thickness of 1.3 mm, a fat layer with a thickness of 10.5 mm, and a muscle layer with a thickness of 20 mm. It is worth noting that the phantom dimensions are approximated from [52]. In the simulation, the antenna is initially positioned in direct contact with the multi-layer phantom, meaning that the gap between the antenna ground plane and the phantom is 0 mm. For actual measurements, a pork trunk with size 110 mm × 70 mm × 31 mm is utilized, and the measurement setup is illustrated in Fig. 8.17b.

The S-parameters results for the on-body configuration are presented in Fig. 8.18. Specifically, Fig. 8.18a displays the reflection coefficient values, while Fig. 8.18b illustrates the results of the transmission coefficients. In both scenarios, involving simulations and actual

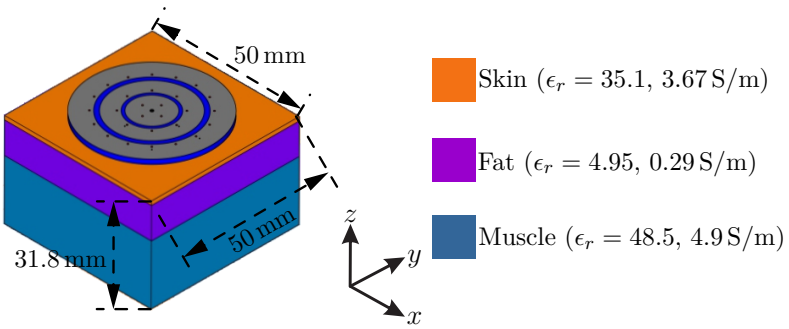

(a)

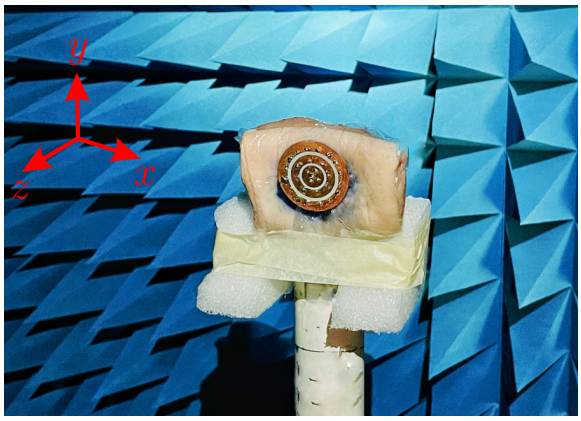

(b)

Figure 8.17: Proposed on-body setup. (a) Simulated three-layer phantom. (b) Measurement setup using a pork trunk.

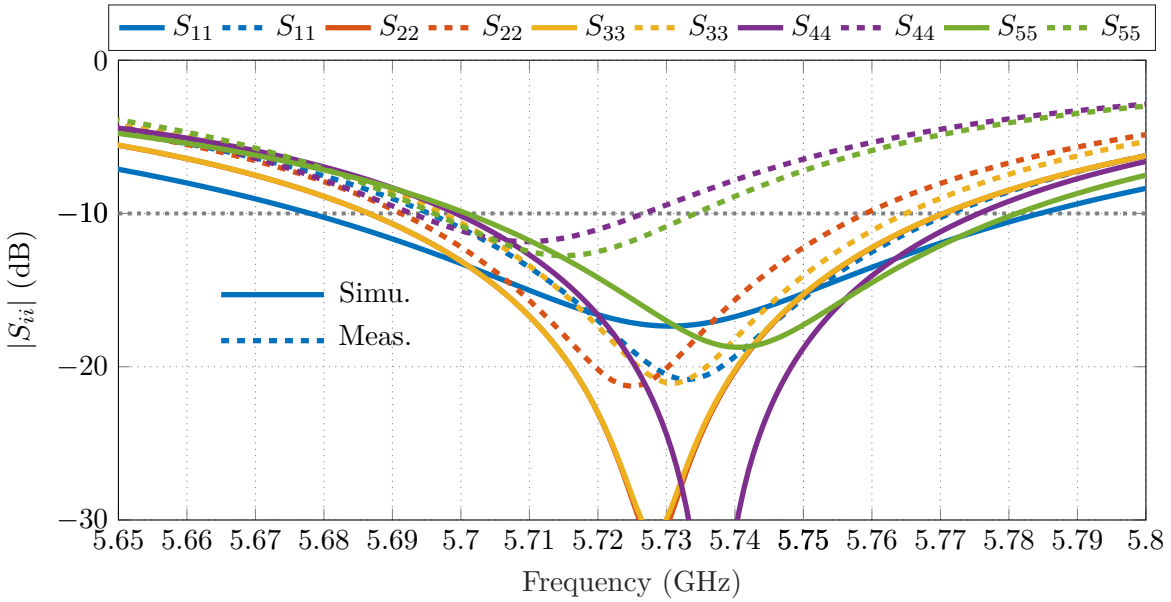

(a)

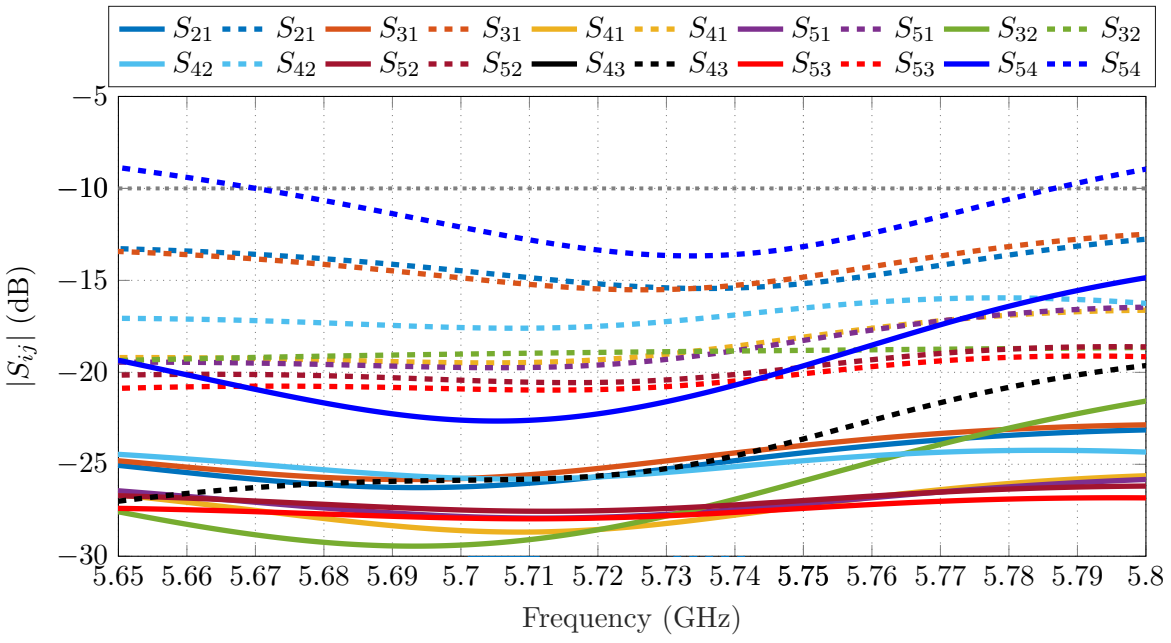

(b)

Figure 8.18: On-body S-parameters results (solid lines: simulations, dashed lines: measurements), port index $i, j = 1, 2, 3, 4, \text{and}, 5$. (a) Reflection coefficient $|S_{ii}|$. (b) Transmission coefficient $|S_{ij}|$ for $i \neq j$

measurements, it is observed that the center frequency $f_0 = 5.75\,\text{GHz}$ has a downward shift when compared to the free space scenario, it shifts to 5.73 GHz in the on-body simulated case and 5.71 GHz in the on-body measured case. The presence of the phantom in simulations leads to a degradation in isolation from 24 dB to 21 dB, while the IBW changes

Table 8.5: Simulated Total Efficiency for Different Gap Values between the Antenna Ground Plane and the Phantom at the Center Frequency of each Case.

gap	Total Efficiency				
	P1	P2	P3	P4	P5
0 mm	82%	81%	80%	58.7%	61%
1 mm	83.5%	81.4%	80.5%	61%	63%
2 mm	84%	81.5%	80.8%	63%	65%
3 mm	85%	81.8%	81%	64.5%	66%
free space	88%	82.5%	82.7%	73%	73%

to 67 MHz as compared to 42.2 MHz in free space. In the measured scenario, the isolation and IBW change from 16 dB and 31 MHz in free space to 13.2 dB and 29 MHz with the phantom.

The total efficiency for each antenna port is illustrated in Table 8.5 as the gap between the antenna ground plane and the phantom changes from 0 to 3 mm, alongside the values for the free space case. It can be seen that the total efficiency increases with the increasing gap, and the optimal values are observed in the free space scenario. Moreover, these findings indicate that the most substantial decrease in efficiency due to the presence of the phantom occurs for ports P4 and P5. This can be attributed to the dual-phase varying modes generated by these ports ($\vec{K}_{1,\pm 2,2}$ modes), which need a larger diameter to accommodate such phase-variations. In contrast, the highest efficiency is observed for the fundamental mode ($K_{1,0,1}$ generated using P1), which is characterized by a constant phase across the azimuthal plane. Nevertheless, even in the least favorable scenario with a gap = 0 mm, the total efficiency of the ports exciting the dual-phase varying modes remains above 58%.

8.3.1 Specific Absorption Rate Analysis

To examine the electromagnetic field exposure, the Specific Absorption Rate (SAR) is calculated according to Federal Communications Comission (FCC) guidelines. The experimental setup is illustrated in Fig. 8.19, and for the wrist-worn scenario, the antenna is positioned in direct contact with a block filled with human hand tissue ($\epsilon_r = 21.3$, $\delta = 0.51$ S/m, and $\rho = 1000\,\mathrm{kg/m^3}$), and a 10 g average is used. The dimensions of the block are depicted in Fig. 8.19, and the input power is set at 10 mW. As indicated in the same figure, the peak

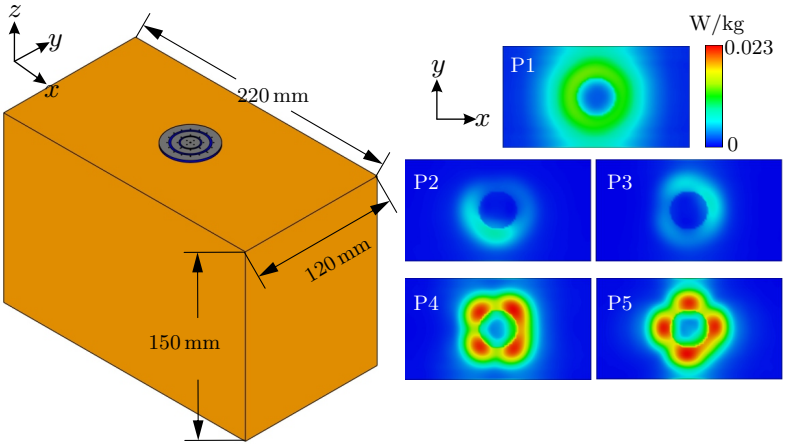

Figure 8.19: SAR analysis following FCC guidelines for the wrist-worn setup.

SAR values for each port are 0.0073 W/kg, 0.0024 W/kg, 0.0032 W/kg, 0.023 W/kg, and 0.023 W/kg, for P1, P2, P3, P4 and P5, respectively. Consequently, the highest SAR value for the antenna is 0.023 W/kg, which is well below the 4 W/kg limit set by FCC [155] and the International Commission on Non-Ionizing Radiation Protection (ICNIRP) limit [160].

The findings also indicate that for the investigate wrist-worn setup, the omnidirectional modes (P1, P4, and P5) exhibit higher SAR values compared to the broadside radiating modes (P2 and P3). This observation may be explained by the fact that, when the antenna is mounted on the multi-layer phantom, the omnidirectional modes have strong $\vec{E}$ along the length and depth of the phantom, leading to increased electromagnetic absorption by the human tissue. In contrast, for P2 and P3, as their main beams point towards $+z$ (away from the phantom's depth and length), the electromagnetic absorption by the tissue is correspondingly diminished.

8.3.2 On-Body Beamforming Performance

Fig. 8.20 displays the measured radiation patterns of the omnidirectional modes, while Fig. 8.21 presents the corresponding phase properties. The measured radiation patterns for the broadside modes are illustrated in Fig. 8.22. The presence of the phantom introduces changes in the radiation patterns of the omnidirectional *spherical modes*, characterized by additional shouldering and dips, particularly noticeable in P4 and P5. Despite the increased phase distortions, the essential phase properties are generally maintained. Note

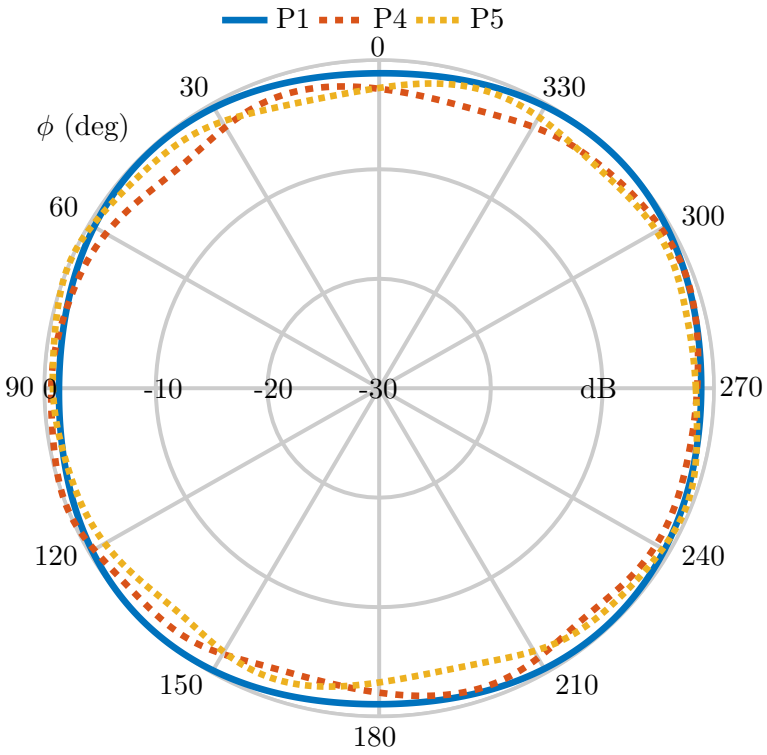

Figure 8.20: On-body measured normalized radiation patterns of the antenna excited omnidirectional *spherical modes* (xy-plane).

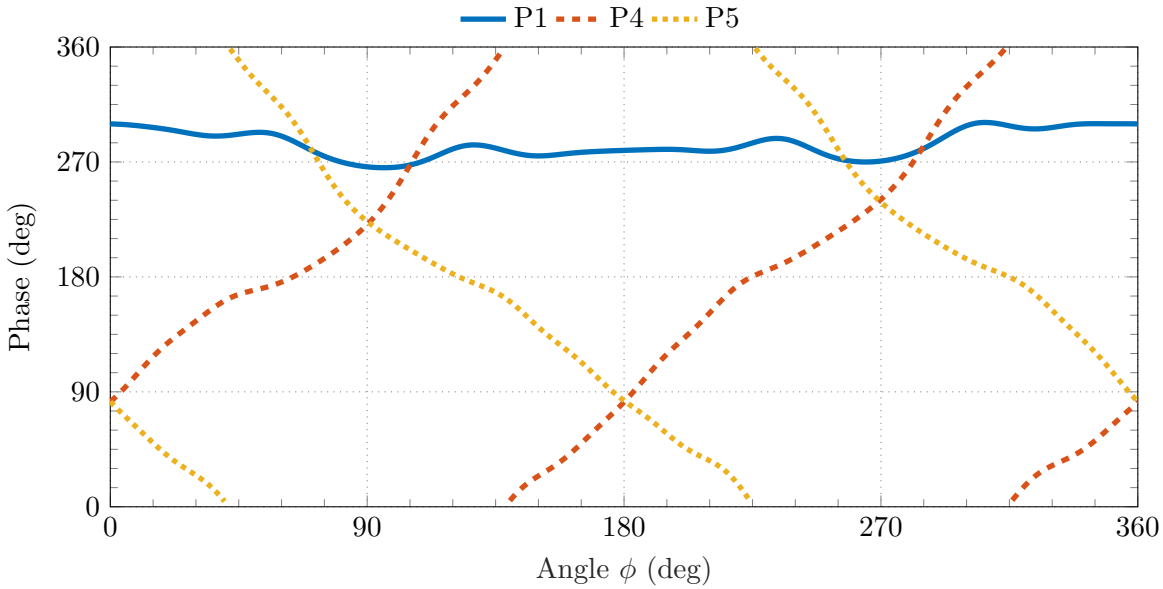

Figure 8.21: On-body measured phase of the radiation pattern of the omnidirectional *spherical modes*.

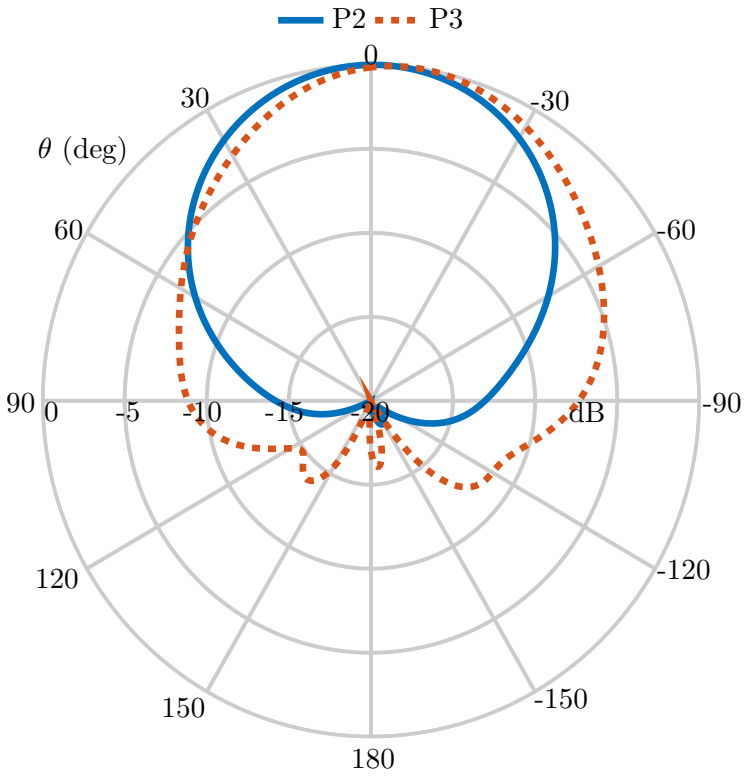

Figure 8.22: On-body measured normalized radiation patterns of the antenna excited broadside radiating modes (xz-plane).

that the reflections originating from the antenna holder and other materials employed in the on-body measurements could contribute to the observed pattern dips, shoulders, and phase asymmetries. Additionally, it should be mentioned that the main beams of the broadside radiating modes (P2 and P3) remain relatively unaffected since their main beams are directed towards the $+z$ direction. However, some impact on the radiation patterns is seen around the $(-z)$ direction, especially for the mode excited using P3. This can be explained by the fact that the P3 excited mode is an x-polarized broadside mode, and the length of the pork trunk ($110\,\text{mm} \times 70\,\text{mm} \times 31\,\text{mm}$) is relatively larger along the x-direction as compared to the y-direction.

The peak realized gain at f_0 in full-wave simulations is 1.4, 7.7, 7.8, 2.8, and 2.9 dBi for P1, P2, P3, P4, and P5, respectively decreasing to 0.8, 6.4, 6.3, 1.5 dBi in measurements. Such discrepancies maybe due to differences in dielectric properties between the phantom used in simulations and the actual pork trunk used for on-body measurements.

8.3.3 Azimuth Plane Beamforming

Fig. 8.23 illustrates the on-body beamforming in the azimuth plane for both simulated and measured cases. The main beam is directed towards four distinct directions, each separated by 90° to cover the entire plane. Specifically, Fig. 8.23a shows the beamforming performance for 0°/180° and 90°/270° directions, while Fig. 8.23b highlights the performance for 45°/225° and 135°/315° directions. In both simulated and measured scenarios, the antenna exhibits the ability to steer the beam effectively in all the desired directions. The minor dips observed in the measured 0°/180° pattern and the variations in beamwidth can be attributed to asymmetries in the pork phantom utilized during measurements, manufacturing tolerances, and the influence of the antenna holder, as well as other materials used in the on-body setup. Lastly, the measured excitations corresponding to each beam direction are provided in Table 8.6.

Table 8.6: Azimuth Plane On-body Beamforming Excitations

Beam direction	$\lvert A_1\rvert$	$\Delta\psi_1$	$\lvert A_4\rvert$	$\Delta\psi_4$	$\lvert A_5\rvert$	$\Delta\psi_5$
$\phi = 0°/180°$	1	0°	1	218°	1	218°
$\phi = 45°/225°$	1	0°	1	125°	1	302°
$\phi = 90°/270°$	1	0°	1	45°	1	43°
$\phi = 135°/335°$	1	0°	1	291°	1	113°

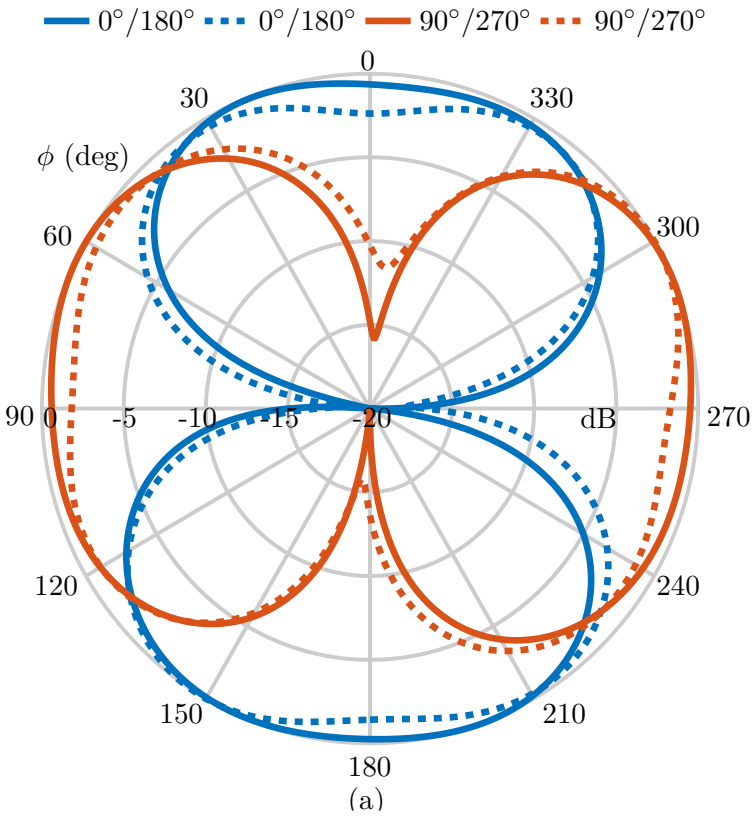

(a)

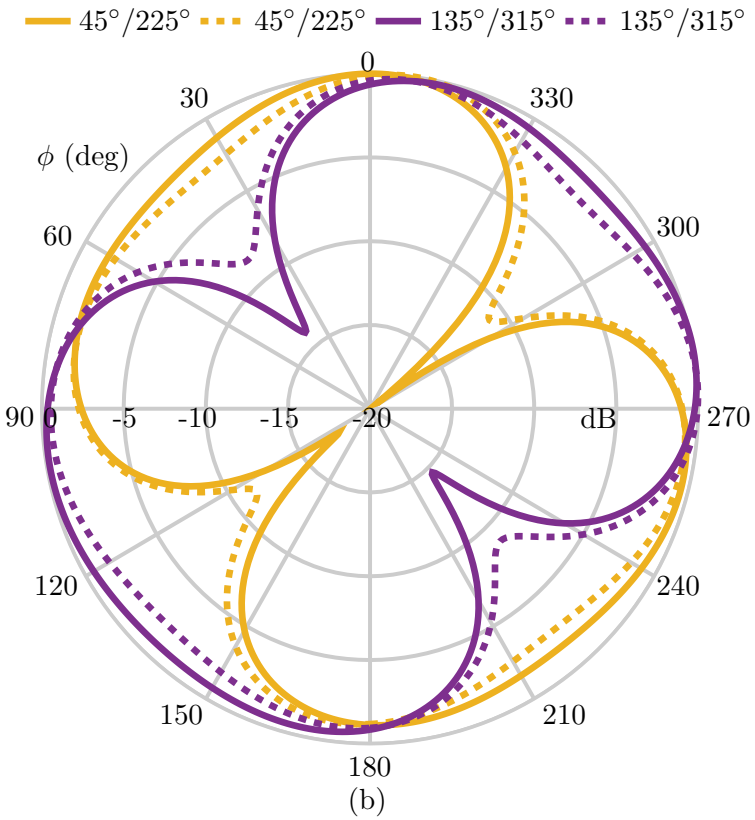

(b)

Figure 8.23: On-body normalized radiation patterns showing xy-plane beamforming, solid lines (simulations) and dashed lines (measurements). (a) 0°/180° and 90°/270°. (b) 45°/225° and 135°/315°.

8.3.4 Elevation Plane Beamforming

Fig. 8.24a presents the simulated and measured beamforming results for the xz-plane, whereas Fig. 8.24b shows the results for the yz-plane. The corresponding excitations for the generated patterns are outlined in Table 8.7. Despite the slight increase in beamwidth in the measured cases, it can be observed that effective beamforming characteristics are achieved in both planes. The discrepancies may arise from the combined effects of the phantom, antenna holder, and other manufacturing inaccuracies. In the on-body setup, the scanning range in the elevation plane is reduced compared to the free space scenario, decreasing from 44° to 32° in the xz-plane and to 33° for the yz-plane.

Table 8.7: Elevation Plane On-Body Beamforming Excitations

Beam direction	$\lvert A_2\rvert$	$\Delta\psi_2$	$\lvert A_4\rvert$	$\Delta\psi_4$	$\lvert A_5\rvert$	$\Delta\psi_5$
$\phi = 0°, \theta = 16°$	1	0°	-	-	1	0°
$\phi = 0°, \theta = -16°$	1	0°	-	-	1	180°
$\phi = 90°, \theta = 16°$	1	0°	1	0°	-	-
$\phi = 90°, \theta = -16°$	1	0°	1	180°	-	-

8.4 Summary

This chapter proposed a planar 3D beamforming antenna for on-body IoT devices. By exploiting the *SMB* principle, advanced beamforming is demonstrated across the entire horizontal plane with vertical polarization, while using planar structures. The method is shown to support beamforming in the xz and yz-planes by exciting two orthogonal broadside radiating modes. For on-body scenarios, the antenna has a 360° scanning range in the azimuthal plane, while a scanning range of 32° and 33° is realized in the xz and yz-planes, respectively. This performance is achieved with a total efficiency $> 58\%$ and a measured peak realized gain of up to 6.24 dBi. Owing to its low profile and compact diameter, the antenna is proposed as a cutting-edge solution to enable directional modulation and angle of arrival estimation in emerging on-body IoT devices like smartwatches.

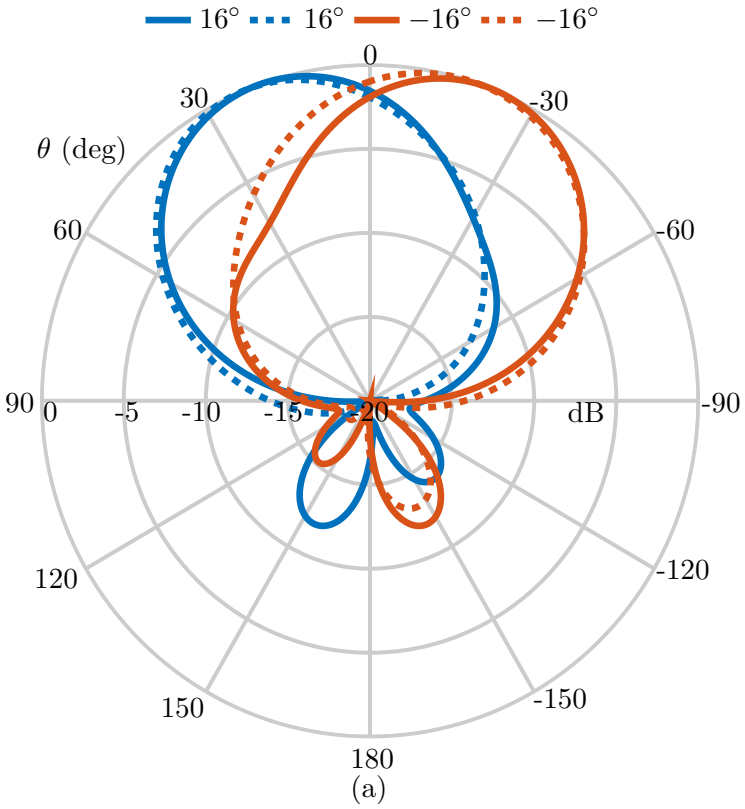

(a)

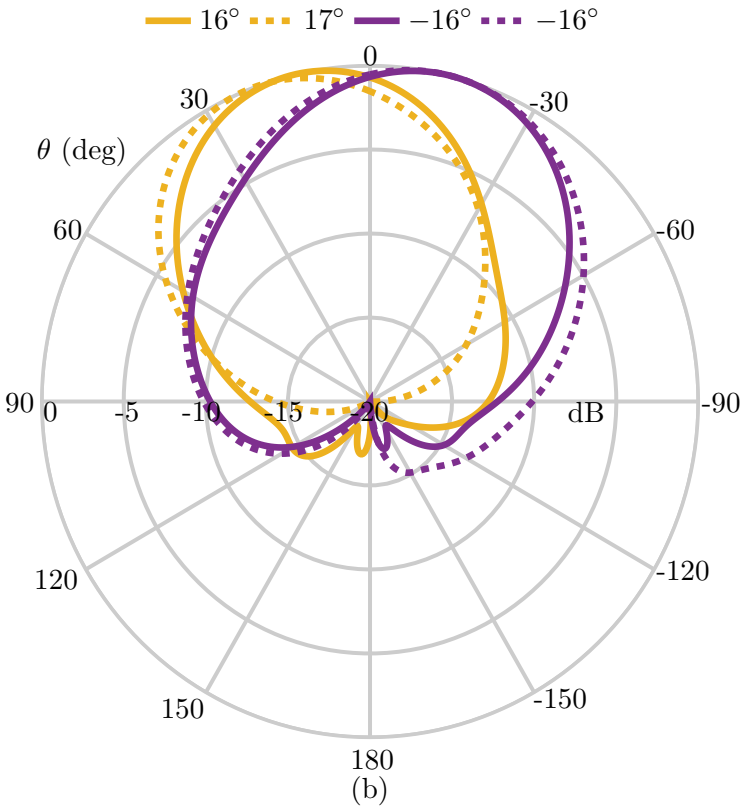

(b)

Figure 8.24: On-body normalized radiation patterns of the elevation plane beamforming, solid lines (simulations), and dashed lines (measurements). (a) xz-plane. (b) $yz-$plane.

9 Dual-Band SMB Antenna

Dual-Band SMB Antenna

In previous chapters, different aspects related to the *Spherical Modes Beamforming (SMB)* principle, including their suitability for Angle of Arrival (AoA) and Directional Modulation (DM) techniques, were investigated. This chapter extends the beamforming principle to realize compact multi-band antennas. The solution is demonstrated using a planar dual-band structure capable of bi-directional beamforming across the entire horizontal plane in the antenna's two operating bands. The chapter further investigates the implementation of the proposed multi-band solution to enable beamforming functionalities in emerging on-body Internet of Things (IoT) devices. Part of the findings discussed in this chapter were submitted to the IEEE Internet of Things Journal [161].

9.1 SMB Multi-Band Concept

As discussed in Section 3.2, to implement the *SMB* principle at a given center operating frequency f_0, we assume that a number of omnidirectional *spherical modes* ($K_{1,\pm n,n}$) can be excited within a constrained space of radius r_0. The highest order at this frequency is $n = N$, i.e., $K_{1,\pm N,N}$ are the highest order modes. To extend the beamforming for multi-band operation, we can assume that the same highest-order modes ($K_{1,\pm N,N}$) can be excited at a higher operating frequency band f_1, such that $f_1 > f_0$. If no miniaturization is performed or material changes are introduced, the total size required to excite the $K_{1,\pm N,N}$ modes at f_1 will be smaller than the size needed to excite the same modes at f_0. In other words, all the omnidirectional *spherical modes* excited at f_0 band can be excited at a higher operating frequency band, while the largest diameter of the enclosing sphere is still r_0. This principle is visualized in Fig. 9.1, where it is highlighted that when the same mode $K_{1,\pm N,N}$,

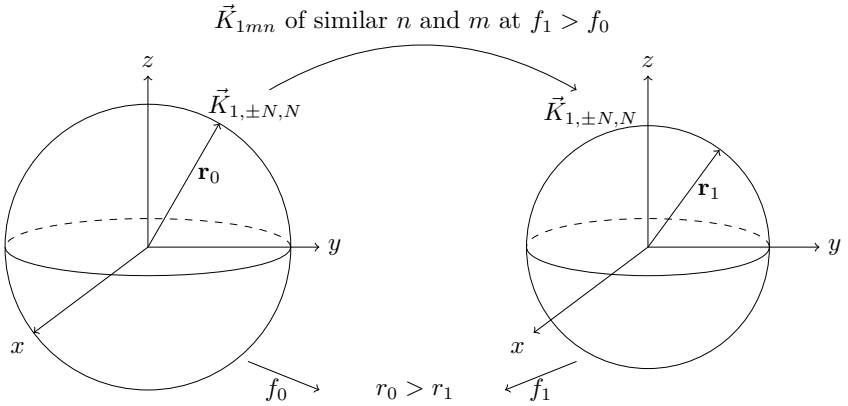

Figure 9.1: Proposed multi-band principle, based on the excitation of omnidirectional *spherical modes* of similar order n, and phase-variations m at different frequency bands, i.e., $f_1 > f_0$, and $r_0 > r_1$.

is excited at $f_1 > f_0$, a relatively smaller sphere is needed for f_1, i.e., $r_0 > r_1$.

The proposed multi-band principle can enable good design flexibility by using different types of antenna configurations. For instance, a stacked structure can be designed to excite the required modes at different bands. Such a design could then hypothetically use the entire volume of the sphere that encloses the largest antenna dimension. However, it would also result in a high profile (since different layers are stacked together). This would ultimately limit the antenna integration in many on-body IoT devices, e.g., wrist-mounted devices. To mitigate this issue, the multi-band principle proposed in this thesis is realized using circular patches and annular ring antennas. The rings are concentrically aligned with the circular patch, realizing a planar structure suitable for on-body integrated IoT devices.

9.2 Antenna Design

The proposed antenna is shown in Fig. 9.2. It comprises a circular patch and two annular ring structures, all made using a 35μm thick copper layer ($\sigma = 5.8 \times 10^7$ S/m) and supported by a TMM6 substrate material ($\epsilon_r = 6.3$, tan$\delta = 0.0023$). The substrate diameter, and thickness are 62 mm and 1.27 mm, respectively. The antenna is designed to operate at the 2.4 and 5.8 GHz bands. To realize the proposed dual-band characteristics, the omnidirectional *spherical modes* of order $n = 1$ and $n = 2$ are used, as they are the lowest orders and offer the first possible beamforming combination, i.e., a bi-directional beamforming across

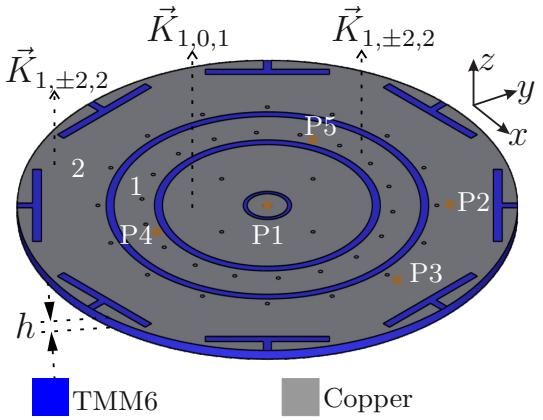

Figure 9.2: Perspective view of the proposed antenna, where $h = 1.34\,\text{mm}$, and the feeding locations from the center of the substrate are P2 = P3 = 22.5 mm, and P4 = P5 = 14.6 mm.

the entire azimuthal plane.

9.2.1 Excitation of Phase-Varying Modes

For the excitation of the phase-varying ($\vec{K}_{1,\pm2,2}$) modes at the lower band (f_0), ring 2 is used. The configuration of this structure is shown in Fig. 9.3a. The ring outer and inner diameters are $d_1 = 62\,\text{mm}$, and $d_2 = 40\,\text{mm}$, respectively. This ring is fed using P2 and P3 located at 2.5 mm from the edges of the inner diameter and rotated by $\alpha_1 = 45°$. The ports are fed in quadrature to enforce the required phase-variations. Ring 2 includes 16 shorting pins located $v_1 = 1\,\text{mm}$ from the inner diameter edges, which also enhances isolation characteristics and provide sfrequency agility. The pins have radii 0.25 mm and are rotated by 22.5° with respect to the center. Additionally, eight T-shaped slots rotated by 45° are used to increase the current path, therefore, providing miniaturization. Fig. 9.3b shows the $\vec{E}$ distribution of the modes excited using P2 and P3. It can be seen that these ports excite two orthogonal modes of the same order, also changing in two opposing directions, as required to realize the *SMB* method.

To excite the $\vec{K}_{1,\pm2,2}$ modes at the upper band (f_1), ring 1 is used as shown in Fig. 9.4a. The ring outer and inner diameters are $d_3 = 38\,\text{mm}$, and $d_4 = 28\,\text{mm}$, respectively. It uses two ports P4 and P5, also fed in quadrature, located at 0.8 mm from the edges of the inner diameter and oriented by $\alpha_2 = 135°$. Eighteen shorting pins located at $v_2 = 1.6\,\text{mm}$ from the inner diameter and rotated by 20° are included in the structure. It is worth

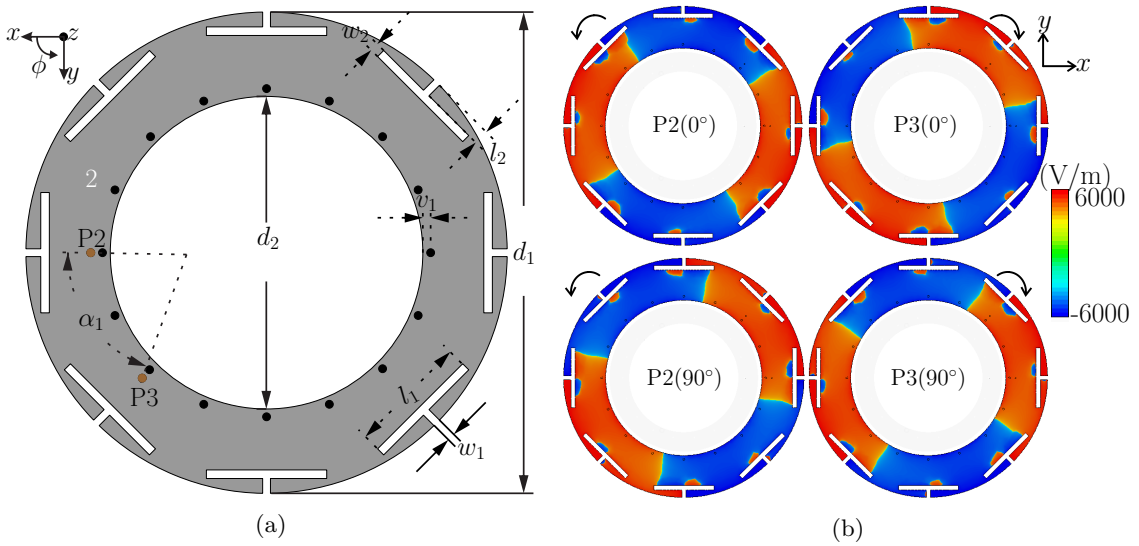

Figure 9.3: Ring 2 used to generate the $\vec{K}_{1,\pm2,2}$ modes at the lower band f_0. (a) Top view with all dimensions in mm: $d_1 = 62,\ d_2 = 40,\ v_1 = 1,\ l_1 = 15.4,\ l_2 = 1.9,\ w_1 = 1,\ w_2 = 1.1, \alpha_1 = 45°$, and P2 = P3 = 22.5. (b) $\vec{E}$ distribution (z-components), where the top images are for 0° phase and the 90° phase is shown on the bottom.

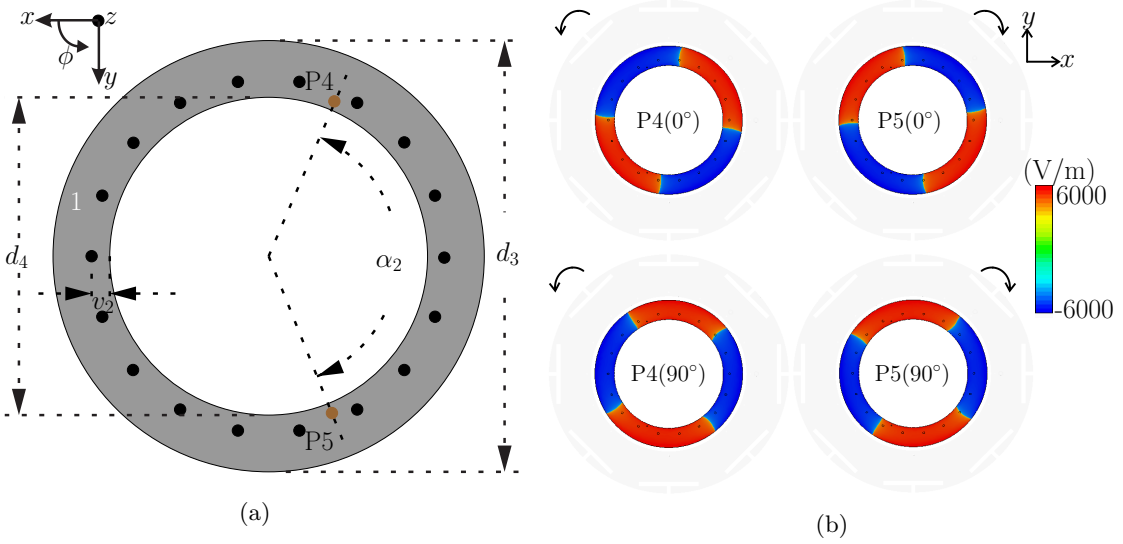

Figure 9.4: Ring 1 used to excite the $\vec{K}_{1,\pm2,2}$ modes at the upper band f_1. (a) Top view with all dimensions in mm: $d_3 = 38,\ d_4 = 28,\ v_2 = 1.6, \alpha_2 = 135°$, and P4 = P5 = 14.6. (b) $\vec{E}$ distribution (z-components), where the top images are for 0° phase and the 90° phase is shown on the bottom.

mentioning that an increased number of pins is used for ring 1 in order to increase the inductive coupling and further shift the frequency toward the desired upper band value. Lastly, Fig. 9.4b shows the $\vec{E}$ distribution when P4 and P5 are excited separately. It can be seen that the ring also generates two orthogonal modes of the same order, changing in two opposite directions.

9.2.2 Excitation of the Fundamental Modes

A center-fed circular patch with a ring slot is used to excite the fundamental $\vec{K}_{1,0,1}$ mode at two bands. The design evolution is shown in Fig. 9.5, all the patches are supported by a TMM6 substrate of diameter $d_1 = 62\,\text{mm}$ as in Fig. 9.2. Ant-A is a center-fed patch with diameter $d_5 = 26\,\text{mm}$ (Fig. 9.5a), and the corresponding S-parameters are outlined in Fig. 9.6. It can be seen that the design center frequency is at the upper band $f_1 = 5.48\,\text{GHz}$, where $|S_{11}| > -4\,\text{dB}$. In the next step, four shorting pins of radius 0.25 mm are placed at $v_3 = 8\,\text{mm}$ (see Ant-B in Fig. 9.5b). The pins are oriented by 90°, and the S-parameters are shown in Fig. 9.6. Ant-B allows for the excitation of $\vec{K}_{1,0,1}$ modes at the upper $f_1 = 5.48\,\text{GHz}$ and lower $f_0 = 2.4\,\text{GHz}$ bands. However, $|S_{11}| > -3\,\text{dB}$ at both bands. A ring slot is used to improve the matching characteristics, as shown in Fig. 9.5c. This configuration produces further capacitance to allow for an $|S_{11}| < -10\,\text{dB}$ at two bands ($f_0 = 2.37\,\text{GHz}$ and $f_1 = 5.67\,\text{GHz}$), as depicted in Fig. 9.6.

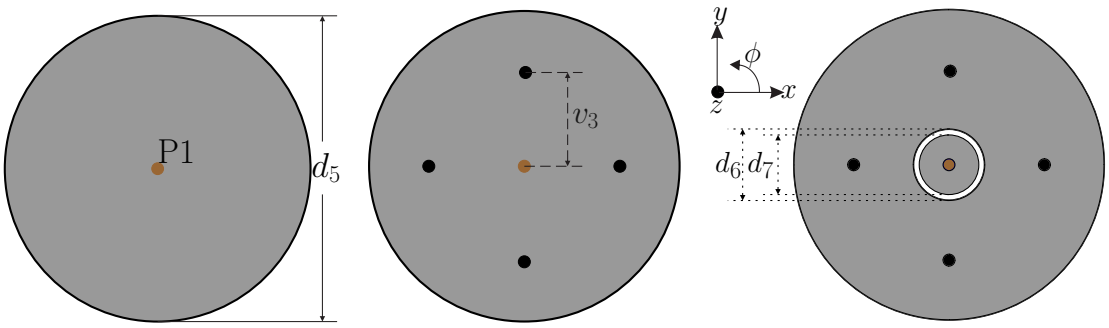

Figure 9.5: Evolution of the patch antenna exciting $\vec{K}_{1,0,1}$ modes at two differents bands. (a) Top view of Ant-A, center-fed patch antenna. (b) Top view of Ant-B, patch with four shorting pins. (c) Top view of Ant-C, patch with shorting pins and ring slot. All dimensions in mm: $d_5 = 26$, $v_3 = 8$, $d_6 = 6$, and $d_7 = 5$.

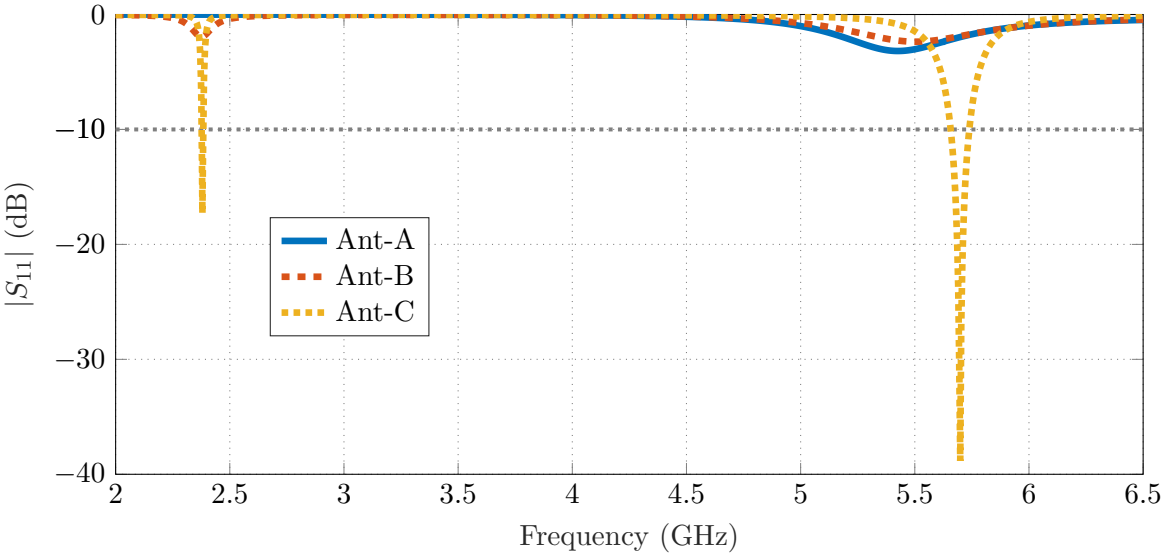

Figure 9.6: Simulated S-parameters of the central patch used to excite the $\vec{K}_{1,0,1}$ mode at two bands.

9.3 Free Space Analysis

To experimentally validate the performance of the proposed dual-band antenna, a prototype was fabricated and is shown in Fig. 9.7. The simulated and measured S-parameters at the lower band are shown in Fig. 9.8a and Fig. 9.8b, respectively. It can be seen that for the simulated case, the center frequency is $f_0 = 2.37\,\text{GHz}$, the antenna's final dimensions with respect to the wavelength at f_0 is $0.49\lambda \times 0.49\lambda \times 0.01\lambda$. At f_0 the isolation is

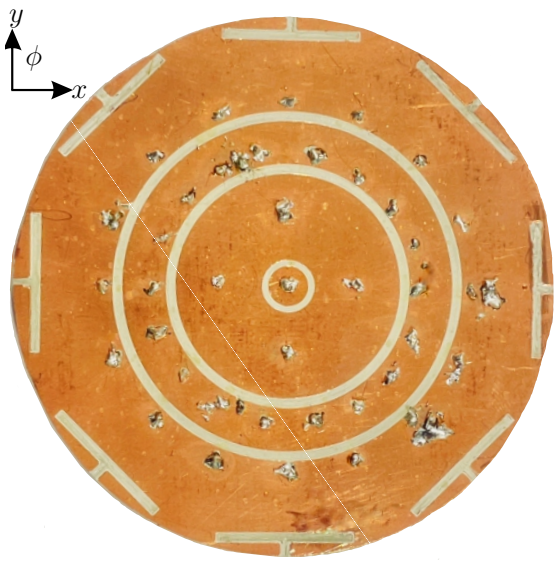

Figure 9.7: Top view of the manufactured dual-band antenna.

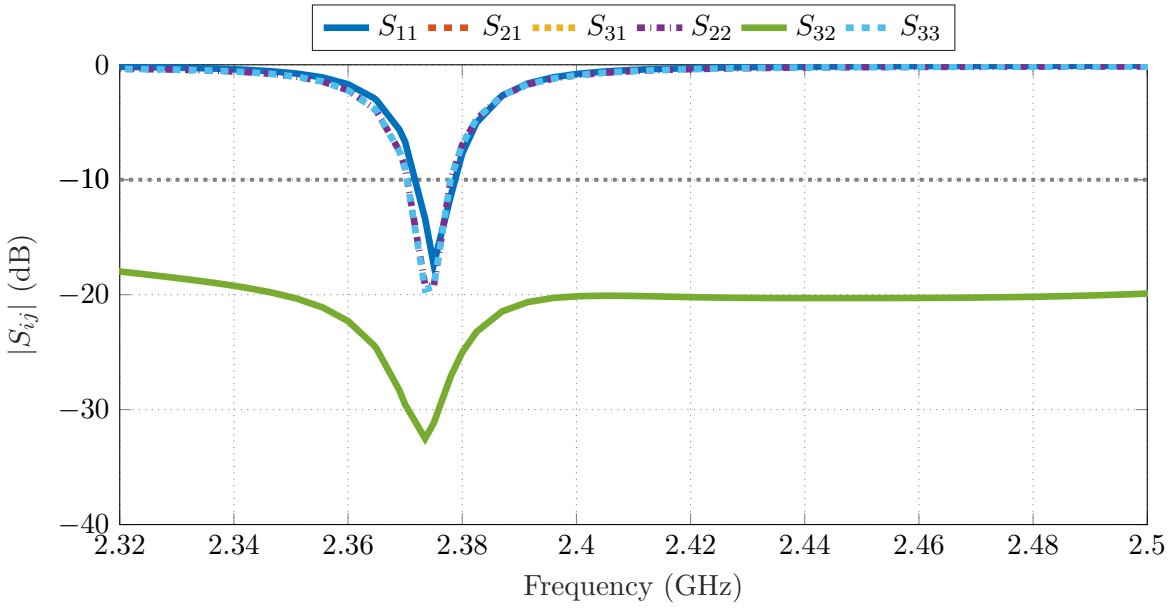

(a)

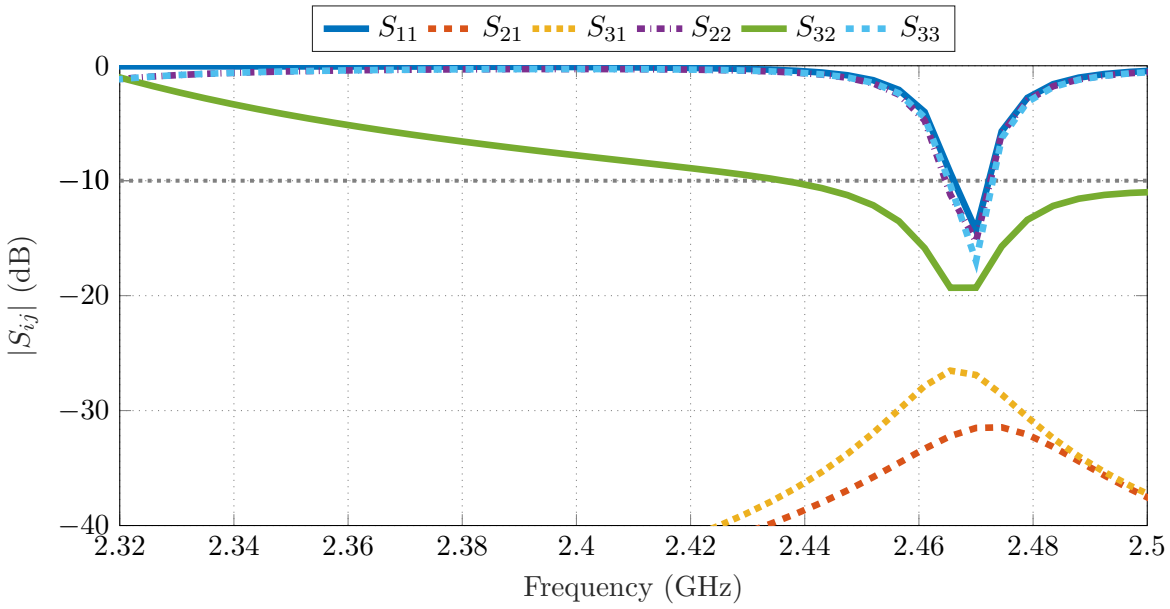

(b)

Figure 9.8: Free space S-parameters results for the lower band. (a) Simulations. (b) Measurements.

$> 30\,\text{dB}$, and the Impedance BandWidth (IBW) is 7.2 MHz. In contrast, for the measured case $f_0 = 2.47\,\text{GHz}$, the isolation and IBW deteriorate to 19 dB and 5.5 MHz, respectively. The observed upward frequency shift and other discrepancies may be explained by manufacturing and substrate permittivity tolerances.

The simulated and measured S-parameters for the upper band are shown in Fig. 9.9a and Fig. 9.8b, respectively. Similar to the characteristics observed at the lower band, the

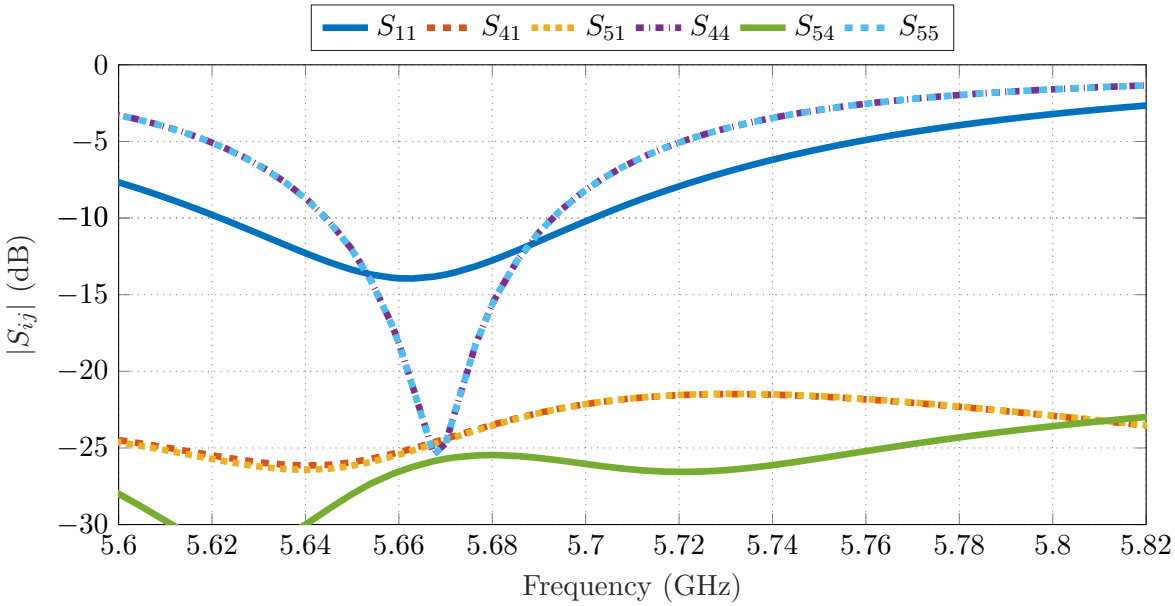

(a)

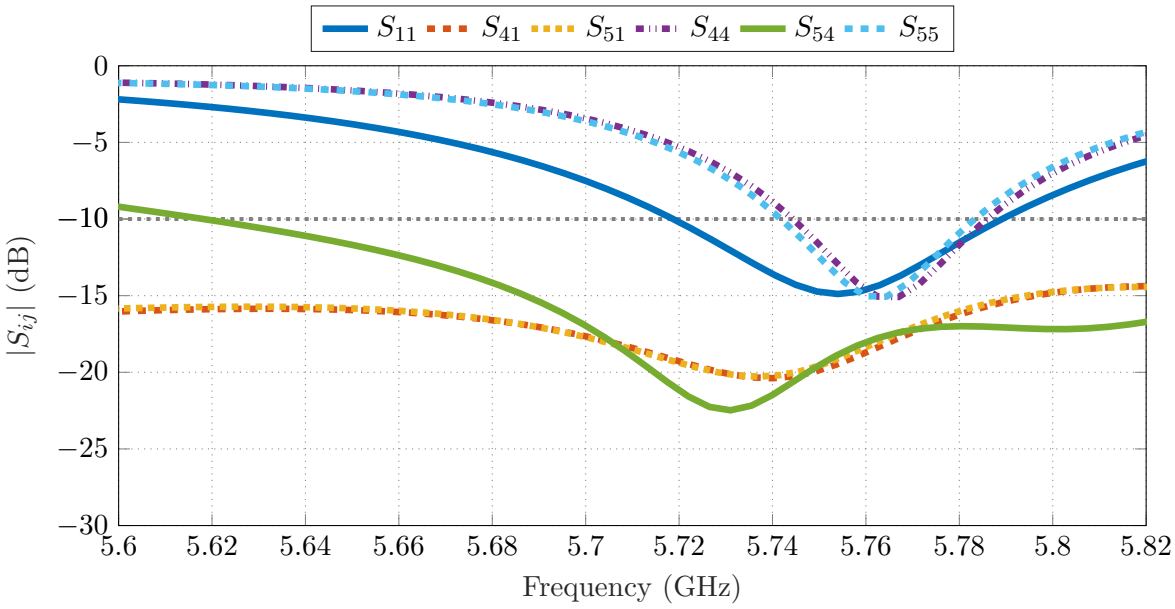

(b)

Figure 9.9: Free space S-parameters results for the upper band. (a) Simulations. (b) Measurements.

center frequency for the measured case shifts upwards from $f_1 = 5.67\,\text{GHz}$ (in simulations) to 5.77 GHz. In simulations the isolation is $> 25\,\text{dB}$ and IBW is 38 MHz, these values change to 17.5 dB and 25 MHz in measurements.

The simulated total efficiency for f_0, is $17\%, 26.8\%$, and 27% for P1, P2, and P3, respectively. For f_1 the simulated total efficiency is $87\%, 71\%$, and 71% for P1, P4, and P5, respectively. Note that the relatively small bandwidth and low antenna efficiency values at

the f_0 band can be explained by the small size of the antenna, as the *spherical modes* are excited using a miniaturized structure (diameter $< \lambda/2$).

9.4 On-Body Analysis

9.4.1 Antenna Performance on a Multi-Layer Phantom

A multi-layer phantom, as shown in Fig. 9.10, is used to investigate the antenna performance in an on-body scenario. The phantom comprises three different layers, and the dielectric properties included in Fig. 9.10 correspond to the $f_0 = 2.37\,\text{GHz}$. For $f_1 = 5.67\,\text{GHz}$, the

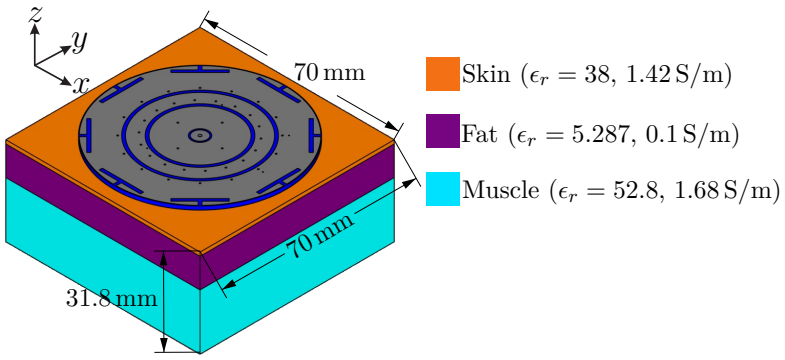

Figure 9.10: Proposed on-body setup, with a three-layer phantom: skin (1.3 mm), fat (10.5 mm), and muscle (20 mm). Note that the antenna is placed in direct contact with the skin-layer, i.e., with 0 mm gap. The dielectric properties shown on the left correspond to the $f_0 = 2.37\,\text{GHz}$ band.

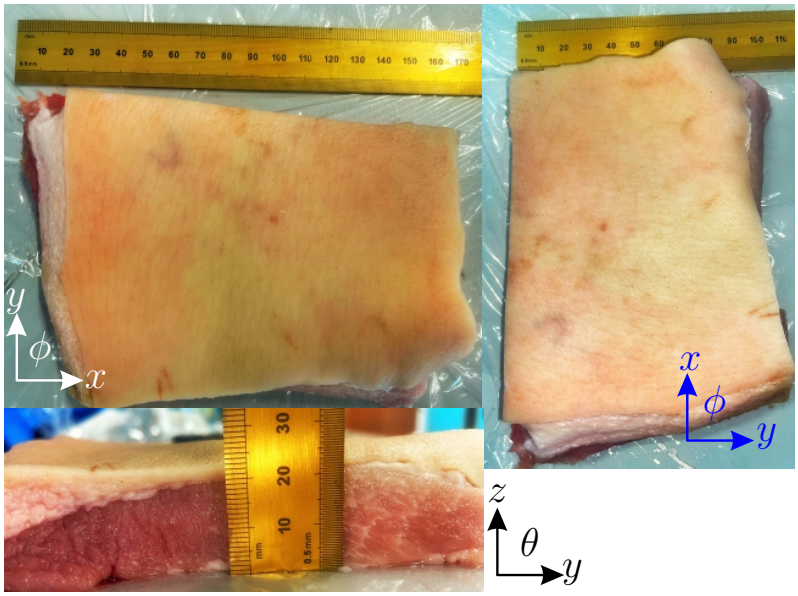

Figure 9.11: Images of the pork trunk used for on-body measurements.

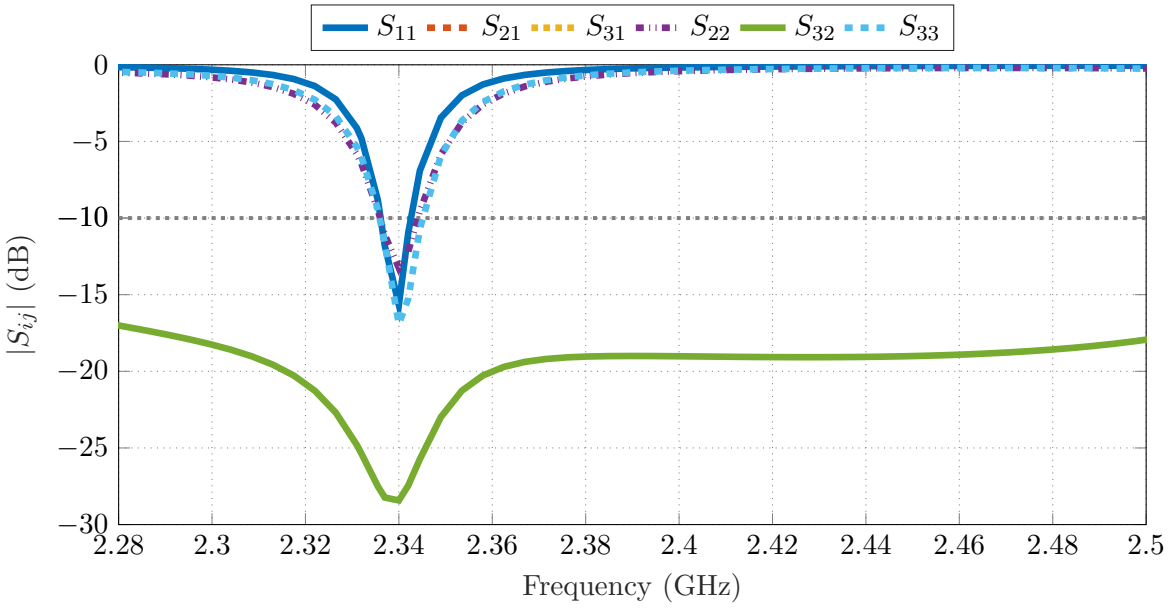

(a)

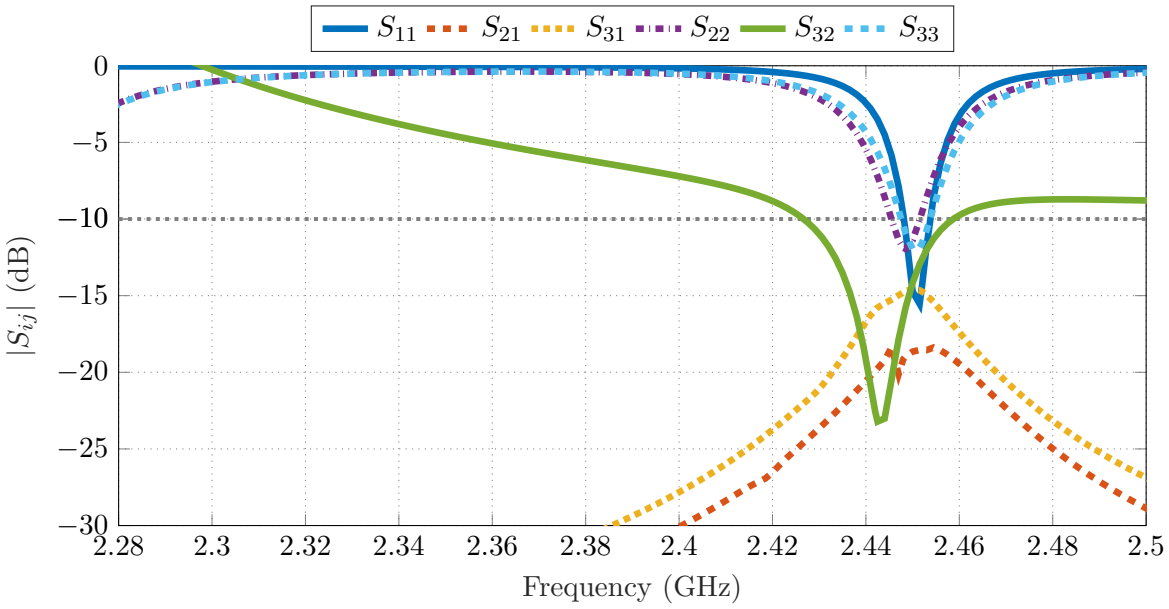

(b)

Figure 9.12: On-body S-parameters for the lower band. (a) Simulations. (b) Measurements.

values are as follows: skin-layer ($\epsilon_r = 35.36, 3.46\,\mathrm{S/m}$), fat-layer ($\epsilon_r = 4.98, 0.27\,\mathrm{S/m}$), and muscle-layer ($\epsilon_r = 48.8, 4.609\,\mathrm{S/m}$). To experimentally test the on-body performance, a pork trunk of approximately 170 mm × 100 mm × 23 mm is used as shown in Fig. 9.11.

The lower band's on-body simulated and measured S-parameters are shown in Fig. 9.12a and Fig. 9.12b, respectively. It can be seen that due to the phantom, a downward frequency shift from 2.37 GHz to 2.34 GHz occurs. The corresponding antenna size for the new center

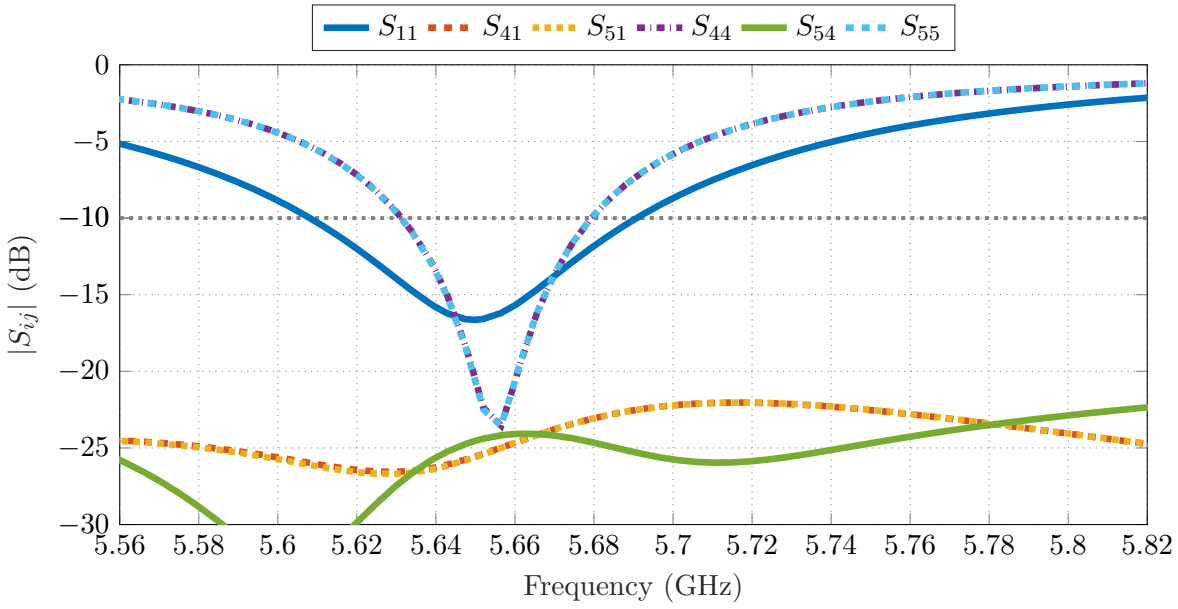

(a)

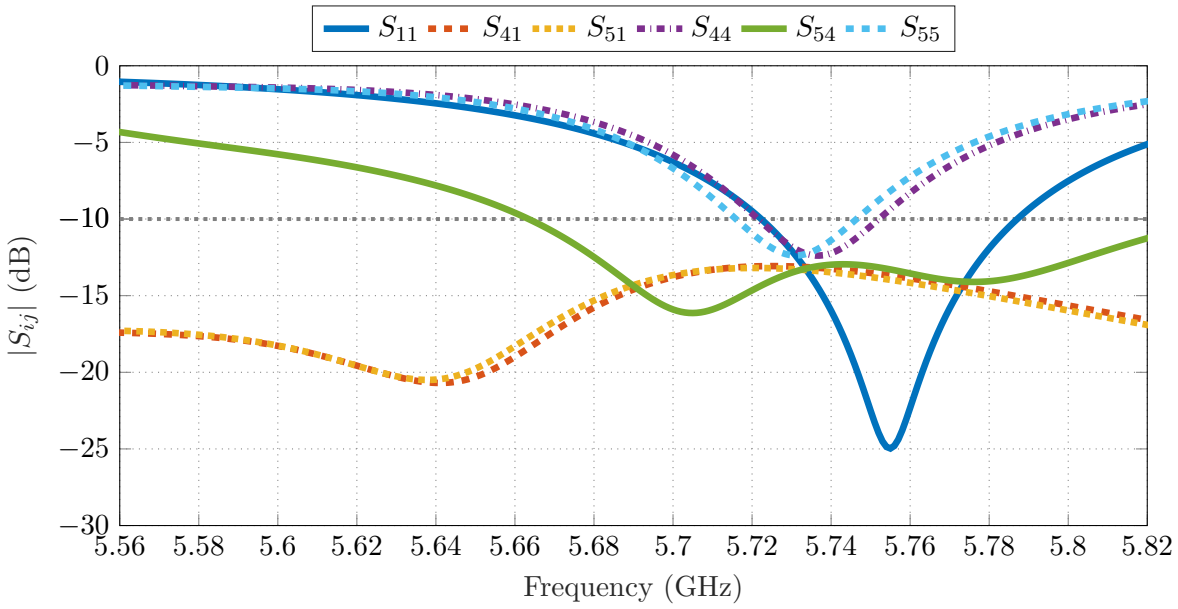

(b)

Figure 9.13: On-body upper band S-parameter results. (a) Simulations. (b) Measurements results.

frequency is $0.48\lambda \times 0.48\lambda \times 0.01\lambda$. A downward frequency shift is also observed in the measured case from 2.47 GHz in free space to 2.45 GHz with the phantom. Additionally, the IBW and isolation change from 6.9 MHz and 28 dB in simulations to 3 MHz and 14 dB, respectively.

Fig. 9.13 illustrates the upper band S-parameter results, where the simulated values are given in Fig. 9.13a, while the measured ones are shown in Fig. 9.13b. The on-body

simulations show a frequency shift from 5.67 GHz (in free space) to 5.65 GHz when the phantom is included. The IBW and isolation are 49 MHz and 25 dB in free space, changing respectively to 48.4 MHz and 23.5 dB for on-body simulated case. The measured results also show the same trend, i.e., due to the phantom effects, the frequency shifts from 5.76 GHz in free space to 5.73 GHz with the phantom. The measured isolation for this band is 13 dB, while the impedance bandwidth is up to 25 MHz.

The simulated total efficiency at f_0 decreases from 17% in free space to 15% with the phantom (for P1), 26.8% to 20.5% for P2, and 27% to 21% for P3. At f_1, the simulated total efficiency drops from 87% (in free space) to 82.7% (including phantom) for P1, and 71% to 66% for P4 and P5.

9.4.2 Antenna Pattern Performance on Gustav Voxel Model

The CST Studio Suite Gustav voxel model [18] is used to evaluate the antenna radiation pattern in a realistic on-body scenario. The results are obtained under two setups: antenna mounted with the elongated hand (Fig. 9.14) and antenna mounted with the forearm bent approximately 45° towards the model (Fig. 9.15).

Fig. 9.14a shows the elongated hand results for f_0. Small pattern deformities occur, especially along the voxel model hand, i.e., along the $+y$ direction. This is mostly due to the reflections from the voxel model. Nevertheless, the phase properties of the generated modes are little affected. The radiation patterns for the same setup at f_1 are shown in Fig. 9.14b. All the excited ports achieve the desired phase characteristics to realize the *SMB* principle despite some dips in the amplitude along the $+y$ direction. However, they are smaller than those observed at f_0.

The results for the bent forearm at f_0 are shown in Fig. 9.15a. The required phase properties for *SMB* are also achieved, and due to the bent, a slight increase in the antenna pattern tilts are seen for P2 and P3. The antenna patterns for f_1 are depicted in Fig. 9.15b. In this case, the patterns are omnidirectional and achieve the required phase properties. Similarly to the elongated hand case for f_1 patterns, the directivity values are higher compared to the f_0 patterns. Overall, these results obtained using a realistic human model further highlight the antenna's suitability for on-body IoT devices.

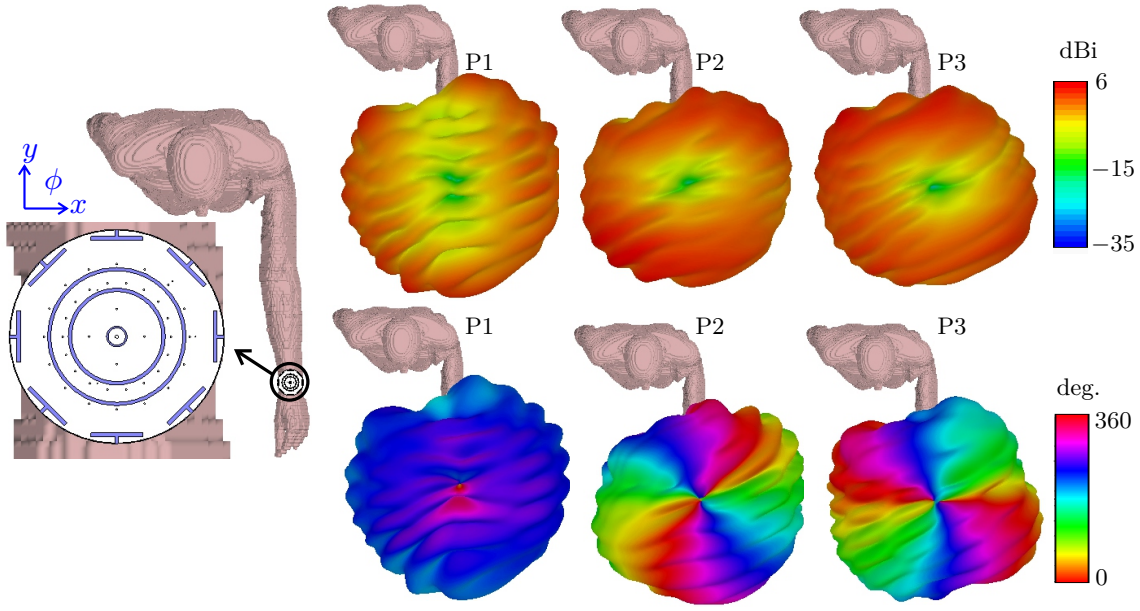

(a)

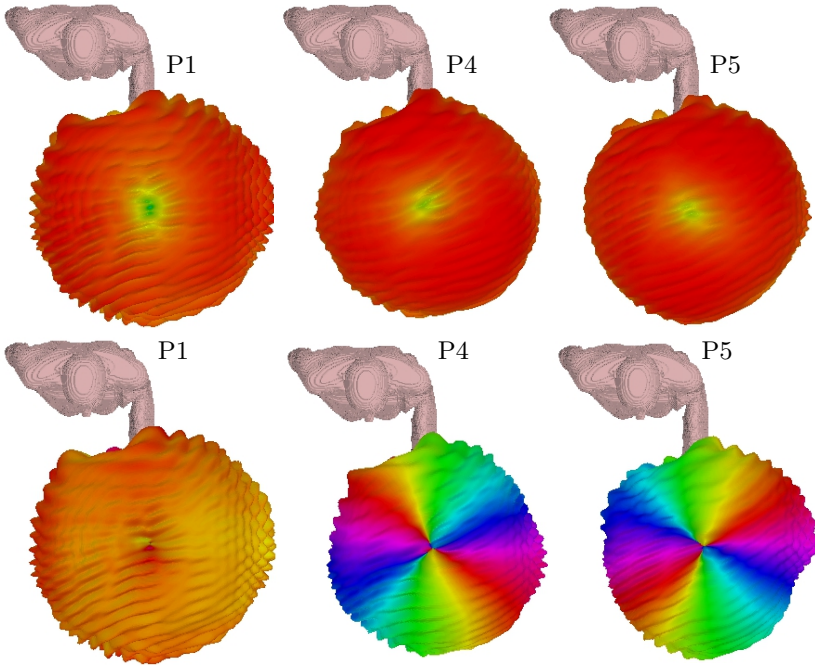

(b)

Figure 9.14: Antenna patterns using the Gustav voxel model with the elongated hand. (a) Lower band f_0. (b) Upper band f_1.

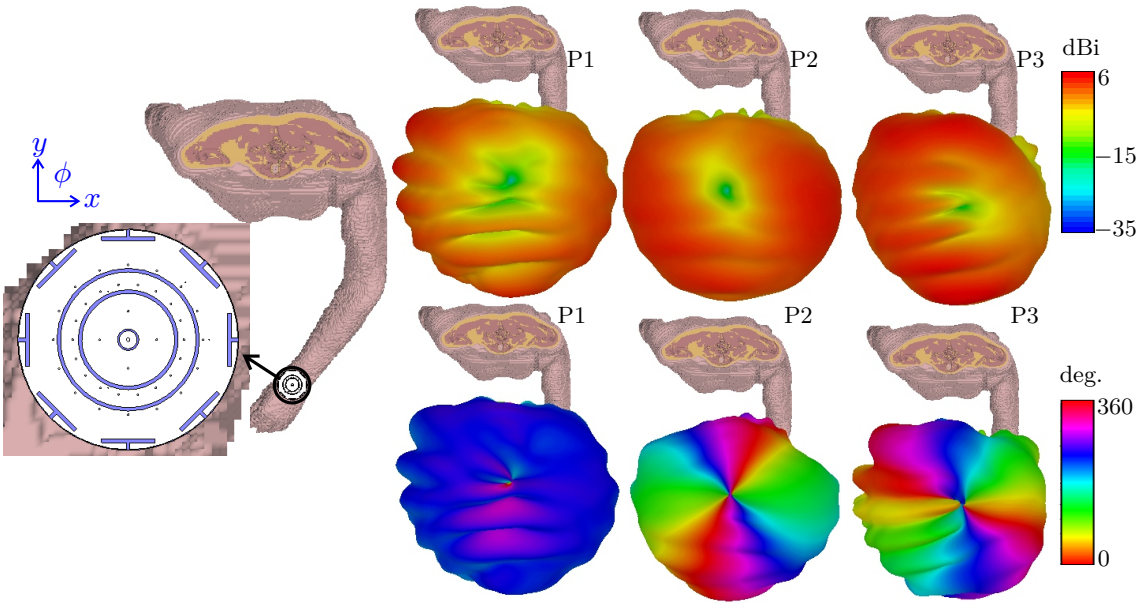

(a)

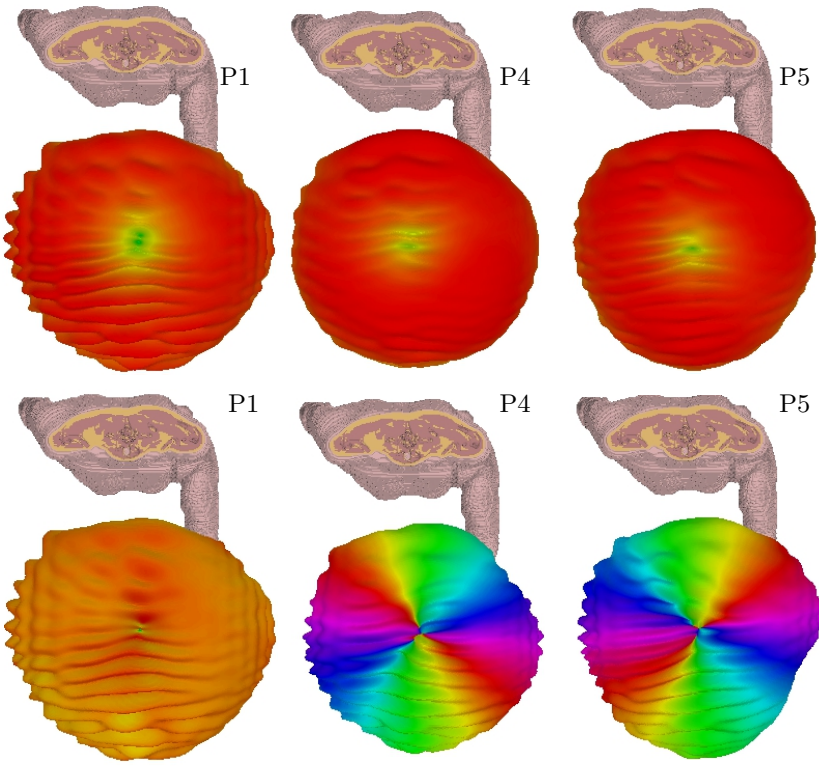

(b)

Figure 9.15: Antenna patterns using the Gustav voxel model with the bent forearm. (a) Lower band f_0. (b) Upper band f_1.

9.4.3 Specific Absorption Rate Analysis

Because the antenna is proposed for on-body IoT applications, the electromagnetic field exposure when exciting each port of the proposed dual-band antenna are investiggated using Specific Absorption Rate (SAR) computations. The setup for this work follows the Federal Communications Comission (FCC) guidelines under two conditions: wrist-worn and the next-to-the-mouth validation steups. For the wirst-worn case the antenna is placed in direct contact with a block filled with human hand tissue and the mass averaging is 10 g. In contrast, for the next-to-the mouth case, the antenna is placed 10 mm from a block filled with human head tissue and the mass averaging is 1 g. Note that both setups use a block with dimensions 220 mm × 120 mm and thickness 150 mm, and the SAR computations are done using an input power of 10 mW for each antenna port.

The wrist-worn setup simulated results are shown in Fig. 9.16a, and the peak SAR values at f_0 are: 0.0025 W/kg (for P1), 0.059 W/kg (for P2), and 0.06 W/kg (for P3). The results for f_1 are: 0.006 W/kg (for P1), 0.01 W/kg (for P4), and 0.01 W/kg (for P5). These results indicate higher SAR values for the f_0. However, all the results are well below the FCC SAR limits for the wrist-worn setup, i.e., $\ll$ 4 W/kg. The SAR results for the next-to-the-mouth setup are shown in Fig. 9.16b. The peak SAR values at f_0 are: 0.149 W/kg (for P1), 0.166 W/kg (for P2), and 0.138 W/kg (for P3). The values at f_1 are: 0.241 W/kg (for P1), 0.395 W/kg (for P4), and 0.392 W/kg (for P5). For this case too, very low SAR values are also obtained, and similarly to the wrist-worn setup, they are all below the FCC limits of 1.6 W/kg.

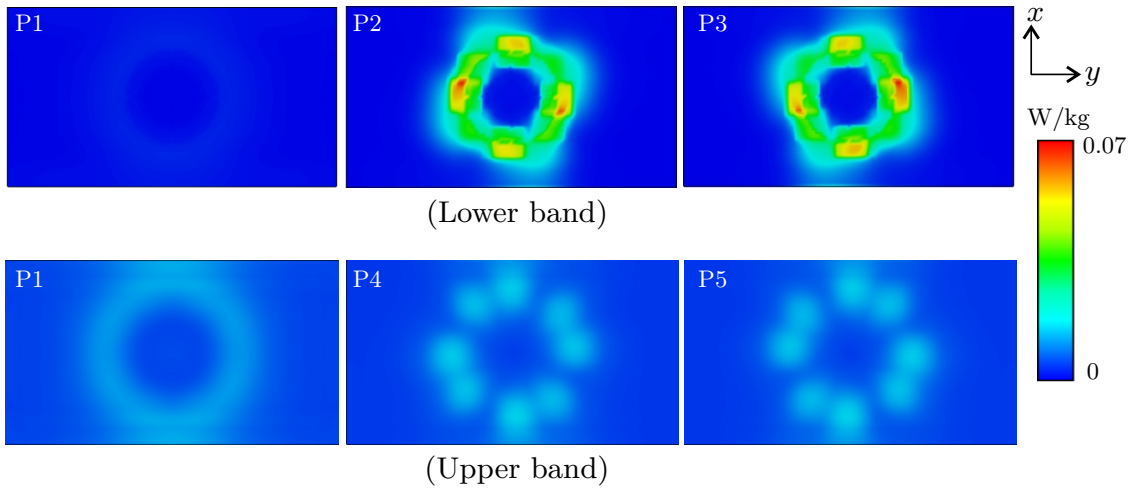

(a)

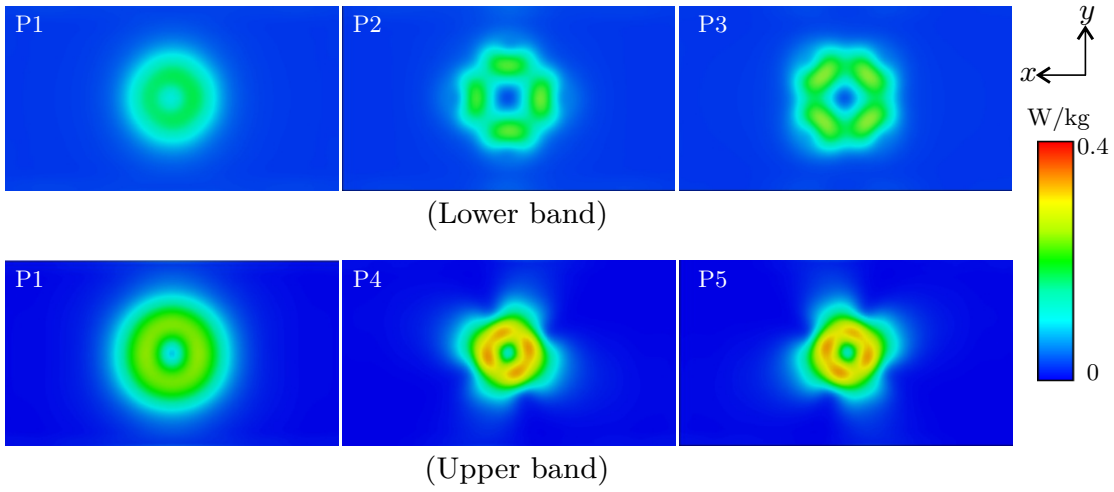

(b)

Figure 9.16: SAR results. (a) Wrist-worn setup results. (b) Next-to-the-mouth setup results.

9.5 Beamforming Performance

To experimentally validate the on-body performance the measurement setup shown in Fig. 9.17 is used. Table 9.1 outlines the ports' excitations used in order to steer the beams towards the desired direction. The obtained beamforming is shown in Fig. 9.18a and Fig. 9.18b, for the Free Space (FS) scenario. The main beam was steered in two directions, separated by 90° to cover the entire azimuthal plane with vertical linear polarization. It can be seen that the antenna is capable of directing the main beam in the desired directions at both bands. Fig. 9.19a and Fig. 9.19b show the On-Body (OB) beamforming performance. In this case, too, the beam is steered into two different directions separated by 90°. In general, beamwidths discrepancies are observed. This may be due to manufacturing tolerances, and phantom discrepancies.

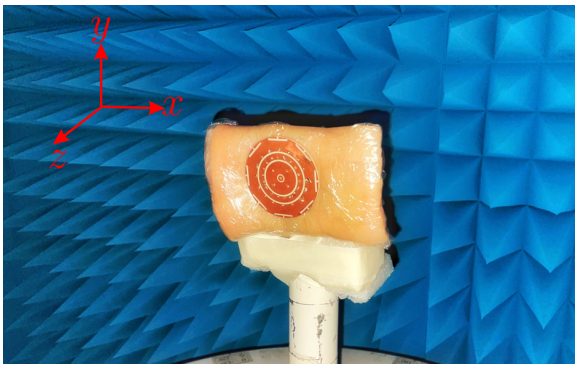

Figure 9.17: On-body anechoic chamber measurement setup.

Table 9.1: Port Excitations for the Beamforming Measured Performance

ϕ_d	Case	$\lvert A_1\rvert$	$\Delta\psi_1$	$\lvert A_2\rvert$	$\Delta\psi_2$	$\lvert A_3\rvert$	$\Delta\psi_3$	$\lvert A_4\rvert$	$\Delta\psi_4$	$\lvert A_5\rvert$	$\Delta\psi_5$
0°/180°, f_0	FS	1	0°	1	60°	1	147°	-	-	-	-
90°/270°, f_0	FS	1	0°	1	75°	1	36°	-	-	-	-
0°/180°, f_1	FS	1	0°	-	-	-	-	1	86°	1	85°
90°/270°, f_1	FS	1	0°	-	-	-	-	1	82°	1	99°
0°/180°, f_0	OB	1	0°	1	33°	1	130°	-	-	-	-
90°/270°, f_0	OB	1	0°	1	214°	1	55°	-	-	-	-
0°/180°, f_1	OB	1	0°	-	-	-	-	1	97°	1	98°
90°/270°, f_1	OB	1	0°	-	-	-	-	1	63°	1	87°

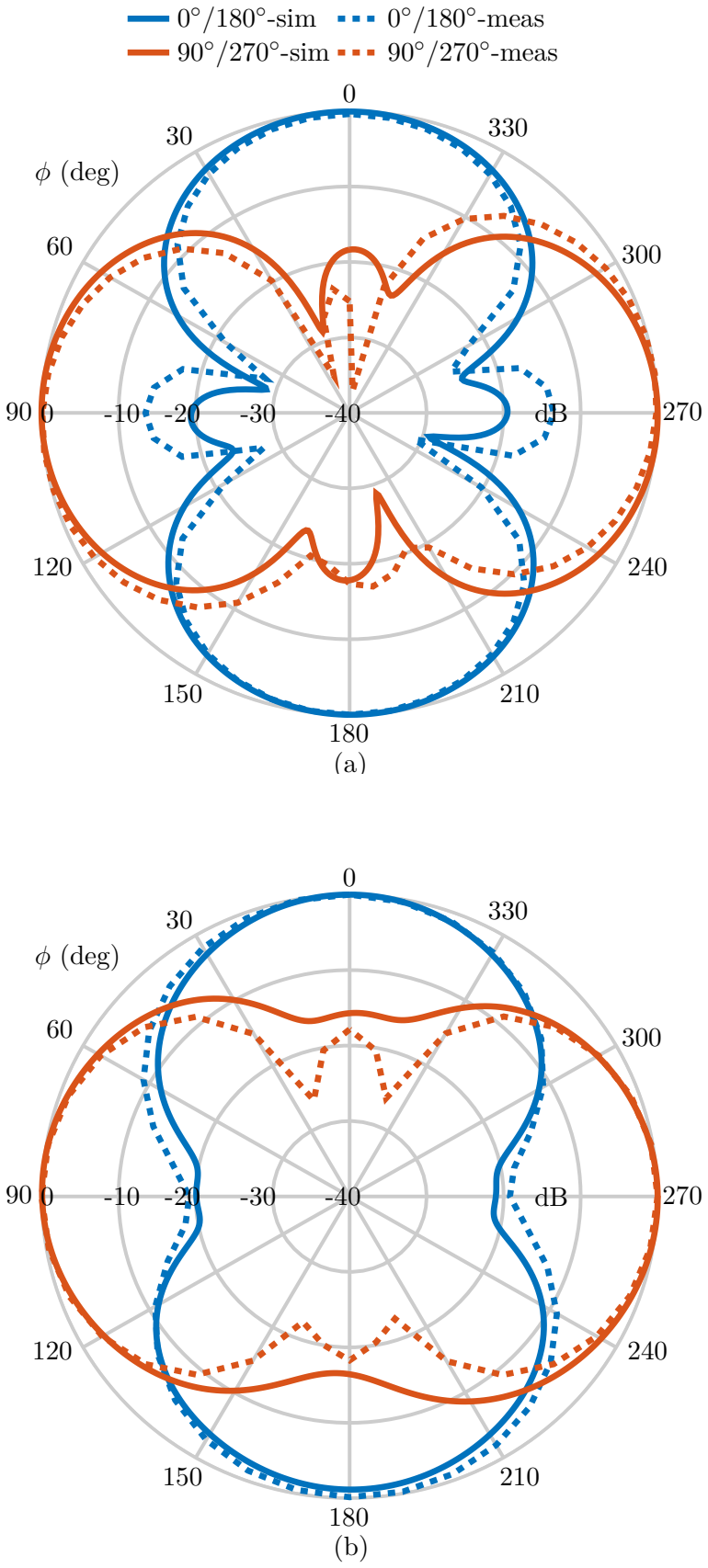

Figure 9.18: Normalized radiation patterns showing xy-plane beamforming, solid lines (simulations) and dashed lines (measurements). (a) Free space lower band. (b) Free space upper band.

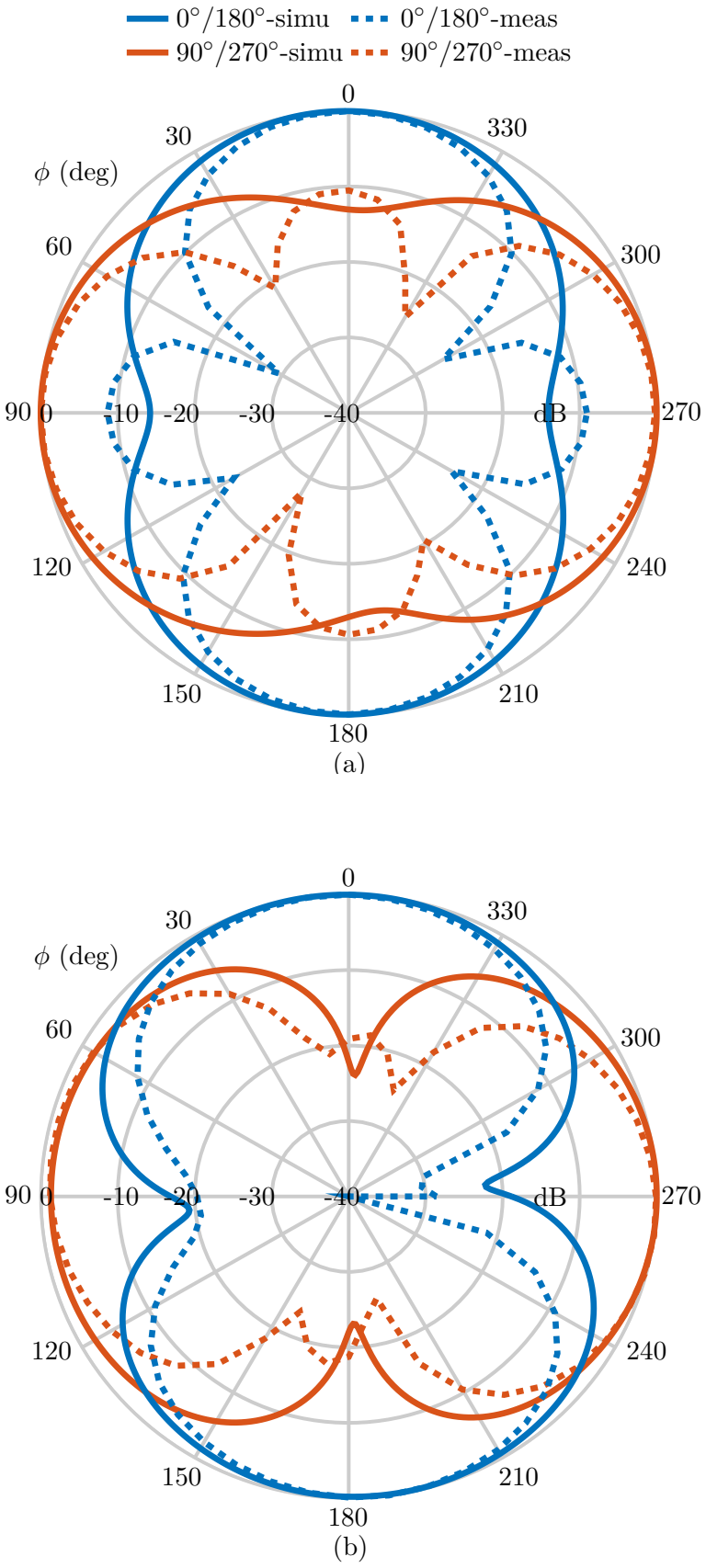

Figure 9.19: Normalized radiation patterns showing xy-plane beamforming, solid lines (simulations) and dashed lines (measurements). (a) On-body lower band. (b) On-body upper band.

9.6 Summary

This Chapter investigated a *SMB* multi-band principle for on-body IoT devices. A 5-port planar antenna of 0.48λ diameter and a very low profile of 0.01λ was proposed to realize dual-band beamforming functionalities across the azimuthal plane. A multi-layer phantom was used to test the antenna for on-body IoT scenarios, and the pattern performance was further validated on a realistic human model. Specific absoprtion rate analyses were conducted to guarantee human body safety. The design was manufactured and experimentally validated, and it was a good agreement was achieved between the simulated and measured results. Overall, the achieved performance demonstrates the potential of the *SMB* multi-band technique as an enabling technology to perform localization and enhance the secrecy and privacy of emerging on-body IoT devices.

10 Conclusions and Outlook

Conclusions and Outlook

10.1 Conclusions

The Internet of Things (IoT) is an increasingly relevant technology that is gaining popularity and being more widely incorporated into various modern applications, such as healthcare and smart homes. However, despite this tremendous growth, several challenges still need to be addressed to enhance the performance of small IoT devices. The main goal of this thesis was to propose new antenna technology and novel beamforming concepts that allow beamforming from compact antennas. The thesis also studied the application of the proposed beamforming principle to realize Directional Modulation (DM) and Angle of Arrival (AoA) estimation techniques.

Building on the theoretical formulation of *spherical modes*, a beamforming concept was proposed in Chapter 3, demonstrating that by exploiting the different phase characteristics of omnidirectional *spherical modes* excited within a constrained antenna size, continuous unidirectional beamforming can be realized across the entire azimuthal plane. Chapter 4 and Chapter 5 investigated the suitability of the *Spherical Modes Beamforming (SMB)* principle for AoA and DM applications, respectively. A number of *SMB* antennas were proposed and benchmarked with classical arrays, demonstrating that the principle realizes comparable AoA and DM performances, with up to 70% miniaturization compared to Uniform Linear Arrays (ULAs), and up to 40% reduction compared to Uniform Circular Arrays (UCAs). The obtained results, therefore, open up the way to a very promising compact solution for AoA-based localization and physical layer security DM in many emerging and size-constrained IoT systems.

In Chapter 6, Three-Dimensional (3D) beamforming antennas were proposed to extend

the DM to cover both the azimuthal and elevation planes. This opens up the possibility to realize secure transmissions across different directions in the 3D space in emerging compact IoT systems. To further address the increasing demand for highly miniaturized antennas in IoT applications, this chapter proposed an Electrically Small Antenna (ESA) capable of 3D beamforming. Such beamforming properties open up a number of applications like AoA and DM, which were previously not feasible to implement using highly compact IoT devices.

The last three chapters Chapter 7, Chapter 8, and Chapter 9 focused on the study of *SMB* antennas performance to enhance the performance of on-body IoT devices. Chapter 8 proposed for the first-time compact planar 3D beamforming antennas to address the need for advanced beamforming in emerging on-body IoT systems, while Chapter 9 extended the *SMB* principle to meet the demand for multi-band operation in on-body IoT devices.

To conclude, this work introduced novel concepts to realize beamforming characteristics from highly miniaturized antennas, enabling advanced beamforming in small IoT devices. The concept was initially validated using stacked-patch structures and then improved to be implemented using compact planar structures. The concept was tested for AoA, DM and extended to enable on-body IoT applications. Therefore, the findings presented in this thesis are expected to be a key enabling technology to advance the field of small IoT platforms.

10.2 Outlook

Firstly, while compact 3D beamforming antennas are discussed in Chapter 6, and planar 3D beamforming designs are presented in Chapter 8, the DM performance realized in Chapter 6 is a dual-plane DM. This means that secure transmissions can be realized in either the azimuth or elevation plane. In other words, this is still a One-Dimensional (1D) DM that can transmit to either ϕ directions with fixed θ or towards θ directions with fixed ϕ. Therefore, future work can explore the 3D beamforming performance to realize a Two-Dimensional (2D) DM, allowing secure transmissions to (θ, ϕ) direction, where both values can be simultaneously varied. This characteristic will then allow secure transmission to-

wards any direction across the entire upper hemisphere.

Another aspect that can be addressed in future works is the limitation of the AoA capabilities discussed in Chapter 4 and Chapter 7, where only a 1D angle of arrival estimation is achieved. Future works can extend this capability to enable 2D AoA estimation from small IoT devices, i.e., the capability to estimate the angle arriving from any point across the upper hemisphere. Lastly, while Chapter 9 presented multi-band antennas capable of beamforming functionalities, the beamforming is limited to a bi-directional radiation pattern in the azimuthal plane. Therefore, unidirectional multi-band characteristics using planar compact designs need to be investigated in future work. In addition, future work can extend the multi-band beamforming to enable 3D scanning characteristics, in order to implement 2D DM and AoA estimation.

Bibliography

[1] L. Atzori, A. Iera, and G. Morabito, "The Internet of Things: A survey," *Computer networks*, vol. 54, no. 15, pp. 2787–2805, 2010.

[2] S. Li, L. D. Xu, and S. Zhao, "The Internet of Things: A survey," *Information systems frontiers*, vol. 17, pp. 243–259, 2015.

[3] Y. Qadri *et al.*, "The Future of Healthcare Internet of Things: A Survey of Emerging Technologies," *IEEE Com. Surveys & Tutorials*, vol. 22, no. 2, pp. 1121–1167, 2020.

[4] H. Habibzadeh *et al.*, "A Survey of Healthcare Internet of Things (HIoT): A Clinical Perspective," *IEEE Internet Things J.*, vol. 7, no. 1, pp. 53–71, 2020.

[5] J. W. Kim *et al.*, "Collecting Health Lifelog Data From Smartwatch Users in a Privacy-Preserving Manner," *IEEE Trans. Consumer Electron.*, vol. 65, no. 3, pp. 369–378, 2019.

[6] A. Mukherjee, "Physical-Layer Security in the Internet of Things: Sensing and Communication Confidentiality Under Resource Constraints," *Proceedings IEEE*, vol. 103, no. 10, pp. 1747–1761, 2015.

[7] J. H. Anajemba, T. Yue, C. Iwendi, P. Chatterjee, D. Ngabo, and W. S. Alnumay, "A Secure Multiuser Privacy Technique for Wireless IoT Networks Using Stochastic Privacy Optimization," *IEEE Internet Things J.*, vol. 9, no. 4, pp. 2566–2577, 2022.

[8] D. Wang, B. Bai, W. Zhao, and Z. Han, "A Survey of Optimization Approaches for Wireless Physical Layer Security," *IEEE Com. Surveys & Tutorials*, vol. 21, no. 2, pp. 1878–1911, 2019.

[9] Y. Liu, H.-H. Chen, and L. Wang, "Physical Layer Security for Next Generation Wireless Networks: Theories, Technologies, and Challenges," *IEEE Com. Surveys Tutorials*, vol. 19, no. 1, pp. 347–376, 2017.

[10] X. Chen *et al.*, "A Survey on Multiple-Antenna Techniques for Physical Layer Security," *IEEE Com Surveys Tutorials*, vol. 19, no. 2, pp. 1027–1053, 2017.

[11] D. Trung, Z. Xiangyun, and H. V. Poor, *Trusted Communications with Physical Layer Security for 5G and Beyond.* Institution of Engineering and Technology, 2018.

[12] M. P. Daly and J. T. Bernhard, "Directional Modulation Technique for Phased Arrays," *IEEE Trans. Antennas. Propag.*, vol. 57, no. 9, pp. 2633–2640, 2009.

[13] Y. Ding and V. Fusco, "A Synthesis-Free Directional Modulation Transmitter Using Retrodirective Array," *IEEE J. Sel. Topics Signal Processing*, vol. 11, no. 2, pp. 428–441, 2017.

[14] A. Babakhani, D. B. Rutledge, and A. Hajimiri, "Transmitter Architectures Based on Near-Field Direct Antenna Modulation," *IEEE J. Solid-State Circuits*, vol. 43, no. 12, pp. 2674–2692, 2008.

[15] Y. Ding and V. F. Fusco, "A Vector Approach for the Analysis and Synthesis of Directional Modulation Transmitters," *IEEE Trans. Antennas. Propag.*, vol. 62, no. 1, pp. 361–370, 2014.

[16] C. A. Balanis, *Antenna theory: analysis and design.* Wiley-Interscience, 2005.

[17] T. E. Tuncer and B. Friedlander, *Classical and Modern Direction-of-Arrival Estimation.* Boston: Academic Press, 2009.

[18] CST-Computer Simulation Technology Studio Suite, SIMULIA, 3DS Dassault Systems. [Online]. Available: https://www.3ds.com/products-services/simulia/products/cst-studio-suite/latest-release/

[19] The MathWorks Inc., "MATLAB version: 9.8.0.1451342 (R2020a) Update 5," Natick, Massachusetts, United States, 2023. [Online]. Available: https://www.mathworks.com

[20] LPKF Laser and Electronics. [Online]. Available: http://www.lpkfusa.com/RapidPCB/CircuitboardPlotters/c60.htm

[21] Vector Network Analyzer R&S ZVA. [Online]. Available: https://www.rohde-schwarz.com/products/test-and-measurement/network-analyzers_64043.html

[22] BBHA 9120 D. Calibrated Double Ridged Broadband Horn Antenna. [Online]. Available: https://www.schwarzbeck.de/en/antennas/broadband-horn-antennas/double-ridged-horn-antenna/404-bbha-9120-d-double-ridged-broadband-horn-antenna.html

[23] "IEEE Standard for Definitions of Terms for Antennas," *IEEE Std 145-2013 (Revision of IEEE Std 145-1993)*, pp. 1–50, 2014.

[24] D. M. Pozar, *Microwave engineering; 3rd ed.* Hoboken, NJ: Wiley, 2005. [Online]. Available: https://cds.cern.ch/record/882338

[25] J. Chalas, K. Fujimoto, J. L. Volakis, and K. Sertel, "CHAPTER 1 Survey of Small Antenna Theory," 2010. [Online]. Available: https://api.semanticscholar.org/CorpusID:110578923

[26] H. Mathis, "A short proof that an isotropic antenna is impossible," *PROCEEDINGS OF THE INSTITUTE OF RADIO ENGINEERS*, vol. 39, no. 8, pp. 970–970, 1951.

[27] J. R. James and P. S. Hall, *Handbook of microstrip antennas.* IET, 1989, vol. 1.

[28] R. Garg, P. Bhartia, B. I., and A. Ittipboon, Eds., *Microstrip Antenna Design Handbook.* Norwood, MA: Artech House, 2001.

[29] M. P. Daly and J. T. Bernhard, "Beamsteering in Pattern Reconfigurable Arrays Using Directional Modulation," *IEEE Trans. Antennas. Propag.*, vol. 58, no. 7, pp. 2259–2265, 2010.

[30] T. Hong, M.-Z. Song, and Y. Liu, "Dual-Beam Directional Modulation Technique for Physical-Layer Secure Communication," *IEEE Antennas Wireless Propagat. Lett.*, vol. 10, pp. 1417–1420, 2011.

[31] J. Butler, "Beam-forming matrix simplifies design of electronically scanned antennas," *Electronic Design*, vol. 9, pp. 170–173, 1961. [Online]. Available: https://api.semanticscholar.org/CorpusID:112814751

[32] Y. Ding and V. Fusco, "Sidelobe manipulation using Butler matrix for 60 GHz physical layer secure wireless communication," in *2013 Loughborough Antennas & Propagation Conference (LAPC)*, 2013, pp. 61–65.

[33] Y. Zhang, Y. Ding, and V. Fusco, "Sidelobe Modulation Scrambling Transmitter Using Fourier Rotman Lens," *IEEE Trans. Antennas. Propag.*, vol. 61, no. 7, pp. 3900–3904, 2013.

[34] N. Valliappan, A. Lozano, and R. W. Heath, "Antenna Subset Modulation for Secure Millimeter-Wave Wireless Communication," *IEEE Trans. Com.*, vol. 61, no. 8, pp. 3231–3245, 2013.

[35] Q. Zhu *et al.*, "Directional Modulation Based on 4-D Antenna Arrays," *IEEE Trans. Antennas. Propag.*, vol. 62, no. 2, pp. 621–628, 2014.

[36] N. N. Alotaibi and K. A. Hamdi, "Switched Phased-Array Transmission Architecture for Secure Millimeter-Wave Wireless Communication," *IEEE Trans. Com.*, vol. 64, no. 3, pp. 1303–1312, 2016.

[37] A. Kalantari *et al.*, "Directional Modulation Via Symbol-Level Precoding: A Way to Enhance Security," *IEEE J. Sel. Topics Signal Processing*, vol. 10, no. 8, pp. 1478–1493, 2016.

[38] M. Hafez *et al.*, "Secure Spatial Multiple Access Using Directional Modulation," *IEEE Trans. Wirel. Com.*, vol. 17, no. 1, pp. 563–573, 2018.

[39] F. Shu *et al.*, "Robust Secure Transmission of Using Main-Lobe-Integration-Based Leakage Beamforming in Directional Modulation MU-MIMO Systems," *IEEE Systems J.*, vol. 12, no. 4, pp. 3775–3785, 2018.

[40] Y. Ding, V. Fusco, J. Zhang, and W.-Q. Wang, "Time-Modulated OFDM Directional Modulation Transmitters," *IEEE Trans. Vehicular Tech.*, vol. 68, no. 8, pp. 8249–8253, 2019.

[41] W.-Q. Wang and Z. Zheng, "Hybrid MIMO and Phased-Array Directional Modulation for Physical Layer Security in mmWave Wireless Communications," *IEEE J. Sel. Areas Com.*, vol. 36, no. 7, pp. 1383–1396, 2018.

[42] L. Chen *et al.*, "An Efficient Directional Modulation Transmitter With Novel Crest Factor Reduction Technique," *IEEE Microw. Wirel. Components Lett.*, vol. 29, no. 8, pp. 554–556, 2019.

[43] J. M. Purushothama, Y. Ding, G. Goussetis, G. Huang, and Y. Xiao, "Synthesis of Energy Efficiency-Enhanced Directional Modulation Transmitters," *IEEE Trans. Green Com. Network.*, vol. 7, no. 2, pp. 635–648, 2023.

[44] G. Huang, Y. Ding, and S. Ouyang, "Multicarrier Directional Modulation Symbol Synthesis Using Time-Modulated Phased Arrays," *IEEE Antennas Wireless Propagat. Lett.*, vol. 20, no. 4, pp. 567–571, 2021.

[45] J. Hou, J. M. Purushothama, H. Fan, C. Song, Y. Ding, and M. Sellathurai, "Energy efficient time-modulated OFDM directional modulation transmitters," *Microw. Optical Techn. Lett.*, vol. 65, no. 1, pp. 5–13, 2023.

[46] A. Narbudowicz, M. J. Ammann, and D. Heberling, "Directional Modulation for Compact Devices," *IEEE Antennas Wireless Propagat. Lett.*, vol. 16, pp. 2094–2097, 2017.

[47] J. Parron, E. A. Cabrera-Hernandez, A. Tennant, and P. de Paco, "Multiport Compact Stacked Patch Antenna With 360° Beam Steering for Generating Dynamic Directional Modulation," *IEEE Trans. Antennas. Propag.*, vol. 69, no. 2, pp. 1162–1167, 2021.

[48] E. A. Cabrera-Hernandez, J. P. Granados, and A. Tennant, "Multiport Compact Stacked Patch Antenna For Multichannel Dynamic Directional Modulation," in *2021 15th European Conference on Antennas and Propagation (EuCAP)*, 2021, pp. 1–4.

[49] A. Abu Arisheh *et al.*, "A Dynamic Pattern Dipole Antenna for Secure Wireless Communications," in *2022 IEEE Inter. Symposium Antennas Propag. and USNC-URSI*, 2022, pp. 1470–1471.

[50] A. A. Arisheh, J. M. Merlo, and J. A. Nanzer, "Design of a Single-Element Dynamic Antenna for Secure Wireless Applications," *IEEE Trans. Antennas. Propag.*, vol. 71, no. 10, pp. 7715–7727, 2023.

[51] A. Zandamela, N. Marchetti, and A. Narbudowicz, "Electrically Small Multimodal 3D Beamforming MIMO Antenna for PHY-Layer Security," in *2023 17th European Conference on Antennas and Propagation (EuCAP)*, 2023, pp. 1–5.

[52] X.-Q. Zhu, Y.-X. Guo, and W. Wu, "Miniaturized Dual-Band and Dual-Polarized Antenna for MBAN Applications," *IEEE Trans. Antennas. Propag.*, vol. 64, no. 7, pp. 2805–2814, 2016.

[53] G. Jin *et al.*, "A Simple Planar Pattern-Reconfigurable Antenna Based on Arc Dipoles," *IEEE Antennas Wireless Propagat. Lett.*, vol. 17, no. 9, pp. 1664–1668, 2018.

[54] J. Ouyang *et al.*, "Center-Fed Unilateral and Pattern Reconfigurable Planar Antennas With Slotted Ground Plane," *IEEE Trans. Antennas. Propag.*, vol. 66, no. 10, pp. 5139–5149, 2018.

[55] A. Darvazehban, S. A. Rezaeieh, and A. Abbosh, "Pattern-Reconfigurable Loop–Dipole Antenna for Electromagnetic Pleural Effusion Detection," *IEEE Trans. Antennas. Propag.*, vol. 68, no. 8, pp. 5955–5964, 2020.

[56] Z. Wu, M.-C. Tang, M. Li, and R. W. Ziolkowski, "Ultralow-Profile, Electrically Small, Pattern-Reconfigurable Metamaterial-Inspired Huygens Dipole Antenna," *IEEE Trans. Antennas. Propag.*, vol. 68, no. 3, pp. 1238–1248, 2020.

[57] Z. Wang, Y. Ning, and Y. Dong, "Compact Shared Aperture Quasi-Yagi Antenna With Pattern Diversity for 5G-NR Applications," *IEEE Trans. Antennas. Propag.*, vol. 69, no. 7, pp. 4178–4183, 2021.

[58] J. A. Liu, Y. F. Cao, and X. Y. Zhang, "A Pattern-Reconfigurable Filtering Patch Antenna Using Embedded Resonators and Switchable Elements," *IEEE Trans. Antennas. Propag.*, vol. 70, no. 5, pp. 3828–3833, 2022.

[59] S. Zhao, Z. Wang, and Y. Dong, "A Planar Pattern-Reconfigurable Antenna With Stable Radiation Performance," *IEEE Antennas Wireless Propagat. Lett.*, vol. 21, no. 4, pp. 784–788, 2022.

[60] Y. Zhang *et al.*, "A Highly Pattern-Reconfigurable Planar Antenna With 360° Single- and Multi-Beam Steering," *IEEE Trans. Antennas. Propag.*, vol. 70, no. 8, pp. 6490–6504, 2022.

[61] D. Rodrigo, L. Jofre, and B. A. Cetiner, "Circular Beam-Steering Reconfigurable Antenna With Liquid Metal Parasitics," *IEEE Trans. Antennas. Propag.*, vol. 60, no. 4, pp. 1796–1802, 2012.

[62] T. Q. Tran and S. K. Sharma, "Radiation Characteristics of a Multimode Concentric Circular Microstrip Patch Antenna by Controlling Amplitude and Phase of Modes," *IEEE Trans. Antennas. Propag.*, vol. 60, no. 3, pp. 1601–1605, 2012.

[63] P.-Y. Qin, Y. J. Guo, and C. Ding, "A Beam Switching Quasi-Yagi Dipole Antenna," *IEEE Trans. Antennas. Propag.*, vol. 61, no. 10, pp. 4891–4899, 2013.

[64] M. Li *et al.*, "Compact Surface-Wave Assisted Beam-Steerable Antenna Based on HIS," *IEEE Trans. Antennas. Propag.*, vol. 62, no. 7, pp. 3511–3519, 2014.

[65] L. Zhang *et al.*, "Planar Ultrathin Small Beam-Switching Antenna," *IEEE Trans. Antennas. Propag.*, vol. 64, no. 12, pp. 5054–5063, 2016.

[66] J. Lin *et al.*, "A Survey on Internet of Things: Architecture, Enabling Technologies, Security and Privacy, and Applications," *IEEE Internet Things J.*, vol. 4, no. 5, pp. 1125–1142, 2017.

[67] M.-C. Tang, B. Zhou, and R. W. Ziolkowski, "Low-Profile, Electrically Small, Huygens Source Antenna With Pattern-Reconfigurability That Covers the Entire Azimuthal Plane," *IEEE Trans. Antennas. Propag.*, vol. 65, no. 3, pp. 1063–1072, 2017.

[68] Q. Cheng *et al.*, "Time-Invariant Angle-Range Dependent Directional Modulation Based on Time-Modulated Frequency Diverse Arrays," *IEEE Access*, vol. 5, pp. 26 279–26 290, 2017.

[69] A. H. Naqvi and S. Lim, "A Beam-Steering Antenna With a Fluidically Programmable Metasurface," *IEEE Trans. Antennas. Propag.*, vol. 67, no. 6, pp. 3704–3711, 2019.

[70] T. Liang, Y. Pan, and Y. Dong, "Miniaturized Pattern Reconfigurable Multi-Mode Antennas with Continuous Beam Steering Capability," *IEEE Trans. Antennas. Propag.*, pp. 1–1, 2023.

[71] M. A. Towfiq *et al.*, "A Reconfigurable Antenna With Beam Steering and Beamwidth Variability for Wireless Communications," *IEEE Trans. Antennas. Propag.*, vol. 66, no. 10, pp. 5052–5063, 2018.

[72] S.-J. Ha and C. W. Jung, "Reconfigurable Beam Steering Using a Microstrip Patch Antenna With a U-Slot for Wearable Fabric Applications," *IEEE Antennas Wireless Propagat. Lett.*, vol. 10, pp. 1228–1231, 2011.

[73] S. Yan and G. A. E. Vandenbosch, "Radiation Pattern-Reconfigurable Wearable Antenna Based on Metamaterial Structure," *IEEE Antennas Wireless Propagat. Lett.*, vol. 15, pp. 1715–1718, 2016.

[74] R. Masood, C. Person, and R. Sauleau, "A Dual-Mode, Dual-Port Pattern Diversity Antenna for 2.45-GHz WBAN," *IEEE Antennas Wireless Propagat. Lett.*, vol. 16, pp. 1064–1067, 2017.

[75] X. Tong *et al.*, "Switchable ON-/OFF-Body Antenna for 2.45 GHz WBAN Applications," *IEEE Trans. Antennas. Propag.*, vol. 66, no. 2, pp. 967–971, 2018.

[76] D. Wen *et al.*, "Design of a MIMO Antenna With High Isolation for Smartwatch Applications Using the Theory of Characteristic Modes," *IEEE Trans. Antennas. Propag.*, vol. 67, no. 3, pp. 1437–1447, 2019.

[77] Z. G. Liu and Y. X. Guo, "Dual Band Low Profile Antenna for Body Centric Communications," *IEEE Trans. Antennas. Propag.*, vol. 61, no. 4, pp. 2282–2285, 2013.

[78] S.-W. Su and Y.-T. Hsieh, "Integrated Metal-Frame Antenna for Smartwatch Wearable Device," *IEEE Trans. Antennas. Propag.*, vol. 63, no. 7, pp. 3301–3305, 2015.

[79] D. Wu and S. W. Cheung, "A Cavity-Backed Annular Slot Antenna With High Efficiency for Smartwatches With Metallic Housing," *IEEE Trans. Antennas. Propag.*, vol. 65, no. 7, pp. 3756–3761, 2017.

[80] B. Wang and S. Yan, "Design of smartwatch integrated antenna with polarization diversity," *IEEE Access*, vol. 8, pp. 123 440–123 448, 2020.

[81] H. Sun *et al.*, "Design of Pattern-Reconfigurable Wearable Antennas for Body-Centric Communications," *IEEE Antennas Wireless Propagat. Lett.*, vol. 19, no. 8, pp. 1385–1389, 2020.

[82] G.-P. Gao *et al.*, "A Compact Dual-Mode Pattern-Reconfigurable Wearable Antenna for the 2.4-GHz WBAN Application," *IEEE Trans. Antennas. Propag.*, vol. 71, no. 2, pp. 1901–1906, 2023.

[83] D. Munoz, F. Bouchereau, C. Vargas, and R. Enriquez, *Position Location Techniques and Applications*. Oxford: Academic Press, 2009.

[84] Z. Chen, G. Gokeda, and Y. Yu, *Introduction to Direction-of-arrival Estimation*. Artech House, 2010.

[85] V. Krishnaveni, T. Kesavamurthy, and B. Aparna, "Beamforming for direction-of-arrival (DOA) estimation-a survey," *International Journal of Computer Applications*, vol. 61, no. 11, 2013.

[86] E. Gentilho Jr, P. R. Scalassara, and T. Abrão, "Direction-of-arrival estimation methods: A performance-complexity tradeoff perspective," *Journal of Signal Processing Systems*, vol. 92, no. 2, pp. 239–256, 2020.

[87] F. Zafari, A. Gkelias, and K. K. Leung, "A Survey of Indoor Localization Systems and Technologies," *IEEE Com. Surveys Tutorials*, vol. 21, no. 3, pp. 2568–2599, 2019.

[88] Y. Li, Y. Zhuang, X. Hu, Z. Gao, J. Hu, L. Chen, Z. He, L. Pei, K. Chen, M. Wang, X. Niu, R. Chen, J. Thompson, F. M. Ghannouchi, and N. El-Sheimy, "Toward Location-Enabled IoT (LE-IoT): IoT Positioning Techniques, Error Sources, and Error Mitigation," *IEEE Internet Things J.*, vol. 8, no. 6, pp. 4035–4062, 2021.

[89] B. Friedlander and A. Weiss, "Direction finding in the presence of mutual coupling," *IEEE Trans. Antennas. Propag.*, vol. 39, no. 3, pp. 273–284, 1991.

[90] A. Weiss and B. Friedlander, "Mutual coupling effects on phase-only direction finding," *IEEE Trans. Antennas. Propag.*, vol. 40, no. 5, pp. 535–541, 1992.

[91] C. Roller and W. Wasylkiwskyj, "Effects of mutual coupling on super-resolution DF in linear arrays," in *[Proceedings] ICASSP-92: 1992 IEEE International Conference on Acoustics, Speech, and Signal Processing*, vol. 5, 1992, pp. 257–260 vol.5.

[92] K. Pasala and E. Friel, "Mutual coupling effects and their reduction in wideband direction of arrival estimation," *IEEE Trans. Aerospace Electronic Sys.*, vol. 30, no. 4, pp. 1116–1122, 1994.

[93] B. C. Ng and C. M. S. See, "Sensor-array calibration using a maximum-likelihood approach," *IEEE Trans. Antennas. Propag.*, vol. 44, no. 6, pp. 827–835, 1996.

[94] I. Solomon, D. Gray, Y. Abramovich, and S. Anderson, "Receiver array calibration using disparate sources," *IEEE Trans. Antennas. Propag.*, vol. 47, no. 3, pp. 496–505, 1999.

[95] R. Adve and T. Sarkar, "Compensation for the effects of mutual coupling on direct data domain adaptive algorithms," *IEEE Trans. Antennas. Propag.*, vol. 48, no. 1, pp. 86–94, 2000.

[96] K. Dandekar, H. Ling, and G. Xu, "Experimental study of mutual coupling compensation in smart antenna applications," *IEEE Trans. Wirel. Communic.*, vol. 1, no. 3, pp. 480–487, 2002.

[97] H. Hui, "Improved compensation for the mutual coupling effect in a dipole array for direction finding," *IEEE Trans. Antennas. Propag.*, vol. 51, no. 9, pp. 2498–2503, 2003.

[98] ——, "Compensating for the mutual coupling effect in direction finding based on a new calculation method for mutual impedance," *IEEE Antennas and Wireless Propagation Letters*, vol. 2, pp. 26–29, 2003.

[99] Q. Bao, C. Ko, and W. Zhi, "Doa estimation under unknown mutual coupling and multipath," *IEEE Trans. Aerospace Electronic Sys.*, vol. 41, no. 2, pp. 565–573, 2005.

[100] Y. Horiki and E. Newman, "A self-calibration technique for a DOA array with near-zone scatterers," *IEEE Trans. Antennas. Propag.*, vol. 54, no. 4, pp. 1162–1166, 2006.

[101] M. Lin and L. Yang, "Blind Calibration and DOA Estimation With Uniform Circular Arrays in the Presence of Mutual Coupling," *IEEE Antennas Wireless Propagat. Lett.*, vol. 5, pp. 315–318, 2006.

[102] R. Goossens and H. Rogier, "A Hybrid UCA-RARE/Root-MUSIC Approach for 2-D Direction of Arrival Estimation in Uniform Circular Arrays in the Presence of Mutual Coupling," *IEEE Trans. Antennas. Propag.*, vol. 55, no. 3, pp. 841–849, 2007.

[103] Z. Ye and C. Liu, "2-D DOA Estimation in the Presence of Mutual Coupling," *IEEE Trans. Antennas. Propag.*, vol. 56, no. 10, pp. 3150–3158, 2008.

[104] Z. Ye, J. Dai, X. Xu, and X. Wu, "DOA Estimation for Uniform Linear Array with Mutual Coupling," *IEEE Trans. Aerospace Electronic Sys.*, vol. 45, no. 1, pp. 280–288, 2009.

[105] J. Dai, D. Zhao, and X. Ji, "A Sparse Representation Method for DOA Estimation With Unknown Mutual Coupling," *IEEE Antennas Wireless Propagat. Lett.*, vol. 11, pp. 1210–1213, 2012.

[106] G. Byun, H. Choo, and H. Ling, "Optimum Placement of DF Antenna Elements for Accurate DOA Estimation in a Harsh Platform Environment," *IEEE Trans. Antennas. Propag.*, vol. 61, no. 9, pp. 4783–4791, 2013.

[107] H.-S. Lui and H. T. Hui, "Direction-of-Arrival Estimation: Measurement using compact antenna arrays under the influence of mutual coupling," *IEEE Antennas Propagat. Mag.*, vol. 57, no. 6, pp. 62–68, 2015.

[108] M. Wang, X. Ma, S. Yan, and C. Hao, "An Autocalibration Algorithm for Uniform Circular Array With Unknown Mutual Coupling," *IEEE Antennas Wireless Propagat. Lett.*, vol. 15, pp. 12–15, 2016.

[109] B. Liao, S.-C. Chan, L. Huang, and C. Guo, "Iterative Methods for Subspace and DOA Estimation in Nonuniform Noise," *IEEE Trans. Signal Processing*, vol. 64, no. 12, pp. 3008–3020, 2016.

[110] C.-L. Liu and P. P. Vaidyanathan, "Super Nested Arrays: Linear Sparse Arrays With Reduced Mutual Coupling—Part I: Fundamentals," *IEEE Trans. Signal Processing*, vol. 64, no. 15, pp. 3997–4012, 2016.

[111] A. M. Elbir, "Direction Finding in the Presence of Direction-Dependent Mutual Coupling," *IEEE Antennas Wireless Propagat. Lett.*, vol. 16, pp. 1541–1544, 2017.

[112] Z.-M. Liu, C. Zhang, and P. S. Yu, "Direction-of-Arrival Estimation Based on Deep Neural Networks With Robustness to Array Imperfections," *IEEE Trans. Antennas. Propag.*, vol. 66, no. 12, pp. 7315–7327, 2018.

[113] W. Hu and Q. Wang, "DOA Estimation for UCA in the Presence of Mutual Coupling via Error Model Equivalence," *IEEE Wireless Commun. Lett.*, vol. 9, no. 1, pp. 121–124, 2020.

[114] S. Kabiri, E. Kornaros, and F. De Flaviis, "Tightly Coupled Array Design Based on Phase Center Contour for Indoor Direction Findings in Harsh Environments," *IEEE Trans. Antennas. Propag.*, vol. 68, no. 4, pp. 2698–2713, 2020.

[115] M. G. Pralon, G. Del Galdo, M. Landmann, M. A. Hein, and R. S. Thoma, "Suitability of Compact Antenna Arrays for Direction-of-Arrival Estimation," *IEEE Trans. Antennas. Propag.*, vol. 65, no. 12, pp. 7244–7256, 2017.

[116] X. Yu and H. Xin, "Direction-of-Arrival Estimation Enhancement for Closely Spaced Electrically Small Antenna Array," *IEEE Trans. Microw. Theory Techn.*, vol. 66, no. 1, pp. 477–484, 2018.

[117] S. Hwang, S. Burintramart, T. K. Sarkar, and S. R. Best, "Direction of Arrival (DOA) Estimation Using Electrically Small Tuned Dipole Antennas," *IEEE Trans. Antennas. Propag.*, vol. 54, no. 11, pp. 3292–3301, 2006.

[118] S. Abielmona, H. V. Nguyen, and C. Caloz, "Analog Direction of Arrival Estimation Using an Electronically-Scanned CRLH Leaky-Wave Antenna," *IEEE Trans. Antennas. Propag.*, vol. 59, no. 4, pp. 1408–1412, 2011.

[119] M. Burtowy, M. Rzymowski, and L. Kulas, "Low-Profile ESPAR Antenna for RSS-Based DoA Estimation in IoT Applications," *IEEE Access*, vol. 7, pp. 17 403–17 411, 2019.

[120] M. J. Slater and J. T. Bernhard, "Study of balun effects with electrically small antennas for a whitespace direction finding system," in *2010 IEEE Antennas and Propagation Society International Symposium*, 2010, pp. 1–4.

[121] M. J. Slater, C. D. Schmitz, M. D. Anderson, D. L. Jones, and J. T. Bernhard, "Demonstration of an Electrically Small Antenna Array for UHF Direction-of-Arrival Estimation," *IEEE Trans. Antennas. Propag.*, vol. 61, no. 3, pp. 1371–1377, 2013.

[122] M. Pralon, L. Pralon, B. Pompeo, G. Beltrao, T. Pasetto, and R. Thomä, "Decoupling Evaluation of Compact Phased Array Radars," in *2018 19th International Radar Symposium (IRS)*, 2018, pp. 1–10.

[123] C. Y. Kataria, G. X. Gao, and J. T. Bernhard, "Design of a Compact Hemispiral GPS Antenna With Direction Finding Capabilities," *IEEE Trans. Antennas. Propag.*, vol. 67, no. 5, pp. 2878–2885, 2019.

[124] R. Pohlmann, S. A. Almasri, S. Zhang, T. Jost, A. Dammann, and P. A. Hoeher, "On the Potential of Multi-Mode Antennas for Direction-of-Arrival Estimation," *IEEE Trans. Antennas Propag.*, vol. 67, no. 5, pp. 3374–3386, 2019.

[125] R. Pohlmann, G. Pedregosa, S. Caizzone, E. Staudinger, and P. A. Hoeher, "Multi-Mode Antenna Enabled Direction-of-Arrival Estimation for Swarm Navigation," in *2019 16th Workshop on Positioning, Navigation and Communications (WPNC)*, 2019, pp. 1–6.

[126] R. Pohlmann, E. Staudinger, S. Zhang, S. Caizzone, A. Dammann, and P. A. Hoeher, "In-Field Calibration of a Multi-Mode Antenna for DoA Estimation," in *2021 15th European Conference on Antennas and Propagation (EuCAP)*, 2021, pp. 1–5.

[127] L. Grundmann, N. Peitzmeier, and D. Manteuffel, "Investigation of Direction of Arrival Estimation Using Characteristic Modes," in *2021 15th European Conference on Antennas and Propagation (EuCAP)*, 2021, pp. 1–5.

[128] L. Grundmann and D. Manteuffel, "Selecting Characteristic Modes in Multi-Mode Direction Finding Antenna Design by Using Reconstructed Incident Fields," in *2022 16th European Conference on Antennas and Propagation (EuCAP)*, 2022, pp. 1–5.

[129] ——, "Evaluation Method and Design Guidance for Direction-Finding Antenna Systems," *IEEE Trans. Antennas. Propag.*, vol. 71, no. 9, pp. 7146–7157, 2023.

[130] A. Zandamela, A. Chiumento, N. Marchetti, and A. Narbudowicz, "Angle of Arrival Estimation via Small IoT Devices: Miniaturized Arrays vs. MIMO Antennas," *IEEE Internet Things Magazine*, vol. 5, no. 2, pp. 146–152, 2022.

[131] W. W. Hansen, "A New Type of Expansion in Radiation Problems," *Phys. Rev.*, vol. 47, pp. 139–143, Jan 1935. [Online]. Available: https://link.aps.org/doi/10.1103/PhysRev.47.139

[132] J. A. Stratton, *Electromagnetic Theory*, 1st ed. McGraw-Hill Companies (New York), 1941, the URL and misc. info are for a re-issue published in 2007 by Wiley-IEEE Press. [Online]. Available: http://www.amazon.com/Electromagnetic-Theory-IEEE-Press-Wave/dp/0470131535%3FSubscriptionId%3D13CT5CVB80YFWJEPWS02%26tag%3Dws%26linkCode%3Dxm2%26camp%3D2025%26creative%3D165953%26creativeASIN%3D0470131535

[133] J. E. Hansen, Ed., *Spherical Near-field Antenna Measurements*, ser. Electromagnetic Waves. Institution of Engineering and Technology, 1988. [Online]. Available: https://digital-library.theiet.org/content/books/ew/pbew026e

[134] F. Jensen, L. T. university of Denmark. Laboratory of electromagnetic theory, DTH., and LEF., *Electromagnetic Near-field - Far-field Correlations*. Technical University of Denmark, Laboratory of Electromagnetic Theory, 1970. [Online]. Available: https://books.google.ie/books?id=GzklHAAACAAJ

[135] A. Schubert, "S. l. belousov, tables of normalized associated legendre polynomials. (mathematical tables series, vol. 18). 379 s. oxford/london/new york/paris 1962. pergamon press. preis geb. £ 7 net," *ZAMM - Journal of Applied Mathematics and Mechanics / Zeitschrift für Angewandte Mathematik und Mechanik*, vol. 43, no. 10-11, pp. 513–513, 1963.

[136] A. R. Edmonds, *Angular Momentum in Quantum Mechanics*. Princeton: Princeton University Press, 1957.

[137] A. Gangi, S. Sensiper, and G. Dunn, "The characteristics of electrically short, umbrella top-loaded antennas," *IEEE Trans. Antennas. Propag.*, vol. 13, no. 6, pp. 864–871, 1965.

[138] Z. Shen and J. Wang, "Top-hat monopole antenna for conical-beam radiation," *IEEE Antennas and Wireless Propagation Letters*, vol. 10, pp. 396–398, 2011.

[139] A. Zandamela, A. Chiumento, N. Marchetti, M. J. Ammann, and A. Narbudowicz, "Exploiting Multimode Antennas for MIMO and AoA Estimation in Size-Constrained IoT Devices," *IEEE Sensors Letters*, vol. 7, no. 3, pp. 1–4, 2023.

[140] A. Zandamela, N. Marchetti, and A. Narbudowicz, "Compact mimo antenna for music-based angle of arrival estimation in wrist-worn devices," in *2022 International Workshop on Antenna Technology (iWAT)*, 2022, pp. 227–230.

[141] R. Schmidt, "Multiple emitter location and signal parameter estimation," *IEEE Trans. Antennas. Propag.*, vol. 34, no. 3, pp. 276–280, 1986.

[142] R. Zekavat and R. M. Buehrer, *Handbook of position location: Theory, practice and advances*. John Wiley & Sons, 2011, vol. 27.

[143] S. Best, "The radiation properties of electrically small folded spherical helix antennas," *IEEE Trans. Antennas. Propag.*, vol. 52, no. 4, pp. 953–960, 2004.

[144] P. Ioannides and C. Balanis, "Uniform circular arrays for smart antennas," *IEEE Antennas Propagat. Mag.*, vol. 47, no. 4, pp. 192–206, 2005.

[145] A. Zandamela, N. Marchetti, M. J. Ammann, and A. Narbudowicz, "Spherical Modes Driven Directional Modulation With a Compact MIMO Antenna," *IEEE Antennas and Wireless Propagation Letters*, vol. 22, no. 3, pp. 477–481, 2023.

[146] A. Narbudowicz and A. Zandamela, "Compact Beamforming Antennas for Directional Modulation in IoT," in *2023 IEEE International Symposium On Antennas And Propagation (ISAP)*, 2023, pp. 1–2.

[147] A. Zandamela, N. Marchetti, and A. Narbudowicz, "Stacked-Patch MIMO Antenna for Dual-Plane Beamsteering," in *2021 IEEE International Symposium on Antennas and Propagation and USNC-URSI Radio Science Meeting (APS/URSI)*, 2021, pp. 311–312.

[148] ——, "Compact Stacked-Patch Antenna for Directional Modulation in Azimuth and Elevation Planes," in *2022 IEEE International Symposium on Antennas and Propagation and USNC-URSI Radio Science Meeting (AP-S/URSI)*, 2022, pp. 1206–1207.

[149] ——, "Electrically Small Multimodal 3D Beamforming MIMO Antenna for PHY-Layer Security," in *2023 17th European Conference on Antennas and Propagation (EuCAP)*, 2023, pp. 1–5.

[150] A. A. Zandamela, K. Schraml, V. Jantarachote, S. Chalermwisutkul, D. Heberling, M. J. Ammann, and A. Narbudowicz, "On the Efficiency of Miniaturized 360° Beam-Scanning Antenna," in *2019 13th European Conference on Antennas and Propagation (EuCAP)*, 2019, pp. 1–4.

[151] A. Zandamela, N. Marchetti, and A. Narbudowicz, "Directional Modulation from a Wrist-Wearable Compact Antenna," in *2022 16th European Conference on Antennas and Propagation (EuCAP)*, 2022, pp. 1–5.

[152] R. J. Maughan, J. S. Watson, and J. R. Weir, "The relative proportions of fat, muscle and bone in the normal human forearm as determined by computed tomography." *Clinical science*, vol. 66 6, pp. 683–9, 1984. [Online]. Available: https://api.semanticscholar.org/CorpusID:24342779

[153] S. M. Gabriel, R. W. Lau, and C. Gabriel, "The dielectric properties of biological tissues: Ii. measurements in the frequency range 10 hz to 20 ghz." *Physics in medicine and biology*, vol. 41 11, pp. 2251–69, 1996. [Online]. Available: https://api.semanticscholar.org/CorpusID:11036295

[154] "IEEE Recommended Practice for Determining the Peak Spatial-Average Specific Absorption Rate (SAR) in the Human Head from Wireless Communications Devices: Measurement Techniques," *IEEE Std 1528-2013 (Revision of IEEE Std 1528-2003)*, pp. 1–246, 2013.

[155] R. E. Fields, *Evaluating compliance with FCC guidelines for human exposure to radiofrequency electromagnetic fields.* Federal Communications Commission Office of Engineering & Technology, 1997. [Online]. Available: https://transition.fcc.gov/bureaus/oet/info/documents/bulletins/oet65/oet65a.pdf

[156] A. Zandamela, N. Marchetti, and A. Narbudowicz, "Directional Modulation for Enhanced Privacy in Smartwatch Devices," *IEEE Antennas and Propagation Magazine*, vol. 2, no. 66, pp. 1–1, 2024.

[157] ——, "Flexible Multimode-Based Beamforming MIMO Antenna," in *2023 17th European Conference on Antennas and Propagation (EuCAP)*, 2023, pp. 1–5.

[158] A. Zandamela, N. Marchetti, M. J. Ammann, and A. Narbudowicz, "3D Beam-Steering MIMO Antenna for On-Body IoT Applications," *IEEE Transactions on Antennas and Propagation*, pp. 1–1, 2024.

[159] TAOGLAS. CAB.058 SMA(F)Jack to 3/3mm 0.047" Strip/Tin Semi-Rigid Cable 50mm(including Connectors). Accessed: 2023-11-01. [Online]. Available: https://www.taoglas.com/product/cab058-smafjack-to-33mm-0-047-striptin-semi-rigid-cable-50mmincluding-connectors/

[160] International Commission on Non-Ionizing Radiation Protection (ICNIRP), "Guidelines for Limiting Exposure to Electromagnetic Fields (100 kHz to 300 GHz)," *Health Physics*, vol. 118, no. 5, pp. 483–524, 2020.

[161] A. Zandamela, N. Marchetti, M. J. Ammann, and A. Narbudowicz, "A Dual-Band Planar Antenna for Angle of Arrival Estimation in On-Body IoT Devices," *IEEE Internet Things J.*, 2024, major revisions.